Modelling and Optimisation of Intelligent Surface-Assisted Communication Systems



Zhi Chai
Hertford College

A thesis submitted for the degree of
Doctor of Philosophy

Supervised by
Professor Justin P. Coon, Professor Stephen M. Morris

Department of Engineering Science
University of Oxford

Trinity Term, 2026

Dedicated to my parents and family, for their unwavering support and encouragement.

Declaration

I declare that this thesis is entirely my own work and, except where stated, describes my own research.

Zhi Chai
Hertford College

Acknowledgements

I would like to express my sincere gratitude to my supervisors, Professor Justin P. Coon and Professor Stephen M. Morris, for their invaluable guidance and support throughout my DPhil studies at the University of Oxford. I am especially grateful to Professor Coon for his insightful advice, encouragement, and patience, which have greatly shaped this work and my understanding of wireless communication systems. I also thank Professor Morris for his support, particularly in the early stages of my research, and for his valuable insights into liquid crystal-based reconfigurable surfaces.

I am grateful to my collaborators, Dr. Jiajie Xu and Professor Mohamed-Slim Alouini, for their helpful discussions and constructive suggestions. My thanks also go to members of the Information and Network Science (INS) Lab, especially Dr. Praneeth Vippathalla, Dr. Mihai Badiu, Yunchuan Huang, and Aniq Rahman, for creating a supportive and stimulating research environment. I also appreciate discussions with colleagues in the Optical Communications Group, including Dr. Abderrahmen Trichili, Professor Dominic O'Brien, and Dr. James Farmer.

I would like to thank Professor Steve Sheard for his valuable feedback as my assessor during the Transfer and Confirmation of Status. I am also grateful to the University of Oxford for providing an excellent research environment, and to the students I taught in Circuits and Communications for the rewarding experience.

Finally, I would like to express my deepest gratitude to my parents and family for their unwavering love, encouragement, and support. Their belief in me has been a constant source of motivation throughout my journey.

Abstract

Thesis Title: Modelling and Optimisation of Intelligent Surface-Assisted Communication Systems

Name: Zhi Chai

College: Hertford College

Degree: Doctor of Philosophy

Terms and Year of Submission: Trinity 2026

With the increasing demand for high data rates and low-latency communications, the currently allocated commercial frequency spectrum has become increasingly scarce. Consequently, substantial attention has been directed towards higher frequency bands, particularly the millimetre wave (mmWave) spectrum. Although mmWave communications offer significantly wider bandwidth and enable higher transmission speeds, their coverage is inherently limited due to the severe path loss and high penetration loss experienced by electromagnetic waves at such high frequencies. Reconfigurable intelligent surfaces (RISs), a promising technology proposed in recent years, have the potential to mitigate the coverage limitation through their anomalous reflection capability, ease of deployment, and low fabrication cost.

In this thesis, we present a comprehensive modelling and analysis of RIS-assisted mmWave networks, with a particular focus on indoor environments. The performance of RIS-assisted mmWave indoor networks is investigated from multiple perspectives, including the coverage probability of a single user and the maximum number of users that can be simultaneously supported in an interference-limited multi-user scenario. To ensure accurate performance evaluation, the indoor environment is modelled in a realistic manner by considering factors such as the height of the indoor space, the presence of obstacles, and the boundary effects of the environment. Based on this analysis, several key insights into the deployment of RIS in indoor mmWave networks

are obtained. In particular, obstacle density is identified as the dominant factor affecting coverage probability, whereas user clustering has a relatively moderate impact. Furthermore, although deploying more RISs can improve coverage, the performance gains gradually diminish as the number of RISs increases, and the benefits of RIS deployment become less pronounced with increasing transmitter density. In addition to the performance analysis, a deep reinforcement learning (DRL)-based joint optimisation framework is proposed to jointly design the precoding at the base station and the phase configuration of the RIS. Numerical results show that, for extremely large RISs, the proposed method can outperform conventional approaches such as zero-forcing (ZF) and regularised zero-forcing (RZF) in terms of sum spectral efficiency, at the cost of increased computational complexity. Overall, the analytical results and the proposed optimisation framework provide complementary perspectives for understanding and improving the performance of RIS-assisted mmWave indoor communication systems.

List of publications

The following is a list of articles that were published or are under review as a result of the research carried out for this thesis.

Articles

- Z.Chai, J. P. Coon, “Wideband RIS Systems: Coherence Bandwidth and Outage Analysis,” in IEEE Wireless Communications and Networking Conference, 2027. Under Review.
- Z. Chai, J. Xu, J. P. Coon and M. -S. Alouini, ”User Capacity Analysis of Intelligent Omni-Surface Assisted Indoor mmWave Networks,” in IEEE Transactions on Vehicular Technology, vol. 75, no. 9, pp. 20561-20574, Sept. 2026. Published.
- Z. Chai, J. Xu, J. P. Coon and M. -S. Alouini, ”Joint Beamforming With Extremely Large Scale RIS: A Sequential Multi-Agent A2C Approach,” in IEEE Wireless Communications Letters, vol. 15, pp. 1662-1666, 2026. Published.
- Z. Chai, J. Xu, J. P. Coon and M. -S. Alouini, ”RIS-Assisted Millimeter Wave Communications for Indoor Scenarios: Modeling and Coverage Analysis,” in IEEE Transactions on Vehicular Technology, vol. 75, no. 4, pp. 6224-6239, April 2026. Published.

Table of contents

Table of contents xiii

List of figures xvii

List of tables xx

Mathematical notation xxi

Glossary xxiii

1 Introduction 1
- 1.1 Background and Motivation 1
- 1.2 Thesis Contributions 7
- 1.3 Thesis Organisation 9

2 Literature Review 13
- 2.1 Hardware Structure 13
  - 2.1.1 RIS Element Design at mmWave 15
  - 2.1.2 RIS Element Design at Terahertz Frequencies 16
- 2.2 Electromagnetic Model of RIS 20
- 2.3 System Model of RIS 22
- 2.4 Channel Estimation for RIS-Assisted Systems 25
- 2.5 Simultaneously Transmitting and Reflecting RIS 26
- 2.6 Performance Analysis of Intelligent Surface-Assisted Communication Systems 27
- 2.7 RIS-Assisted Wideband Communication Systems 31
- 2.8 Deep Reinforcement Learning-Based Joint Optimisation of RIS-Assisted Communication Systems 32
- 2.9 Summary 33

3 RIS Element Modelling at High Frequencies 36
- 3.1 RIS Phase Modelling at mmWave 36
  - 3.1.1 RIS Phase Modelling at Terahertz Frequency 37
- 3.2 Reflecting Element Design and Verification 39
- 3.3 Phase Shift Approximation of a Single Liquid Crystal Reflecting Element 43
- 3.4 Numerical Results 45
- 3.5 Conclusion 52

4 Performance Analysis of RIS-Assisted mmWave Indoor Wireless Networks 53
- 4.1 System Model 53
- 4.2 Distance Distributions 59
  - 4.2.1 Direct Link 59

4.2.2 Indirect Link 62
4.3 Line-of-Sight Probability Characterisation 66
4.3.1 Direct Link Line-of-Sight Probability Calculation 66
4.3.2 Indirect Link Line-of-Sight Probability Calculation 68
4.4 Coverage Probability Characterisation 71
4.4.1 Coverage Probability Characterisation 71
4.4.2 Relationships between Network Parameters and Coverage Probability 72
4.4.3 Threshold-Based Analysis of RIS Contribution 76
4.5 Numerical Results 78
4.6 Conclusion 85

5 User Capacity Analysis of Intelligent Omni-Surface Assisted Millimetre Wave Indoor Networks 87
5.1 Introduction 87
5.2 System Model 88
5.2.1 Spatial Models 88
5.2.2 Multi-User Service 90
5.3 Far-Field Path-Loss and Interference Modelling 91
5.3.1 Propagation Regime Definitions 92
5.3.2 User Geometry: Distance and Angular Distributions 93
5.3.2.1 Distance Distribution between the jth User and the IOS 93
5.3.2.2 Azimuth and Elevation Angle Distributions and Angular Separation 94
5.3.3 Far-Field Path Loss 96
5.3.4 Far-field interference 97
5.4 Near-Field Path-Loss and Interference Modelling 99
5.4.1 Near-field Path Loss 99
5.4.2 Near-Field Interference 99
5.5 Coverage Probability 103
5.6 Computational Complexity Analysis 103
5.7 Impact of Near-Field Effects on User Capacity 105
5.8 Numerical Results 109
5.9 Conclusion 116

6 Wideband RIS Systems: Coherence Bandwidth and Outage Analysis 117
6.1 System Model 117
6.2 RIS Coherence Bandwidth 119
6.3 Outage Probability Analysis 124
6.3.1 Outage probability within the RIS coherence bandwidth .. 124
6.3.2 Outage probability outside the RIS coherence bandwidth . 126
6.4 Numerical Results 129
6.5 Conclusion 133

7 Joint Beamforming with Extremely Large Scale RIS: A Sequential Multi-Agent Advantage Actor Critic Approach 134

7.1 Introduction 134
7.2 System Model and Problem Statement 135
7.3 Sequential Multi-Agent A2C Algorithm 138
7.3.1 Algorithm Structure 139
7.3.2 Implementation Details 141
7.3.3 Complexity Analysis 142
7.4 Numerical Results 143
7.5 Conclusion 147

8 Conclusions and Future Work 148
8.1 Thesis Summary 148
8.2 Future Work 151
8.3 Conclusions 153

Appendix A Liquid Crystal 155
A.1 Introduction 155
A.2 Physical Properties of Liquid Crystal Materials 155
A.2.1 Molecular Structure 155
A.2.2 Order Parameter 156
A.3 Types of Liquid Crystal Materials 156
A.3.1 Thermotropic Liquid Crystals 156
A.3.1.1 Nematic Liquid Crystals 156
A.3.1.2 Smectic Liquid Crystals 157
A.3.1.3 Cholesteric Liquid Crystals 157
A.3.2 Lyotropic Liquid Crystals 157
A.4 Electromagnetic Tunability Mechanism 157
A.4.1 Electric-Field-Induced Molecular Reorientation 157
A.4.2 Effective Refractive Index 158
A.4.3 Phase Shift Mechanism 158
A.5 Liquid Crystal Based RIS at Terahertz Frequencies 159
A.5.1 Why Liquid Crystal is Suitable for Terahertz RIS 159
A.5.2 Typical RIS Unit Cell Structure 159
A.5.3 Challenges at Terahertz Frequencies 160
A.6 Summary 160

Appendix B Stochastic Geometry for Wireless Networks Analysis 161
B.1 Introduction 161
B.1.1 Binomial Point Process 161
B.1.2 Poisson Point Process 162
B.1.2.1 Homogeneous Poisson Point Process 162
B.1.2.2 Inhomogeneous Poisson Point Process 163
B.1.3 Hardcore Point Process 164
B.1.4 Point Processes, Transformations and Distances 164

Appendix C Order Statistics for Wireless Network Analysis 167

Appendix D Deep Reinforcement Learning for Wireless Communications 169

D.1 Introduction 169
D.1.1 Reinforcement Learning Fundamentals 170
D.1.2 Deep Reinforcement Learning 171

Bibliography **174**

List of figures

2.1 Illustration of the RIS hardware structure. 14
2.2 RIS element structure in [1] 16
2.3 RIS element structure/slot-loaded plane in [2] 16
2.4 liquid crystal (LC)-based THz RIS unit-cell architecture employing a complementary split-ring resonator (CSRR) above the LC layer [3]. .. 19
2.5 LC-based terahertz (THz) RIS unit-cell architecture employing a corner-truncated metallic patch and a pixelated ground plane [4]. 19
2.6 An illustration of an RIS-assisted end-to-end wireless communication system. 24

3.1 Cross-section illustration of the proposed reflecting element. 39
3.2 Schematic of the TeraSmart THz spectrometer and the transmission measurement configuration. The LC sample is positioned between the emitter and receiver, and the transmitted time-domain electric field is measured with and without the sample to characterise its frequency-dependent optical properties. 41
3.3 Frequency-dependent refractive indices extracted from transmission measurements of the E7-based 400 μm LC sample. The red and blue curves correspond to the refractive indices obtained at bias voltages of 0 V and 10 V, respectively. Their difference illustrates the voltage-dependent birefringence of the ultra-thick LC layer. 42
3.4 Geometric illustration of the impinging waves interacting with an LC reflecting element. 43
3.5 (a)–(b) Comparison of a single E7 LC element phase shift (relative to the 0-volt bias voltage) between numerical results and measured results with respect to the bias voltage at 0° incidence angle with frequency-invariant (a) and frequency-variant (b) extraordinary and ordinary refractive indices. (c) Phase shift response with respect to the incidence angle of an E7-based single LC element at 1 THz and 10 V bias voltage..... 47
3.6 (a)–(b) Phase shift response with respect to the bias voltage (a) and incidence angle (b) of a GT3-23001-based single LC element with $\varepsilon_{\parallel} = 3.28$, $\varepsilon_{\perp} = 2.46$, and thickness of 400 μm. 48
3.7 Performance comparison between the proposed 10×10 LC-RIS and conventional 10×10 RISs with 1-bit, 2-bit, and 3-bit phase quantisation, expressed as the directivity difference (LC-RIS minus conventional RIS). (a) Directivity difference versus LC layer thickness for E7 at 1.5 THz. (b) Directivity difference versus LC layer thickness for GT3-23001 at 1.5 THz. (c) Directivity difference versus operating frequency for E7. (d) Directivity difference versus operating frequency for GT3-23001. Panels (a) and (b) consider incidence angles of 30° and 60°, while panels (c) and (d) consider an incidence angle of 30°. 51

4.1 Illustration of the 3D RIS-assisted indoor mmWave network. 54
4.2 Illustration of the projected 3D RIS-assisted indoor mmWave network. 60
4.3 Illustration of the first category of the LOS probability calculation (top view). 67
4.4 Illustration of the second category of the LOS probability calculation (side view). 68
4.5 Illustration of the effects of boundary and feasible locations of obstacles on the indirect link LOS probability calculation. 69
4.6 Comparison between the approximate expectation obtained from (4.45) and the exact expectation calculated from (4.42), versus the number of transmitters N_T, with $a = 100$ m and $R_c = 5$ m. The mean horizontal distance $\mathbb{E}[\widetilde{D}_{\mathrm{tc},p}]$ is expressed in metres. 75
4.7 (a)–(c) Coverage probability variation with respect to obstacle density for different numbers of RISs: $N_R = 1$, $N_R = 10$, and $N_R = 20$, with $a = 100$ m. 80
4.8 Contribution of the RIS in terms of coverage probability with respect to obstacle density, with $a = 100$ m and $N_R = 10$. 82
4.9 (a) Coverage probability variation with respect to transmit power. (b) Contribution of the RIS to coverage probability under the same setting, with $a = 100$ m, $N_R = 10$, and $N_o = 236$. 82
4.10 (a) Coverage probability variation with respect to cluster radius R_c. (b) Contribution of the RIS to coverage probability under the same setting, with $a = 100$ m, $N_R = 10$, and $N_o = 236$. 83
4.11 (a) Coverage probability variation with respect to the number of RISs N_R. (b) Contribution of the RIS to coverage probability under the same setting, with $a = 100$ m and $N_o = 236$. 83
4.12 (a) Coverage probability variation with respect to obstacle density when node height is ignored. (b) Coverage probability variation with respect to obstacle density when obstacle radius is ignored, with $a = 100$ m and $N_R = 10$. 85

5.1 Illustration of an IOS-assisted mmWave 3D indoor communication network with hybrid fields 88
5.2 (a) Sidelobe leakage as an interference. (b) Mainlobe overlap as an interference 97
5.3 (a) Coverage probability variations of the first and second user for a total user number of 4, with transmit power being 1000 mW against the IOS/RIS element number. (b) Coverage probability variations of the first and second user for a total user number of 4, with transmit power being 500 mW against the IOS/RIS element number. (c) Coverage probability variations of the first and second user for a total user number of 4, with transmit power being 100 mW against the IOS/RIS element number. 112
5.4 User capacity of the IOS/RIS-assisted mmWave 3D indoor network with and without near-field effects, evaluated under various transmit power levels. Results are obtained for element spacings $e_x = e_y = d_x = d_y = \lambda/2$. 113

5.5 User capacity of the IOS/RIS-assisted mmWave 3D indoor network with and without near-field effects, evaluated under various transmit power levels. Results are obtained for element spacings $e_x = e_y = d_x = d_y = \lambda/4$. 113
5.6 (a) User type distribution of an IOS-assisted mmWave indoor network with an element number of 2048. (b) User type distribution of an IOS-assisted mmWave indoor network with an element number of 4096. 114
5.7 (a) User type distribution of an RIS-assisted mmWave indoor network with an element number of 2048. (b) User type distribution of an RIS-assisted mmWave indoor network with an element number of 4096. 115

6.1 Geometry illustration of the wideband RIS system 121
6.2 RIS coherence bandwidth comparison between the analytical result and the numerical optimisation result. The analytical result is evaluated using the phase-dispersion threshold $\varepsilon = 1$ rad. 128
6.3 Normalised RIS gain against the frequency offset relative to the centre frequency with 400 RIS elements. 129
6.4 Comparison of the outage probability against subcarrier number L within RIS coherence bandwidth with RIS element number of 36, $f_c = 10$ GHz, $B_c^{\mathrm{RIS}} = 543.34$ MHz, and $\Delta f = 100$ KHz. 132
6.5 Outage probability versus subcarrier number for $N = 36$, $f_c = 10$ GHz, and subcarrier spacings of (a) 20 MHz and (b) 40 MHz. Analysis 1 uses the approximation $\mathrm{SNR}_l \approx \gamma_c$ for all subcarriers, neglecting frequency-dependent combining loss. Analysis 2 uses $\mathrm{SNR}_l \approx \eta_l \gamma_c$, accounting for this loss through the gain reduction factor η_l. The vertical dashed line marks the subcarrier number at which the occupied bandwidth reaches the RIS coherence bandwidth. 132

7.1 (a)-(b) The actor network structure of the BS agent and an RIS agent. (c) Central critic network structure..... 138
7.2 Learning curve of the proposed algorithm. 144
7.3 (a) Achievable SE at different RIS sizes with 1-bit phase resolution, uniformly distributed users, and perfect CSI. (b) Achievable spectral efficiency (SE) at different RIS sizes for user cluster radii of 0.5 m and 2 m, with 1-bit phase resolution and perfect channel state information (CSI). (c) Achievable SE at different channel estimation errors with $N_R = 512$, 1-bit phase resolution, and uniformly distributed users. ... 145

List of tables

3.1 Parameter settings 46
3.2 Parameter settings for the performance analysis between the LC-RIS and the conventional RIS. 49

4.1 Rayleigh distances with different D and λ 63
4.2 Parameter setting 79

5.1 Element-size threshold values for different IOS apertures under the mean-field approximation with $\lambda = 0.01$ m and $\varepsilon_{\|} = 1 \times 10^{-3}$ 107
5.2 Parameter setting 111

6.1 Parameter setting 128

7.1 Parameter setting 144

Mathematical Notation

$f_X(x)$	Probability density function of a random variable X
$F_X(x)$	Cumulative distribution function of a random variable X
$\mathbb{E}[X]$	Expectation of a random variable X
$\mathrm{Var}[X]$	Variance of a random variable X
$\Gamma(\cdot)$	Gamma function
$\Gamma(\cdot,\cdot)$	Upper incomplete gamma function
$\gamma(\cdot,\cdot)$	Lower incomplete gamma function
$\arctan(\cdot)$	Inverse tangent function
$C(\cdot)$	Fresnel integral with $\cos(\cdot)$ as the integrand
$S(\cdot)$	Fresnel integral with $\sin(\cdot)$ as the integrand
$\mathcal{O}(\cdot)$	Big-O notation
$\binom{n}{k}$	Binomial coefficient
$\mathcal{CN}(\mu,\sigma^2)$	Circularly symmetric complex Gaussian distribution with mean μ and variance σ^2
Nakagami(m,Ω)	Nakagami distribution with shape parameter m and scale parameter Ω
Rayleigh(σ)	Rayleigh distribution with scale parameter σ
$\lVert\cdot\rVert$	Euclidean norm
$\lVert\cdot\rVert_F$	Frobenius norm
$\mathbb{C}^{m\times n}$	$m \times n$ complex space
$\mathbb{R}^{m\times n}$	$m \times n$ real space
$\lvert\cdot\rvert$	Absolute value
$(\cdot)^T$	Transpose operator

$(\cdot)^H$	Hermitian transpose operator
$(\cdot)^*$	Conjugate operator
$\sim$	Asymptotic equivalence notation

Glossary

A2C	Advantage actor-critic
BCD	Block coordinate descent
BPP	Binomial point process
BS	Base station
CASR	Complementary asymmetrically split ring
CDF	Cumulative distribution function
CMOS	Complementary metal-oxide semiconductor
CP	Coverage probability
CSI	Channel state information
CSRR	Complementary split-ring resonator
CTDE	Centralised-training and decentralised-execution
DDPG	Deep deterministic policy gradient
DF	Depth of focus
DPG	Deterministic policy gradient
DQN	Deep Q-network
DRL	Deep reinforcement learning
EM	Electromagnetic
EU	End user
FF	Far field
FSO	Free-space optics
GB	Gigabytes
GPP	Gaussian point process

HCPP Hard-core point process

HPPP Homogeneous Poisson point process

i.i.d. Independent and identically distributed

IOS Intelligent omni surface

IPPP Inhomogeneous Poisson point process

ISAC Integrated sensing and communication

LC Liquid crystal

LOS Line-of-sight

M2M Mobile-to-mobile

MDP Markov decision process

MISO Multiple-input-single-output

MLP Multilayer perceptron

MMSE Minimum mean square error

mmWave Millimetre wave

MU-MISO Multi-user multiple-input-single-output

NDF Non-depth-of-focus

NLOS Non-line-of-sight

NOMA Non-orthogonal multiple access

PDF Probability density function

PI Polyimide

PIN Positive intrinsic negative

PPO Proximal policy optimisation

PPP Poisson point process

QoS Quality-of-service

RF Radio frequency

RIS Reconfigurable intelligent surface

RL Reinforcement learning

RZF Regularised zero-forcing

SE Spectral efficiency

SINR Signal-to-interference-plus-noise ratio

SNR Signal-to-noise ratio

TD Temporal difference

TD3 Twin delayed DDPG

THz Terahertz

UAV Unmanned aerial vehicle

ZF Zero-forcing

Chapter 1

Introduction

1.1 Background and Motivation

With the rapid growth of mobile data traffic and the increasing demand for high-data-rate wireless services, the currently allocated frequency spectrum has become increasingly congested [5, 6]. Recent research indicates that global mobile data traffic and mobile subscriptions are expected to increase exponentially, reaching 250 gigabytes (GB) per user per month and 100 billion mobile-to-mobile (M2M) user subscriptions by the end of 2030 [7]. This rapid escalation in traffic demand has driven the evolution of cellular networks towards wider bandwidths, denser deployments, and more flexible use of the radio propagation environment.

One natural response to this challenge has been the exploitation of higher-frequency spectrum. The evolution from 4G to 5G already demonstrated the value of this approach: while conventional cellular systems mainly relied on sub-6 GHz bands to provide wide-area coverage, 5G New Radio introduced the use of both lower-frequency bands and millimetre wave (mmWave) frequency bands to support enhanced mobile broadband and high-capacity services. Looking beyond 5G, the future development of 6G, also referred to as IMT-2030, is expected to extend this trend further. According to the ITU framework for IMT-2030, future systems are envisaged to use a wide range of frequency bands, from sub-1 GHz to frequency bands above 100 GHz, in order to satisfy diverse requirements on coverage, capacity, latency, and service types [8]. In particular, applications requiring extremely high data rates and low latency may benefit from very large contiguous bandwidths, potentially on the order of tens of GHz, motivating the investigation of spectrum above 92 GHz as a complement to lower-frequency bands [8]. The move towards

higher frequencies is therefore not only a natural response to spectrum scarcity, but also an important enabling direction for future data-intensive services.

Building on this motivation, growing attention has been directed towards mmWave bands, spanning 30 GHz to 300 GHz. Moving wireless communications from the conventional sub-6 GHz bands to mmWave frequencies offers several compelling advantages, including: 1) higher transmission rates (e.g., peak data rates up to 20 Gbps [9]), 2) lower latency (e.g., around 1 ms [9]), and 3) higher connection density (e.g., up to 10^6 devices per square kilometre [9]). These characteristics make mmWave and potentially even higher-frequency bands attractive candidates for 5G-Advanced and future 6G networks.

However, raising the operating frequency also introduces significant side effects that cannot be overlooked. An important one among these is the greatly reduced coverage area caused by high path loss and high penetration loss at mmWave frequencies. The propagation of high-frequency signals is also more sensitive to blockage, human-body shadowing, and weak diffraction around obstacles. These effects are particularly pronounced in indoor environments, where walls, furniture, human bodies, and other objects can frequently obstruct the direct propagation path. As a result, although higher-frequency bands offer abundant spectrum resources, they also create a fundamental coverage challenge that must be addressed before their full potential can be realised in practical cellular networks.

To address this coverage problem, several solutions have been proposed in the literature. On one front, Busari et al. introduced two types of densification schemes: space densification, where small cells (e.g., picocells) are densely deployed, and frequency densification, where larger portions of the spectrum across multiple frequency bands are utilised [10]. It was further pointed out in [10] that full wireless network densification can only be achieved if the backhaul network is also sufficiently densified and if receivers are capable of performing effective interference cancellation. On another front, relay-assisted communication has also been investigated to mitigate

rapid signal attenuation in mmWave systems [11, 12]. In [11], a joint relay selection and dynamic scheduling algorithm was proposed for an unmanned aerial vehicle (UAV)-aided two-way relaying system operating at mmWave frequencies, while [12] developed a joint policy for relay selection and beam management based on deep reinforcement learning for mmWave vehicular communications.

Despite their merits, these solutions carry their own practical limitations. For network densification, the requirement to also densify the backhaul network [10] significantly increases deployment cost, and when network density becomes sufficiently high, the interference cancellation required at the receiver may impose substantial computational complexity. For relay-based solutions, cost remains a critical constraint: since relays are active devices equipped with radio frequency (RF) chains, power supplies, and signal processing units, large-scale relay deployment can lead to considerable hardware and energy expenditure. In parallel, network-controlled repeaters have attracted attention in standardisation discussions as a practical coverage-enhancement technology. In 3GPP Release 18, network-controlled repeaters were considered as part of the 5G-Advanced evolution to improve coverage and support deployment flexibility. Although these devices offer a lower-complexity forwarding mechanism compared to conventional relays, they remain active and require power supply, amplification, and network coordination. These persistent limitations motivate the search for alternative technologies that can enhance high-frequency coverage with lower energy consumption and lower hardware complexity.

In this context, reconfigurable intelligent surfaces (RISs) have emerged in recent years as a promising solution for enhancing coverage in mmWave communication systems [13, 14]. An RIS typically consists of a large number of passive or nearly passive antenna elements arranged on a planar surface. Each element is equipped with tunable components, such as diodes or varactors, which enable adjustable phase shifts of the reflected signals. By intelligently configuring these phase shifts, the RIS can manipulate the propagation of electromagnetic (EM) waves to achieve functional-

ities such as beam focusing, interference mitigation, and beam redirection. Compared with conventional active relays, nearly passive RISs offer potential advantages in terms of hardware complexity and power consumption, as they can manipulate incident electromagnetic waves without requiring dedicated signal amplification or decoding and re-encoding operations. Nevertheless, RISs are not entirely passive, since their reconfigurable elements and control circuitry still consume power [15]. Moreover, lower hardware power consumption does not necessarily translate into higher system-level energy efficiency. As demonstrated in [16], sufficiently large reflecting surfaces or high target data rates may be required for RIS-assisted systems to outperform conventional decode-and-forward relaying in terms of transmit power and energy efficiency. Therefore, the potential energy-saving benefits of RISs depend on their hardware implementation, deployment geometry, propagation conditions, and communication requirements. In addition, RISs offer the potential for cost-effective fabrication and deployment. For instance, an ETSI report estimates the manufacturing cost of a 256-element RIS at approximately USD 448 (USD 1.75 per element) under high-volume production assumptions [17]. Regarding deployment flexibility, NTT DOCOMO demonstrated a film-shaped transmissive metasurface attached directly to an existing building window to redirect 28 GHz signals, illustrating the feasibility of integrating such surfaces into existing infrastructure with minimal visual impact [18]. Nevertheless, actual fabrication and deployment costs depend on the hardware architecture, production scale, and installation requirements.

The potential role of RIS becomes even more important when considered in the context of the evolution towards 6G. Future cellular systems are expected to integrate communication, sensing, localisation, and intelligent control of the wireless environment. In this broader vision, RIS is not merely a passive reflector, but a candidate technology for making the propagation environment itself programmable. Rather than solely adapting the transmitter and receiver to the channel, an RIS-assisted network attempts to shape the channel directly. This concept is particularly

relevant for mmWave and higher-frequency systems, where propagation is more directional and controllable reflections can significantly affect link availability and coverage reliability.

From a standardisation perspective, however, RIS should be regarded as an emerging but not yet fully mature cellular technology. In 3GPP, RIS was proposed for consideration as a study item in both Release 18 and Release 19, but these proposals were not approved for inclusion in the respective work programmes. In particular, concerns regarding technological maturity and robustness were raised during the Release 18 discussions, while renewed proposals in Release 19 also did not result in an approved study item, leaving RIS for possible consideration in future releases [19, 20, 21]. In contrast, related coverage-enhancement technologies such as network-controlled repeaters have progressed to standardisation in 3GPP Release 18 [22]. In parallel, the ETSI Industry Specification Group on RIS has been established to coordinate pre-standardisation research [23, 24]. ETSI describes RIS as a new type of system node whose reflection, refraction, and absorption properties can be adapted to the radio environment using many small antennas or metamaterial elements [25], and has published reports covering RIS use cases, key performance indicators, deployment scenarios [25], channel models, evaluation methodology [26], and practical implementation aspects including architecture and impact on standardisation [27]. These activities indicate continued interest in RIS from the research and standardisation communities, while also highlighting that several practical challenges remain open.

Given these open challenges, the central question is not only whether RIS can improve an individual communication link, but whether it can provide measurable and cost-effective benefits at the network level. Practical deployment requires careful investigation of channel estimation, control signaling, hardware losses, placement strategies, user mobility, and integration with existing cellular infrastructure. Moreover, the benefits of RIS must be evaluated under realistic conditions involving spatial randomness, blockage, near-field propagation, and heterogeneous user requirements.

This motivates a system-level analytical perspective rather than purely link-level optimisation.

Since the proposal of this technology, numerous investigations have focused on different aspects of RIS-assisted wireless communications, including cascaded channel estimation [28], channel capacity estimation [29], large-scale fading characterisation [30], RIS-assisted UAV networks [31], and RIS-assisted secure communications [32]. Existing works can be broadly categorised into two directions: those that establish fundamental performance limits and those that explore RIS functionalities across various application scenarios. Although some recent studies have begun to investigate system-level performance, the majority of existing works focus on the link level, where the system typically consists of a base station (BS), an RIS, and one or multiple users, with performance evaluated using metrics such as sum rate, spectral efficiency, or energy efficiency. These link-level metrics, however, do not provide direct insight into the extent of coverage enhancement achievable through RIS deployment, particularly in comparison to conventional mmWave networks.

To bridge this gap, it is important to move beyond link-level analysis and consider system-level performance from a broader perspective. In practical wireless networks, users are spatially distributed, and the propagation environment is inherently random, making metrics such as coverage probability more suitable for characterising system-level behaviour, as they capture both spatial randomness and network-wide effects. The indoor mmWave environment is of particular interest in this regard. Due to the high susceptibility of mmWave signals to blockage and limited scattering indoors, maintaining reliable coverage is especially challenging. At the same time, indoor environments provide abundant surfaces, such as walls, ceilings, pillars, and furniture that can be leveraged for RIS deployment, making RIS a particularly suitable technology for this setting.

Motivated by these observations, this thesis focuses on the system-level performance analysis of RIS-assisted indoor mmWave networks, with particular emphasis

on practical indoor environment modelling and user fairness. Alongside this primary focus, the thesis also investigates RIS-assisted communication systems from multiple complementary perspectives, including RIS element modelling and large-scale optimisation. These studies collectively provide a more comprehensive understanding of RIS technologies across different layers of the communication system and help clarify whether RIS can play a meaningful role in future 6G networks.

1.2 Thesis Contributions

Building upon the above discussion, this thesis addresses the challenges associated with RIS-assisted communication systems, with a particular focus on system-level performance in indoor mmWave environments. Complementary investigations are also conducted to provide a broader understanding of RIS technologies. The main contributions are summarised as follows.

This thesis begins by examining the phase response characteristics of RIS elements across different frequency regimes, including mmWave and terahertz (THz) bands. At millimetre-wave frequencies, commonly adopted phase models are introduced to describe the behaviour of RIS elements. In addition, a liquid crystal (LC)-based RIS element operating at terahertz frequencies is investigated to enable continuous and wide-range phase modulation. The work focuses on modelling and analysing the phase response of individual reflecting elements and the directivity of the resulting RIS, while experimental results obtained by collaborators demonstrate the tunability of the thick LC cell. This investigation demonstrates that continuous phase modulation can be achieved using a thick LC cell at THz frequencies and characterises how the resulting element phase response influences the directivity of the reflecting surface. It serves as an independent high-frequency hardware investigation, and the specific LC-based element model is not directly employed in the subsequent system-level analyses and optimisation frameworks presented in Chapters 4-7.

Building upon the RIS phase modelling work, a comprehensive system-level

framework is developed to analyse RIS-assisted mmWave communications in indoor environments. Realistic indoor characteristics, including user clustering, blockage effects, boundary effects, and height variations of network nodes, are explicitly incorporated into the modelling. Based on this framework, approximated analytical expressions for key quantities such as distance distributions, line-of-sight (LOS) probabilities, and coverage probability are derived. The results identify obstacle density as a dominant factor affecting coverage probability, while user clustering has a comparatively moderate influence. Increasing the RIS deployment density improves coverage, although the incremental gains diminish as more RISs are deployed or as the transmitter density increases.

To further understand system performance from a user-centric perspective, user capacity is introduced to characterise the maximum number of users that can be simultaneously supported in intelligent omni surface (IOS)/RIS-assisted indoor mmWave networks. A stochastic geometry-based analytical framework is developed to evaluate user capacity under practical conditions, including near- and far-field propagation, heterogeneous quality-of-service (QoS) requirements, and inter-user interference. The results demonstrate that near-field propagation must be considered for sufficiently large surface apertures, while far-field approximations remain appropriate for smaller apertures. Moreover, IOS-assisted networks support more users than conventional RIS-assisted networks under the evaluated configurations, and an increasing proportion of high-QoS users significantly reduces the achievable user capacity.

Furthermore, the performance of RIS-assisted wideband communication systems is investigated, with particular emphasis on the frequency-dependent loss of coherent combining gain. The concept of RIS coherence bandwidth is introduced to characterise the frequency range over which a frequency-flat RIS can maintain effective phase alignment, and an analytical approximation is derived to quantify its dependence on the RIS geometry and propagation conditions. Based on this

characterisation, the outage probability is analysed for operating bandwidths both within and beyond the RIS coherence bandwidth, providing insights into the impact of frequency-dependent phase mismatch and the number of subcarriers on system performance. The analysis highlights the bandwidth limitations of frequency-flat RIS architectures and provides a theoretical framework for evaluating their performance in wideband communication systems.

While the preceding analyses focus on characterising system-level performance, it is equally important to develop efficient methods to enhance this performance in practical implementations. To this end, a learning-based framework is developed for joint optimisation of the BS precoding matrix and RIS phase configuration. In particular, a sequential multi-agent advantage actor-critic (A2C) approach is proposed to handle discrete RIS phase constraints, inter-user channel correlation, and imperfect channel state information. The proposed framework enables scalable optimisation for extremely large RIS systems and demonstrates improved performance compared to conventional beamforming methods.

1.3 Thesis Organisation

To provide the reader with a clear overview, the remainder of this thesis is organised as follows.

Chapter 2 presents the literature review on RIS-assisted wireless communication systems. The chapter begins with an overview of the fundamental principles and hardware architectures of RIS, including reflecting element designs at both mmWave and THz frequencies. The electromagnetic and system-level models of RIS are then reviewed, followed by discussions on advanced architectures, channel estimation techniques, performance analysis frameworks, wideband RIS systems, and learning-based optimisation approaches. This chapter establishes the theoretical foundation and research background for the work presented in the subsequent chapters.

Chapter 3 focuses on RIS element modelling at high frequencies, with particular

emphasis on phase modulation mechanisms at mmWave and THz bands. The chapter first reviews the commonly adopted phase models for electronically controlled RIS operating at mmWave frequencies. It then investigates LC-based RIS designs at THz frequencies, where material-dependent phase modulation becomes essential due to the limitations of conventional electronic tuning mechanisms. An LC-based reflecting element is proposed and experimentally validated, and its phase response characteristics are analysed under different operating conditions. The chapter concludes with a comparison between LC-based and conventional RIS designs, demonstrating the feasibility of phase tuning in thick LC cells and characterising the resulting phase response and directivity performance at THz frequencies. This element-level investigation complements, but does not directly feed into, the system-level models developed in Chapters 4-7.

Chapter 4 develops a stochastic geometry-based framework for analysing the performance of RIS-assisted indoor mmWave wireless networks. The proposed framework incorporates practical indoor characteristics, including blockage effects, user clustering, boundary effects, and node-height variations. Based on this framework, analytical expressions are derived for distance distributions, LOS probabilities, and coverage probability. The impact of key system parameters, such as obstacle density, RIS deployment density, transmit power, and user distribution, is then investigated, showing that obstacle density strongly affects coverage probability, while RIS deployment improves coverage with diminishing gains as the RIS or transmitter density increases.

Chapter 5 investigates the user capacity of IOS/RIS-assisted indoor mmWave networks from a user-centric perspective. A stochastic geometry-based analytical framework is developed to characterise the maximum number of users that can be simultaneously supported while satisfying heterogeneous QoS requirements. The analysis explicitly accounts for both far-field and near-field propagation regimes, inter-user interference, and heterogeneous user types. Numerical and analytical

results reveal the impact of near-field effects, transmit power, and surface size on the achievable user capacity, showing that IOS-assisted networks can support more users than conventional RIS-assisted networks under the considered configurations, while the achievable capacity is strongly constrained by the proportion of users with stringent QoS requirements.

Chapter 6 extends the analysis to wideband RIS-assisted communication systems by investigating the coherence bandwidth and outage performance of RIS. Analytical expressions for the RIS coherence bandwidth are first derived to characterise the frequency range over which coherent combining can be maintained. Building upon this analysis, outage probability expressions are developed for wideband systems operating under different bandwidth conditions. The results demonstrate that the RIS coherence bandwidth decreases as the surface aperture increases, revealing a trade-off between coherent array gain and effective operating bandwidth. Furthermore, when the operating bandwidth exceeds the RIS coherence bandwidth, frequency-dependent phase mismatch reduces the coherent combining gain and affects outage performance, highlighting the limitations of frequency-flat RIS configurations.

Chapter 7 addresses the joint beamforming problem in extremely large-scale RIS-assisted systems. A sequential multi-agent A2C framework is proposed to jointly optimise the BS precoding matrix and the RIS phase configuration under discrete phase constraints. The proposed framework explicitly considers practical factors such as channel correlation and imperfect channel state information (CSI), while maintaining scalability for very large RIS deployments. Numerical results demonstrate that the proposed approach achieves improved spectral efficiency compared with conventional beamforming techniques, including zero-forcing (ZF) and regularised ZF.

Finally, Chapter 8 concludes the thesis by summarising the main findings and discussing several directions for future research, including dynamic RIS environments, advanced intelligent-surface architectures, and the integration of RIS technologies

into future 6G wireless communication systems.

Chapter 2

Literature Review

The concept of a RIS has been briefly introduced in the previous chapter. An RIS is an engineered surface composed of numerous sub-wavelength reflecting elements, each of which can be electronically controlled—typically via diodes or varactors—to adjust the phase of the reflected signal. In this chapter, we provide a more comprehensive overview of this emerging technology, including its hardware architecture, element design across different frequency bands, and commonly adopted modelling approaches.

2.1 Hardware Structure

We begin by introducing the hardware architecture of an RIS, followed by a discussion on the design of its reflecting elements across different frequency regimes. A typical RIS is composed of three layers. The top layer consists of an array of reflecting elements, each integrated with tunable components (e.g., diodes or varactors) that enable dynamic control of the reflected signal. The element spacing is usually sub-wavelength. The middle layer contains the control circuitry, which governs the operation of these tuning elements, either individually or in groups. The bottom layer is a metallic ground plane that prevents electromagnetic wave penetration and ensures that the incident signals are efficiently reflected [1, 2]. An illustration is given in Fig. 2.1 to show the hardware structure of an RIS. An RIS is typically equipped with a transceiver module, such as an antenna combined with a simple RF chain, to acquire CSI from either users or the BS. In some implementations, a wired connection between the RIS and the BS or users can also be employed for CSI acquisition and control signaling, as demonstrated in [1]. This part is essential as the RIS needs the input to instruct the reconfiguration.

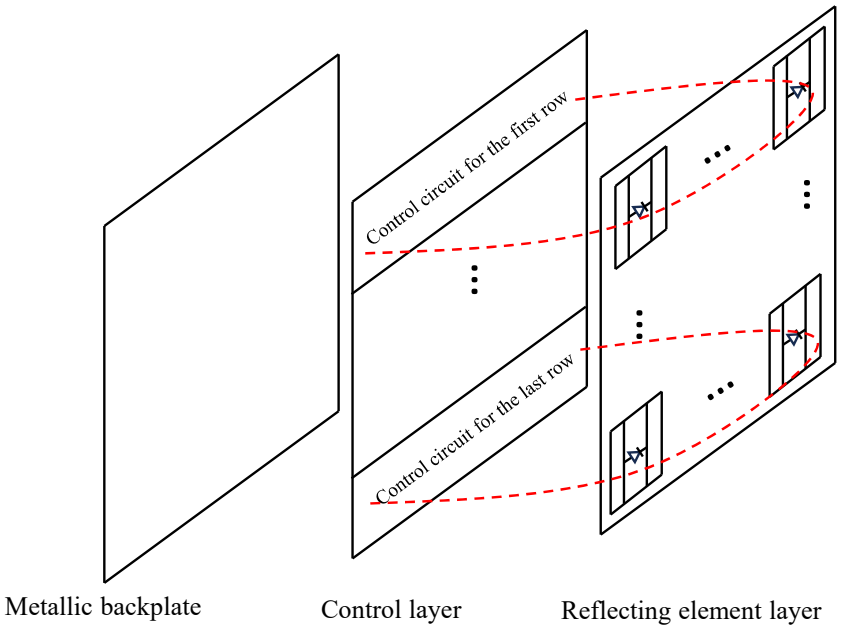

Figure 2.1: Illustration of the RIS hardware structure.

The aforementioned architecture corresponds to the conventional RIS design, which operates in a nearly passive manner without incorporating signal amplification. In contrast, an alternative architecture, known as the active RIS, has been proposed in [33]. In this design, the reflected signal is not only phase-adjusted but also amplified, thereby mitigating the severe multiplicative fading inherent in RIS-assisted channels. In active RIS architectures, each reflecting element integrates a reflection-type amplifier, which enables simultaneous phase adjustment and signal amplification at the electromagnetic level. This amplifier operates by coupling the incident RF signal with an externally supplied pump signal, thereby transferring energy to the reflected wave. At first glance, such a structure may appear similar to an active relay, particularly an amplify-and-forward (AF) relay, since both can enhance the received signal without decoding and re-encoding the transmitted information. The key distinction therefore lies not simply in the absence of baseband decoding, but in their signal-processing and hardware architectures. An AF relay operates as an active receive-and-retransmit node, in which the incident signal is received through a dedicated receiving chain, amplified, and subsequently retransmitted

through a transmitting chain. In contrast, an active RIS retains the reflective operating principle of a conventional RIS: amplification and phase adjustment are implemented locally within the reflection response of each element, without employing separate receive and transmit chains. Consequently, an active RIS can be regarded as an intermediate architecture between a passive RIS and a conventional active relay, providing additional reflected-signal gain at the expense of increased power consumption and hardware complexity compared with a passive RIS.

2.1.1 RIS Element Design at mmWave

After the discussion of the hardware structure, we now closely look at element design for RISs that operate at mmWave frequencies. A reflecting element is usually made of a patch on top and a substrate beneath it. For example, Fig. 2.2 shows the element structure of the RIS fabricated in [1] and Fig. 2.3 shows the element structure of the RIS fabricated in [2]. On substrate 2 in Fig. 2.2, metallic patches are interconnected through varactor diodes. In addition, vias are placed in close proximity to the varactor diodes to facilitate their connection to the biasing and control circuitry located in the intermediate layer of the RIS. The first substrate is made of FR4, a composite material consisting of woven fibreglass cloth reinforced with an epoxy resin binder. The second substrate is fabricated from F4B, a class of high-frequency dielectric materials specifically designed for microwave and millimetre-wave applications. In [2], the RIS unit cell adopts a slot-loaded ground plane with a square metallic patch placed above it, forming a hybrid structure. The reconfigurability of this design is achieved through five positive intrinsic negative (PIN) diodes, whose on/off states result in four distinct configurations. By appropriately switching these PIN diodes, the RF current paths and electrical lengths within the structure can be altered, thereby modifying the phase response of the wave radiated by the top patch. Fig. 2.2 and Fig. 2.3 show two typical element structures for RISs working in mmWave. Next, we will see the RIS element design in higher frequencies, particularly, in THz

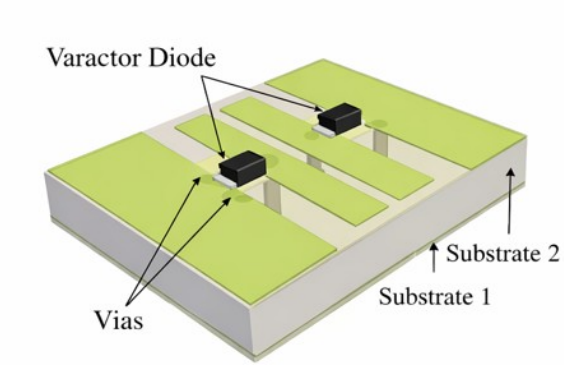

Figure 2.2: RIS element structure in [1]

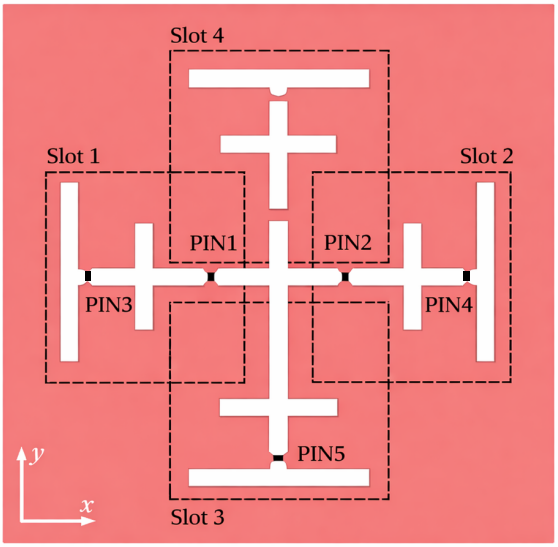

Figure 2.3: RIS element structure/slot-loaded plane in [2]

frequencies.

2.1.2 RIS Element Design at Terahertz Frequencies

At THz frequencies, the design of RIS elements faces fundamental challenges due to the parasitic effects inherent in conventional electronic components. Devices such as PIN diodes and varactors, which are widely used at mmWave frequencies, exhibit significant parasitic resistance, capacitance, and inductance when operating in the THz regime. These parasitic elements distort the intended impedance characteristics of the device, resulting in increased insertion loss, reduced quality factor, and a limited achievable phase tuning range. In addition, the intrinsic material losses

of semiconductor-based components become more pronounced at THz frequencies, further degrading the efficiency of the reflecting element. Consequently, the performance of conventional electronically controlled RIS elements deteriorates in the THz band, motivating the exploration of alternative approaches, such as LC-based and graphene-based tunable materials, which offer improved electromagnetic response at such high frequencies. Fig. 2.4 [3], and Fig. 2.5 [4] show the RIS element structure in THz frequencies. Fig. 2.4 is a side view of the element structure proposed in [3]. The RIS element shown in Fig. 2.4 consists of seven layers arranged from left to right as follows: a silicon substrate, a metallic back plate, a polyimide (PI) layer, an LC layer, a second PI layer, a complementary split-ring resonator (CSRR), and a quartz substrate. LCs are tunable dielectric materials whose permittivity can be controlled via an applied electric field, making them suitable for reconfigurable intelligent surfaces. When applying an external bias voltage, the re-oriented LC molecules will change the permittivity of the substrate, which indirectly changes the phase response of the CSRR above it (see Appendix A for further details about the material). The silicon substrate and the ultrathin quartz layer serve as mechanical supports for the metallic back plate and the CSRR, respectively. The PI layers, which are pre-patterned with parallel grooves, facilitate the initial alignment of the LC molecules in the absence of an applied electric field. Meanwhile, the metallic back plate and the CSRR also function as electrodes, enabling the application of a bias voltage across the LC layer. In Fig. 2.5, two metallic layers are patterned on the top and bottom quartz substrates, respectively. The top metallic layer is designed as a corner-truncated patch connected to a bias line, while the bottom metallic layer forms a pixelated rectangular patch that serves as the ground plane. The LC layer is sandwiched between these two substrates. When a bias voltage is applied across the metallic layers, the orientation of the LC molecules is reconfigured accordingly, resulting in a transition of the effective refractive index from the extraordinary index n_e to the ordinary index n_o. The LC material NJU-LDN-4 is employed in this

design.

Although the LC-based RIS element avoids the parasitic effects introduced by conventional electronic devices, it also brings new challenges. One of the most significant limitations is the switching speed. Compared to semiconductor-based components such as PIN diodes or varactors, the reorientation of LC molecules is governed by electro-optic effects and viscous relaxation processes, which are inherently slow. As a result, the response time of LC-based RIS elements typically lies in the millisecond range, depending on factors such as cell thickness, viscosity, and the strength of the applied electric field. This relatively slow switching speed restricts the applicability of LC-based RIS in dynamic wireless environments, particularly in scenarios involving fast user mobility or rapidly varying channels. In such cases, the RIS configuration may not be updated quickly enough to track channel variations, leading to performance degradation. Nevertheless, LC-based designs remain attractive for quasi-static or low-mobility scenarios, where their low loss and continuous tunability offer significant advantages. Various approaches have been investigated to improve the response time of LC-based devices, including reducing the LC layer thickness, optimising the alignment layers, and employing advanced LC materials with lower viscosity [34, 35]. However, these improvements often come at the cost of reduced phase tuning range or increased fabrication complexity, highlighting a fundamental trade-off between tunability and switching speed.

An alternative approach to THz RIS element design exploits the unique electromagnetic properties of graphene. Graphene is a two-dimensional carbon allotrope whose surface conductivity can be dynamically tuned via electrostatic gating or chemical doping [36]. This tunability arises from the dependence of graphene's intraband and interband conductivity contributions on the Fermi energy level, which shifts in response to an applied gate voltage. In the THz regime, the surface plasmon polariton modes supported by graphene are strongly confined and exhibit low propagation loss, making graphene a compelling candidate for high-frequency reconfigurable elements.

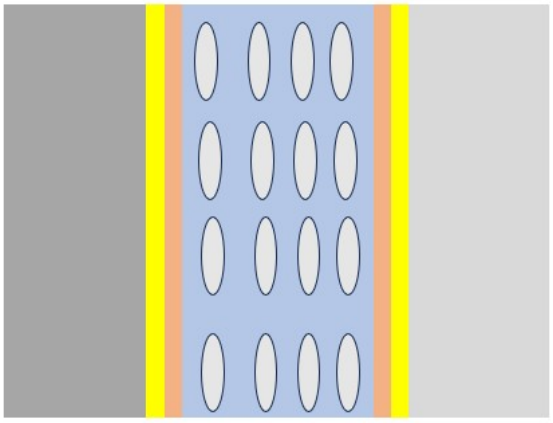

Figure 2.4: LC-based THz RIS unit-cell architecture employing a CSRR above the LC layer [3].

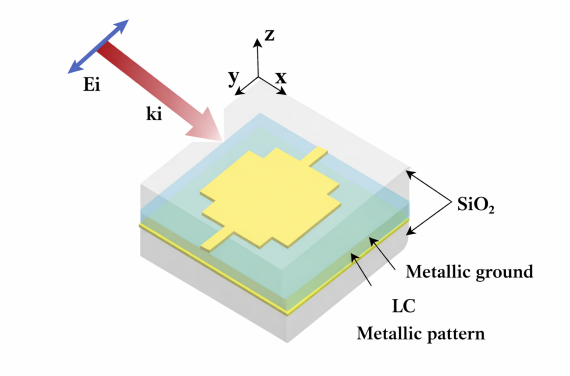

Figure 2.5: LC-based THz RIS unit-cell architecture employing a corner-truncated metallic patch and a pixelated ground plane [4].

A graphene-based RIS element typically consists of a graphene sheet patterned into a resonant structure—such as a ribbon or disk—placed above a dielectric substrate with a metallic back reflector. By applying a bias voltage between the graphene layer and a gate electrode embedded in the substrate, the resonant frequency and phase response of the element can be continuously adjusted. Compared to LC-based designs, graphene-based elements offer significantly faster switching speeds, on the order of nanoseconds, which is more compatible with dynamic wireless environments [37]. However, graphene-based RIS elements also face practical challenges, including the difficulty of large-area graphene synthesis with uniform quality, the sensitivity of graphene's properties to environmental contamination, and the need for precise nanofabrication processes. Furthermore, the achievable phase tuning range of

graphene-based elements is often limited compared to LC-based designs due to the narrow bandwidth of the plasmonic resonances. Nevertheless, the combination of fast reconfigurability and low loss makes graphene-based RIS an active and promising area of research at THz frequencies.

It is also worth noting that, in currently prototyped RIS implementations, the phase adjustment capability is effectively discrete at both mmWave and THz frequencies. At mmWave frequencies, this discreteness arises from the finite number of configurations determined by the states of PIN diodes, as it is impractical to integrate an arbitrarily large number of diodes within a single RIS element. At THz frequencies, although LC materials can, in principle, provide a continuous phase response, the achievable performance is constrained by the frequency-dependent behaviour of the resonant structures (e.g., CSRR or patch elements) placed above the LC layer. Specifically, when the operating frequency deviates from the designed resonance of the unit cell, the impedance matching condition deteriorates, leading to an increase in the reflection coefficient (S_{11}). As a result, the reflected signal experiences significant amplitude attenuation, and the phase response can no longer be independently controlled. This amplitude–phase coupling limits the effective phase tuning range and degrades the overall performance of the RIS.

2.2 Electromagnetic Model of RIS

We now proceed to discuss the modelling approaches for RIS. The choice of model is largely dictated by the application scenario and the level of abstraction required. EM models are typically employed to characterise propagation phenomena, such as path loss and reflection properties, with high physical fidelity. In contrast, system-level models provide a more tractable framework for system-level analysis and optimisation, including beamforming design and resource allocation in RIS-assisted communication systems. EM models of RIS are commonly employed to characterise large-scale

fading in RIS-assisted communication systems. In [38], physical optics is utilised to derive the far-field path loss of an RIS-assisted link. The authors further explain that an RIS can be interpreted as a collection of individual scattering elements, which operate independently at the element level but can coherently combine their contributions to form a directional beam. Based on this framework, it is shown that, in the far-field regime, the path loss of an RIS-assisted system is proportional to the product of the squared distances between the BS and the RIS, and between the RIS and the user. Moreover, the same work highlights that this distance-dependent behaviour changes when the RIS becomes electrically large or when the user is located in the near-field region, in which case the path loss scales with the square of the sum of the distances rather than their product. Similarly, [39] develops a physical-optics-based framework, leveraging Green's theorem, to analyse the path loss of RIS-assisted systems. In contrast to [38], this work considers multiple RIS functionalities, including specular reflection, anomalous reflection, and focusing. Moreover, asymptotic expressions for the path loss are derived for each functionality in both the near-field and far-field regimes. In contrast to the analytical studies in [38] and [39], [30] presents a prototype RIS and experimentally evaluates the performance of its unit cells. The results reported in [30] indicate that the energy efficiency of a unit cell decreases proportionally to the square of the increasing operating frequency, highlighting a fundamental challenge for RIS deployment at higher frequencies. Furthermore, the measurement campaign demonstrates good agreement with the analytical path loss models developed in the same work.

While EM models provide valuable insights into the physical propagation mechanisms and large-scale fading characteristics of RIS-assisted systems, their high level of detail often makes them less tractable for system-level analysis and optimisation. In particular, incorporating full-wave or physical-optics-based models into communication-theoretic frameworks is generally impractical due to their complexity. To enable efficient analysis and design, it is therefore common to adopt simplified

signal-level models that abstract the RIS as a reconfigurable transformation of the wireless channel. These models retain the essential impact of the RIS on signal propagation while providing a mathematically tractable framework for tasks such as beamforming design, resource allocation, and performance analysis. In the following, we introduce the signal model of RIS-assisted communication systems, which serves as the foundation for subsequent optimisation and analytical developments.

2.3 System Model of RIS

In an RIS-assisted communication system, the RIS is commonly modelled as a scattering matrix with each of the diagonal entries being an element on the RIS. This matrix is often given by

$$\mathbf{\Phi} = \begin{bmatrix} \beta_1 e^{j\theta_1} & 0 & \cdots & 0 \\ 0 & \beta_2 e^{j\theta_2} & \cdots & 0 \\ \vdots & \vdots & \ddots & \vdots \\ 0 & 0 & \cdots & \beta_N e^{j\theta_N} \end{bmatrix}, \tag{2.1}$$

where β_n and θ_n denote the reflection amplitude and phase shift of the nth RIS element, respectively. For a passive RIS, the reflection amplitude is ideally equal to unity for all elements. However, in practical implementations, it is typically smaller than one due to energy losses caused by absorption and hardware imperfections. In contrast, for an active RIS, the reflection amplitude can exceed unity, as discussed in [33], where amplification components are introduced. The value of θ_n is ideally continuous from 0 to 2π. Some of the work adopted this assumption when conducting the system resource optimisation or performance analysis [40, 41]. From a practical point of view, discrete phase adjustment is more reasonable as the current prototyped RISs do not have the capability to change the phase continuously.

Observing (2.1), the scattering matrix $\mathbf{\Phi}$ is diagonal, i.e., all off-diagonal entries are zero. This implies that the signal reflected by the nth RIS element is solely

controlled by that element itself, and no interaction exists among different elements. While such an independent element-wise configuration simplifies implementation, it inherently restricts the capability of the RIS to jointly manipulate the impinging wavefront. In particular, this structure limits interference control [42] and leads to performance saturation in multi-user scenarios [43]. To overcome these limitations, the authors in [44] pose a fundamental question: can the zero off-diagonal entries of the scattering matrix $\mathbf{\Phi}$ be exploited as additional design variables to enable more flexible wave manipulation? This insight has led to the concept of beyond-diagonal RIS (BD-RIS), where RIS elements are intentionally interconnected through a reconfigurable impedance network [45, 46].

In a BD-RIS, the scattering matrix $\mathbf{\Phi}$ is no longer constrained to be diagonal, but instead takes the form of a general unitary or symmetric matrix depending on the underlying circuit topology. The non-zero off-diagonal entries represent signal coupling between elements, which can be exploited to achieve more flexible wavefront shaping. From a circuit implementation perspective, the interconnection network is realised using tunable reactive components (e.g., varactors or switched capacitors) connected between the ports of adjacent or non-adjacent elements [45]. Three canonical circuit topologies have been studied in the literature: the *fully-connected* architecture, in which every pair of elements is directly interconnected; the *group-connected* architecture, which partitions elements into groups within which interconnections are permitted; and the *tree-connected* architecture, which constrains the interconnection graph to a tree structure to reduce hardware complexity [46]. These topologies offer a continuous trade-off between performance and hardware complexity, with the fully-connected architecture providing the maximum degrees of freedom at the cost of the most complex interconnection network. Theoretical results have demonstrated that BD-RIS can achieve strictly higher capacity than its diagonal counterpart in both single-user and multi-user settings, particularly when the number of users approaches the number of RIS elements [44]. However,

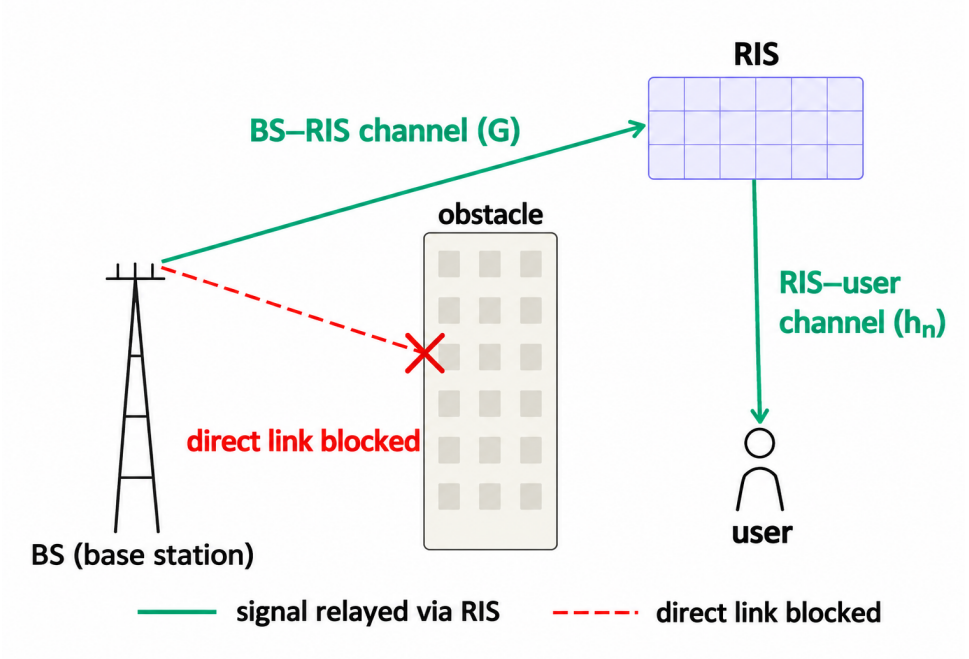

Figure 2.6: An illustration of an RIS-assisted end-to-end wireless communication system.

the joint optimisation of the interconnection network and the precoding vectors at the BS presents new algorithmic challenges, as the constraint set for $\mathbf{\Phi}$ is non-convex and topology-dependent. Efficient optimisation algorithms based on manifold optimisation and successive convex approximation have been proposed to address this problem [46].

Based on the above RIS system model, the received signal in a multiple-input-single-output (MISO) system can be expressed as

$$y = \mathbf{h_2}^T \mathbf{\Phi} \mathbf{H_1} \mathbf{w} x + n, \tag{2.2}$$

where x, y, $\mathbf{h_2}$, $\mathbf{\Phi}$, $\mathbf{H_1}$, $\mathbf{w}$, and n denote the transmitted information symbol, the received signal at the user side, the channel vector between the RIS and the user, the RIS scattering matrix, the channel matrix between the BS and the RIS, the precoding vector, and the noise. Fig. 2.6 is an illustration of a typical RIS-assisted wireless communication system. Due to the blockage in the direct link, the BS utilises the RIS to redirect the signal to the user.

2.4 Channel Estimation for RIS-Assisted Systems

An implicit assumption underlying the system model in (2.1) is the availability of accurate CSI. In practice, however, acquiring CSI in RIS-assisted systems is significantly more challenging than in conventional systems. The core difficulty arises from the fact that a passive RIS lacks signal processing capabilities of its own: it cannot transmit pilot signals, perform channel sounding, or directly estimate the channels associated with its elements. As a result, the BS or users must estimate the RIS-related channels indirectly from received pilot signals, which leads to a *cascaded channel estimation* problem [47].

In a typical cascaded estimation setup, the quantity of interest is the product $\mathbf{h_2^T \Phi H_1}$, which combines the BS-RIS channel $\mathbf{H_1}$ and the RIS-user channel $\mathbf{h_2}$. Since these two channel matrices appear as a product and cannot be disentangled without additional structure, the estimation problem is inherently ill-conditioned. Furthermore, as the number of RIS elements N grows, the number of channel parameters to be estimated scales as $\mathcal{O}(N)$, imposing a substantial pilot overhead that reduces spectral efficiency. This overhead problem is particularly severe in large-RIS deployments where N may be in the hundreds or thousands.

Several approaches have been proposed to address these challenges. A first class of methods exploits the spatial sparsity of mmWave and THz channels, which exhibit a limited number of dominant propagation paths. By representing the channel in an angular domain dictionary, compressed sensing techniques such as orthogonal matching pursuit (OMP) and its variants can recover the channel parameters from a reduced number of pilot observations [48]. A second class of methods develops matrix factorisation-based estimators that jointly recover $\mathbf{H_1}$ and $\mathbf{h_2}$ by leveraging structural assumptions such as rank constraints or common angle-of-departure information shared across users [49]. A third and increasingly prominent class of methods applies deep learning to the channel estimation problem, training neural networks to map received pilot signals directly to channel estimates [48]. Deep learning-based

estimators can implicitly exploit complex statistical structures in the channel that are difficult to model analytically, and have demonstrated promising performance in simulation studies. More recently, model-driven deep learning approaches, which embed physical channel models into the network architecture, have been proposed to improve generalisation and reduce training data requirements [50, 51].

A further complication in RIS-assisted channel estimation arises when the RIS operates at mmWave or THz frequencies, where the near-field propagation model becomes relevant for electrically large surfaces. In this case, the plane-wave assumption underlying most far-field channel models breaks down, and the channel must be described using a spherical wavefront model. Estimation algorithms designed for far-field conditions may suffer significant performance degradation when applied to near-field scenarios, motivating the development of dedicated near-field channel estimation techniques for RIS [52].

2.5 Simultaneously Transmitting and Reflecting RIS

The conventional RIS architectures discussed above operate in a purely reflective mode: the incident wave is redirected back into the half-space from which it originated. While this is sufficient for many scenarios, it fundamentally limits the coverage of a single RIS to only one side of the surface. To overcome this limitation, the concept of a simultaneously transmitting and reflecting RIS (STAR-RIS), also referred to as an IOS, has been proposed [53, 54]. In a STAR-RIS, each element splits the incident signal into a reflected component directed into the reflection half-space and a transmitted component propagating into the transmission half-space. This enables full-space coverage from a single surface and allows users on both sides of the RIS to be served simultaneously.

The operation of a STAR-RIS is governed by energy conservation constraints. Let β_n^r and β_n^t denote the amplitude coefficients of the reflected and transmitted signals at the nth element, respectively, with θ_n^r and θ_n^t the corresponding phase

shifts. The energy conservation condition requires that $(\beta_n^r)^2 + (\beta_n^t)^2 \leq 1$ for all n, which couples the design of the transmission and reflection coefficients and introduces a fundamental trade-off between the two modes. Three primary operating protocols have been identified in the literature [54]: *energy splitting* (ES), where each element simultaneously transmits and reflects with continuously adjustable amplitude coefficients; *mode switching* (MS), where each element operates in either pure reflection or pure transmission mode; and *time switching* (TS), where the surface alternates between full reflection and full transmission over time. The ES protocol offers the greatest flexibility but requires more complex hardware, while the MS and TS protocols offer simpler implementations at the cost of reduced spatial and temporal degrees of freedom.

From a physical implementation perspective, STAR-RIS elements can be realised using active components capable of simultaneously controlling the amplitude and phase of both the transmitted and reflected waves. One approach employs a combination of varactor diodes on both sides of the substrate to independently tune the transmission and reflection responses. Another approach leverages metasurface designs based on coupled resonators, where the coupling between adjacent elements governs the transmission-reflection partitioning. The realisation of independent phase control for both the transmitted and reflected signals, which is desirable for maximum flexibility, remains a challenging hardware design problem and is an active area of research.

2.6 Performance Analysis of Intelligent Surface-Assisted Communication Systems

The performance analysis of intelligent surface-assisted communication systems has attracted significant attention in recent years. To evaluate the impact of intelligent surfaces on network performance, stochastic geometry has been widely adopted due to its ability to model the spatial randomness of network nodes and derive

analytical performance metrics in large-scale wireless networks. Existing studies have investigated coverage probability, ergodic capacity, energy efficiency, and outage probability under different deployment strategies, association policies, and propagation environments. Representative works are reviewed as follows. In [55], BSs and RISs are assumed to follow two independent homogeneous Poisson point processes (HPPPs), respectively. It is also assumed that the density of the BS is lower than the density of the RIS, and there is no LOS path. The association policy proposed in [55] follows the shortest distance principle[1]. Through a comparison with conventional networks, it is concluded that the RIS-assisted network can achieve higher capacity and energy efficiency under the condition that the RIS density is higher than the BS density. It is shown in [55] that when the BS density is higher than the RIS density, it is unnecessary to deploy RIS devices. In [56], an application scenario with multiple users, BSs, and RISs in the presence of interference from BSs and RISs is considered, the BSs are assumed to follow an HPPP while the RIS is assumed to follow a binomial point process (BPP), and the Laplace transform of the received signal power, approximated aggregate interference, coverage probability (CP), ergodic capacity, and the energy efficiency are derived based on the assumptions. The analytical results are validated by Monte Carlo simulations. In [57], stochastic geometry is used to analyse the performance of a RIS-aided multi-cell non-orthogonal multiple access (NOMA) network. It is shown in [57] that the achievable data rate reaches an upper limit with the increase in the RIS size, and the path loss intercept can be enhanced to improve the network performance without influencing the bandwidth. In [58], the authors propose to coat RIS on a subset of scatterers in the environment, and the LOS probability is taken into consideration. The authors model the locations of BSs and users following two independent HPPPs. For user association, the minimum average path-loss criterion is adopted, whereby a user selects the communication link offering the lowest average path loss among the available direct and RIS-assisted

[1]The shortest distance principle means the user will associate with the nearest RIS in the indirect path.

links. The scatterers follow the line Boolean model proposed in [59]. It is concluded that the deployment of RIS highly improves the coverage regions of the BSs, and it is shown that 6 RIS/km^2 is enough to maintain the ratio of blind spots over the total area below 10^{-5} when the scatterer density is 300 scatterer/km^2. In [60], the spatial correlation between transmitters and RISs is described by using the Gaussian point process (GPP), and the CP expressions under a fixed association strategy and the nearest association strategy are derived in closed form in the presence of interference. It is also shown that the system performance is independent of the density of transmitters with the nearest association strategy when the scenario is interference-limited. In [61], researchers analysed the RIS-assisted mmWave network with an emphasis on whether fewer large RISs or more small RISs can improve the network performance in terms of CP. Regarding RIS association, the study does not explicitly specify a selection policy among multiple candidate RISs. Instead, the coverage analysis is based on the existence of at least one RIS that can provide an unblocked indirect link satisfying the SNR requirement. The model is built in three dimensions (3D) with the height considered. It is concluded that dense small RISs are more favorable than sparse large RISs in places where the obstacle density is high, while sparse large RISs are more favorable in places where the obstacle density is low. However, the heights of the obstacles (e.g., humans, buildings) are constants. In addition, no association policy is introduced related to RIS selection. Besides the coverage analysis of conventional RIS-assisted wireless communication networks, the coverage analysis of RIS-assisted integrated sensing and communication (ISAC) networks, as an emerging topic, has also been investigated recently [62]. Regarding user association, a low-complexity greedy policy is adopted, in which the nearest LOS BS is selected for direct communication, while the nearest non-line-of-sight (NLOS) BS and nearest LOS RIS are selected for RIS-assisted communication. The user is then associated with the direct or RIS-assisted link providing the higher average channel gain. [62] derived the joint CP of ISAC performance with the consideration

of the coupling effects of the ISAC dual functions. It showed a 62% to 97% ISAC performance enhancement with the deployment of RISs.

For RIS-assisted indoor mmWave network performance analysis, related work includes [63, 64]. [63] discussed small-cell densification and RIS deployment for coverage improvement in a 2-dimensional (2D) room. For the RIS solution, the deployment of RISs was assumed on the walls of a room with the locations following the 1-dimensional HPPP, but the blockage effect was not considered. What's more, the numerical results showed in [63] were merely based on Monte Carlo simulation, which may pose an issue when the indoor mmWave network scales up. [64] considered a human mobility model to calculate the outage probability in a 2D indoor environment, and the RIS locations (assumed to be on the wall) were optimised with respect to coverage. However, the blockage and the RIS amount showed in the simulation section were up to 2 (e.g., 1 and 2 humans as the blockages, and 1 and 2 RISs being deployed on the wall). Such results cannot provide insight when the network scales up. In addition, [64] assumes multi-hop exists between the transmitter and the user[2], which is unclear currently whether RIS is feasible for this functionality.

The aforementioned studies primarily focus on network-level performance metrics such as coverage probability, outage probability, spectral efficiency, and energy efficiency. Although these metrics are useful for evaluating overall system performance, they do not directly characterise the maximum number of users that can be simultaneously supported under individual QoS constraints. In practical wireless networks, ensuring that all users achieve a minimum quality-of-service requirement is often as important as maximising the aggregate system throughput. From this perspective, user capacity, defined as the maximum number of users that can be simultaneously supported while satisfying predefined QoS constraints, provides a fairness-oriented performance metric. Although previous studies have investigated user admission and throughput maximisation in RIS-assisted networks [65], the

[2]The signal can be reflected more than once by the RISs before it reaches the user.

statistical characterisation of user capacity under spatially random user locations and per-user reliability constraints has received comparatively less attention.

Existing studies have investigated IOS-assisted and related STAR-RIS systems in terms of beamforming design, prototyping, coverage performance, and multi-user transmission [66, 67, 68]. For example, prior work on IOS-assisted outdoor-to-indoor mmWave communications jointly optimises the number, locations, and phase shifts of the surfaces together with the transmitter beamforming vectors to maximise energy efficiency while satisfying the rate requirements of multiple indoor users [69]. Other studies investigate sum-rate maximisation through joint beamforming in IOS-assisted multi-user and multi-cell systems [67, 70]. These optimisation-based studies focus on improving performance for a given set of users, rather than determining the maximum number of simultaneously supportable users under spatially random user locations and heterogeneous QoS requirements.

In contrast, the framework developed in Chapter 5 investigates this user-capacity metric through stochastic geometry-based analysis in a three-dimensional indoor environment. It explicitly accounts for inter-user interference, heterogeneous user requirements, and hybrid near-field and far-field propagation, including the depth-of-focus effect. The resulting framework determines the maximum number of users satisfying a prescribed per-user coverage probability requirement and enables a comparison between IOS- and RIS-assisted networks. These features distinguish the present analysis from existing approaches primarily concerned with optimising rate, energy efficiency, or beamforming for a given network configuration.

2.7 RIS-Assisted Wideband Communication Systems

The performance of RIS-assisted wideband communication systems has attracted increasing attention in recent years. Existing studies mainly focus on mitigating the performance degradation caused by the frequency-flat nature of RISs when operating over wide bandwidths. In [71], a deployment strategy was proposed to jointly

optimise the location, orientation, and phase configuration of the RIS in a multi-user scenario. Beamforming design for RIS-assisted wideband systems was investigated in [72], where a low-complexity beamforming framework was developed based on the space–frequency Fourier transform and the stationary phase method. The beam squint effect resulting from frequency-flat RIS phase shifts was studied in [73], where frequency-dependent phase shifts were derived for line-of-sight scenarios and covariance-based solutions were proposed for non-line-of-sight scenarios. Furthermore, [74] introduced a physics-based frequency-selective RIS model using resonant circuit theory to capture the frequency-dependent response of RIS elements and investigated sum-rate optimisation in wideband multi-user MIMO systems.

Although these studies provide valuable insights into the design and optimisation of RIS-assisted wideband systems, several fundamental performance limits remain insufficiently understood. In particular, the intrinsic bandwidth limit of an RIS with a given physical aperture, the degradation of RIS gain as the operating bandwidth increases, and the impact of the number of subcarriers on system performance have received limited attention. Consequently, a theoretical framework capable of characterising these effects is still lacking.

2.8 Deep Reinforcement Learning-Based Joint Optimisation of RIS-Assisted Communication Systems

The performance of RIS-assisted communication systems depends on the joint configuration of the BS precoding matrix and RIS phase shifts. Existing approaches to this joint beamforming problem can be broadly classified into optimisation-based and learning-based methods.

Among optimisation-based approaches, [75] formulated a transmit-power minimisation problem under SINR constraints. A two-layer penalty-based algorithm was used to separate the optimisation variables, while manifold optimisation handled the non-convex unit-modulus constraints. In [76], BS–RIS–user association and beam-

forming were jointly optimised for sum-rate maximisation. Fractional programming and block coordinate descent were used to decouple the problem, with majorisation–minimisation and the alternating direction method of multipliers applied to the resulting subproblems. These studies demonstrate methods for handling the coupled design variables, but their scalability to large surfaces with discrete phase constraints remains an important consideration.

Deep reinforcement learning provides an alternative approach to joint beamforming design [77, 78, 79]. Early studies [77, 78] employed deep deterministic policy gradient algorithms, but assumed continuous RIS phase control and considered relatively small surfaces. To address discrete phase control, [79] proposed a multi-agent framework in which one agent learns the BS precoding matrix and other agents learn RIS beam patterns for different user clusters. However, the agents operate independently, without explicit cooperation.

Large RIS prototypes and propagation studies motivate investigating systems with element counts on the order of thousands [1, 80]. At this scale, the number of discrete phase configurations creates a substantial design challenge. Moreover, inter-user channel correlation and imperfect CSI introduce additional difficulties, particularly when users are spatially clustered. Together, these considerations motivate the framework developed in Chapter 7, which investigates sequential multi-agent advantage actor–critic learning for joint beamforming with large RISs, discrete phase control, channel correlation, and imperfect CSI.

2.9 Summary

In this chapter, we reviewed the key principles, architectures, and research directions associated with RIS-assisted wireless communication systems. The discussion began with the fundamental hardware structure of RISs, including the reflecting element layer, control circuitry, and metallic backplane, followed by an overview of reflecting element designs at both mmWave and THz frequencies. Particular attention was

given to the differences between conventional electronically controlled RIS elements and emerging material-based implementations, such as liquid-crystal- and graphene-based designs, which are more suitable for operation at THz frequencies.

The chapter then reviewed the electromagnetic and system-level models commonly adopted for RIS-assisted systems. Electromagnetic models based on physical optics and Green's theorem were discussed to characterise the propagation behaviour and path-loss characteristics of RIS-assisted links in both near-field and far-field regimes. In parallel, signal-level models based on the RIS scattering matrix were introduced, including conventional diagonal RIS architectures and beyond-diagonal RIS structures with inter-element coupling. In addition, the challenges associated with channel estimation in RIS-assisted systems were discussed, particularly for large-scale and near-field deployments where cascaded channel estimation becomes increasingly difficult.

Beyond conventional RIS architectures, several extensions and emerging research directions were reviewed. These included simultaneously transmitting and reflecting RIS architectures, which provide full-space coverage through simultaneous transmission and reflection. The chapter also surveyed recent advances in the performance analysis of intelligent-surface-assisted wireless networks, with emphasis on coverage probability, spectral efficiency, energy efficiency, and user-centric performance metrics. Furthermore, the challenges introduced by wideband operation were reviewed, including beam squint, frequency selectivity, and RIS coherence bandwidth limitations. Finally, existing approaches for joint optimisation of base station beamforming and RIS phase configuration were discussed, with particular focus on deep reinforcement learning methods and their limitations when applied to extremely large-scale RIS deployments.

Overall, the discussions in this chapter establish the theoretical and practical foundation for the remainder of this thesis. The reviewed hardware architectures, propagation models, performance analysis frameworks, and optimisation techniques

provide the necessary background for the high-frequency RIS element modelling, indoor network performance analysis, user-capacity characterisation, wideband RIS analysis, and learning-based beamforming optimisation developed in the subsequent chapters.

Chapter 3

RIS Element Modelling at High Frequencies

The phase response of an RIS is fundamentally determined by the underlying physical mechanism used to manipulate the EM waves. This mechanism varies significantly across different frequency bands, leading to distinct modelling approaches. In this chapter, we first review phase modelling at mmWave frequencies, where conventional electronic tuning mechanisms are effective. We then extend the discussion to THz frequencies, where material-driven phase modulation becomes essential due to hardware limitations.

3.1 RIS Phase Modelling at mmWave

At mmWave frequencies, RIS elements are typically implemented using electronically tunable components such as PIN diodes or varactors. These elements adjust the reflection phase by altering the resonant characteristics of the unit cell. As a result, the phase shift is commonly modelled as a discrete set of values, corresponding to finite-resolution phase control (e.g., 1-bit, 2-bit, or 3-bit quantisation). From a system-level perspective, the RIS is often represented as a diagonal phase shift matrix, where each element introduces an independent phase shift to the incident signal. The phase response is typically assumed to be frequency-flat over the bandwidth of interest, and idealised models often neglect amplitude variations and hardware imperfections. Under these assumptions, the phase shift of the nth RIS element can be expressed as

$$\theta_n \in \mathcal{F},$$

where $\mathcal{F}$ denotes the finite set of quantised phase values. Such discrete phase models are widely adopted due to their simplicity and analytical tractability, and can be implemented using electronically tunable components such as varactors at microwave and mmWave frequencies. However, these conventional tuning mechanisms become less effective at higher frequencies due to increased losses, parasitic effects, and fabrication constraints, limiting their applicability in the THz regime.

3.1.1 RIS Phase Modelling at Terahertz Frequency

The extension of RIS technology to the THz band introduces new challenges in phase modulation. Unlike mmWave systems, conventional electronic tuning mechanisms become less effective due to increased losses, fabrication limitations, and pronounced parasitic effects. Consequently, alternative approaches based on material properties are required. One promising solution is to employ LC materials, which exhibit anisotropic permittivity and can be tuned through external electric fields.

Previous work has been carried out on LC-based RIS (LC-RIS) [81, 3]. For example, [81] proposed a transmissive metasurface with 1-bit resolution at 0.426 THz using a nematic LC as the substrate. The unit cell in this case comprises a quartz superstrate, a complementary asymmetrically split ring (CASR) on the gold electrode, a PI layer, an LC layer, another PI layer, a gold electrode, and a quartz substrate. Researchers in [3] have proposed a reflective 1-bit metasurface at 0.675 THz, whereby the unit cell comprised a very similar configuration, except here a metallic back plate replaced the quartz substrate and a CSRR was used instead of a CASR. In addition, [3] designed and fabricated a 32-element metasurface and tested it at the working frequency. The result showed that the proposed metasurface has a steering range of 40° for a normal incidence beam. Nematic LCs as a tunable substrate [81, 3] provide a solution for phase adjustment at THz frequencies. However, the change in the permittivity will also cause a change in the resonant frequency of the antenna element. With a shifted resonant frequency, the radiation efficiency

of the antenna element may degrade. Even though the LC substrate provides a continuous and wide-range phase shift, only a small portion of this phase shift range can be utilised in case the radiation efficiency degradation happens. This is also the reason why most of the previous work proposes the unit cell structure with 1-bit, 2-bit, or 3-bit phase shift [4]. In this subsection and the following subsection, we refer to RIS configurations that use an indirect modulation of the LC,i.e., LC as a tunable substrate, as conventional RIS.

Besides using the LC cell as a tunable substrate to indirectly introduce the phase shift to the impinging waves, the LC cell itself can also be a phase shifter [82]. Researchers have previously proposed a power-amplifying RIS for optical communication systems with LC cells as its reflecting elements [83]. The reflecting element comprised a glass superstrate, an indium tin oxide (ITO) layer, an LC layer sandwiched between PI layers, a second ITO layer, and a complementary metal-oxide semiconductor (CMOS) back plate. Similarly, [84] also adopted such a reflecting element structure for RIS when designing an RIS-assisted free-space optics (FSO)/RF satellite-aerial-ground network. In direct phase modulation, the phase shift is introduced when the wave travels inside the LC cell. Compared to indirect modulation, the unit cell structure in direct phase modulation does not have an antenna element, which indicates that the continuous and wide phase shift change can be fully utilised. Furthermore, because the electromagnetic properties of LC materials vary relatively slowly over the THz frequency range of interest, direct phase modulation can provide a broadband response. However, it is also noted that typically direct phase modulation is exploited in the optical domain because the wavelength in the optical domain is small (on the order of nanometres), and a thin LC cell (e.g., of the order of 5 μm) can achieve a continuous full-range phase shift. It is unclear whether direct phase modulation can be applied to THz frequencies because a much thicker LC cell is needed. Whether the thicker LC cell maintains

certain alignment and can be tuned under relatively low voltage[1] remains an open problem.

3.2 Reflecting Element Design and Verification

In the following of this section, we propose to use an ultra-thick LC cell as the reflecting element for LC-RIS at THz frequencies and verify its feasibility through the experiment. Then, we analyse the performance of the LC-RIS with conventional RIS (the RIS that uses the LC as a tunable substrate) as the benchmark in terms of the directivity. The reflecting element comprises a metallic back plate, a poly(3,4-ethylene dioxythiophene):poly(styrene sulfonate) (PEDOT:PSS) electrode [85, 86], a PI alignment layer, an LC layer, a second PI alignment layer, a PEDOT:PSS electrode, and a sapphire superstrate from bottom to top. The corresponding layers for the proposed reflecting element are shown in Fig. 3.1. With the sapphire superstrate and metallic back plate, the transmission coefficient is high at the upper interface, and the reflection coefficient is high at the lower interface. With PEDOT:PSS as the electrode, transparency can be maintained. To verify that such a proposed reflecting element is feasible for RIS, it is important to demonstrate that the ultra-thick cell could be sufficiently aligned [2] and can be tuned under a relatively low voltage. In this subsection, we present the experimental results obtained by our collaborators using a THz spectrometer (TeraSmart) to characterise an E7-based 400 μm LC

[1]The requirement of a low bias voltage comes from the definition of the RIS. When this concept was proposed, it was defined as a low-cost, low-energy consumption technology.

[2]With the thickness of the LC layer increasing, the LC director (the average pointing direction of the molecules) in the middle of the LC layer tends to fluctuate when no bias voltage is applied, which will cause the birefringence of the element to decrease. With the thickness of the element increasing to an extent, the anisotropy property will tend to reduce.

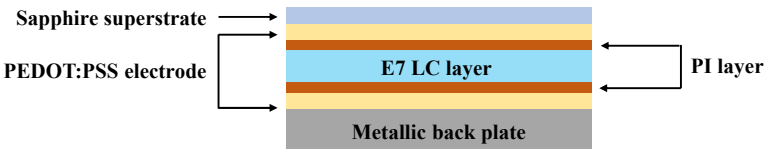

Figure 3.1: Cross-section illustration of the proposed reflecting element.

element at THz frequencies. The fabrication of the sample and the experimental measurements were conducted by our collaborators, while my contribution focuses on the subsequent analytical modelling and performance analysis. The measured ordinary and extraordinary refractive indices are presented as functions of frequency, while the relationship between phase shift and bias voltage is examined later in this chapter.

The experiment aims to measure the THz response and dielectric properties of a single LC element made up of the nematic LC mixture, E7 (sourced from Synthon Chemicals Ltd). The core measurement equipment in this experiment is a TeraSmart, where THz pulses are generated using laser stimulation of THz crystals and detected by a mode-locked synchronous amplifier. The system was configured in a transmissive measurement layout where the emitted pulse enters the device at normal incidence to the surface of the element, and the transmitted pulse is then measured. The polarisation direction of the emitted pulse was aligned with the receiver orientation, which was also in the same direction as the LC director.

A single LC element was fabricated by our collaborators for transmissive measurements, based on a structure similar to that presented in Fig. 3.1. Unlike the proposed reflecting element, which employs a metallic back plate, the experimental sample consists of a 400 μm LC layer sandwiched between two sapphire substrates. This configuration allows the THz waves to propagate through the LC layer, enabling the characterisation of its dielectric properties and voltage-dependent phase response using transmission measurements. Therefore, the experiment directly validates the alignment and tunability of the ultra-thick LC layer, while the reflection phase response of the proposed element is evaluated analytically in the subsequent sections. The substrate size was 20 mm by 15 mm, and the thickness was 1.1 mm. The surface roughness was around 0.3 nm. Its surface orientation was C-plane, which means it is uniform no matter what its orientation is when the beam illuminates the board surfaces. The beam size at the sample plane was much smaller than the active region

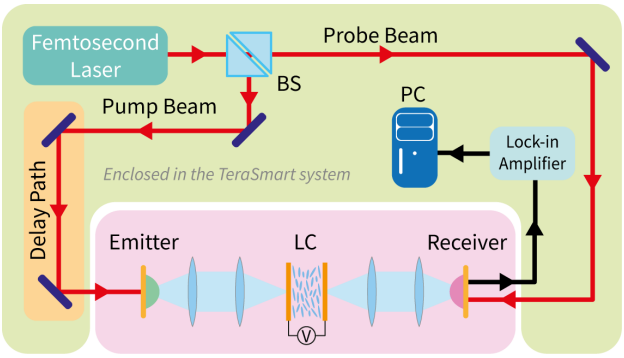

Figure 3.2: Schematic of the TeraSmart THz spectrometer and the transmission measurement configuration. The LC sample is positioned between the emitter and receiver, and the transmitted time-domain electric field is measured with and without the sample to characterise its frequency-dependent optical properties.

of the LC element, which ensured that the THz beam was fully modulated by the LC element. The polarisation direction of the THz beam was parallel to the rubbing direction of the LC director, which utilised the full modulation dynamic range of the LC element. To demonstrate the dynamic range of LC modulation, different voltages were applied across the LC layer, and the phase shift at different frequencies was compared with the corresponding initial phase when no voltage was applied at each frequency. A schematic of the TeraSmart THz spectrometer, as well as the measurement setup for a single LC element, is presented in Fig. 3.2. The refractive indices of the LC sample were extracted from the measured time-domain THz signals. Specifically, the transmitted electric fields with and without the sample, denoted by $E_s(t)$ and $E_r(t)$, respectively, were measured and transformed into the frequency domain. The complex transmission coefficient was then obtained as

$$\tilde{T}(\omega) = \frac{\tilde{E}_s(\omega)}{\tilde{E}_r(\omega)}. \tag{3.1}$$

The frequency-dependent refractive index was subsequently extracted from the phase response of $\tilde{T}(\omega)$, accounting for the sample thickness and the transmission characteristics of the material [87, 88]. For the thick sample considered here, higher-order internal reflections were neglected in the extraction model, as their delayed contributions fell outside the measurement time window. Here, we show the variation of the ordinary and extraordinary refractive indices with respect to the frequency

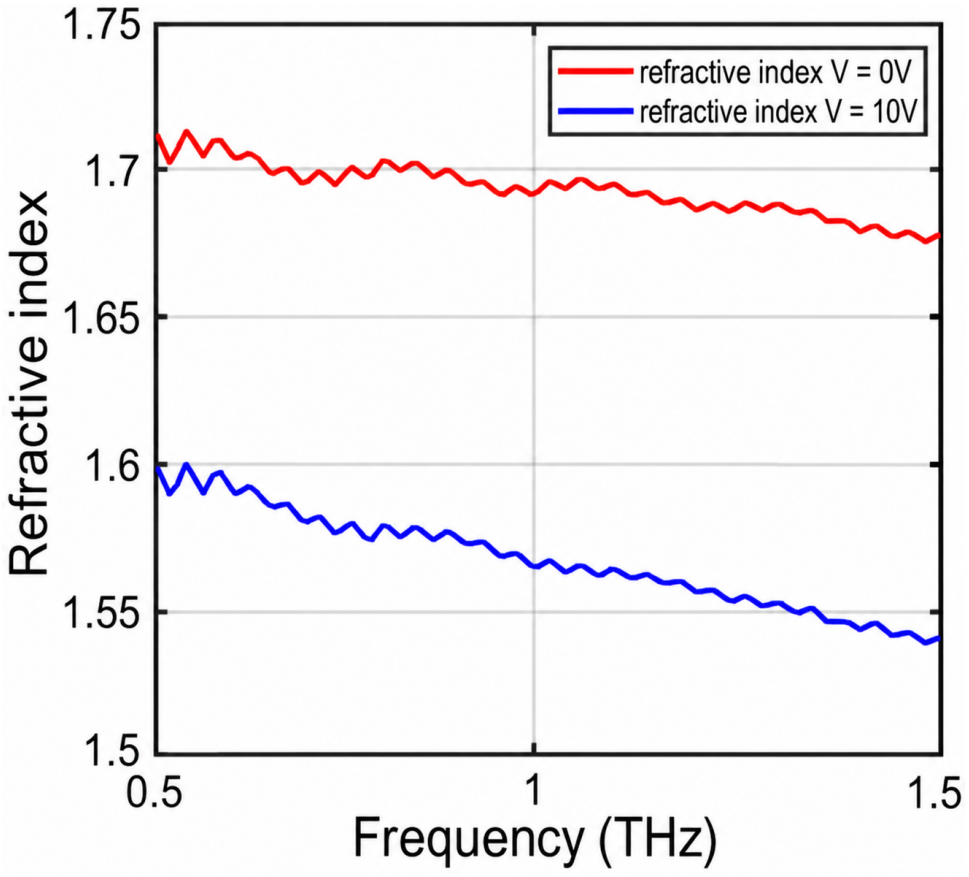

Figure 3.3: Frequency-dependent refractive indices extracted from transmission measurements of the E7-based 400 μm LC sample. The red and blue curves correspond to the refractive indices obtained at bias voltages of 0 V and 10 V, respectively. Their difference illustrates the voltage-dependent birefringence of the ultra-thick LC layer.

in Fig. 3.3. The red and blue curves represent the extraordinary and ordinary refractive indices, respectively. The average difference between the two refractive indices in Fig. 3.3 is approximately 0.13, indicating that the ultra-thick LC layer retains appreciable voltage-dependent birefringence. This provides experimental evidence that molecular alignment and electrical tunability can be maintained at a thickness of 400 μm. However, these transmission measurements do not directly characterise the reflection phase response of the proposed element with a metallic back plate, which is investigated analytically in the following sections.

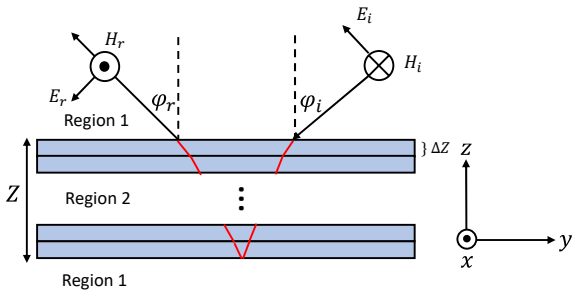

Figure 3.4: Geometric illustration of the impinging waves interacting with an LC reflecting element.

3.3 Phase Shift Approximation of a Single Liquid Crystal Reflecting Element

After confirming that tunability is preserved at this thickness, it is also important to determine the phase shift the reflecting element can provide under arbitrary incidence angles. In this section, we derive an approximation of the phase shift for the proposed reflecting element at a given frequency and arbitrary angle of incidence. In this work, we assume that the superstrate has a transmission coefficient of 1 and that the substrate has a reflection coefficient of 1. We assume the higher-order waves (e.g., waves that have undergone more than one reflection) can be neglected. Under these assumptions, we give the geometric illustration of the impinging waves interacting with an LC reflecting element. In Fig. 3.4, the impinging waves are assumed to be transverse magnetic (TM) waves, and the reorientation plane of the LC director is restricted to be in the yz plane. E_i, H_i, E_r, H_r, φ_i, φ_r, and Z denote the incident electric field, incident magnetic field, reflected electric field, reflected magnetic field, incidence angle, reflected angle, and thickness of the element. Traditionally, the phase shift introduced by a homogeneous medium is computed by:

$$\Delta\phi = k(n_2 - n_1)L, \tag{3.2}$$

where k, n_2, n_1, and L denote the wavenumber, the refractive index in the medium, the refractive index in free space, and the interaction length inside the medium,

respectively. However, there are two fundamental refractive indices in an LC reflecting element because of the anisotropic nature of the material, which are the extraordinary refractive index and the ordinary refractive index. The inhomogeneous property of the LC material suggests that we need to consider how n_2 (3.2) is represented for the LC. To tackle this problem, we use the effective refractive index [89].

$$n_{\text{eff}} = \frac{n_e n_o}{\sqrt{n_e^2 \sin^2(\psi) + n_o^2 \cos^2(\psi)}}, \tag{3.3}$$

where n_e, n_o, and ψ denote the extraordinary refractive index, ordinary refractive index, and the angle between the LC director profile (also known as the tilt angle) and the impinging waves' electric field polarisation direction, respectively. To simplify the calculation of the effective refractive index, we assume the inhomogeneous LC reflecting element can be divided vertically into N segments each with thickness ΔZ. In each segment, we assume that the tilt angle remains the same (see Fig. 3.4). Another difficulty when it comes to calculating n_{eff} is that we need to know the refracted angle of the nth segment (φ_n) to calculate the angle ψ. But the refracted angle can only be computed when the n_{eff} of the nth segment is known. To solve this dilemma, we propose to set an initial value to n_{eff} first and then update n_{eff} and the refracted angle in an iterative way. With the refracted angle and the segment thickness, the interaction length for each segment can also be calculated. With the interaction length of each segment, the total accumulated phase shift can then be approximated. We summarise the phase shift approximation in Algorithm 1. In Algorithm 1, φ_n, L_{LC}, and $\boldsymbol{\theta}$ denote the refracted angle in the nth segment, the interaction length, and the tilt angle vector under a specific bias voltage. Note that the phase shift calculated from Algorithm 1 is relative to free space. A common term $\Delta\phi_{V_0}$ (phase shift when the bias voltage is 0-volt) should be subtracted from all phase shift values to obtain the phase shift relative to when the LC element is operating in the 0-volt bias voltage condition. With the approximated phase shift of each element of the LC-RIS, we can calculate the directivity of the LC-RIS given a desired reflection direction [90]. In this context, we assume the incidence plane

is always parallel to the yz plane and the diffraction of the impinging waves also resides in the upper yz plane[3] (because we assume the reflection coefficient of the metallic back plate is 1).

Algorithm 1: Phase shift approximation for an LC reflecting element

Input : n_e, n_o, n_1, φ_i, φ_n, ΔZ, k, N, $\boldsymbol{\theta}$
Output: $\Delta\phi$, L_{LC}

Initialise $n_{\mathit{eff}} = (n_e + n_o)/2$
Initialise $n_{\mathit{temp}} = n_1$
Initialise $L_{LC} = 0$
Initialise $\Delta\phi = 0$
for $n \leftarrow 1$ **to** $2N$ **do**
  $\varphi_n = \arcsin\left(n_{\text{eff}} \sin\varphi_i / n_{\text{temp}}\right)$
  if $n \leq N$ **then**
    $\psi = \varphi_n + \boldsymbol{\theta}(n)$
  else
    $\psi = \varphi_n - \boldsymbol{\theta}(n)$
  $\Delta\phi = \Delta\phi + k(n_{\text{eff}} - n_1)\Delta Z / \cos\varphi_n$
  $L_{LC} = L_{LC} + \Delta Z / \cos\varphi_n$
  $n_{\text{temp}} = n_{\text{eff}}$
  $\varphi_i = \varphi_n$
  $n_{\text{eff}} = \frac{n_e n_o}{\sqrt{n_e^2 \sin^2(\psi) + n_o^2 \cos^2(\psi)}}$
Return $\Delta\phi$, L_{LC}

3.4 Numerical Results

We give the parameter settings in Table 3.1. It is noted that the parallel and perpendicular dielectric permittivity is a sequence. Each entry in the sequence has a corresponding frequency, which is also given in the table. The numerical and measured results are shown in Fig. 3.5. In Fig. 3.5(a), dots represent the measured results, dashed lines represent the numerical results obtained from the approximation[4] relative to the 0-volt bias voltage with the parallel and perpendicular permittivity taken from [91], and solid lines represent the numerical results obtained

[3]This assumption can also be interpreted as a 2-dimensional diffraction process

[4]Due to the phase shift extracted from the experiment being for transmission, the approximated phase shift is halved to match the measured results.

Table 3.1: Parameter settings

Parameter	**Value**
LC material type	E7
LC layer thickness	400 μm
LC layer parallel dielectric permittivity	[2.95, 2.89, 2.89, 2.89]
LC layer perpendicular dielectric permittivity	[2.56, 2.49, 2.43, 2.43]
Incidence angle	0°
Centre frequency range	[0.31, 0.60, 0.81, 1.00] THz
bias voltage range	[0, 1, 3, 5, 7, 9, 10] V

from the approximation relative to the 0-volt bias voltage with the parallel and perpendicular permittivity taken from the experiment. It is assumed in Fig. 3.5(a) that the parallel and perpendicular permittivity do not change with respect to frequency (the values used for parallel and perpendicular permittivity are 2.89 and 2.43, respectively).

Firstly, it is observed that there is a good match between the solid lines and the dots at different frequencies. This verifies that the approximated phase shift is accurate. Secondly, the dashed lines match well the solid lines, which indicates the extracted values from the experiment are reliable. Thirdly, it is noted that the phase shift range will increase with increasing frequency. Last, it is shown that the phase shift will saturate around 5 volts. This is due to most of the LC directors being aligned towards the direction of the external electric field. By observing the solid lines, it is concluded that the phase shift is continuous in a certain range under the condition that the bias voltage can be tuned continuously. In Fig. 3.5(b), the variation of the parallel and perpendicular permittivity with respect to the frequency is considered. However, by comparing the phase shift range with Fig. 3.5(a) at different frequencies, no significant difference is observed. Hence, in the rest of the subsection, we assume the parallel and perpendicular permittivity does not change

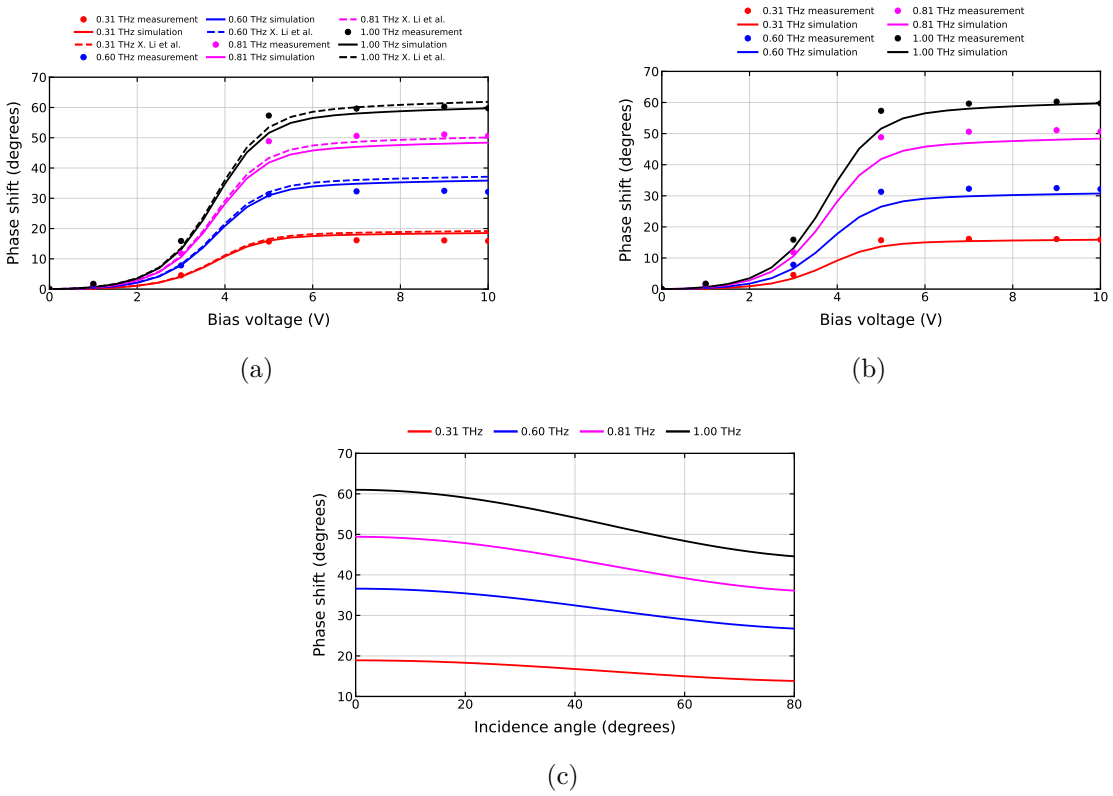

Figure 3.5: (a)–(b) Comparison of a single E7 LC element phase shift (relative to the 0-volt bias voltage) between numerical results and measured results with respect to the bias voltage at 0° incidence angle with frequency-invariant (a) and frequency-variant (b) extraordinary and ordinary refractive indices. (c) Phase shift response with respect to the incidence angle of an E7-based single LC element at 1 THz and 10 V bias voltage.

with respect to the frequency.

In Fig. 3.5(c), the phase shift response of the E7-based LC element with respect to the incidence angle is revealed. It is observed that the phase shift will decrease with the increase in the incidence angle. This can be explained by examining the single-cell phase shift approximation process. With the increase in the incidence angle, the ratio of $(n_{\text{eff}} - n_1)\Delta Z / \cos\varphi_n$ decreases, which will cause a decrease in the phase shift range.

As we will incorporate a GT3-23001-based LC-RIS for LC-RIS performance comparison in the following[5], we provide the phase shift response with respect to

[5]As stated in the abstract, the reason for introducing GT3-23001 LC material is that E7-based LC-RIS cannot outperform the conventional RIS in most cases due to its low birefringence, which

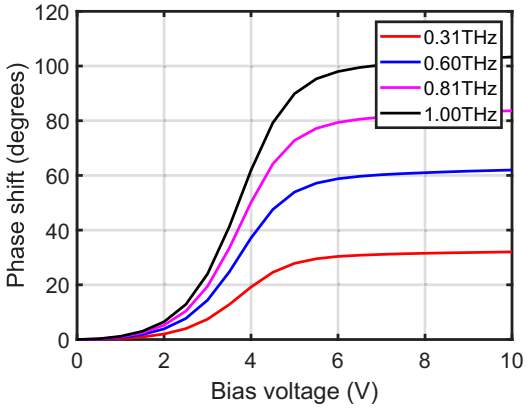

(a)

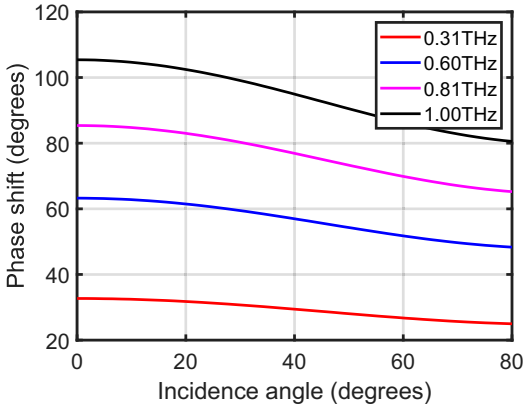

(b)

Figure 3.6: (a)–(b) Phase shift response with respect to the bias voltage (a) and incidence angle (b) of a GT3-23001-based single LC element with $\varepsilon_{\parallel} = 3.28$, $\varepsilon_{\perp} = 2.46$, and thickness of 400 μm.

the bias voltage and the incidence angle for the GT3-23001 LC element here. The parallel and perpendicular dielectric permittivity of GT3-23001 are set to be 3.28 and 2.46 at THz frequencies [91]. Other parameters are the same as in Table 3.1. It is observed in Fig. 3.6(a) that the phase shift range is larger than the E7-based LC element at every frequency. This is because GT3-23001 has a larger birefringence at THz frequencies. In Fig. 3.6(b), the same trend is observed as in Fig. 3.5(c). However, the phase shift range at every frequency decreases faster than that of the E7-based LC element.

We then move forward to analyse the performance of such LC-RIS in terms of

will be revealed later.

Table 3.2: Parameter settings for the performance analysis between the LC-RIS and the conventional RIS.

Parameter	**E7**	**GT3-23001**
Parallel dielectric permittivity	2.89	3.28 [91]
Perpendicular dielectric permittivity	2.43	2.46 [91]
Desired direction for elevation angle	10°	
Centre frequency of the impinging waves	[1.000, 1.125, 1.250, 1.375, 1.500] THz	
Element spacing [6]	$\lambda/2$	
Discrete phase shift for conventional RISs	1-bit: [0°, 180°], 2-bit: [0°, 90°, 180°, 270°], 3-bit: [0°, 45°, 90°,135°, 180°, 225°, 270°,315°]	
Total illuminated power on the surface	1 mW	

the directivity. We assume the LC reflecting element can always be fully tuned at all thicknesses below 400 μm. The performance evaluations in this chapter are based on a lossless assumption, i.e., the radiated power equals the incident power[7]. In practice, non-ideal factors such as dielectric absorption in the LC layer, finite electrode conductivity, and substrate losses will lead to performance degradation. These effects are not included here because the main objective of this study is to assess the intrinsic beamforming potential of the proposed ultra-thick LC element and to establish an ideal performance upper bound. Incorporating such losses requires detailed, material- and fabrication-specific THz loss parameters, which are highly variable and beyond the scope of this proof-of-concept work. Future studies will incorporate these factors for a more comprehensive and practical performance assessment. Other relevant parameters for the simulation are listed in Table 3.2, where λ denotes the wavelength of the impinging THz wave. The performance comparisons with respect to the thickness using E7 are shown in Fig. 3.7(a). The

[7]This assumption is critical because we need to ensure the denominator for the directivity calculation is the same for the LC-RIS and the conventional RIS.

horizontal axis represents the thickness of the LC reflecting element, and the vertical axis represents the directivity difference between the LC-RIS and the conventional RIS. It is observed that the performance of E7-based LC-RIS is below the 2-bit and 3-bit RIS at all thicknesses and all incidence angles, and it can outperform the 1-bit RIS when the element thickness is greater than 350 μm by around 2 dB. The unsatisfied performance of E7-based LC-RIS is mainly caused by the limited phase shift generated by the E7-based LC reflecting element. Although the E7-based LC-RIS cannot outperform the conventional RIS in most cases, some insights can be extracted from Fig. 3.7(a). It is noted that the performance of E7-based LC-RIS will increase with an increase in the element thickness. The incidence angle negatively correlates with the performance of the LC-RIS, as explained in the previous section. In Fig. 3.7(b), we show the performance comparisons between the GT3-23001-based LC-RIS and the conventional RIS. It is observed that the directivity difference will increase with the increase in the element thickness. For a fixed element thickness, it is also observed that the increase in the incidence angle will cause performance degradation to the LC-RIS (around 1 dB). It is noted that the LC-RIS outperforms the 1-bit RIS by around 10 dB, the LC-RIS outperforms the 2-bit RIS by around 3 dB, and the LC-RIS outperforms the 3-bit RIS by around 2 dB at 400 μm, and frequency of 1.5 THz.

The performance comparisons with respect to the impinging waves' frequency are shown in Fig. 3.7(c) and Fig. 3.7(d). It is observed in Fig. 3.7(c) that the performance of E7-based LC-RIS is below that of the 2-bit and 3-bit RIS at all frequencies. However, it can outperform the 1-bit RIS when the frequency is above 1.3 THz, and the directivity difference is around 3 dB when the frequency reaches 1.5 THz. Fig. 3.7(d) shows the performance comparisons between the GT3-23001 LC-RIS and the 1,2,3-bit conventional RIS. It is observed that the GT3-23001 LC-RIS can outperform the 1-bit RIS at all frequencies, reaching a directivity difference of 10 dB when the frequency is 1.5 THz. The GT3-23001 LC-RIS can also outperform

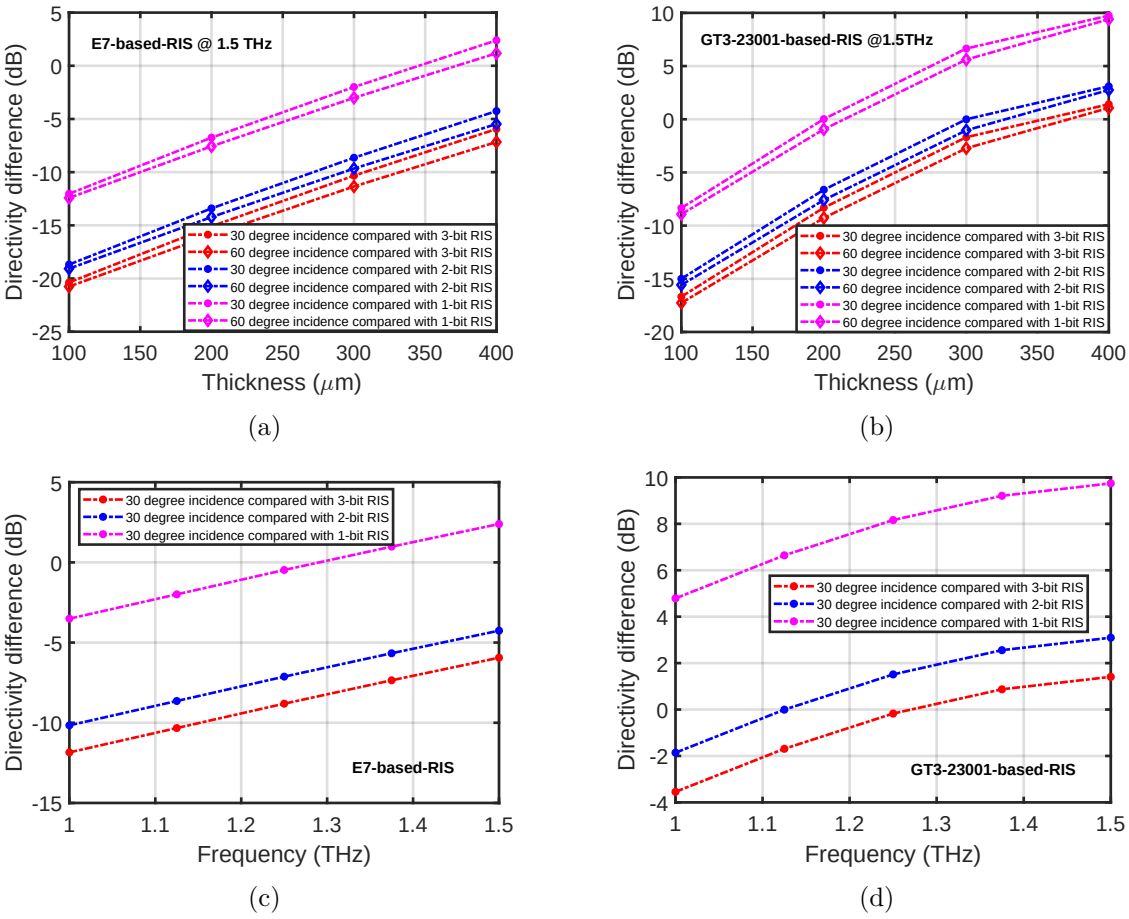

Figure 3.7: Performance comparison between the proposed 10×10 LC-RIS and conventional 10×10 RISs with 1-bit, 2-bit, and 3-bit phase quantisation, expressed as the directivity difference (LC-RIS minus conventional RIS). (a) Directivity difference versus LC layer thickness for E7 at 1.5 THz. (b) Directivity difference versus LC layer thickness for GT3-23001 at 1.5 THz. (c) Directivity difference versus operating frequency for E7. (d) Directivity difference versus operating frequency for GT3-23001. Panels (a) and (b) consider incidence angles of 30° and 60°, while panels (c) and (d) consider an incidence angle of 30°.

the 2-bit RIS when the frequency is above 1.12 THz, and the directivity difference can reach 3 dB at 1.5 THz. Lastly, unlike the E7-based element, the GT3-23001 LC-RIS can also outperform the 3-bit RIS when the frequency is above 1.25 THz, and the directivity difference can reach nearly 2 dB at 1.5 THz.

3.5 Conclusion

In this chapter, we investigated the design of an ultra-thick LC reflecting element for RIS operating at THz frequencies. Unlike conventional RIS (using LC as a tunable substrate) designs, the proposed structure enables direct phase modulation, allowing a wide and continuous phase shift range without relying on resonant antenna elements. The feasibility of the design was experimentally validated, confirming that even with a thickness on the order of hundreds of micrometres, the LC layer can maintain sufficient alignment and tunability under practical bias voltages. Building upon this, an analytical phase shift approximation method was developed and shown to closely match the measured responses, providing a tractable tool for system-level analysis. Using this model, we compared the performance of the proposed LC-RIS with conventional LC-substrate RIS architectures. The results highlight that material birefringence plays a critical role: high-birefringence LCs (e.g., GT3-23001) enable substantial directivity improvements, whereas low-birefringence materials (e.g., E7) offer only marginal gains. It is important to note that the analysis was conducted under a lossless assumption to isolate the impact of phase modulation and establish an upper bound on performance. In practice, dielectric and conductor losses will degrade performance, and incorporating these effects represents an important direction for future work.

Chapter 4

Performance Analysis of RIS-Assisted mmWave Indoor Wireless Networks

This chapter marks the transition from RIS hardware and element-level modelling to system-level performance analysis. While Chapter 3 focused on the physical behaviour of RIS elements, the ultimate objective of RIS deployment is to improve network performance in practical wireless environments.

To investigate this aspect, we develop a stochastic geometry framework for RIS-assisted indoor millimetre-wave networks. Particular attention is paid to realistic indoor characteristics, including blockage effects, user clustering, boundary constraints, and three-dimensional node locations. Based on this framework, analytical expressions for distance distributions, line-of-sight probabilities, and coverage probability are derived. The resulting analysis provides insights into how network parameters influence coverage performance and offers guidance for RIS deployment in practical indoor environments.

4.1 System Model

We consider downlink communication in a three-dimensional RIS-assisted indoor mmWave network, as illustrated in Fig. 4.1. The ceiling-mounted transmitters send signals to the end users (EUs), either directly or via reflection from a RIS. The network comprises transmitters, RISs, EUs, and obstacles. Due to the blockage effects and the large-scale fading, some of the users cannot be covered (e.g., EU1 in

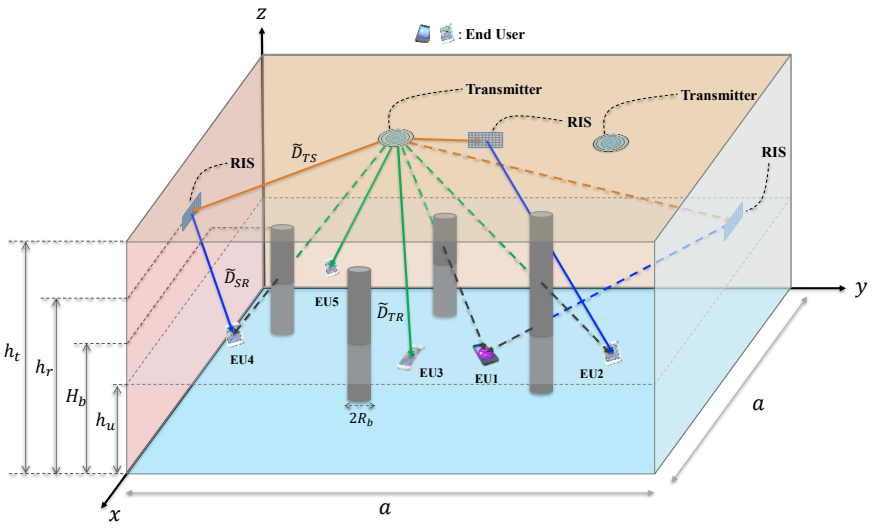

Figure 4.1: Illustration of the 3D RIS-assisted indoor mmWave network.

Fig. 4.1), while others can only be covered by the indirect link (e.g., EU2 and EU4 in Fig. 4.1) or the direct link (EU3 and EU5 in Fig. 4.1). To analyse how well a user is covered by this network, coverage probability (CP) is used. Next, we introduce the system model and the essential components for the CP calculation. The room has a length and width of a and a height of h_t (this room can be a conference centre, a hospital, a library, or a shopping mall). There are N_T transmitters that are all deployed on the ceiling following a BPP model [92]. Each transmitter is equipped with an antenna array [55]. There are N_c clusters with radius R_c in the room, where the cluster centres are modelled as BPP. Cluster centres represent real-world objects such as poster panels, information desks, or kiosks. We assume the number of users in each cluster follows an independent and identically distributed (i.i.d.) Poisson distribution, reflecting the natural variability in cluster population size, while ensuring the user count remains a non-negative integer. The users' locations in each cluster also follow BPP [93]. For better tractability and without loss of generality, we assume that mmWave terminals with EUs are held at the height of h_u. The obstacles are modelled as cylinders with radius R_b and height H_b. The

spatial distribution of the obstacle follows BPP[1]. The height of the obstacle H_b is a uniform random variable, i.e., $H_b \sim \mathcal{U}(h_{\min}, h_{\max})$. It is reasonable to have $h_{\min} \leq h_u \leq h_{\max} < h_t$. The RISs are deployed on the four side walls with N_R RISs on each wall and a height of h_r [96]. To reduce the impact of obstacles on RIS-assisted communications, we place RISs higher than obstacles, i.e., $h_r \geq h_{\max}$ [61]. Because there is no dependency between the obstacle distribution and RIS distribution, all cluster centres follow BPP, user numbers in different clusters follow i.i.d. Poisson, and users in a cluster follow BPP, we assume the spatial distribution of each RIS follows a uniform distribution $\mathcal{U}(0, a)$ on each wall. Next, we introduce the communication strategy and the association policy between the transmitter, RIS, and user. The communication strategy includes two steps: 1) the transmitter will choose the direct link to communicate with the user, and 2) the transmitter will choose an RIS to redirect the signal to the intended user if step 1 fails. If both steps fail, we claim this communication attempt as a failure. In the direct-link association model, i.e., the first step, each cluster is assigned to the transmitter nearest to its centre, and all users within the cluster are assumed to associate with that transmitter. This approximation simplifies the analysis while retaining the variation in transmitter–user distance caused by users' locations within the cluster. Since interference is omitted from the model, these locations affect coverage through link distances and blockage probabilities. The approximation is appropriate when the cluster radius R_c is small relative to the local transmitter spacing, and the cluster lies predominantly within the nearest transmitter's Voronoi cell. More precisely, let d_1 and d_2 denote the horizontal distances from the cluster centre to its nearest and second-nearest transmitters, respectively. A sufficient condition for every user in the cluster to share the centre's nearest transmitter is $d_2 - d_1 > 2R_c$. Thus, a small

[1]Because obstacles cannot overlap, their spatial distribution is more appropriately modelled by a hard-core point process, which enforces a minimum separation between obstacles. However, obstacles typically occupy less than 20% of the room area (7.86% in [94] and 2.36% in[95]). Under the considered conditions, the probability that two obstacles are separated by less than $2R_b$ is small: approximately 0.005 for $a = 100$ m, $R_b = 1.25$ m, and $N_o = 408$. Hence, a BPP provides a tractable approximation to the spatial distribution of obstacles.

cluster radius relative to the room size alone does not guarantee the validity of the approximation. For a fixed room area, increasing the number of transmitters generally reduces the size of their association regions. Consequently, a cluster of fixed radius is more likely to intersect multiple association regions, making the shared-transmitter approximation less reliable. In the second step, the RIS geometrically nearest to the user is selected to reflect the signal from the associated transmitter. This selection is made irrespective of the instantaneous blockage configuration. If the selected RIS–user link is blocked or its received signal-to-noise ratio (SNR) is below the required threshold, the communication attempt is declared unsuccessful; the model does not consider reassociation with another RIS. This policy is motivated by the shorter propagation distance and reduced blockage exposure of nearby RISs, and is adopted for analytical tractability. Under nearest-visible-RIS association, the selected surface could be the nearest, second-nearest, or a higher-ranked RIS, depending on which links are blocked. Its distance distribution would therefore depend jointly on the ordered RIS locations and the blockage events of the candidate links. These blockage events can also be correlated because an obstacle may block multiple RIS-user links. Accounting for these dependencies would substantially complicate the analysis. Geometric nearest-RIS association is adopted in this work as a simple reference policy that does not require blockage-aware selection among candidate RISs. It allows the analysis to isolate the effects of deployment geometry and blockage under a fixed association rule. In practice, a system could assess alternative RIS-assisted links and reassociate when the selected link becomes unavailable. However, incorporating such selection into the present framework would require the joint characterisation of candidate-link distances and their potentially correlated blockage events. This extension is beyond the scope of the present analysis. Consequently, the model does not capture the additional coverage achievable by exploiting alternative available RIS-assisted links. Other association policies considered in the literature include selecting the RIS nearest to the transmitter, or selecting the RIS that minimises the

sum or product of the transmitter-RIS and RIS-user distances [58, 97, 98].

Multiple users, including users from different clusters, may associate with the same RIS. Resource contention among these users is not considered in the present analysis. Instead, the selected surface is assumed to be fully available to the considered link, with all elements configured to assist that user. The resulting coverage probability is therefore interpreted as an idealised upper bound on per-user link coverage in a shared-resource system where resource allocation reduces the effective aperture or coherent gain available to each link, under otherwise identical propagation and interference assumptions. It does not characterise the simultaneous coverage of all associated users or account for scheduling effect. It is widely recognised that the mmWave transmitter generally has an antenna array that can apply beamforming to users in a cluster. In this chapter, we do not consider the interference between users inside a cluster. A convincing reason is indicated in the IEEE 802.11 ad, where time division multiple access (TDMA) is applied when serving multiple users. This means even if the users are spatially close, they can still be separated in the time domain[2]. Interference from other transmitters and signals reflected by other RISs is assumed to be negligible. This assumption is motivated by directional beamforming: each transmitter concentrates its radiated power towards its intended user or selected RIS, while the RIS phase configuration directs the reflected signal towards the intended user. Such spatial selectivity reduces the coupling of unintended transmissions into the desired link. The analysis therefore considers a noise-limited operating regime. Residual interference caused by sidelobes, overlapping beams, and unintended reflections is neglected. This approximation is appropriate when the aggregate interference power at the user is small relative to the receiver noise power; it becomes less accurate when simultaneous transmissions produce substantial interference. Under the noise-limited assumption, the CP is determined by link blockage

[2]For users that are spatially close to each other if they share the same resource (e.g., frequency, time), there will be interference because the beamforming vectors for different users will no longer be orthogonal to each other. They tend to align with each other while the spatial user correlation increases.

and the received SNR. Let $\widetilde{D}_{\mathrm{tr}}$, $\widetilde{D}_{\mathrm{ts}}$, and $\widetilde{D}_{\mathrm{sr}}$ denote the three-dimensional distances from the associated transmitter to the user, from the associated transmitter to the selected RIS, and from the selected RIS to the user, respectively. For unblocked links, we adopt a free-space propagation approximation. The direct-link received power therefore scales as $\widetilde{D}_{\mathrm{tr}}^{-2}$, corresponding to a path-loss exponent of two. For the RIS-assisted link, the adopted far-field model gives a received-power dependence proportional to $(\widetilde{D}_{\mathrm{ts}}\widetilde{D}_{\mathrm{sr}})^{-2}$, together with the antenna and coherent surface gains [38, 30]. This approximation represents directional indoor mmWave links dominated by the direct path or the intended RIS-assisted path. Additional environmental reflections, scattering, and diffraction are neglected. Blockage is represented by a binary link-availability model: a blocked path contributes no received power, rather than being assigned a separate NLOS path-loss exponent. A blocked direct path may nevertheless be served through the selected RIS.

Small-scale fading is omitted consistently with this dominant-path approximation. Conditional on node locations and blockage states, the received power is determined by the adopted propagation and gain models, without an additional random fading coefficient. This allows the analysis to isolate the effects of spatial geometry and blockage. The approximation is less representative of environments where multiple propagation components contribute substantially to the received signal. Let $\mathrm{SNR}_{\mathrm{d}}$ and $\mathrm{SNR}_{\mathrm{id}}$ denote the received SNRs of the direct and RIS-assisted indirect links, respectively, and let τ denote the minimum SNR required for successful reception. For the direct link, $P_{\mathrm{LOS,D}}(\widetilde{D}_{\mathrm{tr}})$ denotes its LOS probability, and $P_{\mathrm{NLOS,D}}(\widetilde{D}_{\mathrm{tr}}) = 1 - P_{\mathrm{LOS,D}}(\widetilde{D}_{\mathrm{tr}})$ denotes its NLOS probability. For the indirect link, $P_{\mathrm{LOS,ID}}(\widetilde{D}_{\mathrm{sr}})$ denotes the probability that the selected RIS–user link is unblocked. Since the transmitter–RIS link is assumed to be unblocked, this also represents the LOS probability of the indirect path. The total coverage probability, denoted by P_{Cov}, comprises the direct-link contribution $P_{\mathrm{Cov\text{-}D}}$ and the indirect-link contribution $P_{\mathrm{Cov\text{-}RIS}}$, with the latter applying only when the direct link fails. Therefore, the CP

through the direct link is given by the product $P_{\text{Cov-D}} = P(\text{SNR}_\text{d} \geq \tau) P_{\text{LOS,D}}(\widetilde{D}_{\text{tr}})$.

It is important to note that the indirect link does not influence the direct link analysis, as the base station always attempts to establish a connection through the direct link first. If the direct link is either blocked or its SNR falls below the required threshold, the system resorts to the indirect link. The failure of the direct link can be mathematically expressed as

$$1 - P_{\text{Cov-D}} = P(\text{SNR}_\text{d} < \tau) + P(\text{SNR}_\text{d} \geq \tau) P_{\text{NLOS,D}}(\widetilde{D}_{\text{tr}}),$$

which captures the cases where the SNR is too low or the link is NLOS. Consequently, the CP via the indirect link is given by

$$\begin{aligned} P_{\text{Cov-RIS}} &= P(\text{SNR}_{\text{id}} \geq \tau) P_{\text{LOS,ID}}(\widetilde{D}_{\text{sr}}) (P(\text{SNR}_\text{d} < \tau) \\ &+ P(\text{SNR}_\text{d} \geq \tau) P_{\text{NLOS,D}}(\widetilde{D}_{\text{tr}})). \end{aligned}$$

This reflects the CP that the direct link fails while the indirect path (via the RIS) offers sufficient SNR and is unblocked. Combining these mutually exclusive coverage contributions, the total CP is given by

$$\begin{aligned} P_{\text{Cov}} &= P(\text{SNR}_\text{d} \geq \tau) P_{\text{LOS,D}}(\widetilde{D}_{\text{tr}}) \\ &+ P(\text{SNR}_{\text{id}} \geq \tau) P_{\text{LOS,ID}}(\widetilde{D}_{\text{sr}}) (P(\text{SNR}_\text{d} < \tau) \\ &+ P(\text{SNR}_\text{d} \geq \tau) P_{\text{NLOS,D}}(\widetilde{D}_{\text{tr}})). \end{aligned} \tag{4.1}$$

Given (4.1), to obtain the final expression of P_{Cov}, SNR_d, SNR_{id}, $P_{\text{LOS,D}}$ and $P_{\text{LOS,ID}}$ need to be derived, where various distributions of distances are involved in the calculation. In the next section, we show the derivations of the related distributions of distances for direct and indirect links.

4.2 Distance Distributions

4.2.1 Direct Link

In this section, we first derive the distributions of the projected distances on the floor (shown in Fig. 4.2) and then extend them to the 3D case. We use the tilde

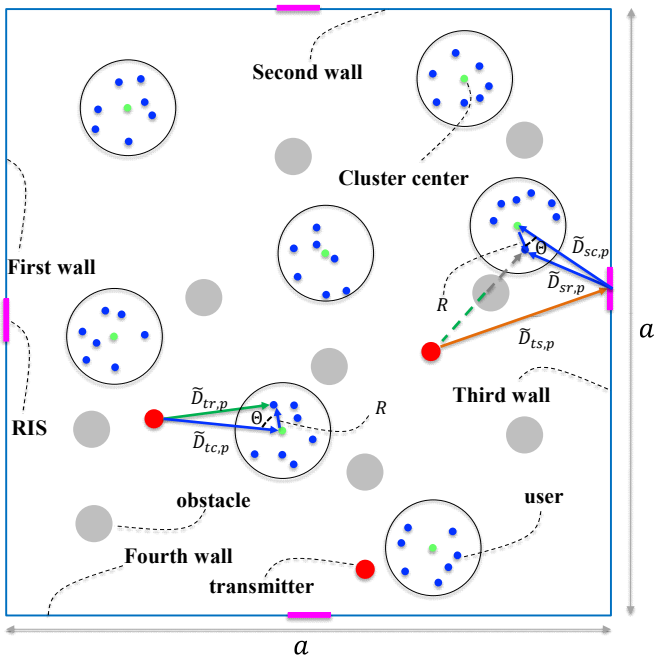

Figure 4.2: Illustration of the projected 3D RIS-assisted indoor mmWave network.

to represent the distance between the user and an associated node (transmitter or RIS), the symbol without a tilde represents the distance between the user and a node (transmitter or RIS). We use subscript p to represent the projected lengths. We define the distance between the associated transmitter and the user in Fig. 4.2 as $\widetilde{D}_{\mathrm{tr,p}}$ (the projected length of $\widetilde{D}_{\mathrm{tr}}$). The square of it is given by[3]

$$\widetilde{D}^2_{\mathrm{tr,p}} = \widetilde{D}^2_{\mathrm{tc,p}} + R^2 - 2\widetilde{D}_{\mathrm{tc,p}} R\cos\Theta, \tag{4.2}$$

where $\widetilde{D}_{\mathrm{tc,p}}$, R, and Θ denote the distance between the associated transmitter and the cluster centre, the radial distance from the user to the cluster centre, and the direction of the user inside the cluster. we define $D_{\mathrm{tc,p}}$ as the distance between a random transmitter and a random cluster centre. The probability density function (PDF) is given by [99]

$$f_{D_{\mathrm{tc,p}}}(d_{\mathrm{tc,p}}) = \frac{4d_{\mathrm{tc,p}}}{(a-R_c)^4}\phi(d_{\mathrm{tc,p}}), \tag{4.3}$$

[3]Without a specific statement, we will derive the distances' squared distributions in the rest of this section for the convenience of the later sections.

where $\phi(d_{\mathrm{tc,p}})$ is given by

$$\phi(d_{\mathrm{tc,p}}) = \begin{cases} \frac{(a-R_c)^2\pi}{2} - 2(a-R_c)d_{\mathrm{tc,p}} + \frac{d_{\mathrm{tc,p}}^2}{2}, \\ \qquad\qquad 0 \le d_{\mathrm{tc,p}} \le a - R_c \\ (a-R_c)^2\left[\sin^{-1}\left(\frac{a-R_c}{d_{\mathrm{tc,p}}}\right) - \cos^{-1}\left(\frac{a-R_c}{d_{\mathrm{tc,p}}}\right)\right] \\ -(a-R_c)^2 - \frac{d_{\mathrm{tc,p}}^2}{2} + 2(a-R_c) \\ \times\sqrt{d_{\mathrm{tc,p}}^2 - (a-R_c)^2}, \\ \qquad\qquad a - R_c \le d_{\mathrm{tc,p}} \le \sqrt{2}(a-R_c), \end{cases} \tag{4.4}$$

it is noted that the room length used in (4.3) and (4.4) is $a - R_c$ rather than a. This is because the cluster centre can only exist in the interior of the room with distance R_c to the boundary. Hence, $D_{\mathrm{tc,p}}$ is equivalent to the distance of two independently and uniformly distributed points in a square room with length $a - R_c$. With the PDF of $D_{\mathrm{tc,p}}$, and leverage order statistics, the PDF of $\widetilde{D}_{\mathrm{tc,p}}$ is given by

$$f_{\widetilde{D}_{\mathrm{tc,p}}}(\tilde{d}_{\mathrm{tc,p}}) = N_T f_{D_{\mathrm{tc,p}}}(\tilde{d}_{\mathrm{tc,p}})(1 - F_{D_{\mathrm{tc,p}}}(\tilde{d}_{\mathrm{tc,p}}))^{N_T-1}, \tag{4.5}$$

where $F_{D_{\mathrm{tc,p}}}(x)$ denotes the cumulative distribution function (CDF) of $D_{\mathrm{tc,p}}$. Next, we show the derivation of R's PDF. Because the users are uniformly distributed inside the circular cluster, the PDF for the location of a user in polar coordinates is given by $f_R(r,\theta) = 1/(\pi R_c^2)$, after taking the integral with respect to θ (a uniform random variable from 0 to 2π), the PDF of R is given by $f_R(r) = 2r/R_c^2$. The PDF of $\Omega = \cos\Theta$ is given by $f_\Omega(\omega) = 1/(\pi\sqrt{1-\omega^2})$, where $\omega \in [-1, 1]$ (See proof in Appendix B). With the PDFs of $\widetilde{D}_{\mathrm{tc,p}}$, R, and $\cos\Theta$, the CDF of $\widetilde{D}_{\mathrm{tr,p}}$ can be expressed as

$$\begin{aligned} F_{\widetilde{D}_{\mathrm{tr,p}}^2}(\tilde{d}_{\mathrm{tr,p}}^2) &= P(\widetilde{D}_{\mathrm{tc,p}}^2 + R^2 - 2\widetilde{D}_{\mathrm{tc,p}}R\cos\Theta \le \tilde{d}_{\mathrm{tr,p}}^2) \\ &= P\left(\cos\Theta \ge \frac{\widetilde{D}_{\mathrm{tc,p}}^2 + R^2 - \tilde{d}_{\mathrm{tr,p}}^2}{2\widetilde{D}_{\mathrm{tc,p}}R}\right) \\ &= \int f_{\widetilde{D}_{\mathrm{tc,p}}}(\tilde{d}_{\mathrm{tc,p}}) \int f_R(r)\left[1 - \frac{\sin^{-1}\left(\frac{\tilde{d}_{\mathrm{tc,p}}^2 + r^2 - \tilde{d}_{\mathrm{tr,p}}^2}{2\tilde{d}_{\mathrm{tc,p}}r}\right) + \frac{\pi}{2}}{\pi}\right] \mathrm{d}r\mathrm{d}\tilde{d}_{\mathrm{tc,p}}. \end{aligned} \tag{4.6}$$

Hence, the CDF of $\widetilde{D}_{\mathrm{tr}}^2$ can be expressed as

$$F_{\widetilde{D}_{\mathrm{tr}}^2}(\tilde{d}_{\mathrm{tr}}^2) = \int f_{\widetilde{D}_{\mathrm{tc,p}}}(\tilde{d}_{\mathrm{tc,p}}) \int f_R(r) \times \left[1 - \frac{1}{\pi} \sin^{-1}\left(\frac{\tilde{d}_{\mathrm{tc,p}}^2 + r^2 + (h_t - h_u)^2 - \tilde{d}_{\mathrm{tr}}^2}{2\tilde{d}_{\mathrm{tc,p}} r}\right) - \frac{1}{2}\right] \mathrm{d}r \mathrm{d}\tilde{d}_{\mathrm{tc,p}}. \tag{4.7}$$

4.2.2 Indirect Link

As stated in the system model section, the associated RIS should be the closest one to the user. This means the path loss for the RIS-EU link should be minimised by the associated RIS. The path loss is proportional to the square of the distance product for the indirect link in the far-field, while the path loss is proportional to the square of the distance summation for the indirect link in the near-field [38, 30]. To decide whether the communication is in the far-field or near-field, we leverage the Rayleigh distances, i.e., $Z = 2D^2/\lambda$, where D is the dimension of the RIS and λ is the wavelength of the impinging waves[4]. Table 4.1 lists various RIS dimensions, operating frequency (wavelength), and their corresponding Rayleigh distance, assuming the element spacing is $\lambda/4$ [2, 1]. It is observed in Table 4.1 that both the near-field and far-field exist in the indoor scenarios. Given the general indoor application scenarios considered in this work (with dimensions of 50 m $\times$ 50 m), compared with the Rayleigh distance of 12.5 m, corresponding to a 100 $\times$ 100 RIS operating at 30 GHz, the far-field region is the major application scenario. Moreover, smaller RIS dimensions or higher operating frequencies result in even shorter Rayleigh distances, as verified in Table 4.1. Meanwhile, we acknowledge that the presence of a near-field region in indoor environments is inevitable. However, our analysis can be readily adapted by substituting the path-loss and RIS gain models while leaving the remainder of the framework unchanged.

We define the distance product square as $\widetilde{D}_{\mathrm{m}}^2$. In order to find the distribution

[4]Rayleigh distance indicates the boundary between the near-field and far-field. If the communication distance is smaller than the Rayleigh distance, it is in the near-field, otherwise, it is in the far-field.

Table 4.1: Rayleigh distances with different D and λ

D (m)	λ (mm)	Z (m)
$30\lambda/4$ (30-by-30 RIS)	10; 6; 5	1.13; 0.68; 0.56
$40\lambda/4$ (40-by-40 RIS)	10; 6; 5	2.00; 1.20; 1.00
$50\lambda/4$ (50-by-50 RIS)	10; 6; 5	3.13; 1.88; 1.56
$100\lambda/4$ (100-by-100 RIS)	10; 6; 5	12.50; 7.50; 6.25

of $\widetilde{D}^2_{\mathrm{m}}$, it is necessary to know the distribution of $\widetilde{D}^2_{\mathrm{m},1}$, $\widetilde{D}^2_{\mathrm{m},2}$, $\widetilde{D}^2_{\mathrm{m},3}$, $\widetilde{D}^2_{\mathrm{m},4}$, where $\widetilde{D}^2_{\mathrm{m},1}$, $\widetilde{D}^2_{\mathrm{m},2}$, $\widetilde{D}^2_{\mathrm{m},3}$, and $\widetilde{D}^2_{\mathrm{m},4}$ denote the distance product square on the first side wall, the second side wall, the third side wall, and the fourth side wall, because $\widetilde{D}^2_{\mathrm{m}} = \min\{\widetilde{D}^2_{\mathrm{m},1}, \widetilde{D}^2_{\mathrm{m},2}, \widetilde{D}^2_{\mathrm{m},3}, \widetilde{D}^2_{\mathrm{m},4}\}$. Here, we show the derivation step of $\widetilde{D}^2_{\mathrm{m},1}$, as others are all similar. $\widetilde{D}^2_{\mathrm{m},1} = \widetilde{D}^2_{\mathrm{sr},1}\widetilde{D}^2_{\mathrm{ts},1}$, where $\widetilde{D}^2_{\mathrm{sr},1}$ is the distance square from the associated RIS to the user and $\widetilde{D}^2_{\mathrm{ts},1}$ is the distance square from the transmitter to the associated RIS. Using the law of cosine, $\widetilde{D}^2_{\mathrm{sr},1}$ can be expanded as

$$\widetilde{D}^2_{\mathrm{sr},1} = \widetilde{D}^2_{\mathrm{sc},1} + R^2 - 2R\widetilde{D}_{\mathrm{sc},1}\cos\Theta, \tag{4.8}$$

where $\widetilde{D}_{\mathrm{sc},1}$ is the distance from the associated RIS to the cluster centre. Conditioning on the location of the cluster centre (x_c, y_c, h_u), the expression of $\widetilde{D}_{\mathrm{sc},1}$ is given by

$$\widetilde{D}_{\mathrm{sc},1} = \sqrt{y_c^2 + \widetilde{L}^2 + (h_r - h_u)^2}, \tag{4.9}$$

where $\widetilde{L}$ is the distance from the nearest RIS to $(x_c, 0, h_r)$. The CDF of $\widetilde{L}$ is given by

$$F_{\widetilde{L}}(l) = 1 - (1 - F_L(l))^{N_R}, \tag{4.10}$$

where L denotes the distance along the first wall from an arbitrary RIS to the point $(x_c, 0, h_r)$, which is the projection of the cluster centre onto that wall at the RIS height. Its CDF is given by

$$F_L(l) = \frac{1}{a}\Big(\min\{a, x_c + l\} - \max\{0, x_c - l\}\Big). \tag{4.11}$$

Hence, the CDF of $\widetilde{D}_{\mathrm{sc},1}$ conditioning on the location of the cluster centre can be expressed as

$$\begin{aligned} &F_{\widetilde{D}_{\mathrm{sc},1}|(x_c,y_c,h_u)}(\tilde{d}_{\mathrm{sc},1}) = P(\sqrt{y_c^2+\widetilde{L}^2+(h_r-h_u)^2} \leq \tilde{d}_{\mathrm{sc},1}) \\ &= P\left(\widetilde{L} \leq \sqrt{\tilde{d}_{\mathrm{sc},1}^2-(h_r-h_u)^2-y_c^2}\right) \\ &\times \mathbf{1}(\tilde{d}_{\mathrm{sc},1}^2,(h_r-h_u)^2+y_c^2), \end{aligned} \tag{4.12}$$

where $\mathbf{1}(\cdot,\cdot)$ denotes the indicator function. After taking the integral with respect to the cluster centre's location, the CDF of $\widetilde{D}_{\mathrm{sc},1}$ is reformulated as

$$\begin{aligned} &F_{\widetilde{D}_{\mathrm{sc},1}}(\tilde{d}_{\mathrm{sc},1}) = \int_0^{a-2R_c} f_{X_c}(x_c) \int_0^{a-2R_c} f_{Y_c}(y_c) \\ &\times F_{\widetilde{L}}\left(\sqrt{\tilde{d}_{\mathrm{sc},1}^2-(h_r-h_u)^2-y_c^2}\right) \\ &\times \mathbf{1}(\tilde{d}_{\mathrm{sc},1}^2,(h_r-h_u)^2+y_c^2)\mathrm{d}y_c\mathrm{d}x_c, \end{aligned} \tag{4.13}$$

where $f_{X_c}(x_c) = 1/(a-2R_c)$ and $f_{Y_c}(y_c) = 1/(a-2R_c)$ denote the PDFs of the cluster-centre coordinates X_c and Y_c, respectively, over their respective supports. Based on the derivation of $\widetilde{D}_{\mathrm{tr}}^2$, the CDF of $\widetilde{D}_{\mathrm{sr},1}^2$ is given by

$$\begin{aligned} &F_{\widetilde{D}_{\mathrm{sr},1}^2}(\tilde{d}_{\mathrm{sr},1}^2) = \int f_{\widetilde{D}_{\mathrm{sc},1}}(\tilde{d}_{\mathrm{sc},1}) \int f_R(r) \\ &\times\left[1-\frac{1}{\pi}\sin^{-1}\left(\frac{\tilde{d}_{\mathrm{sc},1}^2+r^2+(h_r-h_u)^2-\tilde{d}_{\mathrm{sr},1}^2}{2\tilde{d}_{\mathrm{sc},1}r}\right)-\frac{1}{2}\right]\mathrm{d}r\mathrm{d}\tilde{d}_{\mathrm{sc},1}. \end{aligned} \tag{4.14}$$

Next, we move forward to deriving the CDF of $\widetilde{D}_{\mathrm{ts},1}^2$. Conditioning on the locations of the associated transmitter (x_t,y_t,h_t) and the cluster centre (x_c,y_c,h_u), $\widetilde{D}_{\mathrm{ts},1}^2$ can be expressed as

$$\widetilde{D}_{\mathrm{ts},1}^2 = (x_t-x_c-\widetilde{L})^2+y_t^2+(h_t-h_r)^2. \tag{4.15}$$

The CDF of $\widetilde{D}^2_{\mathrm{ts},1}$ conditioning on the locations of associated transmitter and cluster centre can be described as

$$\begin{aligned}
&F_{\widetilde{D}^2_{\mathrm{ts},1}|(x_c,y_c,h_u),(x_t,y_t,h_t)}(\tilde{d}^2_{\mathrm{ts},1}) \\
&= P((x_t - x_c - \widetilde{L})^2 + y_t^2 + (h_t - h_r)^2 \leq \tilde{d}^2_{\mathrm{ts},1}) \\
&= P(\widetilde{L} \geq x_t - x_c - \sqrt{\tilde{d}^2_{\mathrm{ts},1} - y_t^2 - (h_t - h_r)^2}) \\
&+ P(\widetilde{L} \leq x_t - x_c + \sqrt{\tilde{d}^2_{\mathrm{ts},1} - y_t^2 - (h_t - h_r)^2}) \\
&= F_{\widetilde{L}}(x_t - x_c + \sqrt{\tilde{d}^2_{\mathrm{ts},1} - y_t^2 - (h_t - h_r)^2})\mathbf{1}(\tilde{d}^2_{\mathrm{ts},1}, y_t^2 + (h_t - h_r)^2) \\
&- F_{\widetilde{L}}(x_t - x_c - \sqrt{\tilde{d}^2_{\mathrm{ts},1} - y_t^2 - (h_t - h_r)^2})\mathbf{1}(\tilde{d}^2_{\mathrm{ts},1}, y_t^2 + (h_t - h_r)^2).
\end{aligned} \tag{4.16}$$

After taking the integral with respect to the locations of the associated transmitter and cluster centre, the CDF of $\widetilde{D}^2_{\mathrm{ts},1}$ is reformulated as

$$\begin{aligned}
&F_{\widetilde{D}^2_{\mathrm{ts},1}}(\tilde{d}^2_{\mathrm{ts},1}) = \int_0^a f_{X_t}(x_t) \int_0^a f_{Y_t}(y_t) \int_0^{a-2R_c} f_{X_c}(x_c) \\
&\times \Big(F_{\widetilde{L}}(x_t - x_c + \sqrt{\tilde{d}^2_{\mathrm{ts},1} - y_t^2 - (h_t - h_r)^2})\mathbf{1}(\tilde{d}^2_{\mathrm{ts},1}, y_t^2 + (h_t - h_r)^2) \\
&- F_{\widetilde{L}}(x_t - x_c - \sqrt{\tilde{d}^2_{\mathrm{ts},1} - y_t^2 - (h_t - h_r)^2})\mathbf{1}(\tilde{d}^2_{\mathrm{ts},1}, y_t^2 + (h_t - h_r)^2) \Big) \\
&\times \mathrm{d}x_c \mathrm{d}y_t \mathrm{d}x_t,
\end{aligned} \tag{4.17}$$

where $f_{X_t}(x_t) = 1/a$, $f_{Y_t}(y_t) = 1/a$ denote the PDFs of X_t and Y_t. Here, we briefly discuss why the marginal distribution of the associated transmitter remains uniform. Intuitively thinking, the marginal distribution of the associated transmitter should be dependent on the location of the cluster centre based on the association policy. With N_T increasing, the probability density of X_t concentrates at $X_t = x_c$, the probability density of Y_t concentrates at $Y_t = y_c$. Hence, the associated transmitter's marginal distribution will no longer remain uniform when the location of the cluster centre is fixed. However, in our system model, the cluster centre is assumed to follow BPP. Under this assumption, the marginal distribution of the associated transmitter's location can be viewed as the average of all the marginal distributions of every possible cluster centre's location. For instance, if infinite transmitters exist on the ceiling, the probability density of $X_t = x_c$ and $Y_t = y_c$ will be 1 and 0 in

other places. By taking the average of every possible location of the cluster centre, the marginal distribution of the associated transmitter will be uniform. With the CDF of $\widetilde{D}^2_{\mathrm{sr},1}$ and $\widetilde{D}^2_{\mathrm{ts},1}$, the CDF of $\widetilde{D}^2_{\mathrm{m},1}$ can be calculated.The CDF of $\widetilde{D}^2_{\mathrm{m}}$ can then be given by

$$F_{\widetilde{D}^2_{\mathrm{m}}}(\tilde{d}^2_{\mathrm{m}}) = 1 - \prod_{i=1}^{4}(1 - F_{\widetilde{D}^2_{\mathrm{m,i}}}(\tilde{d}^2_{\mathrm{m,i}})), \tag{4.18}$$

where $F_{\widetilde{D}^2_{\mathrm{m,i}}}(x)$ denotes the CDF of $\widetilde{D}^2_{\mathrm{m,i}},\ i = 1, 2, 3, 4$.

4.3 Line-of-Sight Probability Characterisation

4.3.1 Direct Link Line-of-Sight Probability Calculation

Because the height factor is considered in this model, the condition of having the LOS path for the direct link can be categorised as: 1) every obstacle is at least R_b away from the link (top view), or 2) the distance from the obstacle centre to the link is smaller than R_b, but none of these obstacles intercept the link in the z direction (side view). The first category of the LOS path can be interpreted as there is no obstacle falling into the rectangular area shown in Fig. 4.3, where the width is the diameter of the obstacle and the length is $\widetilde{D}_{\mathrm{tr,p}}$. We define the CDF of $\widetilde{D}_{\mathrm{tr,p}}$ as $F_{\widetilde{D}_{\mathrm{tr,p}}}(\tilde{d}_{\mathrm{tr,p}})$, which can be obtained through the CDF of $\widetilde{D}^2_{\mathrm{tr,p}}$. We define the probability of no obstacle falling into the rectangular region as $P_{\mathrm{LOS,D},1}$, and its expression is given by

$$P_{\mathrm{LOS,D},1} = \int f_{\widetilde{D}_{\mathrm{tr,p}}}(\tilde{d}_{\mathrm{tr,p}})\Big(1 - \frac{2\tilde{d}_{\mathrm{tr,p}}R_b}{a^2}\Big)^{N_o}\mathrm{d}\tilde{d}_{\mathrm{tr,p}}. \tag{4.19}$$

The second category can be interpreted as there are n obstacles inside the rectangular region, but none of them intercept the link in the z direction. The illustration is shown in Fig. 4.4. The green and grey obstacles do not intercept the link while the red one intercepts the link. We define the probability that an obstacle does not intercept the link in the z direction as $P_{\mathrm{NI,D}}$. Because of the height difference between the user and the transmitter, the location of the obstacle inside the rectangular region

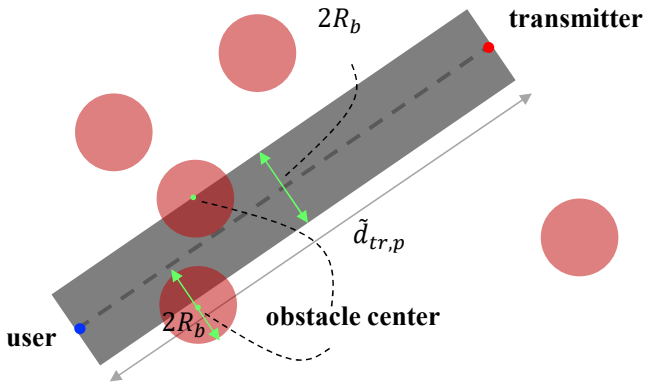

Figure 4.3: Illustration of the first category of the LOS probability calculation (top view).

also affects whether it blocks the link or not. More precisely speaking, the location of the obstacle projected point on the projected-transmitter-user line segment (the red line shown in Fig. 4.4) affects whether the obstacle blocks the link. Conditioning on the distance between the projected transmitter location and the projected obstacle centre on the line segment[5] v and the length of $\tilde{d}_{\mathrm{tr,p}}$, $P_{\mathrm{NI,D}}$ can be expressed as

$$P_{\mathrm{NI,D}} = \frac{\eta(\tilde{d}_{\mathrm{tr,p}}, v + R_b) + h_u - h_{\min}}{h_{\max} - h_{\min}}, \tag{4.20}$$

where $\eta(\tilde{d}_{\mathrm{tr,p}}, v)$ is given by

$$\eta(\tilde{d}_{\mathrm{tr,p}}, v + R_b) = \frac{h_t - h_u}{\tilde{d}_{\mathrm{tr,p}}}(\tilde{d}_{\mathrm{tr,p}} - (v + R_b)), \tag{4.21}$$

After taking the integral with respect to $\tilde{d}_{\mathrm{tr,p}}$ and v, $P_{\mathrm{NI,D}}$ can be reformulated as

$$P_{\mathrm{NI,D}} = \int f_{\widetilde{D}_{\mathrm{tr,p}}}(\tilde{d}_{\mathrm{tr,p}}) \int f_V(v) \frac{\eta(\tilde{d}_{\mathrm{tr,p}}, v+R_b)+h_u-h_{\min}}{h_{\max}-h_{\min}} \mathrm{d}v \mathrm{d}\tilde{d}_{\mathrm{tr,p}}, \tag{4.22}$$

where $f_V(v)$ is the PDF of the distance between the projected transmitter location and the projected obstacle centre on the line segment. As we analysed previously

[5]Note that there are two projections for the obstacle centre. The first time, it is projected onto the 2D plane, i.e., the plane with height h_u. The second time, it is projected on the line segment connected by the projected transmitter location and the user.

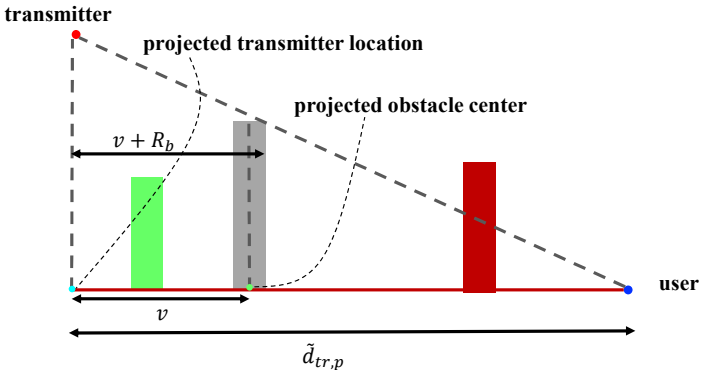

Figure 4.4: Illustration of the second category of the LOS probability calculation (side view).

the obstacle spatial distribution can be approximated to BPP, the random variable V follows uniform distribution on the line segment, i.e., $f_V(v) = 1/\tilde{d}_{\mathrm{tr,p}}$. We define the probability $P_{\mathrm{LOS,D,2}}$ as there are obstacles inside the rectangular region but none of them can block the link in the z direction. Its expression is given by

$$P_{\mathrm{LOS,D,2}} = \int f_{\widetilde{D}_{\mathrm{tr,p}}}(\tilde{d}_{\mathrm{tr,p}}) \sum_{i=1}^{N_o} \binom{N_o}{i} \Big(\frac{2P_{\mathrm{NI,D}}\tilde{d}_{\mathrm{tr,p}}R_b}{a^2}\Big)^i \times \Big(1 - \frac{2\tilde{d}_{\mathrm{tr,p}}R_b}{a^2}\Big)^{N_o - i} \mathrm{d}\tilde{d}_{\mathrm{tr,p}}. \tag{4.23}$$

The LOS probability for the direct link $P_{\mathrm{LOS,D}}$ is then given by

$$P_{\mathrm{LOS,D}} = P_{\mathrm{LOS,D,1}} + P_{\mathrm{LOS,D,2}}. \tag{4.24}$$

4.3.2 Indirect Link Line-of-Sight Probability Calculation

As we assumed $h_r \geq h_{\max}$, $\widetilde{D}_{\mathrm{ts}}$ cannot be blocked. The blockage can only happen in the associated RIS-user link. Similar to the direct link, we need the distance distribution between the associated RIS and the user, which is given by

$$F_{\widetilde{D}_{\mathrm{sr}}}(x) = 1 - \prod\nolimits_{i=1}^{4} (1 - F_{\widetilde{D}_{\mathrm{sr,i}}}) \tag{4.25}$$

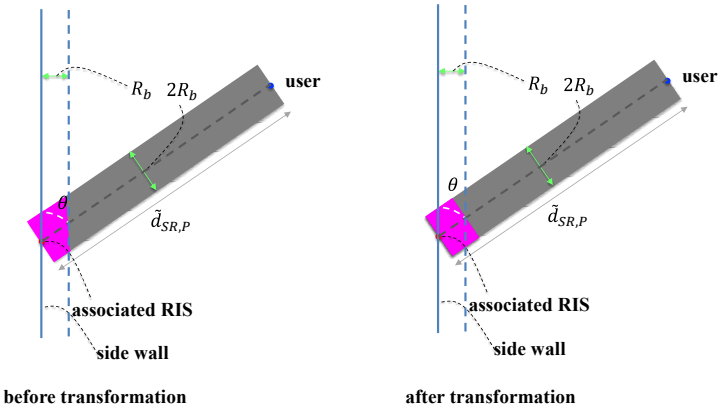

Figure 4.5: Illustration of the effects of boundary and feasible locations of obstacles on the indirect link LOS probability calculation.

where the CDF of $\widetilde{D}_{\mathrm{sr,i}}$ can be obtained from the CDF of $\widetilde{D}^2_{\mathrm{sr,i}}$, $i = 1, 2, 3, 4$. We define the projected length of $\widetilde{D}_{\mathrm{sr}}$ as $\widetilde{D}_{\mathrm{sr,p}}$. As the CDF of $\widetilde{D}_{\mathrm{sr,p}}$ can be easily obtained once knowing the CDF of $\widetilde{D}_{\mathrm{sr}}$, we will not show the derivation of $F_{\widetilde{D}_{\mathrm{sr,p}}}(\tilde{d}_{\mathrm{sr,p}})$ here. For the indirect link, there are also two categories similar to the direct link, however, the boundary effect must be taken into consideration. To better understand how the boundary affects the LOS probability for the indirect link, an illustration is given. Because the obstacle has a radius of R_b, it only exists on the right side of the vertical dashed line shown in Fig. 4.5, left. This means the pink region (a right-angle trapezoid) should be deducted from the rectangular region to count the boundary effect. The area of this right-angle trapezoid is equal to the pink rectangle shown on the right side in Fig. 4.5 after the transformation. The pink rectangle area S_r is given by

$$\begin{aligned} S_r &= \int_{\theta_1}^{\theta_2} f_{\Theta}(\theta) \frac{2R_b^2}{\sin\theta} \mathrm{d}\theta = \int_{\theta_1}^{\theta_2} \frac{2}{\pi} \frac{2R_b^2}{\sin\theta} \mathrm{d}\theta \\ &= \frac{-2R_b^2}{\pi} \left(\ln \frac{1+\cos\theta_2}{1-\cos\theta_2} - \ln \frac{1+\cos\theta_1}{1-\cos\theta_1} \right), \end{aligned} \tag{4.26}$$

where Θ is the orientation angle from θ_1 to θ_2. Because the variation of the pink rectangle area is symmetric in $[0, 90°]$ and $[90°, 180°]$. We set $\theta_2 = 90°$. It is noted in (4.26) that $\theta_1 = 0°$ will lead to an invalid expression. Hence, we set θ_1 to a small

value just above 0° (e.g., $\theta_1 = 1°$). Then, (4.26) can be reformulated as

$$S_r = \frac{2R_b^2}{\pi}\Big(\ln\frac{1+\cos\theta_1}{1-\cos\theta_1}\Big). \tag{4.27}$$

Next, we give the expression of the LOS probability for the first category, which is

$$P_{\text{LOS,ID},1} = \int f_{\widetilde{D}_{\text{sr,p}}}(\tilde{d}_{\text{sr,p}})\Big(1-\frac{2\tilde{d}_{\text{sr,p}}R_b - S_r}{a^2}\Big)^{N_o}\mathrm{d}\tilde{d}_{\text{sr,p}}. \tag{4.28}$$

Then, we move forward to derive the LOS probability for the second category. We define the probability that an obstacle does not intercept the link in the z direction as $P_{\text{NI,ID}}$. Its expression is given by

$$P_{\text{NI,ID}} = \frac{\omega(\tilde{d}_{\text{sr,p}}, g+R_b) + h_u - h_{\min}}{h_{\max}-h_{\min}}, \tag{4.29}$$

where g denotes the projected obstacle location on the associated RIS-user line segment and $\omega(\tilde{d}_{\text{sr,p}}, g)$ is given by

$$\omega(\tilde{d}_{\text{sr,p}}, g+R_b) = \frac{h_r - h_u}{\tilde{d}_{\text{sr,p}}}(\tilde{d}_{\text{sr,p}} - (g+R_b)). \tag{4.30}$$

After taking the integral with respect to $\tilde{d}_{\text{sr,p}}$ and g, $P_{\text{NI,ID}}$ can be reformulated as

$$P_{\text{NI,ID}} = \int f_{\widetilde{D}_{\text{sr,p}}}(\tilde{d}_{\text{sr,p}})\int f_G(g)\frac{\omega(\tilde{d}_{\text{sr,p}}, g+R_b) + h_u - h_{\min}}{h_{\max}-h_{\min}}\mathrm{d}g\mathrm{d}\tilde{d}_{\text{sr,p}}, \tag{4.31}$$

where $f_G(g) = 1/\tilde{d}_{\text{sr,p}}$. We define the LOS probability of the second category as $P_{\text{LOS,ID},2}$. Its expression is given by

$$\begin{aligned} P_{\text{LOS,ID},2} = \int f_{\widetilde{D}_{\text{sr,p}}}(\tilde{d}_{\text{sr,p}})\sum_{i=1}^{N_o}\binom{N_o}{i}\Big(\frac{P_{\text{NI,ID}}(2\tilde{d}_{\text{sr,p}}R_b - S_r)}{a^2}\Big)^i \\ \times\Big(1-\frac{2\tilde{d}_{\text{sr,p}}R_b - S_r}{a^2}\Big)^{N_o-i}\mathrm{d}\tilde{d}_{\text{sr,p}}. \end{aligned} \tag{4.32}$$

The LOS probability for the indirect link $P_{\text{LOS,ID}}$ is then given by

$$P_{\text{LOS,ID}} = P_{\text{LOS,ID},1} + P_{\text{LOS,ID},2}. \tag{4.33}$$

Considering that RISs are typically deployed on the side walls of indoor environments, incorporating the boundary effect leads to a more practical and realistic system model. In bounded spaces such as conference centres or shopping malls, the LOS probability for the indirect link requires careful characterisation, as the RIS is located at the boundary of the environment.

4.4 Coverage Probability Characterisation

4.4.1 Coverage Probability Characterisation

Because the interference is not considered in this chapter, we use SNR to calculate the CP. The CP for the direct link is given by

$$P_{\text{cov,D}} = P_{\text{LOS,D}} P\Big(\frac{G_t G_r P_{\text{Tx}}}{\sigma_n^2}\Big(\frac{\lambda}{4\pi \widetilde{D}_{\text{tr}}}\Big)^2 \geq \tau\Big), \tag{4.34}$$

where G_t, G_r, σ_n, λ, P_{Tx} and τ denote the transmitter antenna gain, the receiver antenna gain, the noise power, the wavelength of the signal, the transmit power, and the threshold. By leveraging the CDF of $\widetilde{D}_{\text{tr}}^2$, $P_{\text{Cov,D}}$ can be reformulated as

$$P_{\text{Cov,D}} = P_{\text{LOS,D}} F_{\widetilde{D}_{\text{tr}}^2}\Big(\frac{G_t G_r P_{\text{Tx}} \lambda^2}{(4\pi)^2 \sigma_n^2 \tau}\Big). \tag{4.35}$$

Next, we derive the CP for the indirect link. Based on [38, 30], the RIS gain is proportional to the square of the RIS size. We define the total element number of an RIS as M_R. Define the element width as e_x, the element length as e_y. Then, the CP for the indirect link is given by

$$P_{\text{Cov,ID}} = P_{\text{LOS,ID}} P\Big(\frac{G_t G_r P_{\text{Tx}} e_x e_y M_R^2 \lambda^2}{(4\pi)^2 \sigma_n^2 \widetilde{D}_{\text{m}}^2} \geq \tau\Big), \tag{4.36}$$

as we have the CDF of $\widetilde{D}_{\text{m}}^2$, the CP for the indiect link can be reformulated as

$$P_{\text{Cov,ID}} = P_{\text{LOS,ID}} F_{\widetilde{D}_{\text{m}}^2}\Big(\frac{G_t G_r P_{\text{Tx}} e_x e_y M_R^2 \lambda^2}{(4\pi)^2 \sigma_n^2 \tau}\Big). \tag{4.37}$$

(4.37) assumes that all elements of the selected RIS are dedicated to the considered link. The corresponding full-surface gain provides the idealised upper-bound reference discussed in Section 4.1; resource sharing among users associated with the same surface is not modelled. Plug (4.24), (4.33), (4.35), and (4.37) into (4.1), the CP can be calculated, with the CDF of $\widetilde{D}_{\text{tr}}^2$, and $\widetilde{D}_{\text{m}}^2$ previously derived, which is given in (4.38). Although the resulting coverage expression requires multidimensional numerical integration, it provides an explicit mathematical description of how deployment geometry, blockage, and received-power thresholds determine coverage.

$$P_{\mathrm{Cov}}=P_{\mathrm{LOS,D}}F_{\widetilde{D}^2_{\mathrm{tr}}}\Big(\frac{G_tG_rP_{\mathrm{Tx}}\lambda^2}{(4\pi)^2\sigma_n^2\tau}\Big)+P_{\mathrm{LOS,ID}}\bigg(F_{\widetilde{D}^2_{\mathrm{tr}}}(\frac{G_tG_rP_{\mathrm{Tx}}\lambda^2}{(4\pi)^2\sigma_n^2\tau})P_{\mathrm{NLOS,D}}$$
$$+\Big(1-F_{\widetilde{D}^2_{\mathrm{tr}}}(\frac{G_tG_rP_{\mathrm{Tx}}\lambda^2}{(4\pi)^2\sigma_n^2\tau})\Big)\bigg)F_{\widetilde{D}^2_{\mathrm{m}}}\Big(\frac{G_tG_rP_{\mathrm{Tx}}e_xe_yM_R^2\lambda^2}{(4\pi)^2\sigma_n^2\tau}\Big) \tag{4.38}$$

Unlike direct Monte Carlo estimation alone, the derivation exposes how individual system parameters enter the distance distributions and blockage probabilities. This structure provides a basis for the approximate parameter relationships and the analysis of RIS contribution developed in the following subsections.

4.4.2 Relationships between Network Parameters and Coverage Probability

It is noted that the CP expression (4.38) is wrapped with multiple integrals, which leads to the relationships between the network parameters and the CP being difficult to extract. In this section, we reveal the relationships between network parameters (e.g., N_T, N_o, R_c, and N_R) and the CP by simplifying distance distributions (e.g., (4.7),(4.14)) and expressions of LOS probabilities (e.g., (4.19), (4.23)). These relationships will also be verified through numerical results in the next section.

These relationships provide qualitative guidance for deployment planning. In particular, the dependence on N_T helps assess the benefit of adding transmitters, while the dependence on N_o indicates the sensitivity of coverage to blockage. The dependence on R_c characterises how coverage changes with the spatial extent of user clusters under the adopted association policy. Together, these relationships help identify which deployment or environmental parameters warrant closer examination. Quantitative dimensioning for a specified coverage target should use the full coverage expression rather than the simplified relationships alone.

We start from (4.7) as it is a key component in (4.35). As the following inequality

holds

$$-1 \leq \underbrace{\left(\frac{\tilde{d}_{\mathrm{tc,p}}^2 + r^2 + (h_t - h_u)^2 - \tilde{d}_{\mathrm{tr}}^2}{2\tilde{d}_{\mathrm{tc,p}} r}\right)}_{Q} \leq 1, \tag{4.39}$$

$\tilde{d}_{\mathrm{tr}}^2$ is in the range of $[(\tilde{d}_{\mathrm{tc,p}} - r)^2 + (h_t - h_u)^2,\ (\tilde{d}_{\mathrm{tc,p}} + r)^2 + (h_t - h_u)^2]$. We apply a Taylor series expansion around $Q = 0$. Hence, $\sin^{-1}(Q)$ can be approximated as[6]

$$\sin^{-1}(Q) = Q + \mathcal{O}(Q^3). \tag{4.40}$$

The higher-order terms are neglected when $|Q|$ is sufficiently small, so that $\arcsin(Q) \approx Q$. Using this approximation and conditioning on $\tilde{d}_{\mathrm{tc,p}}$, (4.7) can be reformulated as

$$F_{\widetilde{D}_{\mathrm{tr}}^2}(\tilde{d}_{\mathrm{tr}}^2) = \frac{\tilde{d}_{\mathrm{tr}}^2 - (h_t - h_u)^2}{\pi R_c \tilde{d}_{\mathrm{tc,p}}} - \frac{\tilde{d}_{\mathrm{tc,p}}}{\pi R_c} - \frac{R_c}{3\pi\tilde{d}_{\mathrm{tc,p}}} + \frac{1}{2} + \mathcal{O}(Q^3). \tag{4.41}$$

For fixed $\tilde{d}_{\mathrm{tc,p}}$ and the other parameters, the approximate conditional CDF in (4.41) decreases as R_c increases, provided that

$$\tilde{d}_{\mathrm{tr}}^2 - (h_t - h_u)^2 > \tilde{d}_{\mathrm{tc},p}^2 - \frac{R_c^2}{3}.$$

This identifies a condition under which increasing the cluster radius reduces the probability of satisfying the direct-link distance threshold. It is also noted that in (4.41), N_T is not shown in the expression due to the conditioning on $\tilde{d}_{\mathrm{tc,p}}$. Next we analyse the expectation of $\widetilde{D}_{\mathrm{tc,p}}$ to show the relationship between N_T and the CP. The expectation of $\widetilde{D}_{\mathrm{tc,p}}$ is given by

$$\mathbb{E}[\widetilde{D}_{\mathrm{tc,p}}] = \int \tilde{d}_{\mathrm{tc,p}} N_T f_{D_{\mathrm{tc,p}}}(\tilde{d}_{\mathrm{tc,p}})(1 - F_{D_{\mathrm{tc,p}}}(\tilde{d}_{\mathrm{tc,p}}))^{N_T - 1} \mathrm{d}\tilde{d}_{\mathrm{tc,p}}. \tag{4.42}$$

Given the PDF expression of $D_{\mathrm{tc,p}}$ in (4.3) and the $N_T - 1$ power term in the integrand, directly calculating (4.42) is difficult. As we know $\widetilde{D}_{\mathrm{tc,p}}$ is the first order statistic of $D_{\mathrm{tc,p}}$, $\widetilde{D}_{\mathrm{tc,p}}$ is heavily influenced by the lower tail of its distribution. In other words, most of the possible values of $\widetilde{D}_{\mathrm{tc,p}}$ will concentrate near the lower

[6]When we vary $\tilde{d}_{\mathrm{tr}}^2$ conditioning on $\tilde{d}_{\mathrm{tc,p}}$ and r, Q changes from 1 to -1. Q will not concentrate on a specific value in the region $[-1, 1]$. Hence, we choose the middle point of the region as the expansion point.

bound (0 in this context) of $D_{\mathrm{tc,p}}$. This indicates $F_{D_{\mathrm{tc,p}}}(\tilde{d}_{\mathrm{tc,p}})$ is close to 0. With N_T increasing, the term $(1 - F_{D_{\mathrm{tc,p}}}(\tilde{d}_{\mathrm{tc,p}}))^{N_T-1}$ can be approximated as

$$(1 - F_{D_{\mathrm{tc,p}}}(\tilde{d}_{\mathrm{tc,p}}))^{N_T-1} \approx e^{-N_T F_{D_{\mathrm{tc,p}}}(\tilde{d}_{\mathrm{tc,p}})}. \tag{4.43}$$

This approximation follows from $\ln(1-x) = -x + \mathcal{O}(x^2)$ for $x \ll 1$. Here, $x = F_{D_{\mathrm{tc,p}}}(\tilde{d}_{\mathrm{tc,p}})$. The correction to the exponent is of order $(N_T - 1)x^2$, which should be small for an accurate multiplicative approximation. For sufficiently large N_T, $N_T - 1$ is further approximated by N_T in the subsequent derivation. Then, we use Taylor expansion on $F_{D_{\mathrm{tc,p}}}(\tilde{d}_{\mathrm{tc,p}})$ around the point $\tilde{d}_{\mathrm{tc,p}} = 0$.

$$\begin{aligned} F_{D_{\mathrm{tc,p}}}(\tilde{d}_{\mathrm{tc,p}}) &\approx F_{D_{\mathrm{tc,p}}}(0) + f_{D_{\mathrm{tc,p}}}(0)\tilde{d}_{\mathrm{tc,p}} + \frac{1}{2} f'_{D_{\mathrm{tc,p}}}(0)\tilde{d}^2_{\mathrm{tc,p}} \\ &= \frac{1}{2} f'_{D_{\mathrm{tc,p}}}(0)\tilde{d}^2_{\mathrm{tc,p}}. \end{aligned} \tag{4.44}$$

Eq. (4.42) can be reformulated as

$$\begin{aligned} \mathbb{E}[\widetilde{D}_{\mathrm{tc,p}}] &\approx N_T \int \tilde{d}_{\mathrm{tc,p}} f_{D_{\mathrm{tc,p}}}(\tilde{d}_{\mathrm{tc,p}}) e^{-N_T F_{D_{\mathrm{tc,p}}}(\tilde{d}_{\mathrm{tc,p}})} \mathrm{d}\tilde{d}_{\mathrm{tc,p}} \\ &\overset{(a)}{\approx} N_T f'_{D_{\mathrm{tc,p}}}(0) \int \tilde{d}^2_{\mathrm{tc,p}} e^{-N_T F_{D_{\mathrm{tc,p}}}(\tilde{d}_{\mathrm{tc,p}})} \mathrm{d}\tilde{d}_{\mathrm{tc,p}} \\ &\overset{(b)}{\approx} N_T f'_{D_{\mathrm{tc,p}}}(0) \int \tilde{d}^2_{\mathrm{tc,p}} e^{-\frac{N_T}{2} f'_{D_{\mathrm{tc,p}}}(0)\tilde{d}^2_{\mathrm{tc,p}}} \mathrm{d}\tilde{d}_{\mathrm{tc,p}} \\ &= \frac{\sqrt{2\pi}}{2\sqrt{N_T f'_{D_{\mathrm{tc,p}}}(0)}}, \end{aligned} \tag{4.45}$$

where (a) comes from using Taylor expansion of $f_{D_{\mathrm{tc,p}}}(\tilde{d}_{\mathrm{tc,p}})$ at point $\tilde{d}_{\mathrm{tc,p}} = 0$, and (b) comes from (4.44). A comparison between the approximated expectation of $\widetilde{D}_{\mathrm{tc,p}}$ and the true expectation is shown in Fig. 4.6 over different N_T. Under the lower-tail approximation used above, the mean horizontal distance from the cluster centre to its nearest transmitter scales as

$$\mathbb{E}[\tilde{D}_{\mathrm{tc,p}}] \approx C N_T^{-1/2}, \quad C = \sqrt{\frac{\pi}{2 f'_{D_{\mathrm{tc,p}}}(0)}}. \tag{4.46}$$

Here, C is independent of N_T for fixed spatial geometry. This distance scaling helps explain the coverage benefit of increasing transmitter number. However, it does not

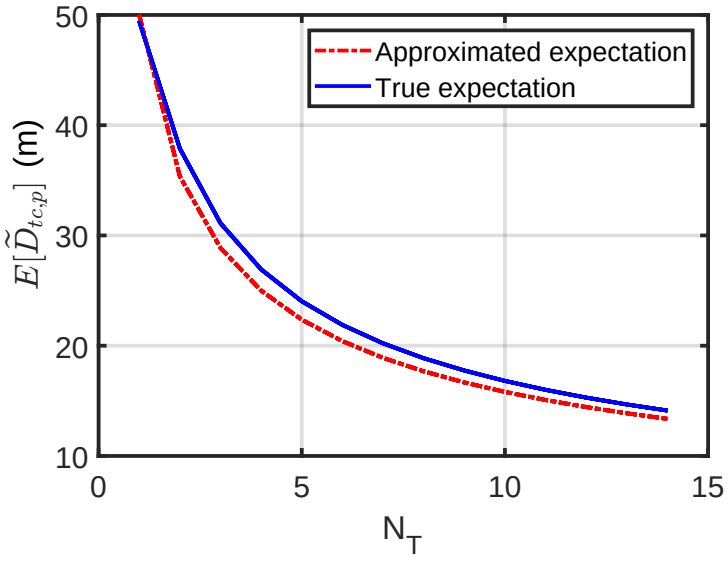

Figure 4.6: Comparison between the approximate expectation obtained from (4.45) and the exact expectation calculated from (4.42), versus the number of transmitters N_T, with $a = 100$ m and $R_c = 5$ m. The mean horizontal distance $\mathbb{E}[\widetilde{D}_{\mathrm{tc},p}]$ is expressed in metres.

establish a proportional relationship between $P_{\mathrm{Cov,D}}$ and $\sqrt{N_T}$, since coverage also depends on user displacement within the cluster, blockage, and the received-power threshold. Next, we examine the dependence of the geometric blockage factors on the obstacle number N_o. For a fixed projected link distance, define $p = 2\tilde{d}_{\mathrm{tr,p}} R_b / a^2$. When $p \ll 1$, the geometric blockage factors can be approximated as

$$\begin{aligned} (1-p)^{N_o} &\approx \exp(-N_o p), \\ (1-p)^{N_o - i} &\approx \exp(-(N_o - i)p). \end{aligned} \tag{4.47}$$

Thus, this blockage factor decays approximately exponentially with obstacle number, with decay coefficient p, when the link geometry, obstacle radius, and room dimensions are held fixed. This conditional relationship explains the sensitivity of coverage to obstacle number. After averaging over link distances and obstacle heights, however, the overall coverage probability need not follow a single exponential law. Accordingly, the relationship is used as a qualitative blockage-sensitivity indicator. For N_T, N_o and R_c, the relationship will not change when switching to the indirect link. Hence, we will not derive these relationships separately for the indirect link. For N_R. We

will make a brief discussion here. The relationship of N_R with the CP resembles N_T because $\widetilde{L}$ is also the first order statistic of L, and the PDF of $\widetilde{L}$ resembles (4.5). Following the same procedure on deriving the approximated expectation of $\widetilde{D}_{\text{tc,p}}$, the approximated expectation of $\widetilde{D}_{\text{sc,1}}$ (4.14) can also be derived.

The simplified relationships derived above are subject to the conditions of the underlying approximations. The first-order approximation $\sin^{-1}(Q) \approx Q$ is accurate near $Q = 0$ and becomes less accurate as $|Q|$ approaches one. Consequently, the cluster radius relationship should be interpreted subject to the monotonicity condition stated above and within the region where this linearisation is accurate. The nearest-transmitter distance approximation relies on sufficiently large N_T, such that the relevant distances lie in the lower-tail region where the Taylor expansion of the distance distribution is accurate. The exponential approximation $(1-p)^n \approx e^{-np}$ requires a small single-obstacle blocking probability p; large obstacle number alone does not guarantee its accuracy. These results also retain the assumptions of the system model, including noise-limited operation, full-surface availability for the considered link, and the cluster-centre association approximation. In particular, increasing N_T can improve the lower-tail distance approximation while making shared cluster-centre association less accurate for a fixed cluster radius. The simplified expressions should therefore be used as conditional trend indicators, with quantitative predictions checked against the full analytical model.

4.4.3 Threshold-Based Analysis of RIS Contribution

Based on the previously introduced communication strategy, the BS always prioritises the direct link; the indirect RIS-assisted link is only used if the direct link fails. As the number of transmitters and the transmit power increase, the likelihood of successfully communicating via the direct link also increases. This leads to a critical question: at what transmitter number and power level does the contribution of the RIS become negligible? We define $P_{\text{Cov-D}} = P_{\text{Cov}} - P_{\text{Cov-RIS}}$ as the CP of the direct

link. We define ε, $\varepsilon \in (0,1)$ as the threshold at which the contribution of RIS is negligible. Then the following inequality holds,

$$P_{\text{Cov-RIS}} \leq \varepsilon. \tag{4.48}$$

(4.48) can be reformulated as

$$\begin{aligned} &P_{\text{LOS,ID}}(1-P_{\text{Cov-D}})F_{\widetilde{D}^2_{\text{m}}}\left(\frac{G_tG_rP_{\text{Tx}}e_xe_yM_R^2\lambda^2}{(4\pi)^2\sigma_n^2\tau}\right) \leq \varepsilon \\ &= P_{\text{LOS,ID}}\left(1-P_{\text{LOS,D}}F_{\widetilde{D}^2_{\text{tr}}}\left(\frac{G_tG_rP_{\text{Tx}}\lambda^2}{(4\pi^2)\sigma_n^2\tau}\right)\right) \\ &\times \underbrace{F_{\widetilde{D}^2_{\text{m}}}\left(\frac{G_tG_rP_{\text{Tx}}e_xe_yM_R^2\lambda^2}{(4\pi)^2\sigma_n^2\tau}\right)}_{J(P_{\text{Tx}})} \leq \varepsilon. \end{aligned} \tag{4.49}$$

It is hard to observe a nice and clean relationship between N_T, P_{Tx}, and ε from (4.49). As $P_{\text{LOS,ID}}$ is irrelevant from N_T and P_{Tx}, we treat $P_{\text{LOS,ID}}$ as a constant A. For $J(P_{\text{Tx}})$, the large RIS element number (M_R) will push it to one. The original inequality (4.48) now becomes

$$1-P_{\text{LOS,D}}F_{\widetilde{D}^2_{\text{tr}}}\left(\frac{G_tG_rP_{\text{Tx}}\lambda^2}{(4\pi^2)\sigma_n^2\tau}\right) \leq \frac{\varepsilon}{A}. \tag{4.50}$$

As previously discussed, one of the conditions for satisfying (4.50) is a large number of transmitters (e.g., 10 or 20). Under this condition, the user tends to be located closer to a transmitter, and consequently, the LOS probability of the direct link, $P_{\text{LOS,D}}$, approaches one. Hence, (4.50) can be further simplified as

$$1-F_{\widetilde{D}^2_{\text{tr}}}\left(\frac{G_tG_rP_{\text{Tx}}\lambda^2}{(4\pi^2)\sigma_n^2\tau}\right) \leq \frac{\varepsilon}{A}. \tag{4.51}$$

We define $G_tG_r\lambda^2/(4\pi)^2\sigma_n^2\tau$ as B. Using (4.41), $F_{\widetilde{D}^2_{\text{tr}}}(BP_{\text{Tx}})$ can be reformulated as

$$F_{\widetilde{D}^2_{\text{tr}}}(BP_{\text{Tx}}) = \frac{BP_{\text{Tx}}-(h_t-h_u)^2}{\pi R_c\tilde{d}_{\text{tc,p}}} - \frac{\tilde{d}_{\text{tc,p}}}{\pi R_c} - \frac{R_c}{3\pi\tilde{d}_{\text{tc,p}}} + \frac{1}{2} + \mathcal{O}(Q^3). \tag{4.52}$$

N_T can be incorporated into (4.52) by using the expectation of $\widetilde{D}_{\text{tc,p}}$, which is given in (4.45). We define $\sqrt{2\pi}/2\sqrt{f'_{D_{\text{tc,p}}}(0)}$ as C. (4.51) can be written as

$$\begin{aligned} &1-\frac{\sqrt{N_T}(BP_{\text{Tx}}-(h_t-h_u)^2)}{\pi R_cC} + \frac{C}{\pi R_c\sqrt{N_T}} \\ &+\frac{R_c\sqrt{N_T}}{3\pi C} - \frac{1}{2} - \mathcal{O}(Q^3) \leq \frac{\varepsilon}{A}. \end{aligned} \tag{4.53}$$

By doing some transformations on (4.53), it can be expressed as

$$P_{\mathrm{Tx}} \geq \frac{1}{B}\Bigg[(h_t - h_u)^2 + \frac{\pi R_c C}{\sqrt{N_T}}\Bigg(1 - \frac{1}{2} - \frac{\varepsilon}{A} - \mathcal{O}(Q^3) + \frac{C}{\pi R_c \sqrt{N_T}} + \frac{R_c\sqrt{N_T}}{3\pi C}\Bigg)\Bigg]. \tag{4.54}$$

For fixed N_T, the right-hand side of (4.55) provides an approximate transmit-power threshold above which the additional coverage contribution of the RIS is no greater than ε, subject to the preceding approximations. This threshold does not imply that the coverage contribution decreases linearly with P_{Tx}.

Neglecting the higher-order remainder, the right-hand side of (4.54) can be written as

$$\frac{1}{B}\left[(h_t - h_u)^2 + \frac{R_c^2}{3} + \frac{\pi R_c C}{\sqrt{N_T}}\left(\frac{1}{2} - \frac{\varepsilon}{A}\right) + \frac{C^2}{N_T}\right]. \tag{4.55}$$

Thus, the approximate threshold contains both $N_T^{-1/2}$ and N_T^{-1} terms, together with a constant term, rather than being proportional to N_T^{-1}. For fixed positive A, B, C, and R_c, and $\varepsilon/A \leq 1/2$, this expression decreases with increasing N_T within the validity range of the approximations. It therefore indicates that increasing the transmitter number can reduce the transmit power required for the additional RIS coverage contribution to become negligible.

4.5 Numerical Results

The numerical parameters are summarised in Table 4.2. The wavelength of 10 mm and noise power of −60 dBm are consistent with [61]. The remaining values specify an illustrative large indoor venue. The 100×100 m^2 floor and 4 m ceiling represent an exhibition or conference hall. An obstacle radius of 1.25 m gives a 2.5 m footprint diameter, comparable in horizontal extent to a large desk, kiosk, or display stand. The height range of 1–3 m accommodates low furniture and taller displays or partitions, represented here by idealised cylinders. The obstacle counts span nominal footprint fractions of approximately 1%–20% of the floor area. A cluster radius of

Table 4.2: Parameter setting

Parameter	**Value**
a	100 m
N_T, N_R	[2 5 10], [1 10 20]
N_o	[21 64 107 150 193 236 279 322 365 408]
M_R	10000
R_b, R_c	1.25 m, 5 m
λ	10 mm
e_x, e_y	$\lambda/2$, $\lambda/2$
h_t, h_u, h_r, $h_{\min}$, $h_{\max}$	4 m, 1.8 m, 3.5 m, 1 m, 3 m
τ	1
iteration time for Monte-Carlo simulation	100000
G_t, G_r, P_{Tx}, σ_n^2	100 (20 dB), 10 (10 dB), 1 mW, 1×10^{-6} mW

5 m represents a group gathering around a demonstration, information point, or exhibition display. The terminal height of 1.8 m represents a device held near head level by a standing user. RISs are mounted at 3.5 m, above the modelled obstacles and below the ceiling, preserving an unobstructed transmitter–RIS path. The transmitter and RIS counts compare sparse and denser deployments. The RIS element count and dimensions specify a large reflecting surface, while the antenna gains, transmit power, and 0 dB SNR threshold define the reference link budget. These settings are illustrative assumptions rather than measurements from a particular venue. We first validate the analytical results by comparing them with Monte Carlo simulations. We first validate the analytical results by comparing them with Monte Carlo simulations. Observing Fig. 4.7, it is found that the analytical results match the Monte Carlo simulations very well under different transmitter numbers, obstacle densities, and RIS numbers. It is also found that the CP exponentially decays with the increase of the obstacle density, which agrees with the relationship given in the previous section (note that the CP is in log-scale in Fig.4.7). What's more, as N_T increases,

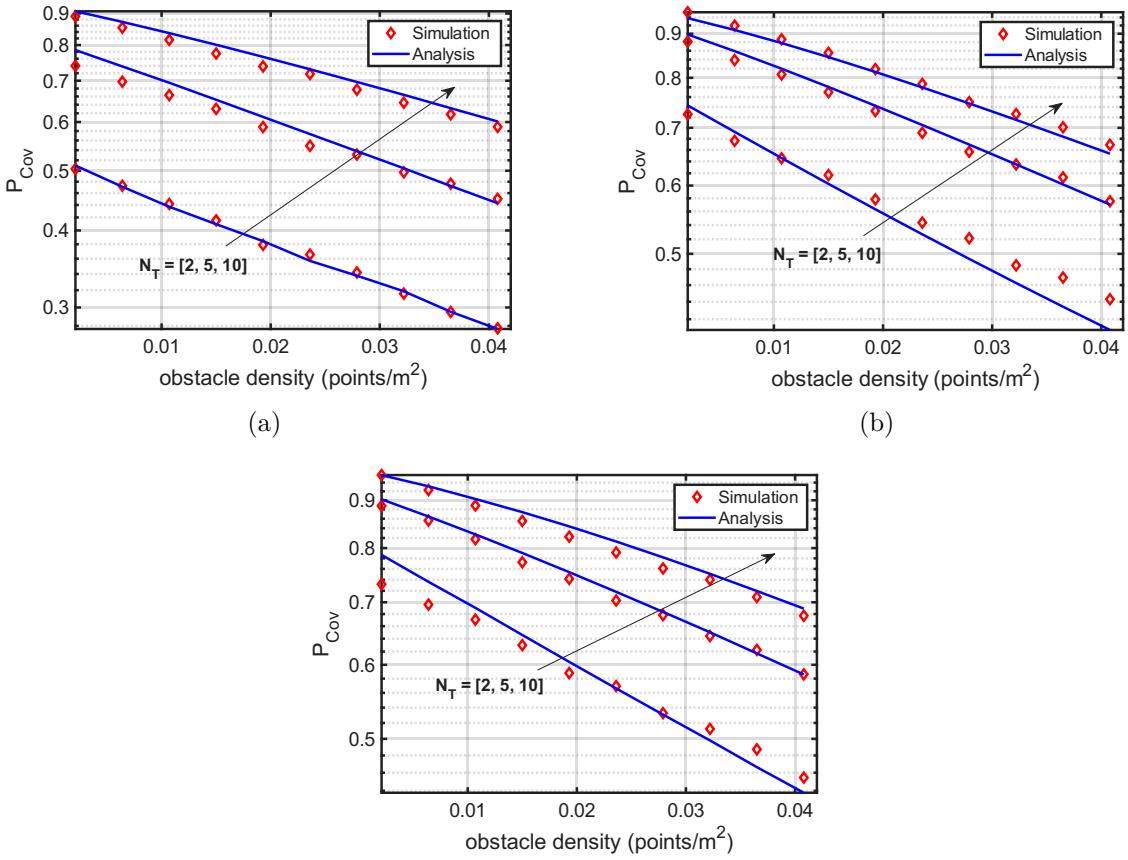

Figure 4.7: (a)–(c) Coverage probability variation with respect to obstacle density for different numbers of RISs: $N_R = 1$, $N_R = 10$, and $N_R = 20$, with $a = 100$ m.

the decay rate decreases, which is due to the decrease of the expected value of $\widetilde{D}_{\text{tr}}$. Now, we examine the CP variation with respect to the transmitter number. We take Fig. 4.7 (b) as an example. Observing the CP variation at a fixed obstacle density, we find that the CP increases with the increase in the transmitter number. However, the increase rate decreases with the increase in the transmitter number. For instance, the increased CP amount is around 0.2 from $N_T = 2$ to $N_T = 5$ at obstacle density =0.02 points/m^2, while there is only around 0.1 CP increase from $N_T = 5$ to $N_T = 10$ at the same obstacle density. Such a phenomenon agrees with what has been discussed in the previous section. As the CP is composed of direct and indirect links, it is hard to see the contribution of RISs to the total CP. Hence, we provide Fig. 4.8 to clearly show how the contribution of RISs varies with respect to obstacle

density. Note that there are two vertical axes in Fig. 4.8. The left one represents the absolute CP contributed by the associated RIS (or the increased CP in the presence of RIS), and the right one represents the percentage of the RIS contribution over the total CP. It is noted that with the obstacle density increasing, the CP improved by RIS decreases. This phenomenon may seem to be counterintuitive at the beginning because RIS is designed for creating the indirect links in a rich scattering environment. In the system model, the RIS is deployed at a height exceeding that of all obstacles, ensuring that the BS-RIS link is always unblocked, regardless of obstacle density. However, an increase in obstacle density negatively impacts the LOS probability of the RIS-user link, as it becomes more susceptible to blockage. Moreover, since RISs are mounted on side walls, their placement inherently limits how close they can be to users, resulting in longer RIS-user distances on average. These two factors, reduced LOS probability and constrained deployment geometry, jointly cause the diminishing CP improvement of RIS as the obstacle density increases. Now, we fix the obstacle density and observe the contribution of RIS under different transmitter numbers. We find that the contribution of RIS decreases with the increase in the transmitter number. Such a phenomenon can be explained in the following way: more transmitters mean the expected value of $\widetilde{D}_{\text{tr}}$ decreases, which leads to the increase in the LOS probability in the direct link. As the communication strategy stated: the transmitter will always try the direct link. It will choose an RIS for communication when the direct link fails. More transmitters indicate a low direct link failure probability. Hence, an RIS will not be selected even if the indirect link condition is feasible for communication.

Next, we show the CP variation with respect to the transmit power in Fig. 4.9. Fig. 4.9(a) shows the total CP and Fig.4.9(b) shows the CP contributed by the RIS. Observing Fig. 4.9(a), we find that the CP increases as the transmit power increases. However, the increase amount will decrease with the increase in the number of transmitters (e.g., the increase amount is around 0.5 from -10 dBm to

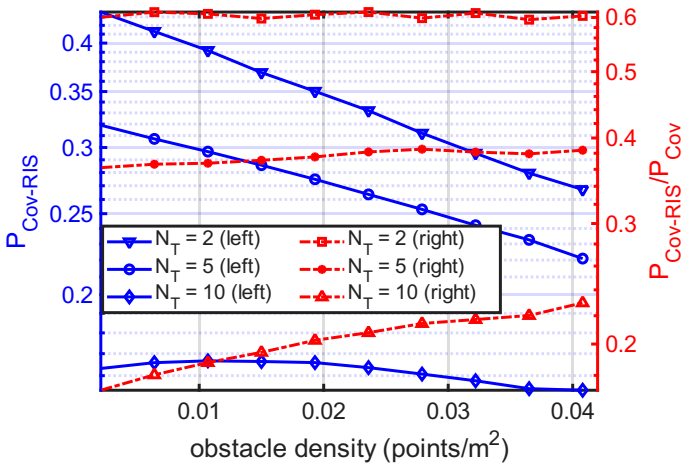

Figure 4.8: Contribution of the RIS in terms of coverage probability with respect to obstacle density, with $a = 100$ m and $N_R = 10$.

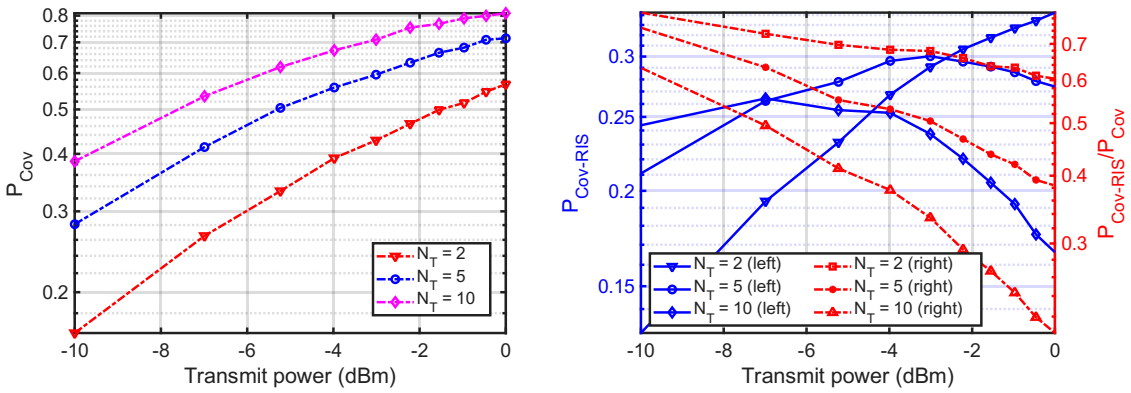

Figure 4.9: (a) Coverage probability variation with respect to transmit power. (b) Contribution of the RIS to coverage probability under the same setting, with $a = 100$ m, $N_R = 10$, and $N_o = 236$.

0 dBm when $N_T = 2$, while the increase amount is around 0.4 from -10 dBm to 0 dBm when $N_T = 10$). Observing Fig. 4.9(b), we find that the contribution of RIS decreases with the increase of the transmit power (right vertical axis in Fig. 4.9(b)). However, the decrease rate varies with different transmitter numbers. The decrease rate is small at low transmitter numbers(e.g., $N_T = 2$) and large at high transmitter numbers (e.g., $N_T = 5, 10$). Such a phenomenon can be explained in the following way: when the transmitter number is low, the direct link failure probability is high. Hence, the contribution of RIS decreases slowly with the increase of the

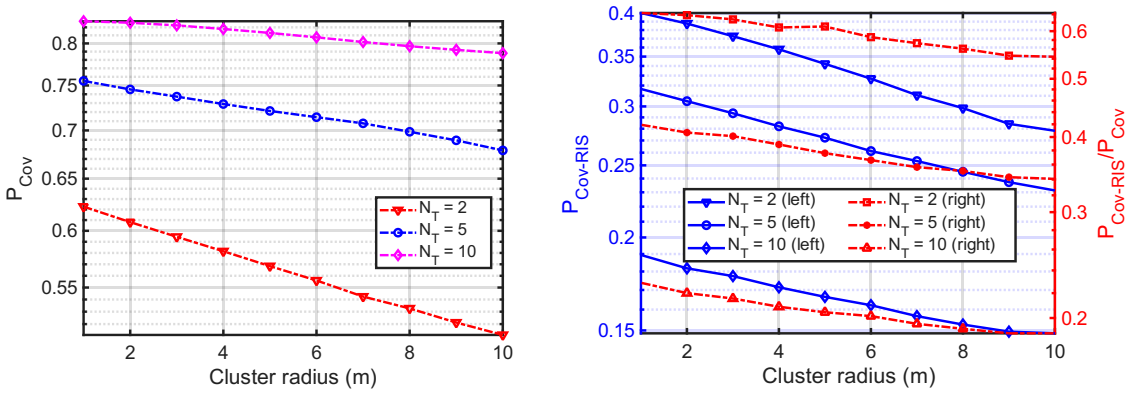

(a) (b)

Figure 4.10: (a) Coverage probability variation with respect to cluster radius R_c. (b) Contribution of the RIS to coverage probability under the same setting, with $a = 100$ m, $N_R = 10$, and $N_o = 236$.

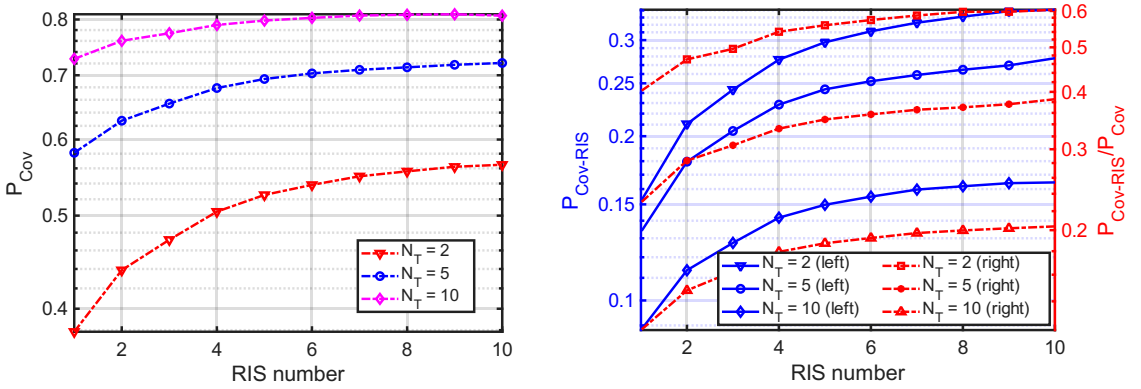

(a) (b)

Figure 4.11: (a) Coverage probability variation with respect to the number of RISs N_R. (b) Contribution of the RIS to coverage probability under the same setting, with $a = 100$ m and $N_o = 236$.

transmit power. With the increase of the transmitter number, the direct link failure probability decreases, and the contribution of RIS decreases fast with the increase in the transmit power. Another thing to note in Fig. 4.9(b) is that when the transmit power is low (e.g., -10 dBm), the contribution of RIS is very high (around 80%). This means most of the communications are assisted by the associated RIS.

Then, we show the CP variation with respect to the cluster radius. In Fig.4.10(a), we find that the CP decreases with the increase of the cluster radius in a linear way, which matches the discussion in the previous section. However, the slope of

the decrease is slower at a high transmitter number. There is around 0.05 decrease from $R_c = 1$ m to $R_c = 10$ m at $N_T = 10$ while there is around 0.15 decrease for $N_T = 2$. Observing Fig. 4.10(b), we find that the decrease rate of the RIS contribution does not change with respect to the transmitter number or the cluster radius (right vertical axis in Fig. 4.10(b)). It is also noted in Fig. 4.10(b) that the contribution of RIS is relatively high (around 40%) at medium transmitter number (e.g., $N_T = 2, 5$).

Finally, we show the CP variation with respect to the RIS number. Through Fig. 4.11, we find that the CP will increase with the increase of the RIS number at different transmitter numbers. However, the increase rate of the CP will decrease with the increase in the RIS number. This also agrees with what has been discussed in the previous section. In Fig. 4.11(b), we find that the contribution of the RIS increases with the increase of the RIS number. The contribution increase amount is roughly the same at different transmitter numbers (around 15%). However, the absolute CP of the RIS decreases with the increase in the transmitter number. This is because the direct link failure probability decreases. Furthermore, because the CP will eventually saturate with the increase of the RIS number, the optimal RIS number that can achieve the maximum spectral efficiency (SE) of a user can also be determined. For instance, when $N_T = 2$, the optimal RIS number for SE maximisation should be 10. The optimal RIS number will decrease to 8 when $N_T = 5$, and 7 when $N_T = 10$.

Throughout the numerical analysis towards different network parameters, it is noted that the obstacle density is a dominant factor on the CP. With the increase of obstacle density, the CP exponentially decreases. Cluster radius, on the other hand, has a gentle effect on the CP. With the increase of the cluster radius, the CP linearly decreases. Although increasing the RIS number can mitigate the negative effects caused by the blockage and the user clustering behaviour, its improvement will saturate as the RIS number increases to a certain value.

To highlight the importance of incorporating practical factors such as height

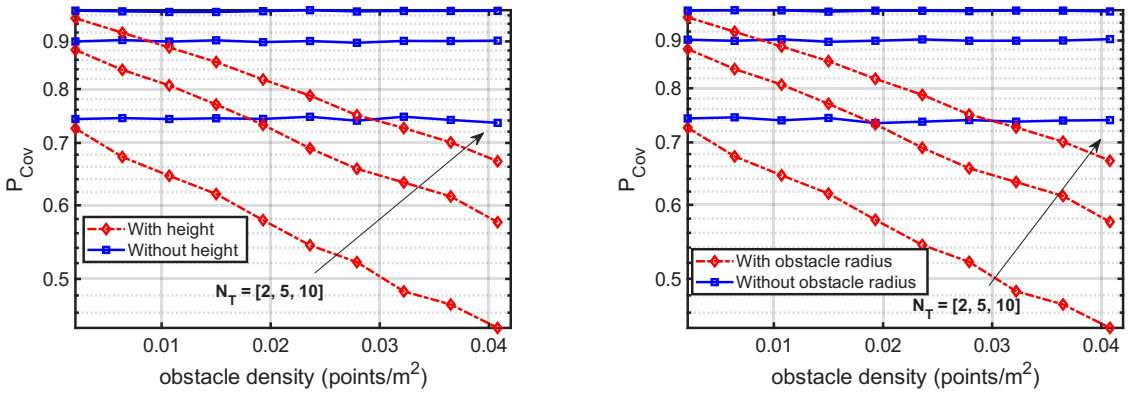

Figure 4.12: (a) Coverage probability variation with respect to obstacle density when node height is ignored. (b) Coverage probability variation with respect to obstacle density when obstacle radius is ignored, with $a = 100$ m and $N_R = 10$.

and obstacle radius, we also compare the variation in CP with respect to obstacle density under two simplified models: one that neglects all nodes' heights and another that ignores the obstacle radius. The comparisons are shown in Fig. 4.12. In Fig.4.12(a), it is observed that when the height of the nodes is neglected, the CP becomes significantly insensitive to the obstacle density due to the links blocked by the height of the obstacle now becoming unblocked. This simplification will overestimate the performance of the RIS-assisted indoor mmWave network. In Fig. 4.12(b), the comparison is made using a simplified obstacle model, where each obstacle is treated as an infinitesimal point without radius. It is observed that the CP becomes significantly less sensitive to obstacle density. This is because omitting the obstacle radius substantially increases the LOS probability for both direct and indirect links, thereby diminishing the impact of obstacle density on CP and leading to an overestimation of the network performance in terms of CP.

4.6 Conclusion

In this chapter, a comprehensive analytical framework has been developed to characterise the downlink performance of RIS-assisted indoor mmWave networks. A

three-dimensional indoor environment has been considered, where both user clustering and blockage effects are explicitly incorporated. Based on the adopted communication strategy and association policy, the distance distributions for both direct and indirect links have been derived. Furthermore, the LOS probabilities have been characterised by accounting for height variations and boundary effects, which are essential features of realistic indoor environments.

The analytical results have been validated through Monte Carlo simulations, demonstrating the accuracy of the proposed framework. Based on this analysis, several key insights into the system behaviour have been obtained. In particular, obstacle density is identified as the dominant factor affecting the CP, leading to significant performance degradation as blockage becomes more severe. However, this degradation can be effectively mitigated through RIS deployment, especially in scenarios where the number of transmitters is limited or the transmit power is constrained.

In contrast, the impact of user clustering, characterised by the cluster radius, is found to be relatively moderate. Moreover, its influence diminishes as the number of transmitters increases, indicating that network densification can partially compensate for user spatial heterogeneity. It is also observed that the relative performance gain provided by RIS decreases with an increasing number of transmitters. This suggests that the benefit of RIS deployment is most pronounced in sparse networks, whereas its contribution becomes less significant in highly dense transmitter deployments.

Overall, the results presented in this section provide useful design insights for RIS-assisted indoor mmWave systems. In particular, they highlight the trade-offs between infrastructure deployment and RIS-assisted enhancement, and offer guidance on when RIS deployment is most beneficial in practical indoor scenarios.

Chapter 5

User Capacity Analysis of Intelligent Omni-Surface Assisted Millimetre Wave Indoor Networks

5.1 Introduction

In Chapter 4, the performance of RIS-assisted indoor mmWave networks was evaluated using coverage probability. While coverage probability characterises the reliability experienced by an individual user, it does not directly indicate how many users can be simultaneously supported by the network. As future wireless systems are expected to accommodate an ever-increasing number of users with diverse service requirements, understanding the user-serving capability of intelligent surfaces has become an important problem alongside conventional coverage analysis.

To address this question, this chapter shifts the focus from single-user coverage to user capacity, defined as the maximum number of users that can be simultaneously served while satisfying predefined quality-of-service requirements. Unlike coverage probability, which evaluates the communication performance of a single user, user capacity provides a system-level metric that reflects the scalability of the network under practical resource constraints. This perspective is particularly important for dense indoor environments, where multiple users compete for limited wireless resources and inter-user interference becomes increasingly significant.

Building upon the indoor network framework developed in Chapter 4, we develop a stochastic geometry-based analytical model that incorporates heterogeneous user

requirements, inter-user interference, and both far-field and near-field propagation effects. Furthermore, the proposed framework considers the impact of intelligent surface size, transmit power, and user distribution on the achievable user capacity. The resulting analysis provides insights into the scalability and fairness of intelligent surface-assisted wireless networks, while quantifying the conditions under which IOS can provide capacity improvements over conventional RIS deployments.

5.2 System Model

5.2.1 Spatial Models

As illustrated in Fig. 5.1, we consider downlink communication from a transmitter to multiple users through an IOS in a cuboidal indoor environment with width W, length L, and height h_t. Throughout this chapter, we assume a square floor plan, i.e., $L = W$. The origin of the Cartesian coordinate system is located at the centre of the floor. The IOS is deployed at $(0, 0, h_r)$, and the transmitter (Tx) is deployed at $(L/2, 0, h_t)$. The IOS consists of M_I elements and operates in the energy splitting mode, where the magnitudes of the reflection and transmission coefficients

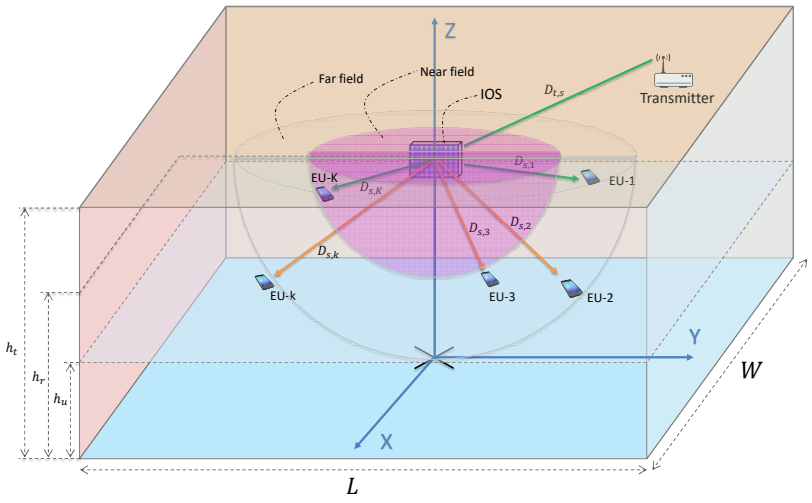

Figure 5.1: Illustration of an IOS-assisted mmWave 3D indoor communication network with hybrid fields

are $R = T = 1/\sqrt{2}$. For simplicity and tractability, we assume that the phase shifts of each element on the two sides of the IOS are independent, which can be realised by inserting more layers into the metasurface design [100].

There are K users in the room, each at height h_u, and their spatial locations follow a BPP. Users fall into three categories: video, audio, and text users, whose QoS requirements are defined by the signal-to-interference-plus-noise ratio (SINR) thresholds τ_v, τ_a, and τ_t, respectively. These user types are introduced to impose differentiated SINR constraints in the user capacity evaluation via the CP. We consider a downlink coverage-extension scenario in which the users lie in a region shadowed from the transmitter by a wall or other large obstruction. The IOS is positioned to provide an alternative propagation path, with an unobstructed transmitter-IOS link and unobstructed IOS-user links. This represents a deployment condition under which the surface can serve users without direct coverage, rather than an assumption that surface-assisted links are unaffected by blockages. Conditioning on these links being available allows the analysis to isolate the user-serving capability of the IOS under inter-user interference and heterogeneous QoS requirements. An obstacle blocking a user's direct link may also block its IOS-assisted link if it intersects the IOS-user path. Furthermore, a sufficiently large obstacle may block the surface-assisted paths of multiple users, resulting in correlated blockage events. Such events are not explicitly modelled in this chapter. The resulting coverage probabilities and user capacity are therefore conditional on the availability of the IOS-assisted paths. Due to the high operating frequency and the large aperture of the IOS, some EUs are located in its near-field region while others lie in the far-field region[1].

[1]The detailed definitions of near-field and far-field as well as the near-field effects are explained in section 5.3.

5.2.2 Multi-User Service

Since multiple EUs are served simultaneously, we divide the IOS into K subarrays, each dedicated to one EU [101, 102] with the same element number. In this work, the IOS is partitioned along its column dimension, such that each subarray consists of an integer number of adjacent columns spanning the full number of rows. This column-wise partitioning enables independent beam control for each user while maintaining a simple and practical subarray structure. To determine the user capacity, we adopt an incremental feasibility-checking procedure based on the users' coverage probabilities. For a given number of users K, the IOS is partitioned into K equal-sized subarrays, each serving one user. Users are indexed according to their ordered IOS–user distances obtained via order statistics. For the jth user, the CP is evaluated by accounting for the probabilities of residing in the depth of focus (DF), non-depth-of-focus (NDF), and far field (FF) regions. Within each region, the CP is further conditioned on the user type, characterised by SINR thresholds τ_v, τ_a, and τ_t, and weighted by the corresponding occurrence probabilities p_v, p_a, and p_t. The overall CP of the jth user is obtained by combining the region-specific coverage probabilities with the associated region and user-type probabilities. The IOS is considered capable of supporting K users if the CP of every user exceeds a predefined target threshold. Starting from $K = 1$, this procedure is repeated by incrementally increasing K until the coverage constraint is violated for at least one user. The maximum feasible value of K is defined as the user capacity. Note that "user capacity" in this context is used in a service-oriented sense and should not be interpreted as an information-theoretic rate capacity; it refers to the maximum number of users that can be simultaneously supported under a target per-user CP requirement.

One may note that equal partitioning of the IOS does not necessarily yield the optimal subarray configuration for all users, since users closer to the IOS may require fewer elements, whereas users farther away may benefit from a larger allocation. As a

result, equal partitioning may incur performance loss compared with location-aware partitioning strategies that adapt the subarray sizes according to user positions. This loss mainly arises from inter-user interference. In particular, a user located close to the IOS may be allocated more elements than actually needed, leading to unnecessarily strong reflected power and, consequently, stronger interference to other users, which may degrade the overall system performance. This observation is true. However, in this work, we adopt equal partitioning as a deliberate modelling choice to enable a tractable and interpretable system-level analysis. In particular, our objective is not to optimise the element allocation across users, but to characterise the maximum number of users that can be simultaneously supported under stochastic network conditions and heterogeneous QoS requirements. Allowing a variable element allocation M_j,i.e., the allocated IOS element number to the jth user, would introduce strong coupling between users, as the optimal allocation would depend on each realisation of user locations, user types, and propagation conditions. A theoretically optimal approach would require solving, for each realisation, an optimisation problem over M_j and subsequently averaging the resulting performance over all realisations. Such a procedure would lead to prohibitive computational complexity, especially given that the evaluation of CP already involves multiple integrals. Moreover, due to the inherent randomness of user locations and QoS demands, the optimal allocation is itself realisation-dependent, making it difficult to define a globally optimal strategy in a stochastic geometry framework. In contrast, equal partitioning provides a consistent and fairness-oriented baseline that allows us to isolate the impact of spatial randomness, propagation regimes, and QoS heterogeneity on the achievable user capacity. Optimising the element allocation across users is therefore left as an important direction for future work.

5.3 Far-Field Path-Loss and Interference Modelling

5.3.1 Propagation Regime Definitions

Before proceeding, we briefly clarify the meaning of the term "near-field" in this context. When waves are reflected (or transmitted) from the IOS, they first pass through the reactive near-field region, followed by the radiative near-field region. In the radiative near-field, amplitude variations across the IOS elements become negligible once the distance exceeds the Björnson distance [103]. The region where amplitude variations can be neglected but phase variations remain non-negligible, extending up to the Rayleigh distance (also known as the Fraunhofer distance), is referred to as the Fresnel region. Beyond the Rayleigh distance, the waves enter the far-field region. Unless otherwise specified, the term "near-field" in this section specifically refers to the Fresnel region. When performing beamforming in the Fresnel region, there exists a subregion, ranging from the Björnson distance to one tenth of the Rayleigh distance, where the DF effect occurs [103]. In this region, any displacement of the receiver along the beam axis away from the focal point results in antenna array gain degradation, regardless of the direction of the displacement. This behaviour originates from the spherical wavefront curvature in the near field, which induces a nonlinear phase profile across the IOS aperture and enables spatial focusing at a specific point rather than along a single direction. As a result, the received signal power becomes sensitive to spatial mismatch in both angle and distance. In particular, users located away from the focal point, either along the beam axis or perpendicular to it, experience phase misalignment across the IOS elements, which leads to a reduction in the effective gain. This mechanism also affects the inter-user interference. Compared to the far field, where interference is mainly determined by angular separation under a planar wave assumption, the wavefront curvature introduces an additional dependence on distance. Consequently, even users who are aligned in angle may experience reduced interference when they are located at different depths, which can lower the interference floor. In this section, we refer to this subregion as the DF region. The remaining part of the Fresnel region, where

the DF effect is negligible, is termed the NDF region, while the region beyond the Rayleigh distance is referred to as the FF region.

5.3.2 User Geometry: Distance and Angular Distributions

Before introducing the far-field path loss and interference models, we first characterise the geometric statistics of the distance and angular distributions, which serve as inputs to the subsequent analysis.

5.3.2.1 Distance Distribution between the jth User and the IOS

In the far-field path loss model, the only random variable is the distance between the jth user and the IOS, according to the given system model[2]. We define the distance distribution from the IOS to the jth user as $D_{s,j}$. Here we focus on deriving its squared distribution, i.e., $D_{s,j}^2$. To derive the distribution of $D_{s,j}^2$, the CDF of D^2 is needed, i.e., the distance square between the IOS and a random user. The CDF of D^2 follows directly from the square-floor geometry. Let $\Delta h = h_r - h_u$. Since the IOS is located above the centre of the floor, $D^2 = X^2 + Y^2 + \Delta h^2$, where (X, Y) is uniformly distributed over $[-L/2, L/2]^2$. Thus, $F_{D^2}(x)$ equals the area of intersection between this square and a disk of radius $\sqrt{x - \Delta h^2}$, divided by L^2. Defining $s = x - \Delta h^2$, we obtain

$$F_{D^2}(x) = \begin{cases} 0, & s < 0, \\ \dfrac{\pi s}{L^2}, & 0 \le s \le \dfrac{L^2}{4}, \\ \dfrac{\pi s - 4s \arccos\left(\dfrac{L}{2\sqrt{s}}\right) + 2L\sqrt{s - \dfrac{L^2}{4}}}{L^2}, & \dfrac{L^2}{4} < s < \dfrac{L^2}{2}, \\ 1, & s \ge \dfrac{L^2}{2}. \end{cases} \tag{5.1}$$

[2]This will be clearer when the path loss equation is given later in this section.

The middle expression subtracts the four circular segments extending beyond the square boundaries from the disk area. By applying order statistic methods to the squared distance D^2, the PDF of the jth ordered distance square $D^2_{s,j}$ can be expressed as

$$f_{D^2_{s,j}}(d_{s,j}) = \frac{K!}{(j-1)!(K-j)!}(F_{D^2}(d_{s,j}))^{j-1}(1-F_{D^2}(d_{s,j}))^{K-j} f_{D^2}(d_{s,j}), \quad (5.2)$$

where K denotes the number of users in the network and $f_{D^2}(d_{s,j})$ represents the PDF of D^2, obtained by differentiating its CDF $F_{D^2}(d_{s,j})$. Having established the ordered distance distributions, we next characterise the angular distributions in the far-field, which are essential for the far-field interference model.

5.3.2.2 Azimuth and Elevation Angle Distributions and Angular Separation

We next characterise the azimuth and elevation angle distributions of two users with respect to the IOS, as well as the resulting angular separation statistics. These distributions depend on the users' spatial locations and are independent of the propagation regime, and they will be used to quantify the probability of mainlobe overlap[3] in the far-field interference model.

In the azimuth plane (XOY plane), we define the user angle as the angle between the projected user direction and the positive Y direction. We define Φ_j and Φ_l as the azimuth user angles for the jth user and the lth user. Because the users' spatial locations follow BPP, Φ_j and Φ_l are two i.i.d. random variables. The azimuth-angle distribution follows from the uniform user distribution over the square floor. Using polar coordinates centred at the floor projection of the IOS, the joint density of the radial distance R and azimuth angle Φ is

$$f_{R,\Phi}(r,\phi) = \frac{r}{L^2}, \qquad 0 \le r \le r_{\max}(\phi), \quad (5.3)$$

[3]A detailed definition of mainlobe overlap will be introduced later in this section.

where the factor r is the Jacobian of the coordinate transformation. The distance from the centre to the square boundary along the direction ϕ is

$$r_{\max}(\phi) = \frac{L}{2\max\{|\cos\phi|, |\sin\phi|\}}. \tag{5.4}$$

Integrating over the radial coordinate gives

$$\begin{aligned} f_{\Phi_j}(\phi) &= \int_0^{r_{\max}(\phi)} \frac{r}{L^2}\,\mathrm{d}r \\ &= \frac{1}{8\max\{\cos^2\phi, \sin^2\phi\}}, \qquad 0 \le \phi < 2\pi. \end{aligned} \tag{5.5}$$

As mentioned earlier, since the analysis is performed on one side of the IOS, we define the set $\mathcal{S}$ as

$$\mathcal{S} = \{\phi : |\phi - \phi_0| \le \frac{\pi}{2}\}, \tag{5.6}$$

where ϕ_0 is the boresight direction on that side, and it is $\pi/2$. Conditioning on the event that both users lie on the same side of the IOS, the azimuth angles are restricted to the set $\mathcal{S}$. Under this conditioning, the azimuth angle separation $\Delta\Phi$ between the jth and lth users is characterised by the convolution of their conditional angle distributions, and its PDF is given by

$$f_{\Delta\Phi}(\delta) = \int_{-\pi}^{\pi} f_{\Phi|\mathcal{S}}(\phi) f_{\Phi|\mathcal{S}}(\phi - \delta)\mathrm{d}\phi, \tag{5.7}$$

where $f_{\Phi_j|\mathcal{S}}(\cdot)$ denotes the jth user's azimuth-angle PDF conditioned on $\Phi_j \in \mathcal{S}$. The PDF of the absolute azimuth angle separation $|\Delta\Phi|$ is then expressed as

$$f_{|\Delta\Phi||_{\mathcal{S}}}(\delta_{\text{abs}}) = f_{\Delta\Phi}(\delta_{\text{abs}}) + f_{\Delta\Phi}(-\delta_{\text{abs}}), \tag{5.8}$$

where $\delta_{\text{abs}} \in [0, \pi]$.

The elevation angle of a user is defined as the angle between the projected user direction and the negative direction of the Z axis in the YOZ plane. We define Θ_j and Θ_l as the elevation user angles for the jth user and the lth user. Because the users' spatial locations follow a BPP, Θ_j and Θ_l are two i.i.d. random variables. The definition of Θ_j (or Θ_l) is given by

$$\Theta_j = \arctan\left(\frac{D_{\text{p}}}{h_r - h_u}\right), \tag{5.9}$$

where D_{p} is the projected distance of D. Since users are uniformly distributed over the rectangular floor region, the CDF of the projected distance D_{p} is obtained by integrating the uniform spatial density over the floor region. With the CDF of D_{p}, the PDF of Θ_j can be derived using Jacobian transformation as

$$f_{\Theta}(\theta) = f_{D_{\mathrm{p}}}(\Delta h \tan(\theta))\Delta h \sec^2(\theta), \tag{5.10}$$

where Δh is defined as $\Delta h = h_r - h_u$, and $f_{D_{\mathrm{p}}}(\cdot)$ is the PDF of D_{p}, which can be obtained by differentiating $F_{d_{\mathrm{p}}}(\cdot)$, and θ ranges from 0 to $\pi/2$. The PDF of the elevation angle separation between the jth user and the lth user $f_{\Delta\Theta}(\cdot)$ is the convolution of the two users' elevation angle distributions, and the PDF of the absolute elevation angle separation is expressed as

$$f_{|\Delta\Theta|}(\delta_{\theta,\mathrm{abs}}) = f_{\Delta\Theta}(\delta_{\theta,\mathrm{abs}}) + f_{\Delta\Theta}(-\delta_{\theta,\mathrm{abs}}), \tag{5.11}$$

where $\delta_{\theta,\mathrm{abs}}$ ranges from 0 to $\pi/2$.

5.3.3 Far-Field Path Loss

Based on [38, 30], the large-scale attenuation from the transmitter to the EU through the IOS is proportional to the square of the product of their distances, i.e., the product of the transmitter–IOS and IOS–EU distances' square. The corresponding path loss factor[4] for the jth subarray is given by [30]

$$G_{\mathrm{path}} = \frac{\lambda^2}{64\pi^3 D_{t,s}^2 D_{s,j}^2}, \tag{5.12}$$

where λ is the carrier wavelength, $D_{t,s}$ denotes the transmitter–IOS distance, and $D_{s,j}$ is the distance between the IOS and the jth subarray's serving user. Accordingly, the received power under large-scale fading can be expressed as (for the reflected

[4]Note that G_{path} is not a unitless antenna gain but a distance-dependent path loss factor; when combined with the IOS element area $e_x e_y$, the received power expression, which is given in (5.13), becomes dimensionally consistent.

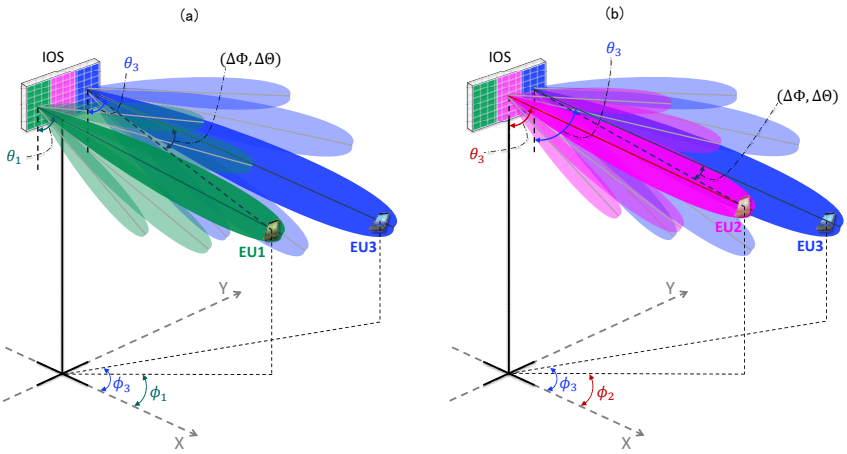

Figure 5.2: (a) Sidelobe leakage as an interference. (b) Mainlobe overlap as an interference

user)

$$\begin{aligned} P_{\text{rx}} &= P_{\text{tx}} R^2 e_x e_y G_t G_r G_j G_{\text{path}} \\ &= \frac{P_{\text{tx}} R^2 e_x e_y G_t G_r G_k \lambda^2}{64\pi^3 D_{t,s}^2 D_{s,j}^2}, \end{aligned} \tag{5.13}$$

where e_x and e_y denote the IOS element's length and width, and $e_x = e_y$, P_{tx} denotes the transmit power of the jth user, G_t and G_r represent the transmitter and receiver antenna gains, respectively, and G_j is the subarray gain. As stated in the system model, the locations of the IOS and the transmitter are given, and the users' spatial locations are modelled as BPP. Hence, the only random variable in (5.13) is the IOS-jth user distance $D_{s,j}$,whose distribution is given in the previous subsection.

5.3.4 Far-field interference

Inter-user interference arises from sidelobe leakage and, when beams are closely aligned, from mainlobe overlap, as illustrated in Fig. 5.2. To model the radiation behaviour of each IOS subarray, we adopt the flat-top antenna model [104, 105, 106], in which the subarray radiation pattern is approximated by constant gains in the mainlobe and sidelobe regions. The mainlobe is characterised by half-power

beamwidths η_B and ν_B in the azimuth and elevation planes, respectively, with a constant gain G_j within these beamwidths, while the sidelobe gain is approximated by a constant level $G_{j,\mathrm{SB}}$, given by

$$G_{j,\mathrm{SB}} = \frac{\sqrt{G_j} - \frac{\sqrt{3}}{2\pi} G_j \sin(\frac{\sqrt{3}}{2\sqrt{G_j}})}{\sqrt{G_j} - \frac{\sqrt{3}}{2\pi} \sin(\frac{\sqrt{3}}{2\sqrt{G_j}})}. \tag{5.14}$$

We next characterise the mainlobe overlap probability for two users located on the same side of the IOS. Owing to the independent phase assumption on the two sides of each element and the symmetry induced by the BPP user distribution, the analysis can be restricted to a single side, with the overall user capacity obtained by doubling the resulting value. The mainlobe overlap probability in the azimuth plane is given by

$$p_{\mathrm{az}} = P\left(|\Delta\Phi| \leq \frac{\eta_B}{2} \middle| \Phi_j \in \mathcal{S}, \Phi_l \in \mathcal{S} \right), \tag{5.15}$$

where $|\Delta\Phi|$ follows the conditional distribution derived in section 5.3.2.2. For a uniform planar array, the azimuth beamwidth can be approximated as [107]

$$\eta_B \approx \frac{0.886\lambda}{N_{\mathrm{col}} d_y \cos(\phi - \phi_0)}, \tag{5.16}$$

which yields

$$p_{\mathrm{az}} = \int_0^{\pi} f_{\Phi|\mathcal{S}}(\phi_c - \phi_0) \int_0^{\frac{0.886\lambda}{2N_{\mathrm{col}} d_y \cos(\phi_c - \phi_0)}} f_{|\Delta\Phi|\big|\mathcal{S}}(\delta_{\mathrm{abs}}) \mathrm{d}\delta_{\mathrm{abs}} \mathrm{d}\phi_c. \tag{5.17}$$

Similarly, the mainlobe overlap probability in the elevation plane is given by

$$p_{\mathrm{el}} = P\left(|\Delta\Theta| \leq \frac{\nu_B}{2} \right), \tag{5.18}$$

where $|\Delta\Theta|$ follows the distribution derived in Section III-B and the elevation beamwidth is approximated as

$$\nu_B \approx \frac{0.886\lambda}{N_{\mathrm{row}} d_x \cos(\theta)}, \tag{5.19}$$

leading to

$$p_{\mathrm{el}} = \int_0^{\pi/2} f_{\Theta}(\theta) \int_0^{\frac{0.886\lambda}{2N_{\mathrm{row}} d_x \cos(\theta)}} f_{|\Delta\Theta|}(\delta_{\theta,\mathrm{abs}}) \mathrm{d}\delta_{\theta,\mathrm{abs}} \mathrm{d}\theta. \tag{5.20}$$

We define the event that mainlobe interference from the lth user affects the jth user as $B_l \sim \text{Bernoulli}(p_{\text{az}}p_{\text{el}})$. Assuming identical transmit power across users, the total far-field interference is given by

$$I_{\text{FF}} = P_{\text{tx}}R^2 e_x e_y G_t G_r G_{\text{path}} \sum_{l=1, l\neq j}^{K} G_{l,\text{SB}} + (G_l - G_{l,\text{SB}})B_l. \tag{5.21}$$

We next turn to the characterisation of path loss and interference in the near-field.

5.4 Near-Field Path-Loss and Interference Modelling

5.4.1 Near-field Path Loss

According to [30], the path loss in the near-field is element-dependent[5] (see (11) in [30]). However, as the distance between the IOS subarray and the EU increases, the far-field approximation progressively converges to the near-field path loss model (see Fig. 9(b) in [30]). This occurs because, beyond the Björnson distance, the amplitude variations across the subarray become negligible [103]. Consequently, since our analysis focuses on the Fresnel region within the near-field, the path loss can be accurately approximated using the conventional far-field path loss model, which is not repeated here for brevity.

5.4.2 Near-Field Interference

In the near-field, we first analyse the interference in the DF region, followed by that in the NDF region. We define the Rayleigh distance as d_{FA} and the Björnson distance as d_{B}. As stated in the system model, the DF region extends from d_{B} to $d_{\text{FA}}/10$, followed by [103]. We denote the coordinate of the jth user as $\mathbf{j} = (X_j, Y_j, h_u)$ (the current serving user), that of the lth user as $\mathbf{l} = (X_l, Y_l, h_u)$ (an interferer), and the unit vector of the beam direction as $\hat{\mathbf{u}} = [\sin(\Theta_j)\cos(\Phi_j), \sin(\Theta_j)\sin(\Phi_j), -\cos(\Theta_j)]$, where Φ_j and Θ_j represent the azimuth and elevation angles of the jth user, respectively. The

[5]That is, the IOS cannot be viewed as a single point source, and the distance differences between each IOS element and the EU must be considered.

displacement of the lth user from the focal point ΔD_{ax} along the direction of $\hat{\mathbf{u}}$ is expressed as

$$\Delta D_{\text{ax}} = |\sin(\Theta_j)\cos(\Phi_j)(X_j - X_l) + \sin(\Theta_j)\sin(\Phi_j)(Y_j - Y_l)|. \tag{5.22}$$

Given the coordinates of both the serving and interfering users, Φ_j and Θ_j can be reformulated as $\Phi_j = \arctan\left(X_j/Y_j\right)$ and $\Theta_j = \arctan\left(\sqrt{X_j^2 + Y_j^2}/(h_r - h_u)\right)$. The degradation coefficient of the subarray gain from the lth user to the jth user along the jth user's beam axial direction can be expressed as [103]

$$\rho_{\parallel} = \left(\frac{8D_{\text{eff}}}{d_{\text{FA}}}\right)^2 \left(C^2\left(\sqrt{\frac{d_{\text{FA}}}{8D_{\text{eff}}}}\right) + S^2\left(\sqrt{\frac{d_{\text{FA}}}{8D_{\text{eff}}}}\right)\right)^2, \tag{5.23}$$

where $D_{\text{eff}} = D_{s,j}(D_{s,j} \pm \Delta D_{\text{ax}})/\Delta D_{\text{ax}}$, and $C(\cdot)$ and $S(\cdot)$ denote the Fresnel integrals, defined as $C(x) = \int_0^x \cos(\pi t^2/2)\mathrm{d}t$ and $S(x) = \int_0^x \sin(\pi t^2/2)\mathrm{d}t$. We define $\rho_{\parallel} \to 1$ when ΔD_{ax} approaches to 0. In addition to the DF effect, the subarray gain from the lth user to the jth user also experiences degradation in the lateral direction. The lateral direction degradation coefficient is given by [103]

$$\rho_{\perp} = \text{sinc}^2\left(\sqrt{\frac{M_{I,E}^l}{2}}\frac{e_x(X_j - X_l)}{\lambda D_{s,l}}\right)\text{sinc}^2\left(\sqrt{\frac{M_{I,E}^l}{2}}\frac{e_y(Y_j - Y_l)}{\lambda D_{s,l}}\right). \tag{5.24}$$

With the beam axial degradation coefficient and the lateral degradation coefficient, the interference seen by the jth user in the DF region can be expressed as

$$I_{\text{DF}} = P_{\text{tx}} R^2 e_x e_y G_t G_r G_{\text{path}} p_{\text{ss}} \sum_{l=1, l\neq j}^{K} \rho_{\parallel}\rho_{\perp} G_l, \tag{5.25}$$

where p_{ss} denotes the probability that a user resides on the same side of the IOS as the serving user. It is noted from (5.25) that each term in the summation is a random variable, since the calculations of $\rho_{\parallel}$ and $\rho_{\perp}$ depend on the coordinates of the jth and lth users, which are random. Obtaining the exact CDF or PDF of I_{DF} is extremely challenging due to the multiple operations involved, including the integral in (5.23), the summation in (5.25), and the computation of the distribution of ΔD_{ax}. To address this, we approximate the distribution of I_{DF} using the moment-matching method with a Gamma distribution. Gamma approximation is adopted due to its

$$\mu_{\text{in}}=\mathbb{E}\left[\rho_{\parallel}\rho_{\perp}\varepsilon G_{\text{path}}\middle|(X,Y)\in\mathcal{A}\cap\mathcal{B}(0,d_{s,j,p}),,X_j=x_j,,Y_j=y_j\right]$$
$$=\frac{1}{|\mathcal{A}\cap\mathcal{B}(0,d_{s,j,p})|}\iint_{\mathcal{A}\text{in}}\rho_{\parallel}\rho_{\perp}\varepsilon G_{\text{path}}\mathrm{d}x\mathrm{d}y, \tag{5.27}$$

$$\mu_{\text{out}}=\mathbb{E}\left[\rho_{\parallel}\rho_{\perp}\varepsilon G_{\text{path}}\middle|(X,Y)\in\mathcal{A}\setminus\mathcal{B}(0,d_{s,j,p}),,X_j=x_j,,Y_j=y_j\right]$$
$$=\frac{1}{|\mathcal{A}\setminus\mathcal{B}(0,d_{s,j,p})|}\iint_{\mathcal{A}\text{out}}\rho_{\parallel}\rho_{\perp}\varepsilon G_{\text{path}}\mathrm{d}x\mathrm{d}y. \tag{5.28}$$

flexibility in modelling sums of non-negative random variables with analytically tractable moments. Specifically, we first derive the expectation and variance of I_{DF}, and then define a Gamma random variable using the expectation and variance to closely approximate I_{DF}. To proceed, we first present the joint PDF of X_j and Y_j, noting that these coordinates no longer follow a uniform distribution once the distance of the jth user has been ordered. The joint PDF is given by

$$f_{X_j,Y_j}(x_j,y_j)=\frac{K}{LW}\binom{K-1}{j-1}\left[F_{D_{\text{p}}}(\sqrt{x_j^2+y_j^2})\right]^{j-1}$$
$$\times\left[1-F_{D_{\text{p}}}(\sqrt{x_j^2+y_j^2})\right]^{K-j}. \tag{5.26}$$

Conditioned on the location of the jth user, the remaining $K-1$ users are no longer identically distributed over the entire floor area due to distance ordering. Specifically, the $j-1$ users closer than the jth user lie within the circular region centred at the origin with radius equal to the projected distance $d_{s,j,p}$, while the remaining $K-j$ users lie outside this region. According to the properties of order statistics for i.i.d. samples [108], users within each region can be regarded as i.i.d. random variables drawn from their respective truncated parent distributions, i.e., uniformly distributed over the corresponding subregions of the floor. Consequently, all users inside (or outside) the serving user circle share the same conditional interference expectation, denoted by μ_{in} and μ_{out}, respectively. Their expressions are given in (5.27) and (5.28), where $\varepsilon = P_{\text{tx}}e_x e_y G_t G_r G_l$, $\mathcal{B}(0,d_{s,j,p})$ denotes a disk of radius $d_{s,j,p}$ centred at the origin, $\mathcal{A}=[-L/2,L/2]\times[-W/2,W/2]$ represents the

$$\begin{aligned}\mathrm{Var}[I_{\mathrm{DF}}] &= \iint_{\mathcal{A}} [(j-1)\sigma_{\mathrm{in}}^2 + (K-j)\sigma_{\mathrm{out}}^2] f_{X_j,Y_j}(x_j,y_j)\mathrm{d}x_j\mathrm{d}y_j \\ &+ \iint_{\mathcal{A}} \Big[(j-1)\mu_{\mathrm{in}} + (K-j)\mu_{\mathrm{out}}\Big]^2 f_{X_j,Y_j}(x_j,y_j)\mathrm{d}x_j\mathrm{d}y_j \\ &- \bigg(\iint_{\mathcal{A}} \Big[(j-1)\mu_{\mathrm{in}} + (K-j)\mu_{\mathrm{out}}\Big] f_{X_j,Y_j}(x_j,y_j)\mathrm{d}x_j\mathrm{d}y_j\bigg)^2 \end{aligned} \tag{5.32}$$

rectangular floor area, $\mathcal{A}_{\mathrm{in}} = \mathcal{A} \cap \mathcal{B}(0, d_{s,j,p})$, and $\mathcal{A}_{\mathrm{out}} = \mathcal{A} \setminus \mathcal{B}(0, d_{s,j,p})$. The factors $1/|\mathcal{A}_{\mathrm{in}}|$ and $1/|\mathcal{A}_{\mathrm{out}}|$ correspond to the uniform spatial density of users within the respective truncated regions. Finally, combining (5.26), (5.27), and (5.28), the expected aggregate interference can be obtained, and is given by

$$\mathbb{E}[I_{\mathrm{DF}}] = \iint_{\mathcal{A}} \Big[(j-1)\mu_{\mathrm{in}} + (K-j)\mu_{\mathrm{out}}\Big] f_{X_j,Y_j}(x_j,y_j)\mathrm{d}x_j\mathrm{d}y_j. \tag{5.29}$$

Next, we derive the variance of I_{DF}. Conditioning on the location of the jth user, the interference variance of a user closer/farther than the jth user is given by ($\mathcal{B}(0, d_{s,j,p})$ is simplified as $\mathcal{B}$)

$$\sigma_{\mathrm{in}}^2 = \frac{1}{\mathcal{A}_{\mathrm{in}}} \iint_{\mathcal{A}_{\mathrm{in}}} (\rho_{\parallel}\rho_{\perp}\varepsilon G_{\mathrm{path}})^2 \mathrm{d}x\mathrm{d}y - \mu_{\mathrm{in}}^2 \tag{5.30}$$

$$\sigma_{\mathrm{out}}^2 = \frac{1}{\mathcal{A}_{\mathrm{out}}} \iint_{\mathcal{A}_{\mathrm{out}}} (\rho_{\parallel}\rho_{\perp}\varepsilon G_{\mathrm{path}})^2 \mathrm{d}x\mathrm{d}y - \mu_{\mathrm{out}}^2. \tag{5.31}$$

The variance of I_{DF} is then given by (5.32). The Gamma random variable that can closely approximate the distribution of I_{DF} is defined as $\hat{I}_{\mathrm{DF}} \sim \Gamma(\alpha_{\mathrm{DF}}, \xi_{\mathrm{DF}})$, where $\alpha_{\mathrm{DF}} = \mathbb{E}[I_{\mathrm{DF}}]^2/\mathrm{Var}[I_{\mathrm{DF}}]$ and $\xi_{\mathrm{DF}} = \mathrm{Var}[I_{\mathrm{DF}}]/\mathbb{E}[I_{\mathrm{DF}}]$.

Next, we describe the interference in the NDF region, i.e., from $d_{\mathrm{FA}}/10$ to d_{FA}. The interference in the NDF region follows a similar formulation to that in the DF region, except that the DF effect is absent, i.e., $\rho_{\parallel} = 1$. The interference in the NDF region is expressed as

$$I_{\mathrm{NDF}} = P_{\mathrm{tx}} R^2 e_x e_y G_t G_r G_{\mathrm{path}} p_{\mathrm{ss}} \sum_{l=1, l\neq j}^{K} \rho_{\perp} G_l. \tag{5.33}$$

We define $\hat{I}_{\mathrm{NDF}} \sim \Gamma(\alpha_{\mathrm{NDF}}, \xi_{\mathrm{NDF}})$ as the Gamma random variable that approximates I_{NDF}. Since the derivation process for $\mathbb{E}[I_{\mathrm{NDF}}]$ and $\mathrm{Var}[I_{\mathrm{NDF}}]$ closely follows that of

$\mathbb{E}[I_{\mathrm{DF}}]$ and $\mathrm{Var}[I_{\mathrm{DF}}]$, it is omitted here for brevity.

5.5 Coverage Probability

In this section, we present the CP expression for the jth user. The CP of the jth user consists of three components corresponding to the DF, NDF, and FF regions. The CP in the DF region is given by

$$\begin{aligned}
P_{\mathrm{DF}}^{j} &= p_v P(\mathrm{SINR}_j \geq \tau_v | d_{\mathrm{B}} \leq D_{s,j} \leq d_{\mathrm{FA}}/10) \\
&+ p_a P(\mathrm{SINR}_j \geq \tau_a | d_{\mathrm{B}} \leq D_{s,j} \leq d_{\mathrm{FA}}/10) \\
&+ p_t P(\mathrm{SINR}_j \geq \tau_t | d_{\mathrm{B}} \leq D_{s,j} \leq d_{\mathrm{FA}}/10) \\
&= p_v P\left(\frac{P_{\mathrm{tx}} R^2 e_x e_y G_t G_r G_j G_{\mathrm{path}}}{I_{\mathrm{DF}} + \sigma_n^2} \geq \tau_v | d_{\mathrm{B}} \leq D_{s,j} \leq d_{\mathrm{FA}}/10\right) \\
&+ p_a P\left(\frac{P_{\mathrm{tx}} R^2 e_x e_y G_t G_r G_j G_{\mathrm{path}}}{I_{\mathrm{DF}} + \sigma_n^2} \geq \tau_a | d_{\mathrm{B}} \leq D_{s,j} \leq d_{\mathrm{FA}}/10\right) \\
&+ p_t P\left(\frac{P_{\mathrm{tx}} R^2 e_x e_y G_t G_r G_j G_{\mathrm{path}}}{I_{\mathrm{DF}} + \sigma_n^2} \geq \tau_t | d_{\mathrm{B}} \leq D_{s,j} \leq d_{\mathrm{FA}}/10\right),
\end{aligned} \tag{5.34}$$

where σ_n^2 denotes the noise power. Similarly, the CP in the NDF region, P_{NDF}^{j}, and that in the FF region, P_{FF}^{j}, can be obtained by replacing the conditions with $d_{\mathrm{FA}}/10 \leq D_{s,j} \leq d_{\mathrm{FA}}$ and $d_{\mathrm{FA}} \leq D_{s,j}$, and substituting the corresponding interference terms I_{NDF} and I_{FF}, respectively. Therefore, the overall CP of the jth user is expressed as $P_{\mathrm{cov}}^{j} = P_{\mathrm{DF}}^{j} + P_{\mathrm{NDF}}^{j} + P_{\mathrm{FF}}^{j}$. To determine whether K users can be simultaneously served by the IOS, the index j is traversed from 1 to K. In other words, the CP must be evaluated for all K users.

5.6 Computational Complexity Analysis

The proposed user capacity evaluation is based on an incremental feasibility check over the candidate user number K. For each K, the CP of all K ordered users must be evaluated. Therefore, if the search is performed from $K = 1$ up to a maximum

value $K_{\max}$, the total number of CP evaluations scales as

$$\sum_{K=1}^{K_{\max}} K = \frac{K_{\max}(K_{\max}+1)}{2} \sim \mathcal{O}(K_{\max}^2). \tag{5.35}$$

We next analyse the complexity of evaluating the CP of a single user. The dominant computational cost arises from the DF and NDF interference contributions. Specifically, these terms involve nested numerical integrations: two-dimensional integrals to compute the interference statistics, followed by an additional two-dimensional averaging over the serving user location. As a result, if each integration dimension is discretised using N points, the computational complexity scales as $\mathcal{O}(N^4)$. The NDF contribution follows the same structure and thus has the same order. In contrast, the FF interference contribution involves lower-dimensional integrations and scales as $\mathcal{O}(N^2)$, which is negligible compared to the DF/NDF terms. Therefore, the overall complexity of evaluating the CP of a single user is dominated by the DF/NDF contributions and is given by

$$\mathcal{O}(N^4). \tag{5.36}$$

Combining the above results, the total computational complexity of the proposed user-capacity evaluation is

$$\mathcal{O}(K_{\max}^2 N^4). \tag{5.37}$$

In the numerical evaluation of the CP expressions, the involved integrals are computed using a discretisation with N points per dimension. The parameter N controls the tradeoff between computational complexity and numerical accuracy. A smaller N leads to a coarser approximation with reduced computational cost, while a larger N improves accuracy at the expense of increased complexity. In this work, we adopt $N = 10$, which is found to provide a good balance between accuracy and computational efficiency, yielding stable and consistent results across all considered scenarios.

5.7 Impact of Near-Field Effects on User Capacity

Beyond evaluating coverage probability and user capacity, the preceding analysis provides the mathematical basis for deriving conditions under which near-field effects can be neglected. Monte Carlo simulation can quantify how including near-field effects changes coverage probability and user capacity for selected configurations. However, these numerical comparisons do not directly provide a general condition on the surface dimensions under which DF effects can be neglected. Here, the analytical expression for the axial degradation coefficient $\rho_{\parallel}$ enables a Taylor expansion and the derivation of approximate element-size bounds for a prescribed tolerance. These bounds explain how the relevance of DF effects depends jointly on wavelength, array dimensions, and user geometry. Their network-level interpretation subsequently uses the stated mean-field approximation. Thus, although coverage evaluation requires numerical integration, the underlying analysis yields a design condition that complements the configuration-specific comparisons obtained through simulation. As discussed previously, there are two interference degradation coefficients: $\rho_{\parallel}$ and $\rho_{\perp}$. The coefficient $\rho_{\parallel}$ quantifies the DF (axial) near-field degradation, whereas $\rho_{\perp}$ captures the lateral degradation, which is equivalently interpreted as the near-field sidelobe leakage. Since sidelobe leakage is present in the DF, NDF, and FF regions, we consider the near-field effects to be negligible when $\rho_{\parallel}$ approaches 1. Recall that $\rho_{\parallel}$ is defined in (5.23). Let $\alpha = D_{\text{eff}}/d_{\text{FA}}$ and $\beta = \sqrt{d_{\text{FA}}/(8D_{\text{eff}})}$. As discussed previously, $\rho_{\parallel} \to 1$ when $\Delta D_{\text{ax}} \to 0$, which corresponds to the regime $\alpha \gg 1$; equivalently, this implies $\beta \ll 1$. For $\beta \ll 1$, the integration variable $t \in [0, \beta]$ is also small. Therefore, we can apply a Taylor expansion of the integrands of the Fresnel integrals around $t = 0$:

$$\cos\left(\frac{\pi t^2}{2}\right) = 1 - \frac{\pi^2 t^4}{8} + \mathcal{O}(t^8), \tag{5.38}$$

$$\sin\left(\frac{\pi t^2}{2}\right) = \frac{\pi t^2}{2} - \frac{\pi^3 t^6}{48} + \mathcal{O}(t^{10}). \tag{5.39}$$

Substituting these expansions into the Fresnel integrals and integrating term by term over $[0, \beta]$, we obtain

$$C(\beta) \approx \int_0^{\beta} (1 - \frac{\pi^2 t^4}{8})\mathrm{d}t = \beta - \frac{\pi^2 \beta^5}{40} + \mathcal{O}(\beta^9), \tag{5.40}$$

$$S(\beta) \approx \int_0^{\beta} (\frac{\pi t^2}{2} - \frac{\pi^3 t^6}{48})\mathrm{d}t = \frac{\pi \beta^3}{6} - \frac{\pi^3 \beta^7}{336} + \mathcal{O}(\beta^{11}). \tag{5.41}$$

Then, $C^2(\beta)$ and $S^2(\beta)$ can be expressed as

$$C^2(\beta) \approx \beta^2 - \frac{\pi^2 \beta^6}{40} + \mathcal{O}(\beta^{10}), \tag{5.42}$$

$$S^2(\beta) \approx \frac{\pi^2 \beta^6}{36} + \mathcal{O}(\beta^{10}). \tag{5.43}$$

Next, the expression of $(C^2(\beta) + S^2(\beta))^2$ is given by

$$\begin{aligned}(C^2(\beta) + S^2(\beta))^2 &= (\beta^2 - \frac{\pi^2}{45}\beta^6 + \mathcal{O}(\beta^{10}))^2 \\ &= \beta^4 - \frac{2\pi^2}{45}\beta^8 + \mathcal{O}(\beta^{12}).\end{aligned} \tag{5.44}$$

Replace β in (5.44) with α, $\rho_{\|}$ can be approximated as

$$\begin{aligned}\rho_{\|} &\approx 1 - \frac{\pi^2}{1440}\frac{1}{\alpha^2} + \mathcal{O}(\alpha^{-3}) \\ &= 1 - \frac{\pi^2}{1440}\left(\frac{d_{\mathrm{FA}}}{D_{\mathrm{eff}}}\right)^2 + \mathcal{O}\left(\left(\frac{d_{\mathrm{FA}}}{D_{\mathrm{eff}}}\right)^3\right).\end{aligned} \tag{5.45}$$

Observing (5.45), it is noted that as long as the second term is smaller than a value, $\rho_{\|}$ approaches 1. We approximate $\rho_{\|} \approx 1$ when the following inequality is satisfied.

$$\frac{\pi^2}{1440}\left(\frac{d_{\mathrm{FA}}}{D_{\mathrm{eff}}}\right)^2 \leq \varepsilon_{\|}, \tag{5.46}$$

where ε is a threshold. Then, the upper bound for the IOS/RIS element size e_x (resp. e_y) can be written as

$$e_x \leq \frac{\sqrt{\lambda D_{\mathrm{eff}}}}{\sqrt{2}N_{\mathrm{col}}}\left(\frac{1440\varepsilon_{\|}}{\pi^2}\right)^{1/4}, \tag{5.47}$$

$$e_y \leq \frac{\sqrt{\lambda D_{\mathrm{eff}}}}{\sqrt{2}N_{\mathrm{row}}}\left(\frac{1440\varepsilon_{\|}}{\pi^2}\right)^{1/4}. \tag{5.48}$$

It is worth noting that the bounds in (5.47) and (5.48) are obtained by analysing

IOS element number	$N_{\text{row}} \times N_{\text{col}}$	Physical dimension (m^2)	$e_x = e_y$	$d_x = d_y$	NF negligible?
512	8×64	0.0375×0.3175	$\lambda/4$	$\lambda/4$	Y
512	8×64	0.075×0.635	$\lambda/2$	$\lambda/2$	N
1024	16×64	0.0775×0.3175	$\lambda/4$	$\lambda/4$	Y
1024	16×64	0.155×0.635	$\lambda/2$	$\lambda/2$	N
2048	32×64	0.1575×0.3175	$\lambda/4$	$\lambda/4$	Y
2048	32×64	0.315×0.635	$\lambda/2$	$\lambda/2$	N
4096	64×64	0.3175×0.3175	$\lambda/4$	$\lambda/4$	Y
4096	64×64	0.635×0.635	$\lambda/2$	$\lambda/2$	N

Table 5.1: Element-size threshold values for different IOS apertures under the mean-field approximation with $\lambda = 0.01$ m and $\varepsilon_{\|} = 1 \times 10^{-3}$.

$\rho_{\|}$ for a given link geometry. In particular, D_{eff} depends on the IOS–EU distance of the serving user (e.g., the jth user) and on the relative positions of the interfering users, and is therefore a link-dependent quantity. As a result, (5.47) and (5.48) formally guarantee that the DF near-field effect is negligible only for the specific link whose geometry is used in D_{eff}. However, we are interested in a network-wide condition under which near-field effects can be neglected for a "typical" IOS–EU link. To this end, we adopt a mean-field approximation that is consistent with the stochastic geometry framework used in this section. Instead of conditioning on the jth user, we model the serving EU as a typical user drawn uniformly at random from the floor, with unordered IOS–EU distance D. Likewise, the coordinates that are involved in the axial displacement ΔD_{ax} are interpreted as the coordinates of two independently and uniformly distributed users, rather than ordered users subject to distance truncation. Under this typical-user model, D_{eff} becomes a random variable $D_{\text{eff}}^{\text{mf}}$ that is no longer indexed by a certain user. We then define the expected value of $D_{\text{eff}}^{\text{mf}}$ as $\mathbb{E}[D_{\text{eff}}^{\text{mf}}]$. Substituting D_{eff} in (5.47) and (5.48) with $\mathbb{E}[D_{\text{eff}}^{\text{mf}}]$ yields an index-free, network-level element-size condition under which the DF near-field degradation remains below the prescribed threshold $\rho_{\|}$ for a typical link in the IOS-assisted indoor network. In this sense, (5.47) and (5.48), together with the mean-field approximation, provide a tractable design rule relating the IOS/RIS element size to the practical relevance of near-field effects in the considered environment.

If e_x and e_y satisfy (5.47) and (5.48) with mean-field approximation, the near-field effects are negligible, and omitting them will not cause a significant deviation in the jth user's CP or in the resulting user capacity. In contrast, if e_x and e_y do not satisfy (5.47) and (5.48) with mean-field approximation, the near-field effects must be taken into account; otherwise, their omission will lead to a substantial estimation error.

From the above discussion, it is noted that the NF effects need to be taken into consideration if (5.47) and (5.48) do not hold. By analysing the NF effects, we see

that the interference decays faster than in the FF region. Ideally, we would like to design an IOS that breaks the two inequalities, which means more users can be supported. However, considering the physical size of the indoor environment, it is not always possible to design such an IOS that breaks the two inequalities. The length and width of the IOS have to satisfy the following inequalities: $W_{\text{IOS}} = M_{\text{col}} e_y \leq \alpha W$ and $L_{\text{IOS}} = M_{\text{row}} e_x \leq \alpha L$, where W_{IOS}, L_{IOS}, M_{row}, M_{col}, and α denote the width of the IOS, the length of the IOS, the number of element per row and the number of element per column, and a coefficient representing the fraction of the length and width of the IOS relative to the indoor environment. Based on different indoor environments, the α may take different values. The new bounds for e_x and e_y can be given by

$$\frac{\sqrt{\lambda D_{\text{eff}}}}{\sqrt{2} N_{\text{col}}} \left(\frac{1440 \varepsilon_{\|}}{\pi^2} \right)^{1/4} \leq e_x \leq \frac{\alpha L}{M_{\text{row}}}, \tag{5.49}$$

$$\frac{\sqrt{\lambda D_{\text{eff}}}}{\sqrt{2} N_{\text{row}}} \left(\frac{1440 \varepsilon_{\|}}{\pi^2} \right)^{1/4} \leq e_y \leq \frac{\alpha W}{M_{\text{col}}}. \tag{5.50}$$

To offer practical design insights, we subsequently include an example table, i.e., Table 5.1, that lists whether the near-field effects can be neglected for various IOS physical dimensions. The table evaluates each physical dimension by comparing its actual element size with the threshold obtained from (5.47) and (5.48) through mean-field approximation. A "Y'' indicates that the DF near-field effect is negligible for a typical link, whereas an "N'' implies that explicit near-field modelling is still required.

5.8 Numerical Results

In this section, we evaluate the proposed analytical framework and quantify the achievable user capacity of IOS-assisted indoor mmWave networks under various propagation regimes and service requirements. We first verify the accuracy of the analysis by comparing the jth user's CP with Monte Carlo simulations. The

parameters are listed in Table 5.2. From Fig. 5.3(a), Fig. 5.3(b), and Fig. 5.3(c), we observe that the analytical results closely match the Monte Carlo simulations across a variety of parameter settings. Moreover, the performance of each user in an IOS-assisted mmWave indoor network is consistently better than that in an RIS-assisted mmWave indoor network, primarily due to the more flexible deployment options available for the IOS compared with the RIS. For comparison, a conventional reflection-only RIS is deployed at $(-L/2, 0, h_r)$, at the horizontal midpoint of the wall opposite the transmitter, with its reflecting side facing the room interior. It has the same height as the IOS, which is located at $(0, 0, h_r)$. Both surfaces are assumed lossless: the RIS has unit reflection amplitude, whereas the IOS splits the incident power equally between reflection and transmission, wit $R = T = 1/\sqrt{2}$. This power splitting does not represent absorption loss. Both configurations use the same total element count, element dimensions, and transmit power. The comparison therefore includes the effects of surface placement as well as the different reflection and transmission capabilities. It should be emphasised that the total number of users is fixed at 4 in Fig. 5.3, which is solely for validating the analytical expressions[6] and does not reflect the user capacity of the network under this parameter configuration[7]. Next, we investigate the user capacity of IOS- and RIS-assisted mmWave indoor networks, with and without near-field effects. By comparing Fig. 5.4(a) with Fig. 5.4(b), and Fig. 5.5(a) with Fig. 5.5(b) (for both the hybrid-field and far-field only regimes), we observe that the IOS-assisted network consistently outperforms the RIS-assisted network for all element numbers and transmit power levels. Although the total power intercepted by an IOS is split between the reflected

[6]The user number $K = 4$ here is set as fixed because the aim of Fig. 5.3 is to show the accuracy of the analysis compared to the Monte Carlo simulation. Not to show the user capacity in the current setting. Regarding the user capacity, numerical results are shown later.

[7]The CP threshold defines the success criterion for serving each user type. For instance, a video user is considered to be successfully served if $P(\text{SINR} \geq \tau_v) \geq 0.95$. When the CP threshold is relaxed, the service requirement becomes less stringent, and consequently, a larger number of users can be supported. Therefore, a lower CP threshold generally leads to an increase in the achievable user capacity.

Table 5.2: Parameter setting

Parameter	**Value**
L, W	50 m
IOS coordinate	(0 m, 0 m, 3 m)
BS coordinate	(25 m, 0 m, 4 m)
IOS/RIS element number	[512, 1024, 2048, 4096, 8192]
G_t, G_r	3,3
P_{tx}	[100, 500, 1000] mW
σ^2	1×10^{-9} mW
h_u	1.5 m
λ	0.01 m
e_x, e_y	$\lambda/2$, $\lambda/2$
τ_v, τ_a, τ_t	0.5, 0.2, 0.1
p_{video}, p_{audio}, p_{text}	0.1, 0.3, 0.6
d_x, d_y	$\lambda/2$, $\lambda/2$
CP threshold	0.95
Iteration time for Monte-Carlo simulation	1000

and transmitted directions, its deployment flexibility allows the IOS to be placed much closer to the users, which more than compensates for the power split. By examining the curves at each element number and transmit power level in Fig. 5.4(a) and Fig. 5.4(b), we see that the user capacities obtained under the hybrid-field model differ significantly from those under the far-field only assumption when $e_x = e_y = d_x = d_y = \lambda/2$. This agrees with the analytical results summarised in Table 5.1. In contrast, the gap between the hybrid-field and far-field only results becomes much smaller in Fig. 5.5(a) and Fig. 5.5(b), where $e_x = e_y = d_x = d_y = \lambda/4$, which again matches the conclusions drawn from Table 5.1. A key insight from Figs. 5.4(a) and 5.5(a) is that when the IOS/RIS aperture is small (as characterised by (5.47) and (5.48) under the mean-field approximation)—equivalently, when the Fresnel region is small—modelling the indoor environment using a pure far-field

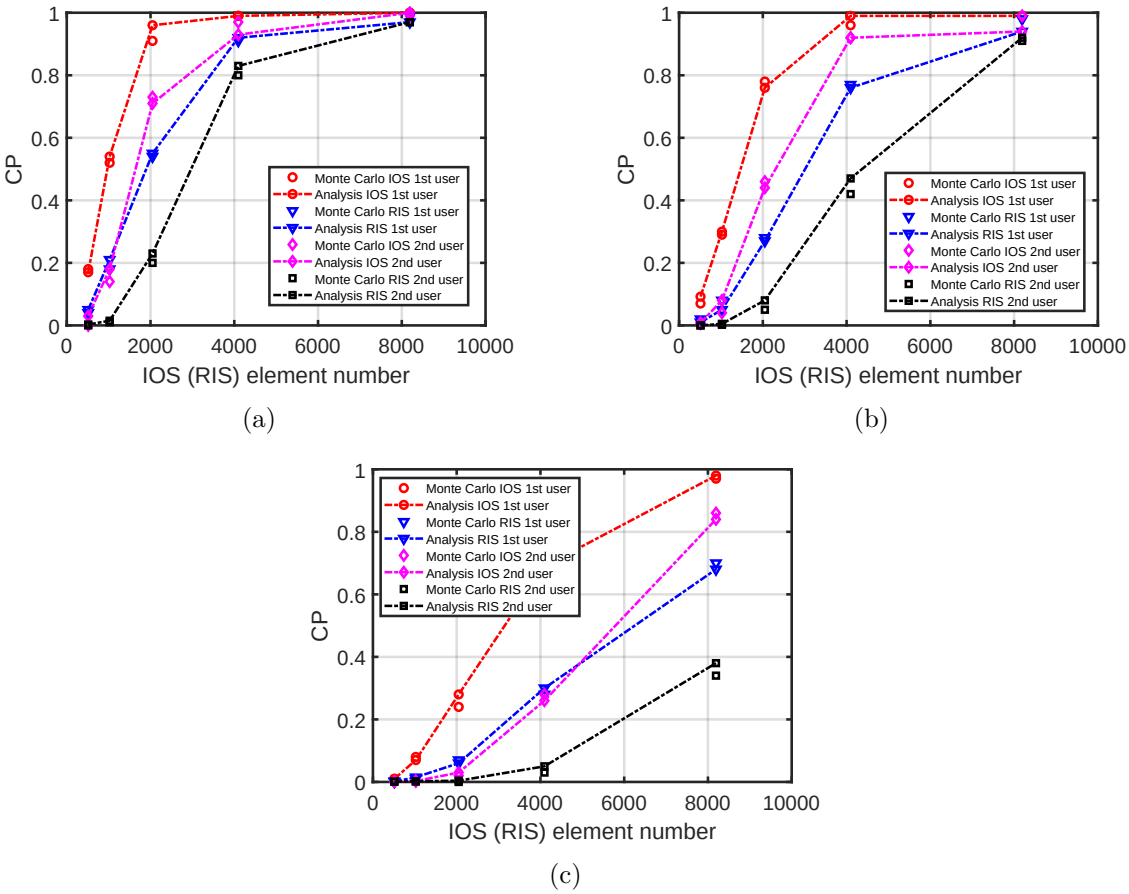

Figure 5.3: (a) Coverage probability variations of the first and second user for a total user number of 4, with transmit power being 1000 mW against the IOS/RIS element number. (b) Coverage probability variations of the first and second user for a total user number of 4, with transmit power being 500 mW against the IOS/RIS element number. (c) Coverage probability variations of the first and second user for a total user number of 4, with transmit power being 100 mW against the IOS/RIS element number.

approximation does not introduce significant errors. In contrast, when the IOS/RIS aperture becomes large, and hence the Fresnel region also expands, it is essential to explicitly account for near-field effects. Since IOS/RIS design principles typically require sub-wavelength element dimensions [1, 109], increasing the physical aperture under a fixed number of elements allows the surface to capture more energy from the BS. Therefore, the configurations in Fig. 5.4(a) and Fig. 5.4(b) (with larger effective apertures) are more representative of practical indoor deployments with a fixed element budget. In the following, we evaluate the user capacity of the IOS- and

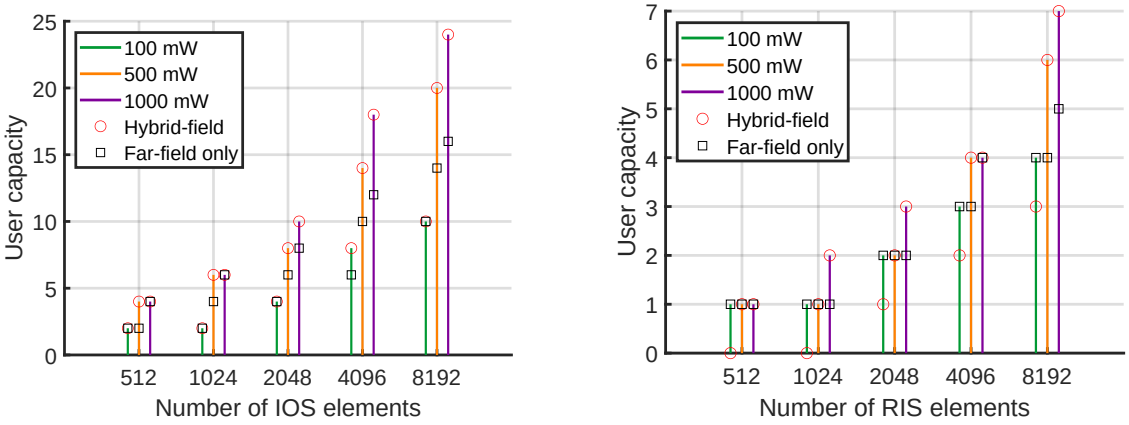

(a) (b)

Figure 5.4: User capacity of the IOS/RIS-assisted mmWave 3D indoor network with and without near-field effects, evaluated under various transmit power levels. Results are obtained for element spacings $e_x = e_y = d_x = d_y = \lambda/2$.

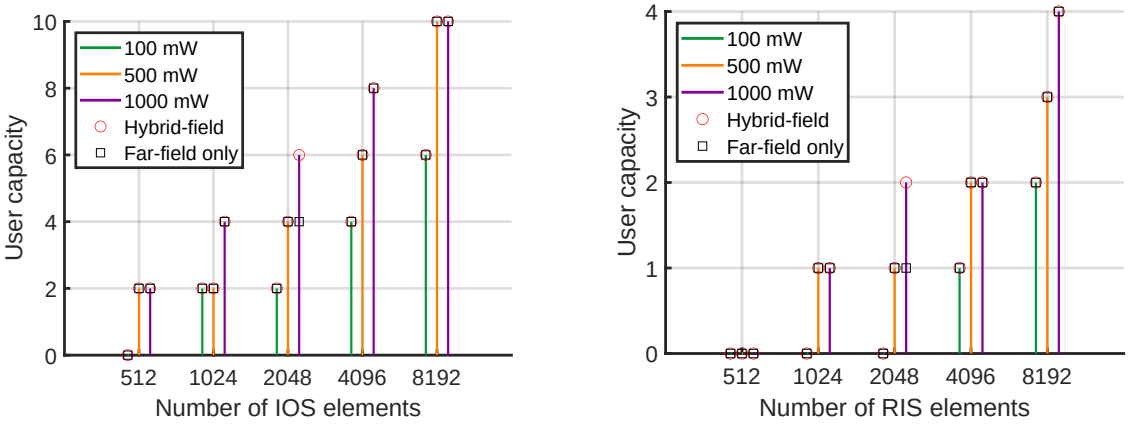

(a) (b)

Figure 5.5: User capacity of the IOS/RIS-assisted mmWave 3D indoor network with and without near-field effects, evaluated under various transmit power levels. Results are obtained for element spacings $e_x = e_y = d_x = d_y = \lambda/4$.

RIS-assisted indoor networks under different user-type distributions, i.e., different proportions of users requiring heterogeneous QoS levels. The results are shown in Figs. 5.6 and 5.7. From Fig. 5.6(a), we observe two clear regions corresponding to user capacities of 6 and 4, with boundaries at $p_{\text{video}} = 0.1$ and $p_{\text{audio}} = 0.4$. The capacity drops from 6 to 4 as soon as either $p_{\text{video}} > 0.1$ or $p_{\text{audio}} > 0.4$. The small yellow block (high-capacity region) indicates that, for most $(p_{\text{audio}}, p_{\text{video}})$ combinations under the considered parameters, the QoS mix has only a limited impact and the

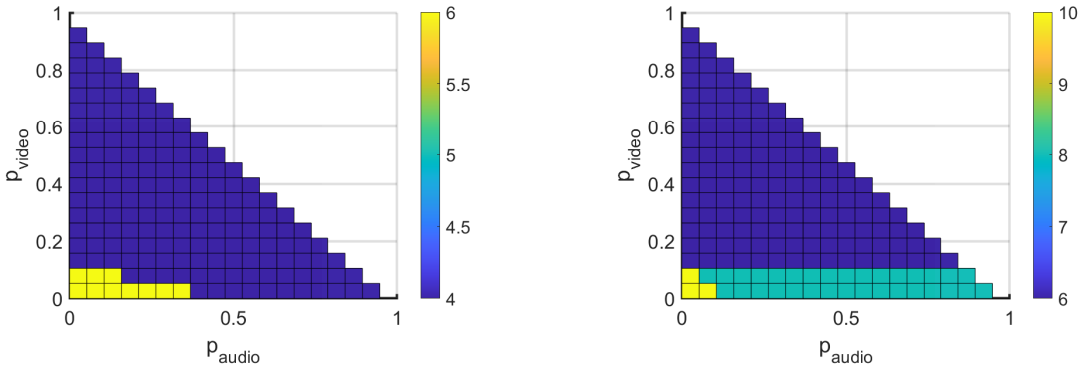

Figure 5.6: (a) User type distribution of an IOS-assisted mmWave indoor network with an element number of 2048. (b) User type distribution of an IOS-assisted mmWave indoor network with an element number of 4096.

network can support at most 4 users. In Fig. 5.6(b), we increase the IOS element number from 2048 to 4096. The corresponding thresholds move to $p_{\text{video}} = 0.1$ and $p_{\text{audio}} = 0.1$, and an additional intermediate region appears. When $p_{\text{video}} \leq 0.1$ and $p_{\text{audio}} \leq 0.1$, the network can support up to 10 users. If $p_{\text{audio}} > 0.1$ while $p_{\text{video}} \leq 0.1$, the capacity reduces to 8, and once $p_{\text{video}} > 0.1$, it further decreases to 6 regardless of p_{audio}. Thus, the proportion of high-QoS (video) users is the dominant factor determining the IOS-assisted network's capacity: once p_{video} exceeds the threshold 0.1, the detailed allocation of the remaining QoS types has little influence on the achievable capacity. Comparing Figs. 5.6(a) and 5.6(b), increasing the IOS element number significantly enhances the maximum user capacity (from 6 to 10). At the same time, because more elements provide more adjustable phase degrees of freedom, the resulting user capacity becomes more sensitive to the proportion of high-QoS users. Equivalently, with a sufficiently large IOS, limiting the fraction of video users offers substantial potential for further capacity gains. Similar qualitative behaviour is observed for the RIS-assisted network in Figs. 5.7(a) and 5.7(b). First, the overall capacity of the IOS-assisted network is consistently higher than that of the RIS-assisted network, highlighting the advantage of IOS-assisted communication in indoor scenarios. In Fig. 5.7(a), the capacity splits at $p_{\text{video}} = 0.1$

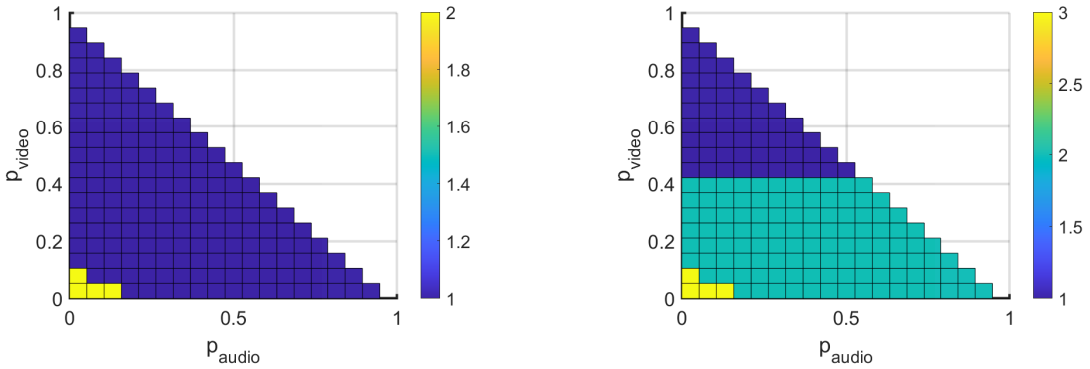

(a) (b)

Figure 5.7: (a) User type distribution of an RIS-assisted mmWave indoor network with an element number of 2048. (b) User type distribution of an RIS-assisted mmWave indoor network with an element number of 4096.

and $p_{\text{audio}} = 0.15$: the small yellow region indicates that the maximum capacity of 2 users is achievable only for a narrow range of user-type distributions, while most combinations yield a capacity of 1 user. This suggests that the RIS-assisted network has a limited adjustable range and that the user-type proportions have a relatively weak effect on improving its performance.

Comparing Figs. 5.7(a) and 5.7(b), the maximum capacity increases only from 2 to 3 users, whereas the IOS-assisted network improves from 6 to 10 users when the number of elements doubles. This contrast indicates that IOSs can exploit reflection-enhanced communication far more effectively than RISs. Moreover, in Fig. 5.7(b), the capacity regions are separated by $p_{\text{video}} = 0.1$, $p_{\text{audio}} = 0.15$, and an additional boundary at $p_{\text{video}} = 0.4$: as p_{video} grows beyond 0.4, the capacity quickly drops to 1 user. In comparison, the IOS-assisted network with 4096 elements maintains a capacity of at least 6 users even for large video fractions. Hence, the RIS-assisted network exhibits a much lower tolerance to high-QoS traffic, while the IOS-assisted network is significantly more robust to an increased proportion of video users.

5.9 Conclusion

In this chapter, we developed a stochastic-geometry framework to analyse the user capacity of IOS-assisted mmWave indoor networks, where near-field effects and heterogeneous QoS requirements are incorporated to ensure accurate and realistic user capacity evaluation. We characterised coverage and user capacity in the DF, NDF, and FF regions and compared IOS- and RIS-assisted architectures. The results show that, for all tested element numbers and transmit power levels, IOS-assisted networks support significantly more users than RIS-assisted ones, mainly because the IOS can be deployed closer to the users and thus better exploits the available power. We further showed that near-field effects must be taken into account when the IOS/RIS aperture is large (i.e., the Fresnel region is non-negligible), while a pure far-field model is accurate when the aperture is small. Finally, the simulations revealed that the fraction of high-QoS (video) users is the dominant factor limiting capacity, and that IOS-assisted networks exhibit a higher tolerance to such traffic than RIS-assisted networks. These insights provide simple design guidelines for choosing the IOS/RIS aperture and for controlling the traffic mix in practical indoor deployments.

The future work can be extended in two major directions: 1) Adaptive Subarray Partitioning: Investigating non-uniform subarray allocation optimised for heterogeneous user conditions and spatial distributions, addressing the challenge of integrating deterministic optimisation with stochastic geometry. 2) Dynamic Energy Splitting: Developing adaptive reflection and transmission protocols that respond to asymmetric user densities or traffic demands. These extensions will facilitate the transition from static analysis to more intelligent, adaptive IOS-assisted wireless networks by combining stochastic modelling with advanced optimisation techniques.

Chapter 6

Wideband RIS Systems: Coherence Bandwidth and Outage Analysis

The analyses presented in the previous chapters focused primarily on spatial performance metrics, including coverage probability and user capacity. However, future millimetre-wave and beyond systems are also expected to operate over increasingly wide bandwidths, making the frequency-domain behaviour of RIS-assisted systems an important consideration. Unlike conventional beamforming architectures, practical RISs typically employ a common phase configuration across the operating bandwidth. Consequently, the phase alignment achieved at one frequency cannot, in general, be maintained across all frequencies. This limitation motivates the concept of RIS coherence bandwidth, which characterises the frequency range over which an RIS can preserve near-coherent combining gain. In this chapter, analytical expressions for the RIS coherence bandwidth are derived, and their impact on outage performance is investigated. The resulting analysis provides insight into the bandwidth limitations of frequency-flat RIS architectures and establishes a framework for evaluating RIS-assisted wideband communication systems.

6.1 System Model

We consider downlink communication from a single antenna BS to a single-antenna user through an N-element RIS. The direct link is blocked, while the BS–RIS and RIS–user links are available. Node positions are fixed during each transmission.

The RIS is a rectangular planar array in the XY plane, with N_x N_y elements along the two axes, respectively, such that $N = N_x N_y$. The corresponding element

spacings are d_x and d_y, giving aperture dimensions $L_x = (N_x - 1)d_x$ and $L_y = (N_y - 1)d_y$. Let $d_{1,n}$ and $d_{2,n}$ denote the distances from the BS to element n and from that element to the user, respectively, and define $d_n = d_{1,n} + d_{2,n}$. The aperture-dependent coherence-bandwidth approximation assumes that both terminals are in the far field of the surface.

The transmission occupies L equally spaced subcarriers centred at f_c, with

$$f_l = f_c + \left(l - \frac{L+1}{2}\right)\Delta f, \qquad l = 1, \dots, L, \tag{6.1}$$

where Δf is the subcarrier spacing. The nominal occupied bandwidth is $B = L\Delta f$. The RIS is assumed lossless and frequency-flat, meaning that each element applies the same unit-amplitude reflection coefficient across all subcarriers:

$$\Phi = \operatorname{diag}\left(e^{j\theta_1}, \dots, e^{j\theta_N}\right). \tag{6.2}$$

Continuous phase control and ideal centre-frequency phase alignment are assumed. Under the adopted geometric phase model, $\theta_n = k_c d_n \pmod{2\pi}$, where $k_c = 2\pi f_c/c$ and c is the speed of light.

Unlike Chapters 4 and 5, this chapter introduces small-scale amplitude fluctuations to evaluate outage under random channel conditions. Large-scale attenuation is retained as the deterministic factor G_{PL}, while frequency-dependent residual phases across the RIS elements characterise the loss of coherent combining as the operating bandwidth increases.

Let $\mathbf{h}_{1,l}, \mathbf{h}_{2,l} \in \mathbb{C}^{N\times 1}$ denote the normalised BS–RIS and RIS–user channel vectors on subcarrier l. The propagation phase of the cascaded path through element n on subcarrier l is $-k(f_l)d_n$, where $k(f_l) = 2\pi f_l/c$ and $d_n = d_{1,n} + d_{2,n}$. For the outage analysis, the centre-frequency channel magnitudes are assumed independent across elements and links, with

$$|h_{1,c,n}|,\ |h_{2,c,n}| \sim \text{Rayleigh}(1/\sqrt{2}). \tag{6.3}$$

Rayleigh amplitude statistics are adopted as a tractable baseline, following their use in RIS performance analysis [110]. This assumption permits explicit calculation

of the moments required for the subsequent Gamma approximation. It is not intended to describe a dominant specular LoS component. Such a component is more appropriately represented by a Rician model, which combines deterministic LoS and random scattered contributions [111]. The outage results are therefore interpreted under the adopted Rayleigh amplitude abstraction, rather than as quantitative predictions for LoS-dominated deployments. The deterministic cascaded large-scale power gain is denoted by G_{PL} and is approximated as constant over the operating bandwidth.

With equal transmit power P per subcarrier and receiver noise power σ^2 per subcarrier, the received SNR is

$$\mathrm{SNR}_l = \frac{PG_{\mathrm{PL}}}{\sigma^2} \left| \mathbf{h}_{2,l}^T \Phi \mathbf{h}_{1,l} \right|^2 . \tag{6.4}$$

Consequently, the total transmit power is LP. The outage probability is defined as

$$P_{\mathrm{out}} = \Pr\left(\sum_{l=1}^{L} \log_2(1 + \mathrm{SNR}_l) \leq \tau \right), \tag{6.5}$$

where τ is the target threshold for the sum of the subcarrier spectral efficiencies, with units of bit/s/Hz. The corresponding rate in bits per second is $\Delta f \sum_{l=1}^{L} \log_2(1 + \mathrm{SNR}_l)$, neglecting transmission overhead.

The subsequent outage derivations use additional frequency-domain approximations. Within the RIS coherence bandwidth, the subcarrier SNRs are approximated by the centre-frequency SNR. Beyond this bandwidth, their variation is approximated using a geometry-dependent gain reduction factor. These are analytical approximations rather than consequences of the fading distribution alone.

6.2 RIS Coherence Bandwidth

Originally, coherence bandwidth is defined as the bandwidth of the frequency separation over which the channel response is highly correlated. For instance [112],

$$\frac{\mathbb{E}[h(f)h^*(f + \Delta f)]}{\mathbb{E}[|h(f)|^2]} \geq \rho_0, \tag{6.6}$$

where $h(\cdot)$ and ρ_0 denote the channel response and the correlation threshold. Based on this definition, operating bandwidth within the coherence bandwidth B_c indicates that channel variations across frequencies are confined. Empirically, coherence bandwidth is estimated by the maximum delay spread,

$$B_c \approx \frac{1}{\tau_{\max}}, \tag{6.7}$$

where $\tau_{\max}$ denotes the delay spread between the longest path and the shortest path in a multi-path environment. We now introduce the concept of the "RIS coherence bandwidth," which governs the operation bandwidth of an RIS-assisted wideband system. Assume the RIS is frequency-flat and aligns the phase of the centre frequency f_c. The cascaded channel from the BS to the user through the RIS on frequency f_l is given by

$$h(f_l) = \mathbf{h_{2,l}^T \Phi h_{1,l}} = \sum_{n=1}^{N} |h_{1,l,n}||h_{2,l,n}| e^{-jk(f_l)d_n + j\theta_n}, \tag{6.8}$$

where θ_n is the phase response of the nth element. d_n denotes the distance summation from the BS to the nth element and from the nth element to the user, i.e., $d_n = d_{1,n} + d_{2,n}$. $k(f_l)$ denotes the wavenumber at frequency f_l. As it is assumed the RIS is configured to align the phase on the centre frequency, θ_n can be reformulated as $\theta_n = k(f_c)d_n \pmod{2\pi}$. To further analyse the coherence bandwidth, we redefine d_n as

$$d_n = \bar{d} + \bar{d_n}, \tag{6.9}$$

where $\bar{d}$ serves as a common distance across the elements and $\bar{d_n}$ represents the distance variations across the elements. We use the mean of all distances, i.e.,

$$\bar{d} = \frac{1}{N} \sum_{n=1}^{N} d_n. \tag{6.10}$$

We define the maximum distance difference across elements as $\Delta d = \max_n d_n - \min_m d_m$. With Δd, the range of $\bar{d_n}$ is given by $\bar{d_n} \in [-\Delta d/2, \Delta d/2]$. Then (6.8) can be reformulated as

$$h(f_l) = e^{-j\Delta k \bar{d}} \sum_{n=1}^{N} |h_{1,l,n}||h_{2,l,n}| e^{-j\Delta k \bar{d_n}}, \tag{6.11}$$

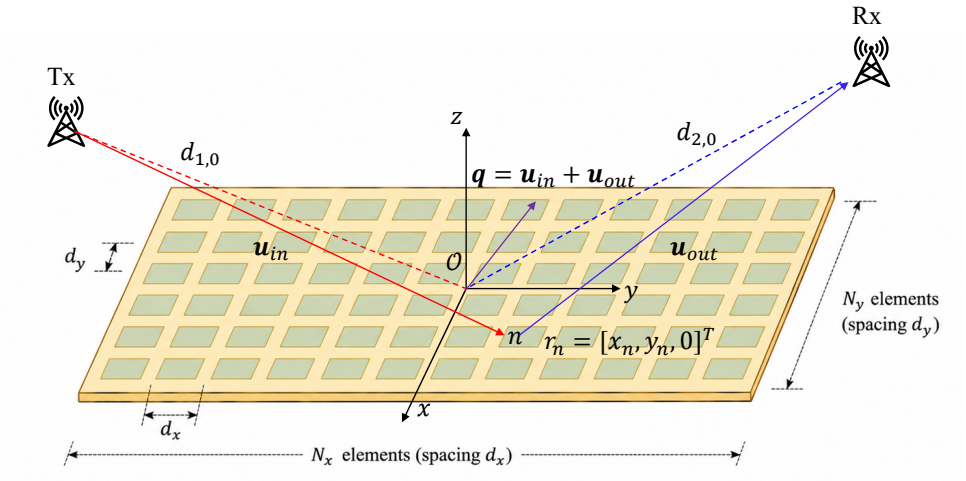

Figure 6.1: Geometry illustration of the wideband RIS system

where $\Delta k = k(f_l) - k(f_c) = 2\pi(f_l - f_c)/c$ with c denoting the speed of light. The phase differences among the terms in the summation of (6.11) determine the quality of the coherent combining. The maximum phase difference is

$$\Delta\phi_{\max} = |\Delta k|\Delta d, \tag{6.12}$$

which happens in the case $\bar{d}_n$ takes $\Delta d/2$ and $-\Delta d/2$, respectively. The quantity $\Delta\phi_{\max}$ in (6.12) characterises the worst-case phase dispersion across RIS elements at frequency f_l relative to the centre frequency f_c. To formalise the notion of coherent RIS operation, we introduce the following definition.

Definition 6.1 (RIS Coherence Bandwidth)**.** Consider a frequency-flat RIS whose phase shifts are configured to achieve coherent combining at a reference frequency f_c. For a prescribed phase-dispersion threshold $\varepsilon > 0$, the RIS coherence bandwidth, denoted by B_c^{RIS}, is defined as the largest frequency interval centred at f_c such that the maximum residual phase difference across all RIS elements satisfies

$$\Delta\phi_{\max}(f) \le \varepsilon, \qquad \forall f \in \left[f_c - \frac{B_c^{\mathrm{RIS}}}{2}, f_c + \frac{B_c^{\mathrm{RIS}}}{2}\right]. \tag{6.13}$$

Using (6.12), the condition in Definition 6.1 becomes

$$|\Delta k|\Delta d \le \varepsilon. \tag{6.14}$$

Substituting $\Delta k = 2\pi(f_l - f_c)/c$ yields

$$2|f_l - f_c| \leq \frac{\epsilon c}{\pi \Delta d}. \tag{6.15}$$

Therefore, the RIS coherence bandwidth is given by

$$B_c^{\mathrm{RIS}} = \frac{\varepsilon c}{\pi \Delta d}. \tag{6.16}$$

For operating bandwidths satisfying $B \leq B_c^{\mathrm{RIS}}$, the residual phase mismatch across RIS elements remains below ε, and near-coherent combining is preserved throughout the considered frequency range. Observing (6.16), it can be observed that the relationship between the RIS coherence bandwidth and the RIS dimensions remains implicit and hidden in Δd. We then provide a reformulation of Δd to explicitly show the relationship between the RIS coherence bandwidth and the dimension of RIS. Firstly, we assume the RIS operates in the far-field both to the BS and the user. We define the plane on which the RIS resides as the XY plane, and the normal direction of the surface as the z direction. Define the position vector of the nth element as $\mathbf{r_n} = [x_n, y_n, 0]^T$. Define the unit vector of the impinging direction as $\mathbf{u}_{\mathrm{in}}$, and the unit vector of the reflected direction as $\mathbf{u}_{\mathrm{out}}$. The geometry setup described here can be viewed in a clearer way in Fig. 6.1. Under the far-field assumption, $d_{1,n}$ and $d_{2,n}$ can be approximated as

$$d_{1,n} \approx d_{1,0} - \mathbf{r_n^T u}_{\mathrm{in}}, \tag{6.17}$$

$$d_{2,n} \approx d_{2,0} - \mathbf{r_n^T u}_{\mathrm{out}}. \tag{6.18}$$

Hence, d_n can be written as

$$d_n \approx d_0 - \mathbf{r_n^T u}_{\mathrm{in}} - \mathbf{r_n^T u}_{\mathrm{out}} = d_0 - \mathbf{r_n^T} \underbrace{(\mathbf{u}_{\mathrm{in}} + \mathbf{u}_{\mathrm{out}})}_{\mathbf{q}}. \tag{6.19}$$

Based on (6.19), Δd can be interpreted as the spread of the projection of the RIS

aperture onto the direction $\mathbf{q} = [q_x, q_y, q_z]^T$. The expression of Δd is given by

$$\begin{aligned}\Delta d &= \max_n d_n - \min_m d_m, \\ &\approx \frac{D_x}{2}|q_x| + \frac{D_y}{2}|q_y| - (-\frac{D_x}{2}|q_x| - \frac{D_y}{2}|q_y|), \\ &= D_x|q_x| + D_y|q_y|, \end{aligned} \tag{6.20}$$

where D_x and D_y denote the length and width of the RIS. (6.16) can then be reformulated as

$$B_c^{\text{RIS}} = \frac{\varepsilon c}{\pi(D_x|q_x| + D_y|q_y|)}. \tag{6.21}$$

Define the number of RIS elements along the horizontal (row) direction as N_x and along the vertical (column) direction as N_y. Let d_x and d_y denote the inter-element spacing along the row and column directions, respectively. Then, the RIS coherence bandwidth can be reformulated as

$$B_c^{\text{RIS}} = \frac{\varepsilon c}{\pi((N_x - 1)d_x|q_x| + (N_y - 1)d_y|q_y|)}. \tag{6.22}$$

It is worth noting that the derivation of the RIS coherence bandwidth is based on the assumption that the RIS phase shifts are optimised to achieve perfect phase alignment at the centre frequency. Under this assumption, the frequency-dependent performance degradation arises solely from the residual phase mismatch across RIS elements at other frequencies. Although this centre-frequency alignment does not necessarily correspond to the globally optimal phase configuration for maximising the wideband performance, it captures the dominant physical mechanism governing the loss of coherent combining, namely the phase dispersion induced by the cascaded path-length differences. As a result, the resulting expression for the RIS coherence bandwidth provides an accurate and insightful characterisation of the effective bandwidth over which the RIS can operate coherently. This observation is further supported by the numerical results, which show close agreement between the analytically derived coherence bandwidth and that obtained using the gradient-ascent numerical benchmark for the evaluated configurations.

It is worth emphasising that many existing works on wideband RIS-assisted systems adopt two commonly used assumptions, namely that the RIS is frequency-flat and that the system operates over a wide bandwidth, which inevitably leads to coherence loss across subcarriers. However, these studies are typically conducted under the far-field assumption. In this case, once the bandwidth exceeds the RIS coherence bandwidth, not only does the coherent combining degrade, but the received power also decays rapidly due to the unfavorable path-loss scaling, which is proportional to the square of the product of the link distances. In contrast, when the RIS operates in the near-field region, the path loss scales with the square of the sum of the link distances, leading to a more favorable power scaling. Therefore, although coherence loss is unavoidable in wideband scenarios, its impact on system performance can be alleviated by operating the RIS in the near-field. This suggests that near-field RIS-assisted wideband systems constitute a more relevant and practically meaningful regime, and thus deserve further investigation.

6.3 Outage Probability Analysis

6.3.1 Outage probability within the RIS coherence bandwidth

In this section, we analyse the outage probability defined in section 6.1 as a function of the number of subcarriers L, assuming that the operating bandwidth remains within the RIS coherence bandwidth. Under this condition, the channel responses across subcarriers are highly correlated and vary slowly with frequency. Consequently, the corresponding SNRs can be approximated as identical, i.e.,

$$\mathrm{SNR}_l \approx \gamma_c, \qquad l = 1, \ldots, L, \tag{6.23}$$

where γ_c denotes the SNR at the centre frequency. Therefore, the outage probability can be approximated as

$$P_{\text{out}} \approx \Pr\big(L \log_2(1+\gamma_c) \le \tau\big) = F_{\gamma_c}\big(2^{\tau/L} - 1\big)\,, \tag{6.24}$$

where $F_{\gamma_c}(\cdot)$ denotes the CDF of γ_c. Under the centre-frequency phase alignment assumption, the effective channel amplitude can be written as

$$X_c = \sum_{n=1}^{N} |h_{1,c,n}||h_{2,c,n}|, \tag{6.25}$$

where $|h_{1,c,n}|$ and $|h_{2,c,n}|$ denote the amplitudes of the BS–RIS and RIS–user channels associated with the nth RIS element, respectively. The corresponding centre frequency SNR is

$$\gamma_c = \rho_c X_c^2, \tag{6.26}$$

where

$$\rho_c = \frac{P\,G_{\text{PL}}}{\sigma^2} \tag{6.27}$$

collects all deterministic quantities, including the transmit power P, the cascaded large-scale path loss G_{PL}, and the noise power σ^2. Assuming that the magnitudes of the channel coefficients follow independent Rayleigh distributions [110], i.e.,

$$|h_{1,c,n}|,\, |h_{2,c,n}| \sim \text{Rayleigh}\left(\frac{1}{\sqrt{2}}\right),$$

we define

$$Z_n = |h_{1,c,n}||h_{2,c,n}|, \tag{6.28}$$

such that

$$X_c = \sum_{n=1}^{N} Z_n. \tag{6.29}$$

Since the exact distribution of X_c is difficult to obtain in closed form, we employ a moment-matching approach and approximate X_c by a Gamma random variable

$$\tilde{X}_c \sim \Gamma(\xi, \zeta), \tag{6.30}$$

where ξ and ζ denote the shape and scale parameters, respectively. Let

$$m_1 = \mathbb{E}[Z_n], \qquad m_2 = \mathbb{E}[Z_n^2]. \tag{6.31}$$

Since $\{Z_n\}$ are independent and identically distributed,

$$\mathbb{E}[X_c] = Nm_1, \tag{6.32}$$

and

$$\mathrm{Var}(X_c) = N(m_2 - m_1^2). \tag{6.33}$$

Applying moment matching yields

$$\xi = \frac{\left(\mathbb{E}[X_c]\right)^2}{\mathrm{Var}(X_c)} = \frac{Nm_1^2}{m_2 - m_1^2},\ \zeta = \frac{\mathrm{Var}(X_c)}{\mathbb{E}[X_c]} = \frac{m_2 - m_1^2}{m_1}. \tag{6.34}$$

Using $\gamma_c = \rho_c X_c^2$, the outage probability can be approximated as

$$P_{\text{out}} = \Pr\left(X_c \leq \sqrt{\frac{2^{\tau/L}-1}{\rho_c}}\right) \approx \frac{1}{\Gamma(\xi)}\gamma\left(\xi, \frac{1}{\zeta}\sqrt{\frac{2^{\tau/L}-1}{\rho_c}}\right),$$

where $\Gamma(\cdot)$ and $\gamma(\cdot,\cdot)$ denote the Gamma function and the lower incomplete Gamma function, respectively.

6.3.2 Outage probability outside the RIS coherence bandwidth

When the operating bandwidth exceeds the RIS coherence bandwidth B_c^{RIS}, the approximation in (6.23) is no longer valid, since the residual phase dispersion across RIS elements becomes significant. Consequently, the coherent combining gain varies across subcarriers, and the corresponding SNRs can no longer be approximated by a common value. In addition, obtaining the exact statistical distribution of the SNR on each subcarrier becomes analytically challenging. To quantify the degradation caused by frequency-dependent coherence loss, we introduce the RIS gain reduction factor

$$\eta_l = \frac{\left|\sum_{n=1}^{N} e^{-j\Delta k_l d_n}\right|^2}{N^2}, \tag{6.35}$$

where $\Delta k_l = 2\pi(f_l - f_c)/c$. The coefficient η_l represents the fraction of coherent RIS gain preserved at the lth subcarrier. By definition, $0 \leq \eta_l \leq 1$, where $\eta_l = 1$

corresponds to perfect coherent combining, while smaller values indicate increasing coherence loss. Using η_l, the SNR at the lth subcarrier can be approximated as

$$\mathrm{SNR}_l \approx \eta_l \gamma_c, \tag{6.36}$$

where γ_c denotes the centre frequency SNR. Accordingly, the outage probability can be expressed as

$$P_{\text{out}} = \Pr\left(\sum_{l=1}^{L} \log_2\left(1+\eta_l\gamma_c\right) \leq \tau\right). \tag{6.37}$$

Define

$$g(\gamma_c) = \sum_{l=1}^{L} \log_2\left(1+\eta_l\gamma_c\right). \tag{6.38}$$

Since $g(\gamma_c)$ is monotonically increasing with respect to γ_c, the outage probability can be rewritten as

$$P_{\text{out}} = F_{\gamma_c}(g^{-1}(\tau)), \tag{6.39}$$

where $F_{\gamma_c}(\cdot)$ denotes the cumulative distribution function of γ_c, and $g^{-1}(\cdot)$ is the inverse function of $g(\cdot)$, which can be evaluated numerically. The impact of the subcarrier number L on the outage probability is closely related to the RIS coherence bandwidth. When the operating bandwidth remains within B_c^{RIS}, the channel responses vary slowly across frequency, and the SNR values across subcarriers can be approximated as identical. Under this condition, increasing the number of subcarriers provides additional spectral efficiency contributions while preserving coherent combining across the entire occupied bandwidth. Consequently, the outage probability decreases as L increases. When the operating bandwidth exceeds B_c^{RIS}, coherent combining can no longer be maintained across all subcarriers. In this regime, the RIS gain on the lth subcarrier is reduced by the factor η_l, which generally decreases with increasing frequency offset from the centre frequency. Although additional subcarriers still contribute to the sum spectral efficiency, their contributions become progressively smaller due to the increasing coherence loss. As a result, the outage probability may continue to decrease with increasing L, but the rate of improvement becomes smaller and smaller. In the limit, when the additional subcarriers provide

negligible RIS gain, the outage performance approaches a saturation point, beyond which further increasing L yields little benefit.

Table 6.1: Parameter setting

Parameter	**Value**
L	100
f_c	10 GHz
element spacing	$\lambda_c/2$
incident angle (azimuth and elevation)	30°, 40°
reflection angle (azimuth and elevation)	20°, 60°
Scanning frequency range	$2B_c^{\mathrm{RIS}}$
iteration number (numerical optimisation)	1000
update step	0.05
restart time	10

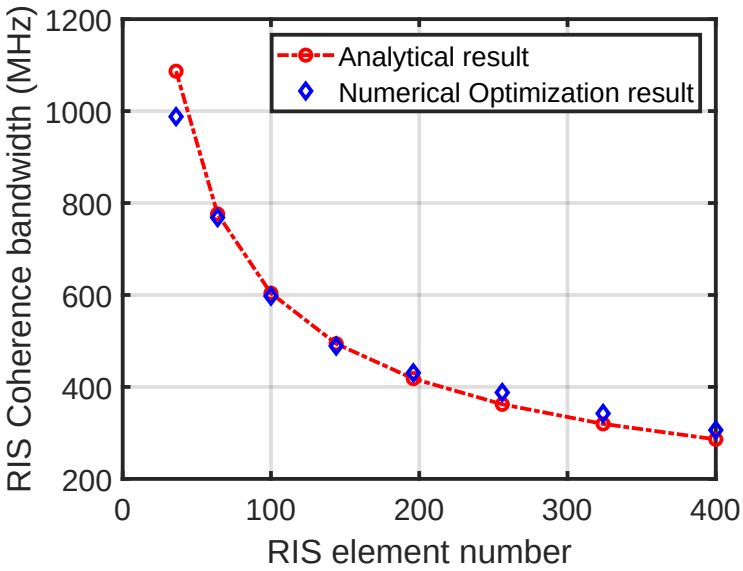

Figure 6.2: RIS coherence bandwidth comparison between the analytical result and the numerical optimisation result. The analytical result is evaluated using the phase-dispersion threshold $\varepsilon = 1$ rad.

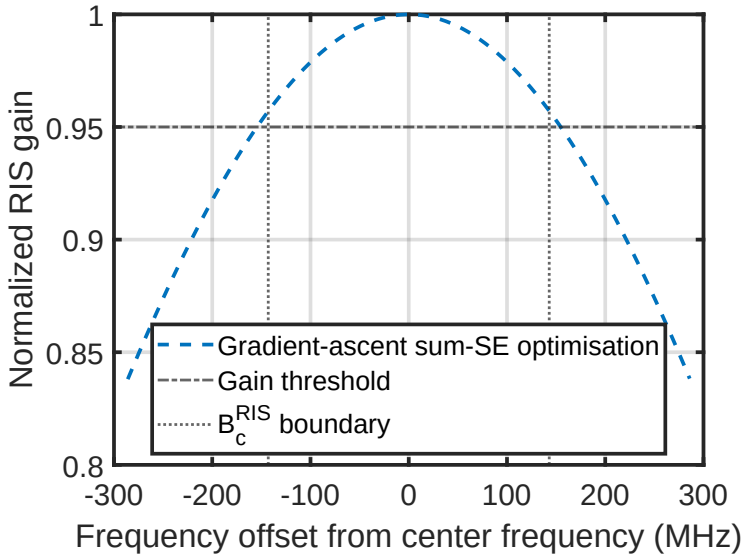

Figure 6.3: Normalised RIS gain against the frequency offset relative to the centre frequency with 400 RIS elements.

6.4 Numerical Results

We first compare the coherence bandwidth obtained under centre-frequency phase alignment with that obtained using a phase configuration numerically optimised across all considered subcarriers. Before discussing Fig. 6.2, we first clarify what is meant by the numerical optimisation benchmark. As stated in the previous sections, the analytical derivations are based on the assumption that the RIS phase shifts are aligned with the centre frequency. This is a critical assumption, since it enables tractable expressions for both the RIS coherence bandwidth and the outage probability. Centre-frequency phase alignment is an analytical simplification: a phase configuration optimised jointly across multiple subcarriers need not maximise the gain at the centre frequency. This simplification enables tractable expressions for the RIS coherence bandwidth and outage probability. To assess its accuracy, we compare its predictions with a numerical benchmark that optimises a common phase configuration across the considered subcarriers. A gradient-ascent benchmark is used to optimise a single RIS phase vector shared by all considered subcarriers.

The objective is the sum spectral efficiency

$$J(\theta) = \sum_{l=1}^{L} \log_2 \left(1 + \mathrm{SNR}_l(\theta)\right), \tag{6.40}$$

where $\theta = [\theta_1, \ldots, \theta_N]^T$. At iteration t, the phase vector is updated as

$$\theta^{(t+1)} = \left[\theta^{(t)} + \mu \nabla_\theta J(\theta^{(t)})\right] \bmod 2\pi, \tag{6.41}$$

where $\mu = 0.05$. Each optimisation run uses 1000 iterations, and the procedure is repeated over 10 restarts. For each restart, the initial phase angles are drawn independently from $\mathcal{U}(0, 2\pi)$. After completing the prescribed iterations for all 10 restarts, the phase configuration with the largest sum spectral efficiency in (6.40) is retained. The resulting frequency-flat phase profile is then used to evaluate the normalised RIS gain across frequency and determine the interval around f_c satisfying the 0.95 gain threshold. Since the objective is non-convex, gradient ascent does not guarantee a globally optimal solution; the result is therefore used as a numerical benchmark. For the numerical evaluation, we use a normalised RIS power-gain threshold of 0.95, corresponding to a maximum 5% reduction from fully coherent combining, as illustrated in Fig. 6.3. This gain criterion can be related to the phase-dispersion threshold in Definition 6.1. For the centre-frequency-aligned, equal-weight RIS model, a maximum phase spread $\varepsilon \leq \pi$ places all element phases within $[-\varepsilon/2, \varepsilon/2]$ after a common phase rotation. Hence,

$$\eta(f) \geq \cos^2(\varepsilon/2). \tag{6.42}$$

Choosing $\varepsilon = 2 \arccos \sqrt{0.95} \approx 0.451$ rad therefore guarantees a normalised gain of at least 0.95. The corresponding simulation parameters are summarised in Table 6.1.

In Fig. 6.2, it can be observed that the analytically derived RIS coherence bandwidth agrees closely with the numerical optimisation benchmark, which indicates that the proposed analytical expression provides a tight approximation to the actual RIS coherence bandwidth. In addition, it is seen that the RIS coherence bandwidth

decreases as the number of RIS elements increases. This trend is also consistent with the result shown in (6.21). One may also note that the scale of the vertical axis in Fig. 6.2 is quite large. It is important to make sure that the proposed RIS coherence bandwidth should not be confused with the conventional channel coherence bandwidth. Unlike the latter, which is determined by the multipath delay spread of the propagation environment, the RIS coherence bandwidth is a geometry-induced quantity determined by the maximum path-length difference across the RIS aperture. Consequently, the RIS coherence bandwidth can be substantially larger than the conventional channel coherence bandwidth and may reach the order of hundreds of MHz or even several GHz for practical RIS dimensions.

We then numerically show the relationship between the outage probability and the subcarrier number L. Before discussing Fig. 6.4, we briefly introduce the process of Monte Carlo simulation. In each Monte Carlo realisation, correlated frequency-domain fading channels are generated across subcarriers to capture the frequency correlation introduced by the finite RIS coherence bandwidth. Specifically, the BS-RIS and RIS-user channels are modelled as correlated Rayleigh fading channels across frequency, where the frequency correlation follows an exponential correlation model [113]. Based on the generated channel realisations, the cascaded RIS-assisted channel at each subcarrier is constructed, and the corresponding subcarrier SNRs are obtained. The sum spectral efficiency is then evaluated by summing the spectral efficiencies across all considered subcarriers, and the outage probability is estimated as the fraction of channel realisations for which the sum spectral efficiency falls below the target threshold. Observing Fig. 6.4, it can be seen that the analysis matches the Monte Carlo simulation very well at different SE thresholds. Furthermore, it is noted that with the increase in the subcarrier number, the outage probability also decreases. However, the decrease rate of the outage probability decreases with the increase of the SE thresholds.

Observing Fig. 6.5, where the vertical dashed line indicates the boundary of the

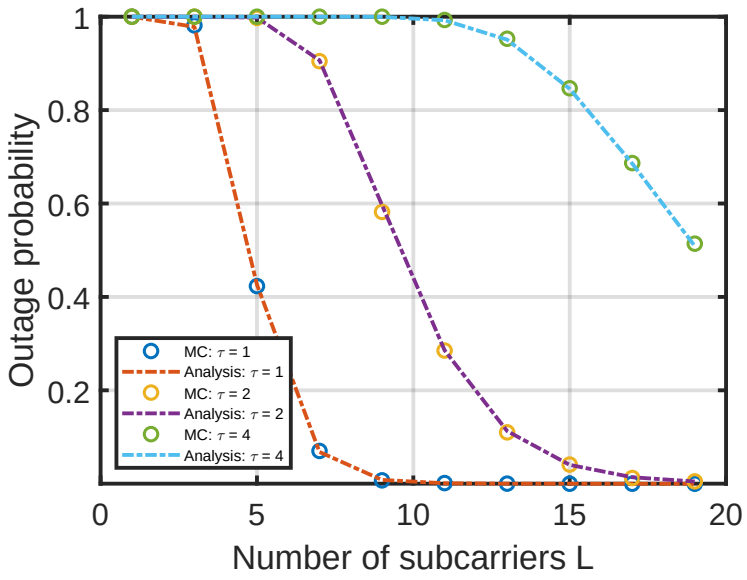

Figure 6.4: Comparison of the outage probability against subcarrier number L within RIS coherence bandwidth with RIS element number of 36, $f_c = 10$ GHz, $B_c^{\text{RIS}} = 543.34$ MHz, and $\Delta f = 100$ KHz.

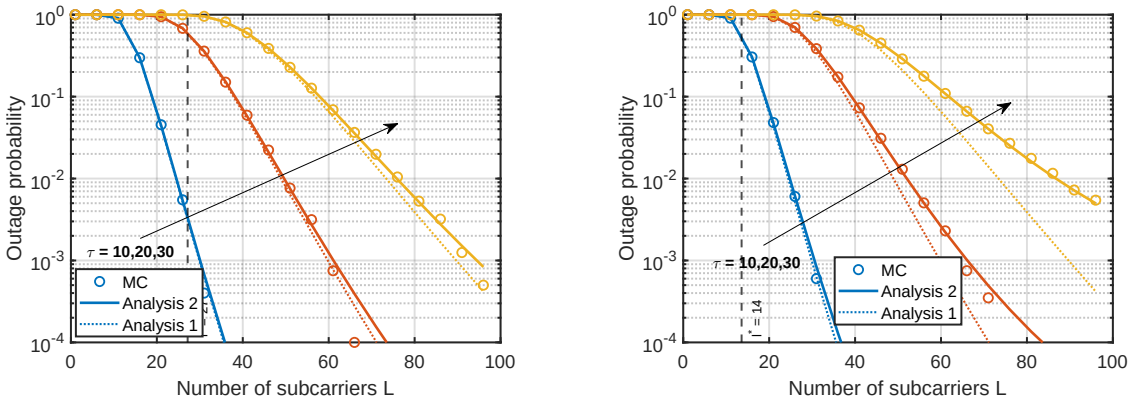

Figure 6.5: Outage probability versus subcarrier number for $N = 36$, $f_c = 10$ GHz, and subcarrier spacings of (a) 20 MHz and (b) 40 MHz. Analysis 1 uses the approximation $\text{SNR}_l \approx \gamma_c$ for all subcarriers, neglecting frequency-dependent combining loss. Analysis 2 uses $\text{SNR}_l \approx \eta_l \gamma_c$, accounting for this loss through the gain reduction factor η_l. The vertical dashed line marks the subcarrier number at which the occupied bandwidth reaches the RIS coherence bandwidth.

RIS coherence bandwidth, it can be seen that the outage analysis developed under the assumption $B \leq B_c^{\text{RIS}}$ (Analysis 1) deviates from the Monte Carlo simulation once the operating bandwidth exceeds B_c^{RIS}. This confirms that the approximation underlying Analysis 1 is no longer valid in the regime $B > B_c^{\text{RIS}}$. In contrast, Analysis

2, which explicitly accounts for the RIS gain degradation through the coefficient η_l, exhibits excellent agreement with the Monte Carlo results over the entire range $B \geq B_c^{\mathrm{RIS}}$. Furthermore, it is observed that the outage probability continues to decrease as the number of subcarriers increases; however, the rate of improvement becomes progressively smaller. This behaviour can be clearly observed in Fig. 6.5(b) for the case $\tau = 30$ bps/Hz. The underlying reason is that subcarriers located farther from the centre frequency experience increasing coherence loss, resulting in a reduced RIS gain. Consequently, although additional subcarriers still contribute to the sum spectral efficiency, their marginal contribution diminishes with increasing frequency offset, leading to a slower reduction in outage probability.

6.5 Conclusion

In this chapter, we derived an analytical expression for the RIS coherence bandwidth in wideband RIS-assisted communication systems. In addition, the relationship between the outage probability and the number of subcarriers L was investigated. It was shown that the proposed analytical expression provides a tight approximation of the true RIS coherence bandwidth. Furthermore, within the RIS coherence bandwidth, the outage probability decreases with increasing subcarrier number L, while the rate of decrease becomes slower for higher SE thresholds. When the operating bandwidth exceeds the RIS coherence bandwidth, additional subcarriers continue to reduce the outage probability under the considered settings, but with diminishing marginal benefit. This occurs because subcarriers farther from the centre frequency experience frequency-dependent phase mismatch and reduced coherent combining gain. Accounting for this loss through η_l provides a more accurate outage approximation than assuming identical SNRs across all subcarriers.

Chapter 7

Joint Beamforming with Extremely Large Scale RIS: A Sequential Multi-Agent Advantage Actor Critic Approach

7.1 Introduction

In the previous chapters, the performance of RIS-assisted wireless communication systems has been systematically analysed from a system-level perspective. In particular, Chapter 4 investigated the coverage performance of RIS-assisted indoor mmWave networks under realistic propagation conditions, while Chapter 5 introduced the concept of user capacity to characterise the maximum number of users that can be simultaneously supported under QoS constraints. These analyses provide fundamental insights into the capabilities and limitations of IOS/RIS-assisted systems, revealing how factors such as propagation environments, user distributions, and interference conditions influence overall network performance.

While such analytical frameworks are essential for understanding system behaviour, they do not directly provide a mechanism to achieve the desired performance in practice. In particular, the performance of RIS-assisted systems critically depends on the joint configuration of the BS precoding matrix and the RIS phase shifts. As reviewed in Chapter 2, existing optimisation- and learning-based approaches leave challenges in jointly configuring large RISs under discrete phase constraints, channel

correlation, and imperfect CSI. These challenges motivate the sequential multi-agent A2C framework developed in this chapter.

It is worth noting that, based on existing RIS prototypes [80, 1] and path loss models for RIS-assisted systems [38], a practical RIS deployment typically requires on the order of 1000 elements. However, most existing studies focus on relatively small RISs [75, 76, 78, 79], leaving the scalability of their approaches to large-scale RISs largely unexplored. Moreover, channel correlation and imperfect CSI are seldom considered, despite their importance in realistic indoor scenarios with spatially clustered users.

Motivated by the aforementioned challenges, we adopt a learning-based approach and propose a sequential A2C framework to solve the joint beamforming for sum spectral efficiency (SE) maximisation. The proposed method explicitly accounts for practical constraints, including discrete RIS phase shifts, inter-user channel correlation, and imperfect CSI. Moreover, to handle the extremely large action space induced by large-scale RISs, the RIS is partitioned into multiple sub-arrays, each controlled by an individual agent, and a sequential training strategy is employed to improve learning stability.

Through this framework, this chapter complements the analytical results presented in the previous chapters by providing a scalable and practical solution for enhancing system performance. In particular, while the earlier chapters characterise what performance can be achieved under given conditions, this chapter focuses on how such performance can be approached through the joint beamforming design.

7.2 System Model and Problem Statement

We consider an indoor RIS-assisted multi-user multiple-input-single-output (MU-MISO) wireless communication system, where the BS is equipped with N_T antennas, the RIS has N_R elements, and there are K users located in a square room of size a^2. To emphasise the role of the RIS, it is assumed that the LOS path is blocked, such

that the indirect BS–RIS–user link is the only viable communication path. To account for different spatial user patterns, two types of user distributions are considered. In the first case, users are uniformly distributed within the room, representing a baseline scenario with spatially independent user locations. In the second case, clustered user distributions are considered to better reflect realistic indoor environments, where users tend to gather around specific areas such as desks, kiosks, or meeting spaces. Specifically, users are uniformly distributed within a circle of radius R_c, forming spatial clusters. We assume that the cascaded BS–RIS–user channel can be estimated, and that the estimates may be subject to errors. Considering that the RIS element length, width, and element spacing are smaller than the sub-wavelength [1], the near-field region typically occupies only a small portion of the overall indoor environment. For example, the Rayleigh distance ranges from approximately 0.5 m to 2 m when the element width, length, and spacing are set to $\lambda/4$, with wavelengths of 10 mm, 6 mm, and 5 mm corresponding to RIS sizes from 900 to 1600 elements. Consequently, the far-field assumption provides an accurate and reasonable approximation in the considered scenarios. Additionally, joint beamforming is carried out based on the estimated CSI, with the objective of maximising the sum SE. The SINR is used for the sum SE calculation. The sum SE is defined as

$$\mathrm{SE} = \sum\nolimits_{k=1}^{K} \log_2(1 + \mathrm{SINR}_k), \tag{7.1}$$

where SINR_k is the SINR of the kth user, and it is defined as

$$\mathrm{SINR}_k = \frac{\|h_{2,k}^T \Phi H_1 w_k\|^2}{\sum_{j=1, j\neq k}^{K} \|h_{2,k}^T \Phi H_1 w_j\|^2 + \sigma^2}, \tag{7.2}$$

where $h_{2,k} \in \mathbb{C}^{N_R \times 1}$ is the channel between the RIS and the kth user, $\Phi \in \mathbb{C}^{N_R \times N_R}$ is the diagonal matrix of the RIS phase response, $H_1 \in \mathbb{C}^{N_R \times N_T}$ is the channel between the BS and the RIS, $w_k \in \mathbb{C}^{N_T \times 1}$ is the precoding vector for the kth user, and σ^2 is the noise power. $H_1 = \sqrt{R_1} H_1^{\mathrm{uncorr}}$, where $R_1 \in \mathbb{R}^{N_R \times N_R}$ is the matrix that captures the correlation between elements on the RIS. The i, jth entry of R_1 is given by $R_{1,i,j} = \rho^{|m_x - n_x|} \rho^{|m_y - n_y|}$. ρ is the correlation coefficient, (m_x, m_y) and (n_x, n_y) are

the coordinates of the ith and jth RIS elements [113]. The amplitude of each entry in H_1^{uncorr} is modelled as an i.i.d. Rayleigh random variable. Correlated Rayleigh fading is adopted as a statistical baseline for evaluating the joint beamforming algorithm. It provides normalised random channel coefficients, while the correlation matrices allow spatial dependence to be specified explicitly. This enables comparisons across RIS sizes, phase resolutions, correlation conditions, and CSI errors within a common channel-generation framework. The choice is an evaluation abstraction rather than a physical justification for LoS propagation. In particular, spatial correlation does not represent a deterministic LoS component, for which a Rician model would be more appropriate [111]. Since that component can affect channel rank and multi-user separability, the reported performance gains are conditional on the adopted channel model. The RIS phase-response matrix is $\Phi = \text{diag}(e^{j\theta_1}, \dots, e^{j\theta_{N_R}})$, where each phase angle satisfies

$$\theta_i \in \mathcal{F}_M = \left\{ \frac{2\pi m}{2^M} : m = 0, \dots, 2^M - 1 \right\}, \qquad i = 1, \dots, N_R. \tag{7.3}$$

Here, M denotes the phase-control resolution in bits, and unit reflection amplitude is assumed. We define W as the precoding matrix, where the kth column corresponds to the precoding vector of the kth user. We define H_2 as the RIS-user channel matrix, where the kth column corresponds to the kth RIS-user channel. We define H_2^{uncorr} as the RIS-user channel matrix without channel correlation. Each entry in H_2^{uncorr} is modelled as an i.i.d. complex normal distribution. The relationship between H_2 and H_2^{uncorr} is given as $H_2 = H_2^{\text{uncorr}} R_2^{1/2}$, where $H_2^{\text{uncorr}} \in \mathbb{C}^{N_R \times K}$, $R_2 \in \mathbb{R}^{K \times K}$ is the user-correlation matrix, and $R_2^{1/2}$ denotes its symmetric positive-semidefinite matrix square root. Assuming the communications are in the far field, the angle separation between users is the dominant factor for the channel correlation. Given the locations of users, RIS, and BS, the i, jth entry of R_2 is defined as $R_{2,i,j} = \exp(-\theta_{i,j}^2/\beta)$ where $\theta_{i,j}$ represents the angle between the ith user and the jth user, and β is a constant [113]. Next, we describe the modelling of channel estimation error. We define the estimated BS-RIS channel and RIS-user channel as $\tilde{H}_1$ and $\tilde{H}_2$. They

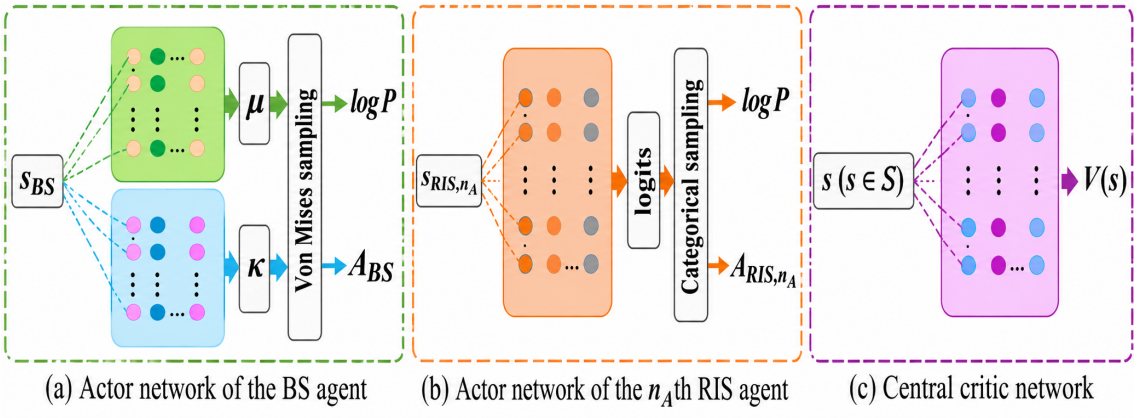

Figure 7.1: (a)-(b) The actor network structure of the BS agent and an RIS agent. (c) Central critic network structure.

are given by $\tilde{H}_1 = H_1 + \Delta H_1$ and $\tilde{H}_2 = H_2 + \Delta H_2$, where ΔH_1 and ΔH_2 are the estimation errors for the BS-RIS channel and RIS-user channel. It is assumed that both ΔH_1 and ΔH_2 are modelled as zero-mean complex Gaussian random matrices, i.e., $\Delta H_1 \sim \mathcal{CN}(0, \Sigma_{H_1})$, $\Delta H_2 \sim \mathcal{CN}(0, \Sigma_{H_2})$, [114]. It is assumed that $\tilde{H}_1$ and $\tilde{H}_2$ are available at the BS beamforming design. This assumption is consistent with the conventional optimisation-based beamforming algorithms [75, 76, 115, 116]. With the channel estimation error, (7.2) can be reformulated as

$$\mathrm{SINR}_k = \frac{\|\tilde{h}_{2,k}^T \Phi \tilde{H}_1 w_k\|^2}{\sum_{j=1, j\neq k}^{K} \|\tilde{h}_{2,k}^T \Phi \tilde{H}_1 w_j\|^2 + \sigma^2}. \tag{7.4}$$

The goal is to select the beamforming vectors and RIS phases such that the sum SE is maximised. Hence, the optimisation problem can be formulated as

$$\max_{\Phi, W} \quad \sum_{k=1}^{K} \log_2(1 + \mathrm{SINR}_k) \tag{7.5}$$

$$\text{s.t.} \quad \|W\|_F^2 \leq P_{\text{tx}}, \tag{7.6}$$

$$\Phi_{ii} \in \left\{ e^{j2\pi m/2^M} \,\middle|\, m = 0, \ldots, 2^M - 1 \right\}, \quad i = 1, \ldots, N_R. \tag{7.7}$$

In the next section, we propose to use a sequential multi-agent A2C algorithm to solve (7.5).

7.3 Sequential Multi-Agent A2C Algorithm

7.3.1 Algorithm Structure

Algorithm 2: Sequential Multi-agent A2C

Input : s, σ^2, $\tilde{H}_1$, $\tilde{H}_2$, N_A, N_R, N_T, K, $\mathcal{R}$

Initialise $\mathcal{R} = 0$;
for $i \leftarrow 1$ **to** Max episode **do**
  Calculate the active agent index using i and N_A;
  Reset $\mathcal{R}$ to 0;
  for $j \leftarrow 1$ **to** Max timesteps **do**
    Extract s^{RIS,n_A} from s and predict the action for the activated sub-array through the RIS actor network;
    Extract s^{BS} from s and predict the BS precoding matrix phase and amplitude using two parallel BS actor networks;
    Use s to predict the state value through the central critic network;
    Combine the actions predicted from the activated RIS actor network and the BS actor network, and transit to the next state;
    Update $\mathcal{R}$;
  Update the activated RIS actor network and the BS actor network through the advantage function and the logarithmic probabilities;
  Update the central critic network through the Huber loss;

The discrete nature of (7.5) makes gradient-based optimisation inapplicable. To address this challenge, we adopt a deep reinforcement learning (DRL) framework based on a multi-agent A2C architecture. We define the state space $\mathcal{S}$ as the joint configuration of the RIS phase shifts and the BS precoding matrix, while the action space $\mathcal{A}$ corresponds to adjusting these configurations. The reward function $\mathcal{R}$ is defined as the instantaneous sum spectral efficiency given in (7.1). At the beginning of training, both the RIS phase configuration and the BS precoder are randomly initialised, and actions are subsequently generated according to the current policy. Due to the extremely large size of the state and action spaces, the RIS is partitioned into N_A sub-arrays, and a separate agent is assigned to each sub-array to learn its local phase configuration. In addition, two agents are employed to learn the BS precoding matrix phases and amplitudes. The resulting architecture follows a centralised-training and decentralised execution (CTDE) paradigm, in which all agents share a central critic during training, while decisions are executed

independently at deployment. To improve training stability under discrete RIS phase constraints, we adopt an A2C-based sequential learning strategy, where only one RIS agent is activated and updated per episode, while the remaining sub-arrays remain fixed [117]. This sequential update mechanism mitigates instability caused by strong coupling among RIS sub-arrays. The overall network architecture consists of a BS actor, multiple RIS actors, and a shared central critic, as illustrated in Fig. 7.1. The BS actor learns the precoding phases and amplitudes, while each RIS actor learns the phase configuration of its associated sub-array. The BS precoding matrix is learned using two parallel actor networks: one dedicated to phase prediction and the other dedicated to amplitude prediction. This separation is adopted because phase and amplitude lie in different domains and exhibit distinct learning characteristics. By decoupling the two, the proposed framework avoids unnecessary coupling in the action space and improves training stability. The central critic evaluates the global state and provides value estimates that enable coordination among agents.

After introducing the actor and central critic network structures, we then move forward to describe the flow of the proposed algorithm, which is given in Algorithm 2. The activated RIS agent index is defined as: active RIS agent index $= i \bmod N_A$. The loss functions for the activated RIS actor network and the BS actor network are given by

$$\mathcal{L}_{\mathrm{RIS},n_A} = -\sum_{j=1}^{N_1} \log\Big(P\Big(A_j^{\mathrm{RIS},n_A} \,\Big|\, s_j^{\mathrm{RIS},n_A}\Big)\Big)\left(\mathcal{R}_j - V(s_j)\right), \tag{7.8}$$

$$\mathcal{L}_{\mathrm{BS}} = -\sum_{j=1}^{N_1} \log\Big(P\Big(A_j^{\mathrm{BS}} \,\Big|\, s_j^{\mathrm{BS}}\Big)\Big)\left(\mathcal{R}_j - V(s_j)\right). \tag{7.9}$$

where N_1 denotes the number of max timesteps. In (7.8) and (7.9), bootstrapping is disabled in the advantage function (e.g., the term $\gamma V(s_{j+1})$ is not involved) to reduce the bias and improve the learning stability. The loss function for the central

critic is defined as

$$\mathcal{L}_{\text{central critic}}=\begin{cases}\sum_{j=1}^{N_1}\frac{1}{2}(R_j-V(s_j))^2 & \text{if } |R_j-V(s_j)|<1\\ \sum_{j=1}^{N_1}\left(|R_j-V(s_j)|-\frac{1}{2}\right) & \text{otherwise.}\end{cases} \tag{7.10}$$

We move forward to analyse the computational complexity of the proposed algorithm and compare it with the benchmark.

7.3.2 Implementation Details

The actor and critic networks are implemented as fully connected multilayer perceptrons (MLPs). Each network consists of one input layer, one hidden layer, and one output layer. For both the actor and critic networks, the hidden-layer dimension is set to twice the dimension of the corresponding input layer, which provides a good balance between representation capability and training stability. ReLU activation is applied to all hidden layers. For the RIS actor network, the output layer produces unnormalised logits corresponding to the discrete phase indices of each RIS element within the activated sub-array. These logits are passed through a softmax function to form a categorical distribution, from which a discrete action index is sampled for each RIS element. The sampled action indices are then converted into physical RIS phase values according to the predefined phase resolution, i.e., each index is mapped to one of the allowable phase shifts in (7.3). For the BS precoding matrix, two parallel actor networks are employed to separately learn the phase and amplitude of each precoding entry. The BS phase actor network predicts the parameters of a circular probability distribution that is used to model the phase of each entry in the BS precoding matrix. During training, the BS precoder phase action is obtained by sampling from this distribution, ensuring that the resulting phase lies within the interval $[0, 2\pi]$. During deployment, the mean phase values are directly used. The BS amplitude actor network predicts the amplitude of each entry in the BS precoding matrix. A Softplus activation function is applied at the output layer to guarantee non-negative amplitude values. During training, the amplitude action is

sampled from a Gaussian distribution centred at the predicted mean to encourage exploration. The sampled amplitude values are clipped to a predefined range to maintain numerical stability. The log-probability of the sampled amplitude action is incorporated into the policy gradient update jointly with the phase action. During deployment, the predicted mean amplitude values are directly used. The critic network outputs a scalar state-value estimate using a ReLU activation at the output layer. All networks are trained using the Adam optimiser with a learning rate of 0.01 and a discount factor of 0.99. During training, only one RIS agent is activated per episode following the sequential learning strategy described previously, while the remaining RIS agents remain fixed. The central critic network is updated at every timestep using the Huber loss.

7.3.3 Complexity Analysis

We adopt the ZF, minimum mean square error (MMSE), and single-agent A2C algorithms as the benchmarks, since ZF and MMSE are widely used in MIMO beamformer design [77, 115]. The computational complexities of the proposed algorithm, ZF, MMSE, and single-agent A2C are then analysed. Before presenting the complexity comparison, we briefly describe how ZF (MMSE also in the same way) is applied when N_R is extremely large and each RIS element has a discrete phase. ZF, as a linear precoder, is used to design the precoding matrix. To address the joint beamforming problem, it alternately optimises the BS precoding matrix and the RIS phase configuration. However, when optimising the RIS phases, the standard gradient descent method suffers from poor scalability due to the large RIS dimension and discrete phase constraints. To mitigate this issue, we employ block coordinate descent (BCD)[1]. For the discrete phase constraint, the RIS phase configuration is first optimised via BCD under continuous phase assumptions, and the result is subsequently quantised into M bits.

[1]When optimising one block (equivalent to a sub-array of the RIS), other blocks remain fixed.

Next, we analyse the computational complexity of the proposed algorithm. We focus on the computational complexity calculation for the forward propagation of the networks and SINR calculation because these happen per timestep, while the back propagation happens per episode. The complexities of the forward propagation for the RIS actor, BS actor, and the central critic are $\mathcal{O}((KN_T)^2)$, $\mathcal{O}((N_R/N_A)^2)$, and $\mathcal{O}((KN_T + N_R/N_A)^2)$, respectively. The complexity of the SINR calculation is $\mathcal{O}(KN_TN_R + K^2N_T)$. We define the number of the maximum episode as N_2. The computational complexity of the proposed algorithm can be summarised as $\mathcal{O}(N_1N_2((KN_T)^2 + (N_R/N_A)^2 + (KN_T + N_R/N_A)^2 + KN_TN_R + K^2N_T))$. We can simplify the expression as N_T and K are much smaller compared to N_R, N_1, and N_2. The complexity expression then becomes $\mathcal{O}(N_1N_2(N_R/N_A)^2)$. As we alternatively optimise the precoding matrix and the RIS phase configuration in the ZF/MMSE algorithm, we define the outer iteration as N_3 and the inner iteration as N_4. The computational complexity of the ZF/MMSE algorithm is $\mathcal{O}(N_3N_4(N_R/N_A))$. The complexity of the single-agent A2C is then given as $\mathcal{O}(N_1N_2N_R^2)$. From the complexity analysis, the proposed algorithm exhibits higher computational complexity than ZF and MMSE owing to the quadratic term, representing a trade-off between performance gains and computational cost.

7.4 Numerical Results

We first give the parameter settings for the proposed algorithm and the ZF algorithm in Table 7.1.

In Table 7.1, it is noted that some of the parameters are sequences, such as N_R, N_A, and Σ_{H_1}. This is because different settings are being simulated. The parameter values in Table 7.1 combine experimentally motivated hardware constraints with author-selected evaluation settings. One-bit and two-bit phase control are considered because both have been demonstrated in experimental RIS prototypes [1, 2]. The 1100-element prototype in [1] also motivates investigating sur-

Table 7.1: Parameter setting

Parameter	**Value**
Learning rate	0.01
Reward discount factor	0.99
N_T, N_R	16, [128, 256, 512, 1024,2048]
N_1, N_2, N_3, N_4	2000, 5000, 2000, 1000
N_A	[1, 2, 4, 8]
K, M, β, ρ	3, [1,2], 0.1371, 0.9
Cluster radius	[0.5, 2] m
Σ_{H_1}	$[0.1, 0.2, 0.3, 0.4, 0.5, 0.6]I$
Σ_{H_2}	$[0.1, 0.2, 0.3, 0.4, 0.5, 0.6]I$
P_{Tx}, σ^2, a	K mW, 1×10^{-6} mW, 50 m

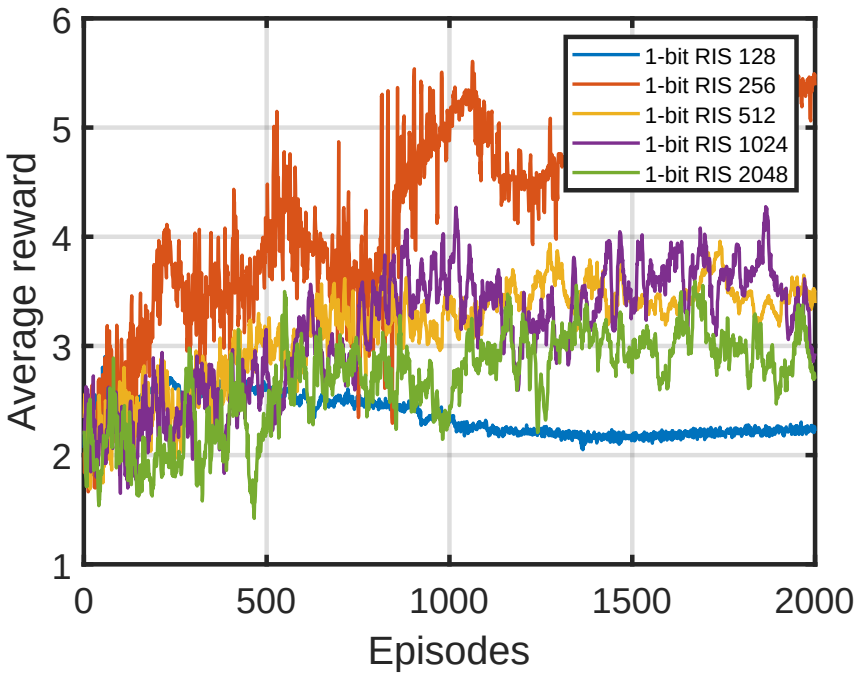

Figure 7.2: Learning curve of the proposed algorithm.

faces with element counts on the order of one thousand. The particular sequence $N_R \in \{128, 256, 512, 1024, 2048\}$ is selected by the author to examine scalability over a sixteenfold increase in surface size. These powers of two also permit equal partitioning for all considered agent counts, $N_A \in \{1, 2, 4, 8\}$. The configuration

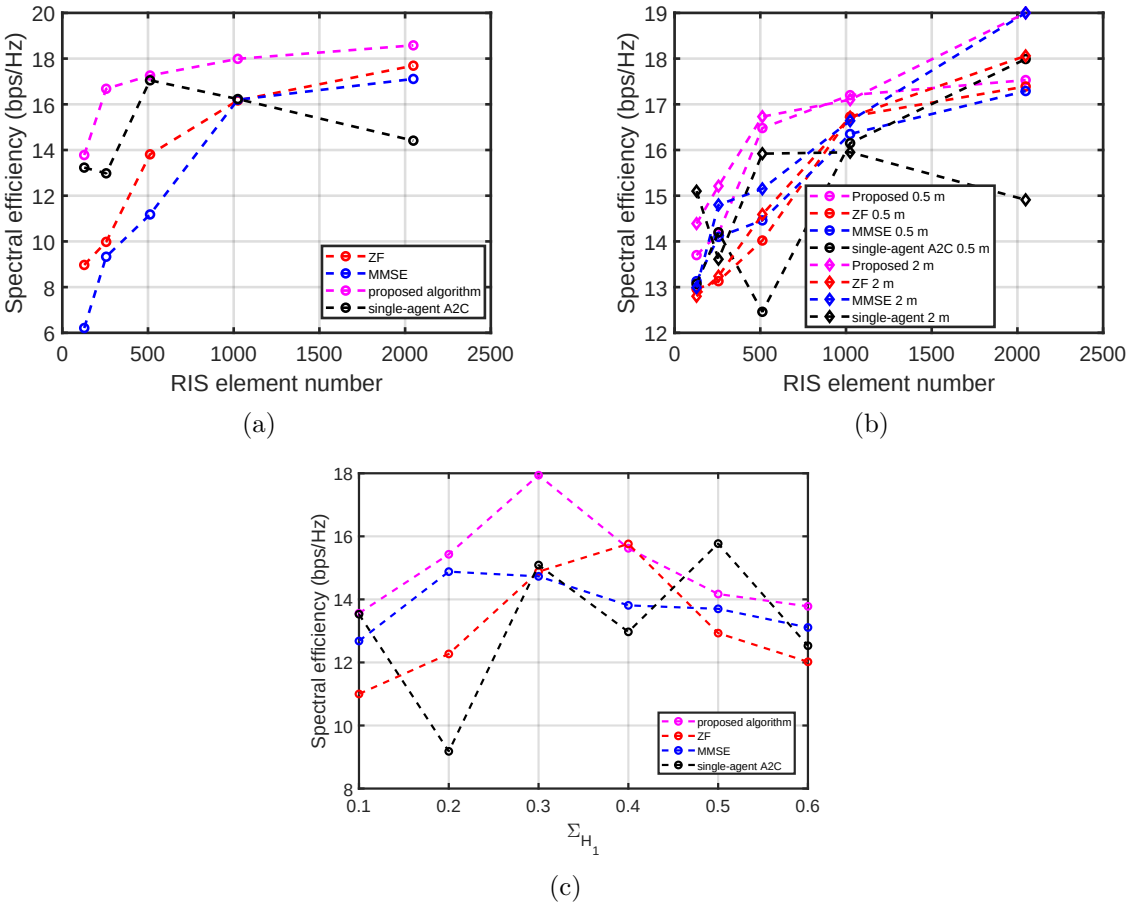

Figure 7.3: (a) Achievable SE at different RIS sizes with 1-bit phase resolution, uniformly distributed users, and perfect CSI. (b) Achievable SE at different RIS sizes for user cluster radii of 0.5 m and 2 m, with 1-bit phase resolution and perfect CSI. (c) Achievable SE at different channel estimation errors with $N_R = 512$, 1-bit phase resolution, and uniformly distributed users.

$N_T = 16$ and $K = 3$ is selected as a multi-user test case with more transmit antennas than users, enabling comparison with the ZF and MMSE benchmarks. The cluster radii of 0.5 m and 2 m provide a fourfold variation in spatial extent. The correlation coefficient $\rho = 0.9$ specifies a strongly correlated test condition. The angular-correlation parameter $\beta = 0.1371$ corresponds to a correlation of e^{-1} at an angular separation of approximately 21.2°. These spatial and correlation settings are author-selected assumptions rather than measurements from a particular deployment. The estimation-error covariance coefficients from 0.1 to 0.6 form an evenly spaced sensitivity sweep. The room dimension $a = 50$ m defines an illustrative

spatial scenario. The total transmit-power budget $P_{\mathrm{Tx}} = K$ mW corresponds to an average power allowance of 1 mW per user, while the noise power 10^{-6} mW is an author-selected reference level for the normalised channel model. The learning rate and iteration budgets are author-selected numerical settings and are not claimed to be optimal. Fig. 7.2 shows the learning curve of the proposed algorithm. It is noted that the average reward for each case gradually converges as the episode number increases. This indicates that the proposed algorithm exhibits stable training behaviour and converges to a stable learned solution for the joint BS precoding matrix and RIS phase configuration, although global optimality is not guaranteed.

Fig. 7.3(a) to Fig. 7.3(c) illustrate the performance of the proposed algorithm with respect to the RIS element number under uniformly distributed users, clustered users, and imperfect CSI conditions. In Fig. 7.3(a), the proposed algorithm consistently outperforms the ZF and MMSE benchmarks across all RIS element numbers and phase resolutions. However, the performance gap between the proposed algorithm and the benchmarks gradually narrows as the number of RIS elements increases. This behaviour is mainly attributed to the exponential growth of the state and action spaces, which reduces the learning efficiency of the algorithm. As illustrated in the figure, the proposed algorithm is therefore most suitable for scenarios with 1-bit phase resolution and RIS element numbers up to 2048. Compared with the single-agent A2C, the proposed algorithm achieves higher SE across all considered RIS element numbers. Under the same training budget specified by N_1 and N_2, the single-agent A2C achieves lower SE, with the performance gap generally increasing as the RIS element number grows. These results demonstrate the advantage of the proposed multi-agent approach for extremely large RISs under the considered simulation settings.

Fig. 7.3(b) illustrates the impact of channel correlation at different RIS element numbers. As expected, higher channel correlation leads to lower achievable SE. In Fig. 7.3(c), the achievable SE of the proposed algorithm first increases and then

decreases as Σ_{H_1} grows. This behaviour occurs because moderate channel estimation errors act as artificial noise, alleviating overfitting and enhancing robustness to imperfect CSI. A similar trend is observed for the ZF and MMSE algorithms, where small estimation errors (e.g., $\Sigma_{H_1} = 0.2I$ for MMSE) initially improve SE by partially compensating for the degradation caused by quantisation.

7.5 Conclusion

In this chapter, we proposed an algorithm that can jointly optimise the precoding matrix and the RIS phase configuration in a MU-MISO scenario when the RIS size is extremely large. We also showed the performance of the proposed algorithm in the presence of channel correlation and imperfect CSI in terms of achievable SE. Throughout simulations, it is shown that the proposed algorithm is also robust to the imperfect CSI. The proposed algorithm also has a better performance compared to the benchmarks.

Chapter 8

Conclusions and Future Work

8.1 Thesis Summary

This thesis investigated the modelling, analysis, and optimisation of intelligent surface-assisted wireless communication systems, with a particular focus on indoor mmWave networks. Motivated by the severe propagation loss and blockage sensitivity of mmWave communications, RISs were studied as a promising technology for improving wireless coverage and enhancing network performance. The thesis addressed several important aspects of RIS-assisted systems, including RIS element modelling, system-level performance analysis, user capacity characterisation, and large-scale beamforming optimisation.

The thesis first examined the phase response modelling of RIS elements at different frequency regimes. In particular, the behaviour of RIS elements at both mmWave and THz frequencies was investigated. An LC-based reflecting element operating at THz frequencies was introduced and experimentally validated. The proposed design demonstrated the feasibility of achieving tunable phase shifts at THz frequencies using LC materials. Furthermore, the relationship between the refractive indices of the LC material and the phase response of the reflecting element was analysed. Numerical results further showed that LC materials with larger birefringence can provide improved beamforming performance. These investigations provided insights into the practical implementation and electromagnetic behaviour of RIS elements at high frequencies.

Building upon the RIS element modelling, the thesis then developed a stochastic geometry-based analytical framework for RIS-assisted indoor mmWave wireless networks. Unlike many existing studies that focus primarily on link-level performance,

this work emphasised system-level analysis under realistic indoor conditions. Practical factors, including blockage effects, user clustering, boundary effects, and height variations of network nodes, were incorporated into the framework. Based on this model, analytical approximations for the distance distributions, LOS probabilities, and coverage probability were derived. The analysis revealed several important observations. For example, the contribution of RISs to the coverage probability becomes less significant under severe blockage conditions. The developed framework, therefore, provided a more realistic understanding of RIS-assisted indoor mmWave systems.

After investigating single-user system-level performance, the thesis focused on the user capacity of IOS/RIS-assisted indoor mmWave networks. A stochastic geometry-based analytical framework was developed to characterise the maximum number of users that can be simultaneously supported under QoS constraints. Both near-field and far-field propagation effects were considered, together with inter-user interference and heterogeneous user requirements. The analysis demonstrated that near-field propagation can significantly influence user capacity, particularly for extremely large intelligent surfaces. Furthermore, the results showed that user type distributions and interference conditions strongly affect the achievable user capacity. Unlike conventional deterministic optimisation metrics, the proposed user-capacity framework provided a statistical characterisation of the ability of RIS-assisted networks to support multiple users fairly under spatial randomness.

The thesis further extended the analysis to wideband RIS-assisted communication systems. In particular, the concept of RIS coherence bandwidth was introduced to characterise the maximum bandwidth over which the RIS can effectively maintain coherent beamforming gain. Analytical expressions relating the RIS coherence bandwidth to the RIS aperture size and propagation geometry were derived. It was shown that increasing the RIS aperture generally reduces the RIS coherence bandwidth due to larger phase variations across the surface. Based on the derived

coherence bandwidth model, the outage probability of wideband RIS-assisted systems was analysed under different operating regimes (e.g., within the RIS coherence bandwidth, outside the RIS coherence bandwidth). Numerical results showed close agreement between the analytical approximation to the RIS coherence bandwidth and the bandwidth obtained using the gradient-ascent numerical benchmark for the evaluated configurations. The numerical results also showed that, when the operating bandwidth exceeds the RIS coherence bandwidth, increasing the number of subcarriers continues to reduce the outage probability, but with diminishing marginal benefit due to frequency-dependent loss of coherent combining gain. The result highlighted a fundamental trade-off between RIS aperture size and wideband performance.

Finally, the thesis investigated the joint optimisation of the BS precoding matrix and RIS phase configuration in extremely large-scale RIS-assisted systems. Since conventional optimisation methods become computationally challenging for large RIS with discrete phase constraints, a DRL-based framework was proposed. In particular, a sequential multi-agent A2C algorithm was developed to jointly optimise the BS beamforming and RIS phase shifts. The proposed method explicitly accounted for practical factors such as discrete RIS phase adjustment, CSI, and inter-user channel correlation. To improve scalability, the RIS was partitioned into multiple sub-arrays, each controlled by an independent agent. Numerical results demonstrated that the proposed framework can outperform conventional methods such as ZF beamforming in terms of spectral efficiency while maintaining reasonable robustness to channel estimation errors.

Overall, the investigations presented in this thesis provide complementary perspectives on RIS-assisted wireless communication systems. The developed analytical frameworks improve the understanding of RIS-assisted indoor mmWave networks under realistic conditions, while the proposed optimisation approaches provide practical methods for enhancing system performance in large-scale deployments.

8.2 Future Work

Although this thesis has addressed several important aspects of RIS-assisted wireless communication systems, many open challenges and research opportunities remain. In this section, several potential directions for future work are discussed.

One important extension is the investigation of RIS-assisted systems in dynamic environments with user mobility. Throughout this thesis, the RIS configuration was primarily optimised based on quasi-static or slowly varying channels. However, in practical wireless systems, user movement and environmental changes may cause rapid channel variations. Due to the finite switching speed and reconfiguration delay of practical RIS hardware, particularly LC-based RIS, outdated RIS configurations may lead to performance degradation. Future work may therefore focus on integrating sensing and prediction mechanisms into RIS-assisted systems. In particular, ISAC-based frameworks may be investigated to predict user locations and future channel states, enabling proactive RIS reconfiguration.

Another promising research direction is the development of more advanced RIS architectures. Most existing works, including this thesis, focus on conventional diagonal RIS models where each element independently adjusts its own reflection coefficient. Recently, beyond-diagonal RIS (BD-RIS) architectures have attracted growing attention due to their ability to introduce coupling among RIS elements. Such architectures provide additional degrees of freedom for wavefront manipulation and interference control. Extending the analytical frameworks and optimisation algorithms developed in this thesis to BD-RIS systems would therefore be an interesting future direction.

Future work may also consider more realistic hardware impairments and implementation constraints. In practice, RIS elements exhibit amplitude-phase coupling, mutual coupling, quantisation errors, and non-linear responses, particularly at high frequencies. Furthermore, practical RIS may consume non-negligible control power, especially in large-scale deployments. Incorporating these hardware effects into the

system-level analysis and optimisation framework would improve the realism of the obtained results and provide more accurate performance predictions.

Another potential direction is the extension of the proposed frameworks to multi-RIS and cell-free architectures. In practical indoor environments, multiple RISs may be deployed simultaneously to improve coverage and reliability. However, cooperative beamforming among multiple RISs introduces additional challenges, including synchronisation, interference management, and scalable optimisation. Investigating how multiple RISs interact under realistic propagation conditions would therefore be valuable for future wireless networks.

In addition, future work may explore RIS-assisted systems operating at higher frequency bands, particularly the THz regime. Although this thesis investigated LC-based RIS element modelling at THz frequencies, the system-level performance of THz RIS-assisted networks remains relatively unexplored. THz communications introduce unique propagation characteristics, including severe molecular absorption, extremely directional beamforming, and stronger sensitivity to blockage. Developing tractable analytical models and optimisation frameworks for THz RIS-assisted systems, therefore, remains an open problem.

Finally, future research may investigate more advanced learning-based optimisation techniques. While the proposed sequential multi-agent A2C framework demonstrated promising performance, DRL training for extremely large RIS systems remains computationally expensive. Future work may focus on improving training efficiency through methods such as hierarchical reinforcement learning, transfer learning, graph neural networks, or model-based reinforcement learning. In addition, combining analytical insights from stochastic geometry with learning-based optimisation may provide more interpretable and computationally efficient solutions.

8.3 Conclusions

This thesis presented a comprehensive study of intelligent surface-assisted wireless communication systems, with a particular focus on RIS-assisted indoor mmWave networks. By combining electromagnetic modelling, stochastic geometry-based analysis, and DRL-based optimisation, the thesis investigated RIS-assisted systems from multiple perspectives, ranging from hardware-level behaviour to system-level performance and large-scale beamforming design.

The obtained results demonstrated that RIS can significantly improve the performance of indoor mmWave communication systems under practical propagation conditions. In particular, the developed analytical frameworks revealed the importance of blockage effects, user clustering, boundary effects, near-field propagation, and RIS coherence bandwidth in determining network performance. Furthermore, the proposed user-capacity framework provided a statistical perspective on the ability of RIS-assisted systems to support multiple users under QoS constraints. Finally, the proposed sequential multi-agent A2C framework demonstrated that learning-based optimisation can effectively address the high-dimensional joint beamforming problem in extremely large-scale RIS-assisted systems.

Beyond the individual technical contributions, this thesis also provides insights into the practical role of RIS in future cellular systems. The analytical and numerical results suggest that the performance gains offered by RIS are highly dependent on the propagation environment, deployment strategy, and system configuration, rather than being universally guaranteed. In particular, practical factors such as realistic blockage conditions, user distribution, near-field propagation, hardware characteristics, and wideband operation must be carefully considered when evaluating the benefits of RIS. These findings indicate that, although RIS has considerable potential to enhance coverage and capacity in high-frequency wireless networks, its successful integration into future cellular systems will require joint consideration of hardware implementation, propagation modelling, network-level performance, and

intelligent resource management.

Overall, this thesis contributes to the understanding of RIS-assisted wireless communications from both analytical and optimisation perspectives. It is hoped that the developed frameworks, analytical results, and design insights will provide useful guidance for the evaluation, design, and eventual deployment of intelligent surface-assisted wireless networks in future generations of cellular communication systems.

Appendix A

Liquid Crystal

A.1 Introduction

LC materials provide electrically tunable anisotropy for controlling electromagnetic waves. Their application to high-frequency devices includes programmable THz metasurfaces [3, 81]. This appendix summarises the material properties underlying the LC element investigated in Chapter 3. General background follows standard treatments of LC physics and electro-optics [118, 119]. Performance advantages are material- and device-dependent; continuous material tunability does not imply lossless operation or an unrestricted device phase range.

A.2 Physical Properties of Liquid Crystal Materials

A.2.1 Molecular Structure

In a nematic LC, molecular orientations have a preferred local axis, described by the unit director $\mathbf{n}$, without the three-dimensional positional order of a crystal. Many nematic mixtures used in electro-optic devices contain elongated molecules, although other molecular shapes and LC phases also exist [120]. For a uniaxial nematic, the relative permittivity tensor is written as [118]

$$\varepsilon_r = \varepsilon_\perp \mathbf{I} + (\varepsilon_\parallel - \varepsilon_\perp)\mathbf{n}\mathbf{n}^T, \tag{A.1}$$

where $\varepsilon_\parallel$ and $\varepsilon_\perp$ are the relative permittivities parallel and perpendicular to the director. The dielectric anisotropy is

$$\Delta\varepsilon = \varepsilon_\parallel - \varepsilon_\perp. \tag{A.2}$$

These quantities depend on frequency and temperature. The dielectric anisotropy at the electrical driving frequency determines the reorientation torque, while the material response at the signal frequency determines wave propagation [119].

A.2.2 Order Parameter

For a uniaxial orientational distribution, the scalar order parameter is [118]

$$S = \left\langle \frac{3\cos^2\theta - 1}{2} \right\rangle, \tag{A.3}$$

where θ is the angle between a molecular long axis and the director, and the brackets denote an average over molecular orientations. Perfect axial alignment gives $S = 1$, while an isotropic distribution gives $S = 0$. Orientational ordering contributes to macroscopic anisotropy and hence to the optical response [119].

A.3 Types of Liquid Crystal Materials

LC phases may be classified by their formation mechanism and molecular organisation. The distinctions below provide background; the device analysis in Chapter 3 concerns nematic materials [120].

A.3.1 Thermotropic Liquid Crystals

Thermotropic materials exhibit LC phases over temperature-dependent ranges. Their phases include nematic, smectic, and chiral nematic organisations, with different degrees of positional and orientational order [120].

A.3.1.1 Nematic Liquid Crystals

Nematic phases possess orientational order without long-range positional order. Their director can be reoriented electrically, enabling tunable optical and electromagnetic responses [120, 119]. Nematic mixtures including E7 and GT3-23001 have been characterised at THz frequencies, with measured birefringence and absorption depending

on the mixture and frequency [91]. Their suitability for a particular device must therefore be assessed using its material data rather than assuming uniformly low loss or fast switching.

A.3.1.2 Smectic Liquid Crystals

Smectic phases possess a layered structure in addition to orientational order. Different smectic phases have distinct molecular arrangements and electro-optic responses [120]. Consequently, no general switching-speed ranking relative to nematic materials is assumed here.

A.3.1.3 Cholesteric Liquid Crystals

Cholesteric, or chiral nematic, phases have a director that twists helically in space. Their helical organisation produces selective reflection and polarisation-dependent optical behaviour, with the response determined by the pitch and refractive indices [120, 119].

A.3.2 Lyotropic Liquid Crystals

Lyotropic LC phases form in mixtures whose ordering depends on composition, including the concentration of amphiphilic constituents in a solvent, as well as temperature [120]. Such materials are outside the scope of the thermotropic nematic cells investigated in this thesis.

A.4 Electromagnetic Tunability Mechanism

A.4.1 Electric-Field-Induced Molecular Reorientation

Surface anchoring establishes preferred director orientations at the cell boundaries. Applying a voltage produces an electric torque that competes with elastic and

anchoring effects, changing the director profile [118, 119]. For a prescribed quasi-static field, the orientation-dependent dielectric energy density is

$$U = -\frac{1}{2}\varepsilon_0 \Delta\varepsilon (\mathbf{E}\cdot\mathbf{n})^2, \tag{A.4}$$

where $\Delta\varepsilon$ is the relative dielectric anisotropy relevant to the applied field. Positive anisotropy favours alignment parallel to the field, whereas negative anisotropy favours perpendicular alignment. Thus, rotation towards the field is not a universal property of all LCs [118].

A.4.2 Effective Refractive Index

For a locally uniform, uniaxial material in the lossless approximation, let α denote the angle between the wavevector and the director. The effective extraordinary refractive index satisfies [119]

$$\frac{1}{n_{\text{eff}}^2(\alpha)} = \frac{\cos^2\alpha}{n_o^2} + \frac{\sin^2\alpha}{n_e^2}, \tag{A.5}$$

where n_o and n_e are the principal ordinary and extraordinary indices. This convention gives $n_{\text{eff}} = n_o$ for propagation along the director and $n_{\text{eff}} = n_e$ for propagation perpendicular to it. For normal incidence with director tilt θ measured from the cell plane in the principal plane, $\alpha = \pi/2 - \theta$, giving the equivalent form

$$\frac{1}{n_{\text{eff}}^2(\theta)} = \frac{\cos^2\theta}{n_e^2} + \frac{\sin^2\theta}{n_o^2}. \tag{A.6}$$

Electrical reorientation changes this effective index. A non-uniform director profile requires its spatial variation to be accounted for, as in the segmented approximation in Chapter 3.

A.4.3 Phase Shift Mechanism

For a homogeneous layer of thickness d at normal incidence, neglecting multiple reflections, the single-pass phase-tuning range is [119]

$$\Delta\phi = \frac{2\pi f d}{c}\left(n_{\text{eff,max}} - n_{\text{eff,min}}\right), \tag{A.7}$$

where the effective indices are evaluated at the signal frequency f. For a non-uniform layer, the index difference is integrated along the propagation path. An ideal double pass through the same profile doubles the propagation contribution; interface and resonant effects require a device-specific treatment. The thickness and birefringence needed for useful THz phase tuning must be evaluated together with absorption [91].

A.5 Liquid Crystal Based RIS at Terahertz Frequencies

A.5.1 Why Liquid Crystal is Suitable for Terahertz RIS

The measured electrical tunability and birefringence of nematic mixtures support their use in THz phase-control devices [91]. Reflective and transmissive programmable metasurfaces demonstrate how this material response can control THz beams [3, 81]. Although molecular reorientation is continuous, practical devices may employ discrete bias states, and their usable phase range depends on amplitude variation and the unit-cell response. Low-power biasing and large-panel integration are motivations for LC-based RIS architectures, but the control electronics, dielectric losses, and conductor losses must also be considered [34].

A.5.2 Typical RIS Unit Cell Structure

A representative reflective THz design combines an LC layer, electrodes, a resonant metallic structure, and a back reflector. Fu et al. demonstrated a programmable reflective structure incorporating a complementary split-ring resonator, an LC layer, and a metallic back plate [3]. Transmissive architectures use a different layer arrangement to permit transmission [81]. Bias-dependent permittivity changes the electromagnetic response of these structures. These resonant implementations should be distinguished from the direct propagation-phase modulation investigated in Chapter 3.

A.5.3 Challenges at Terahertz Frequencies

Birefringence and absorption must be characterised over the intended frequency range: measurements show that these properties differ between nematic mixtures [91]. Director relaxation also creates a trade-off between phase range and response time. In a simple planar nematic cell with strong anchoring and a one-elastic-constant approximation, the field-off relaxation time scales approximately as $\gamma_1 d^2/(\pi^2 K)$, where γ_1 is the rotational viscosity and K is the relevant elastic constant [119]. Thin-layer architectures can improve switching, as demonstrated by a 62 GHz LC-RIS with a measured response time of 72 ms; that result is specific to its device architecture and is not a universal THz switching time [34]. Temperature-dependent material properties, alignment, and fabrication tolerances must likewise be considered [119, 34].

A.6 Summary

The LC element analysis in Chapter 3 relies on dielectric anisotropy, electrical director reorientation, and the resulting propagation-phase change. The background above distinguishes these material mechanisms from device-level phase control. It also identifies the assumptions underlying the simplified tensor, effective-index, and phase expressions. THz device performance must ultimately be assessed using measured material properties and the losses and dynamics of the chosen structure [91, 3].

Appendix B

Stochastic Geometry for Wireless Networks Analysis

B.1 Introduction

Stochastic geometry is a mathematical framework that models spatially distributed objects as random point processes, enabling the statistical characterisation of their geometric relationships [121, 122]. In the context of wireless communications, it is widely used to represent the random locations of network entities such as BSs, users, and scatterers, and to analyse how this spatial randomness impacts system performance. In this section, we introduce several fundamental spatial point processes commonly used in wireless network analysis. Specifically, we begin with the BPP for modelling networks with a finite number of nodes, followed by the Poisson point process (PPP), which serves as a canonical model for large-scale random networks. We then discuss the Homogeneous PPP, a widely adopted special case with constant spatial density, followed by its counterpart, the inhomogeneous Poisson point process (IPPP), and finally introduce the hard-core point process (HCPP) to capture repulsion effects and minimum distance constraints between nodes.

B.1.1 Binomial Point Process

A BPP is a fundamental spatial model in which a fixed number of points, denoted by N, are independently and identically distributed within a compact region $W \subset \mathbb{R}^d$. The locations of these points can be represented as a random vector in the product space W^N, whose distribution may be either uniform or follow a more general

probability measure. When the points are uniformly distributed over W, the resulting process is referred to as a uniform BPP. The term "binomial" arises from the fact that, for any measurable subset $A \subset W$, the number of points falling within A follows a binomial distribution with parameters N and $p = \frac{|A|}{|W|}$, where $|\cdot|$ denotes the Lebesgue measure of the set. The probability of k points in the compact set A is given by [122]

$$P(k \text{ points in } A) = \binom{N}{k} p^k (1-p)^{N-k}. \tag{B.1}$$

Next, we move forward to discuss PPP, which can be viewed as a generalisation of BPP in the way that the point number is no longer fixed, rather, it is a random variable that follows Poisson distribution.

B.1.2 Poisson Point Process

In PPP, there are two subcategories, which are HPPP and IPPP, corresponding to a uniform intensity and a non-uniform intensity PPP.

B.1.2.1 Homogeneous Poisson Point Process

A HPPP with intensity λ is a point process defined on $\mathbb{R}^d$ that satisfies the following two properties: 1) for any compact set $A \subset \mathbb{R}^d$, the number of points in A, denoted by $N(A)$, follows a Poisson distribution with mean $\lambda|A|$, and 2) for any collection of disjoint bounded sets $A_1, A_2, \ldots, A_m$, the random variables $N(A_1), N(A_2), \ldots, N(A_m)$ are mutually independent. The parameter λ is referred to as the intensity of the point process, which represents the average number of points per unit volume (or area in the two-dimensional case). Accordingly, for any compact set $A \subset \mathbb{R}^d$, the probability of observing exactly k points in A is given by [122]

$$\Pr(N(A) = k) = \frac{(\lambda|A|)^k}{k!} e^{-\lambda|A|}. \tag{B.2}$$

The process is termed homogeneous because the intensity λ is constant over space, implying that the statistical properties of the process are invariant with respect

to location. Compared to the BPP, the HPPP does not impose a fixed number of points within a bounded region. Instead, the number of points in any set is random and follows a Poisson distribution. Moreover, the HPPP is defined over the entire space $\mathbb{R}^d$, and therefore does not inherently impose boundary constraints on the spatial domain. In contrast, the BPP is restricted to a finite region $W \subset \mathbb{R}^d$ with a fixed number of points N. As a result, the BPP is more suitable for modelling finite networks within confined areas, whereas the HPPP provides a tractable model for large-scale or unbounded networks. In practice, analyses based on HPPP are often conducted over $\mathbb{R}^d$ or a sufficiently large region to avoid boundary effects.

B.1.2.2 Inhomogeneous Poisson Point Process

Compared to the HPPP, the IPPP provides a more general model by allowing the intensity to vary over space. Specifically, the intensity is described by a location-dependent function $\lambda(a)$, where $a \in \mathbb{R}^d$ denotes the spatial coordinate. For any compact set $A \subset \mathbb{R}^d$, the number of points $N(A)$ follows a Poisson distribution with mean given by the integral of the intensity function over A, i.e.,

$$\mathbb{E}[N(A)] = \int_A \lambda(a)\,\mathrm{d}a. \tag{B.3}$$

Accordingly, the probability of observing exactly k points in A is

$$\Pr(N(A) = k) = \frac{\left(\int_A \lambda(a)\,\mathrm{d}a\right)^k}{k!} \exp\left(-\int_A \lambda(a)\,\mathrm{d}a\right). \tag{B.4}$$

Here, a denotes a location in the spatial domain, and $\mathrm{d}a$ represents an infinitesimal volume (or area in two dimensions), so that $\int_A \lambda(a)\,\mathrm{d}a$ corresponds to the total expected number of points in A. The IPPP is particularly useful for modelling scenarios where the spatial distribution of points is non-uniform, such as environments with hotspots, where the point density is significantly higher in certain subregions compared to others.

B.1.3 Hardcore Point Process

HCPPs are point processes in which no two points are allowed to be closer than a prescribed minimum distance. Compared to a HPPP, they exhibit a more regular spatial structure and reduced clustering. One way to construct such processes is to begin with a baseline Poisson point process and then remove points that violate the minimum distance constraint. Two commonly used hard-core models are defined as follows.

Starting from a homogeneous PPP with intensity λ, all points that have at least one neighbour within distance r are first identified and flagged. All flagged points are then removed. The resulting process is known as the Matérn hard-core process of type I.

Starting from a homogeneous PPP with intensity λ_b, each point x is assigned an independent random mark $m(x)$, uniformly distributed on $[0, 1]$. A point is flagged for removal if it has a neighbour within distance r with a smaller mark. All flagged points are then removed. The resulting process is known as the Matérn hard-core process of type II.

The HCPP is particularly suitable for modelling obstacles within confined environments, such as indoor spaces, including conference centres and shopping malls. In these settings, the physical size of obstacles cannot be neglected, and a minimum separation naturally arises due to their impenetrable nature, which induces a repulsive interaction between nearby obstacles.

B.1.4 Point Processes, Transformations and Distances

After introducing several fundamental point processes, we now focus on the transformation and distance-related properties of point processes, which play a crucial role in wireless network analysis. Transformations of a point process include displacement, mapping, and thinning. These operations are fundamental tools in stochastic geometry for modifying and analysing spatial point patterns.

Displacement refers to independently shifting each point of a point process according to some probability distribution. A key result in stochastic geometry is that independently displacing the points of an HPPP results in another HPPP, provided that the displacement is independent and identically distributed (i.i.d.) across points. This property is particularly useful in wireless communications for modelling user mobility or random perturbations in node locations.

Mapping involves applying a deterministic or random function to each point in the process. One important example is the mapping from Cartesian coordinates to polar coordinates when analysing distances and angles relative to a reference receiver. More generally, if a point process is transformed via a measurable function, the resulting process may no longer be Poisson unless certain conditions are satisfied. However, under specific mappings such as scaling or translation, the Poisson property can be preserved. Mapping is widely used in wireless analysis, for instance, when converting spatial node distributions into distributions of propagation distances or path losses.

Thinning is a transformation in which each point of a point process is independently retained with a certain probability or removed otherwise. For an HPPP with intensity λ, independent thinning with retention probability p results in another HPPP with intensity $p\lambda$. Thinning is commonly used to model random access, blockage effects, or user activity in wireless networks. For example, in indoor environments, thinning can represent the fraction of active users or the probability that a link is not blocked.

Beyond transformations, distance distributions derived from point processes are of fundamental importance in wireless system analysis. In particular, the distance from a typical user (often placed at the origin using Slivnyak's theorem) to its nearest transmitter is a key quantity. For an HPPP with intensity λ in $\mathbb{R}^2$, the CDF of the nearest-neighbour distance R is given by [121]

$$F_R(r) = 1 - \exp(-\lambda \pi r^2), \tag{B.5}$$

and the corresponding PDF is

$$f_R(r) = 2\pi\lambda r \exp(-\lambda\pi r^2). \tag{B.6}$$

These expressions are widely used in the analysis of coverage probability and SINR in cellular and RIS-assisted networks. In summary, transformations and distance-related properties of point processes provide essential tools for bridging spatial randomness and wireless performance metrics. They enable tractable analysis of complex systems by converting spatial configurations into analytically manageable forms, which is particularly important for the study of RIS-assisted indoor networks with realistic geometrical constraints.

Appendix C

Order Statistics for Wireless Network Analysis

Order statistics play a fundamental role in the analysis of wireless networks, particularly when characterising extreme events such as the strongest received signal, the nearest transmitter distance, or the maximum interference. Given a set of random variables, order statistics describe their sorted values, enabling tractable analysis of performance metrics that depend on extrema rather than averages.

Formally, let $\{X_1, X_2, \dots, X_n\}$ be a collection of i.i.d. random variables with CDF $F_X(x)$. The corresponding order statistics are denoted by $X_{(1)} \leq X_{(2)} \leq \cdots \leq X_{(n)}$, where $X_{(k)}$ represents the k-th smallest value. The distribution of $X_{(k)}$ is given by [108]

$$F_{X_{(k)}}(x) = \sum_{i=k}^{n} \binom{n}{i} [F_X(x)]^i [1 - F_X(x)]^{n-i}. \tag{C.1}$$

In particular, the minimum and maximum order statistics are of special interest, corresponding to $X_{(1)}$ and $X_{(n)}$, respectively. In wireless communications, order statistics naturally arise in several key scenarios. One prominent example is user association in cellular networks, where a user typically connects to the transmitter providing the strongest received signal power. Assuming independent fading channels, this corresponds to selecting the maximum among a set of random received powers. Similarly, in stochastic geometry-based models, the distance from a typical user to its nearest transmitter is the minimum of a set of spatial distances, which can be characterised using order statistics. Another important application is in interference analysis. In dense networks, the aggregate interference is often dominated by a few strongest interferers. Order statistics enable the characterisation of these dominant

contributors, allowing simplified yet accurate approximations of the total interference. This is particularly useful in RIS-assisted mmWave systems. Overall, order statistics provide a powerful mathematical framework for analysing extremal behaviour in wireless networks. Their integration with stochastic geometry and fading channel models enables tractable performance analysis of complex systems.

Appendix D

Deep Reinforcement Learning for Wireless Communications

D.1 Introduction

Wireless communication systems have traditionally been analysed and optimised using model-based approaches, where system performance metrics such as SINR, coverage probability, and spectral efficiency are expressed in analytical forms. Based on these models, optimisation techniques such as convex optimisation, fractional programming, and alternating optimisation have been widely applied to problems including power control, resource allocation, and beamforming design [75, 76, 123].

However, the increasing complexity of modern wireless systems poses significant challenges to conventional optimisation-based methods. In particular, emerging technologies such as mmWave communications and RISs introduce high-dimensional design variables and strong coupling between system components. For instance, RIS-assisted systems require the joint optimisation of a large number of discrete or continuous phase shifts, often in conjunction with base station beamforming and user scheduling. These problems are typically non-convex and may not admit tractable closed-form solutions.

Moreover, practical wireless environments are inherently dynamic and uncertain. Factors such as user mobility, channel estimation errors, blockage, and hardware impairments make it difficult to obtain accurate system models. As a result, optimisation methods that rely on precise CSI or simplified assumptions may suffer from performance degradation when deployed in realistic scenarios.

To address these challenges, learning-based approaches have been proposed

as an alternative to traditional model-driven techniques. In particular, reinforcement learning (RL) provides a framework in which an agent can learn optimal decision-making strategies through interaction with the environment, without requiring explicit knowledge of system dynamics. Early applications of RL in wireless communications have demonstrated its effectiveness in problems such as dynamic spectrum access, power control, and user association, where the environment is complex or partially observable [77, 78, 79].

The key advantage of RL lies in its ability to adapt to changing environments and learn directly from data. This makes it particularly suitable for wireless systems with high uncertainty and large design spaces. However, classical RL methods are limited in their ability to handle high-dimensional state and action spaces, which motivates the integration of deep neural networks into RL, leading to the development of DRL. In the following subsection, we introduce the fundamental concepts of RL, which form the basis for DRL-based approaches in wireless communications.

D.1.1 Reinforcement Learning Fundamentals

RL provides a mathematical framework for sequential decision-making problems, where an agent interacts with an environment to maximise a long-term cumulative reward. The problem is commonly modelled as a Markov decision process (MDP), defined by the tuple $(\mathcal{S}, \mathcal{A}, \mathcal{P}, \mathcal{R}, \gamma)$, where $\mathcal{S}$ denotes the state space, $\mathcal{A}$ the action space, $\mathcal{P}(s'|s,a)$ the state transition probability, $\mathcal{R}(s,a)$ the reward function, and $\gamma \in [0,1)$ the discount factor. At each time step t, the agent observes the current state $s_t \in \mathcal{S}$, selects an action $a_t \in \mathcal{A}$ according to a policy $\pi(a|s)$, and receives a reward r_t while the environment transitions to a new state s_{t+1}. The objective of the agent is to learn an optimal policy π^* that maximises the expected discounted return, defined as

$$G_t = \sum_{k=0}^{\infty} \gamma^k r_{t+k}. \tag{D.1}$$

A central concept in RL is the value function, which evaluates the long-term utility of states or state-action pairs under a given policy. The state-value function is defined as

$$V^{\pi}(s) = \mathbb{E}_{\pi}\left[G_t \mid s_t = s\right], \tag{D.2}$$

while the action-value function (Q-function) is defined as

$$Q^{\pi}(s,a) = \mathbb{E}_{\pi}\left[G_t \mid s_t = s, a_t = a\right]. \tag{D.3}$$

These value functions satisfy the Bellman equations, which establish recursive relationships and form the foundation of many RL algorithms [124].

To compute the optimal action-value function, Q-learning is one of the most widely used methods. It is an off-policy temporal-difference learning algorithm that iteratively updates the Q-function according to

$$Q(s_t,a_t) \leftarrow Q(s_t,a_t) + \alpha\left[r_t + \gamma \max_{a'} Q(s_{t+1},a') - Q(s_t,a_t)\right], \tag{D.4}$$

where α is the learning rate. Q-learning converges to the optimal action-value function under suitable conditions, even when the environment dynamics are unknown.

Despite its theoretical appeal, classical RL methods such as tabular Q-learning suffer from the "curse of dimensionality". Specifically, when the state or action space becomes large or continuous, maintaining and updating a table of Q-values becomes computationally infeasible. This limitation motivates the integration of function approximation techniques into RL, leading to the development of deep reinforcement learning.

D.1.2 Deep Reinforcement Learning

DRL extends classical RL by employing deep neural networks as function approximators for value functions or policies. This enables RL algorithms to scale to high-dimensional state and action spaces, which are commonly encountered in wireless communication systems.

One of the seminal works in DRL is the deep Q-network (DQN), which approximates the action-value function using a deep neural network. Instead of maintaining a tabular Q-function [125, 126], DQN parameterises $Q(s, a; \theta)$ with network weights θ, which are optimised by minimising the temporal difference (TD) error. To stabilise training, DQN introduces two key mechanisms: experience replay and target networks. Experience replay stores past transitions (s, a, r, s') in a buffer and samples mini-batches uniformly to break correlation between consecutive samples, thereby improving data efficiency. The target network, which is a delayed copy of the Q-network, is used to compute the TD target, reducing oscillations and divergence during training. Despite its success, DQN is fundamentally limited to discrete action spaces, and its performance degrades when the action space becomes large due to the need to evaluate all possible actions in the maximisation step.

To address continuous control problems, policy gradient methods have been developed. Unlike value-based methods, policy gradient approaches directly parameterise the policy $\pi(a|s; \theta)$ and optimise it by maximising the expected return via gradient ascent. The deterministic policy gradient (DPG) framework extends this idea by considering deterministic policies $\mu(s; \theta)$, which output a specific action for each state. Its deep variant, deep deterministic policy gradient (DDPG), combines an actor-critic architecture with deep function approximation [127, 128]. The actor network generates continuous actions, while the critic network estimates the action-value function. The policy is updated by backpropagating gradients through the critic, enabling efficient learning in continuous action spaces. However, DDPG is known to suffer from training instability due to function approximation errors and overestimation bias in the critic.

To mitigate these issues, twin delayed DDPG (TD3) introduces several improvements [129]. First, TD3 employs two independent critic networks and uses the minimum of their estimates to reduce overestimation bias, a technique known as clipped double Q-learning. Second, it applies delayed updates to the actor network,

allowing the critic to converge more accurately before policy updates. Third, target policy smoothing is used by adding noise to target actions, which improves robustness against sharp value function peaks. These modifications significantly enhance training stability and performance in continuous control tasks.

In addition to deterministic policy methods, stochastic policy gradient algorithms such as A2C and proximal policy optimisation (PPO) have gained popularity [130]. A2C is a synchronous actor-critic method that reduces variance in policy gradient estimates by introducing an advantage function, defined as the difference between the action-value and state-value functions [130]. This allows more stable and efficient policy updates compared to vanilla policy gradient methods. PPO further improves stability by introducing a clipped surrogate objective that restricts the magnitude of policy updates, preventing large and destabilising changes to the policy [131]. As a result, PPO achieves a favorable balance between performance and computational efficiency.

The adoption of DRL is particularly motivated by its ability to handle complex, nonlinear, and high-dimensional problems without requiring explicit mathematical models. In wireless communications, system dynamics are often difficult to characterise analytically due to factors such as user mobility, channel fading, and hardware constraints. DRL provides a data-driven approach that can learn effective control policies directly from interactions with the environment.

Nevertheless, DRL also introduces new challenges, including high sample complexity, training instability, and limited interpretability. These challenges are especially pronounced in wireless systems with stringent real-time constraints and large-scale optimisation variables, such as RIS-assisted networks.

Bibliography

[1] X. Pei, H. Yin, L. Tan, L. Cao, Z. Li, K. Wang, K. Zhang, and E. Björnson, "RIS-aided wireless communications: Prototyping, adaptive beamforming, and indoor/outdoor field trials," *IEEE Transactions on Communications*, vol. 69, no. 12, pp. 8627–8640, 2021.

[2] L. Dai, B. Wang, M. Wang, X. Yang, J. Tan, S. Bi, S. Xu, F. Yang, Z. Chen, M. Di Renzo, *et al.*, "Reconfigurable intelligent surface-based wireless communications: Antenna design, prototyping, and experimental results," *IEEE Access*, vol. 8, pp. 45913–45923, 2020.

[3] X. Fu, L. Shi, J. Yang, Y. Fu, C. Liu, J. W. Wu, F. Yang, L. Bao, and T. J. Cui, "Flexible terahertz beam manipulations based on liquid-crystal-integrated programmable metasurfaces," *ACS Applied Materials & Interfaces*, vol. 14, no. 19, pp. 22287–22294, 2022.

[4] Z. Shen, W. Li, B. Jin, and D. Zhao, "A liquid crystal-based multi-bit terahertz reconfigurable intelligent surface," *APL Photonics*, vol. 9, no. 1, 2024.

[5] M. Alsabah, M. A. Naser, B. M. Mahmmod, S. H. Abdulhussain, M. R. Eissa, A. Al-Baidhani, N. K. Noordin, S. M. Sait, K. A. Al-Utaibi, and F. Hashim, "6g wireless communications networks: A comprehensive survey," *IEEE Access*, vol. 9, pp. 148191–148243, 2021.

[6] B. Hamdaoui, B. Khalfi, and N. Zorba, "Dynamic spectrum sharing in the age of millimeter-wave spectrum access," *IEEE Network*, vol. 34, no. 5, pp. 164–170, 2020.

[7] W. Jiang, B. Han, M. A. Habibi, and H. D. Schotten, "The road towards 6G: A comprehensive survey," *IEEE Open Journal of the Communications Society*, vol. 2, pp. 334–366, 2021.

[8] N. Alliance and G. Düsseldorf, "ITU-R framework for IMT-2030: Review and Future Direction," 2024.

[9] S. A. Busari, K. M. S. Huq, S. Mumtaz, L. Dai, and J. Rodriguez, "Millimeter-wave massive mimo communication for future wireless systems: A survey," *IEEE Communications Surveys & Tutorials*, vol. 20, no. 2, pp. 836–869, 2017.

[10] N. Bhushan, J. Li, D. Malladi, R. Gilmore, D. Brenner, A. Damnjanovic, R. T. Sukhavasi, C. Patel, and S. Geirhofer, "Network densification: the dominant theme for wireless evolution into 5G," *IEEE Communications Magazine*, vol. 52, no. 2, pp. 82–89, 2014.

[11] J. Li, Y. Niu, H. Wu, B. Ai, R. He, N. Wang, and S. Chen, "Joint optimization of relay selection and transmission scheduling for UAV-aided mmWave vehicular networks," *IEEE Transactions on Vehicular Technology*, vol. 72, no. 5, pp. 6322–6334, 2023.

[12] D. Kim, M. R. Castellanos, and R. W. Heath, "Joint relay selection and beam management based on deep reinforcement learning for millimeter wave vehicular communication," *IEEE Transactions on Vehicular Technology*, vol. 72, no. 10, pp. 13067–13080, 2023.

[13] E. Basar, M. Di Renzo, J. De Rosny, M. Debbah, M.-S. Alouini, and R. Zhang, "Wireless communications through reconfigurable intelligent surfaces," *IEEE Access*, vol. 7, pp. 116753–116773, 2019.

[14] M. Di Renzo, A. Zappone, M. Debbah, M.-S. Alouini, C. Yuen, J. De Rosny, and S. Tretyakov, "Smart radio environments empowered by reconfigurable intelligent surfaces: How it works, state of research, and the road ahead," *IEEE Journal on Selected Areas in Communications*, vol. 38, no. 11, pp. 2450–2525, 2020.

[15] J. Wang, W. Tang, J. C. Liang, L. Zhang, J. Y. Dai, X. Li, S. Jin, Q. Cheng, and T. J. Cui, "Reconfigurable Intelligent Surface: Power Consumption Modeling and Practical Measurement Validation," *IEEE Transactions on Communications*, vol. 72, no. 9, pp. 5720–5734, 2024.

[16] E. Björnson, Ö. Özdogan, and E. G. Larsson, "Intelligent Reflecting Surface vs. Decode-and-Forward: How Large Surfaces Are Needed to Beat Relaying?," *IEEE Wireless Communications Letters*, vol. 9, no. 2, pp. 244–248, 2020.

[17] ETSI, "Reconfigurable intelligent surfaces (ris); implementation and practical considerations," ETSI Group Report GR RIS 004 V1.1.1, European Telecommunications Standards Institute, Mar. 2025.

[18] NTT DOCOMO, "DOCOMO Conducts World's First Trial of Transmissive Metasurface on Window to Deliver Indoor Radio Waves to Outdoor Foot of Building." Press Release, Jan. 2023.

[19] C.-K. Wen, L.-S. Tsai, A. Shojaeifard, P.-K. Liao, K.-K. Wong, and C.-B. Chae, "Shaping a smarter electromagnetic landscape: Iab, ncr, and ris in 5g standard and future 6g," *IEEE Communications Standards Magazine*, vol. 8, no. 1, pp. 72–78, 2024.

[20] Y. Sun, B. Duan, X. Su, H. Wang, Q. Gu, J. Jin, and Y. Yuan, "Performance analysis on reconfigurable intelligent surface and network-controlled repeater in 3gpp release-18," *Frontiers of Information Technology & Electronic Engineering*, vol. 24, no. 12, pp. 1815–1828, 2023.

[21] RIS TECH Alliance, "White paper on potential standardization work for reconfigurable intelligent surface," tech. rep., RIS TECH Alliance, May 2025.

[22] 3GPP, "Revised WID on NR network-controlled repeaters," Tech. Rep. RP-223005, 3GPP TSG RAN Meeting #98-e, 2022.

[23] G. C. Alexandropoulos *et al.*, "Sustainable wireless networks via reconfigurable intelligent surfaces (RISs): Overview of the ETSI ISG RIS," *arXiv preprint arXiv:2406.05647*, 2024.

[24] ETSI ISG RIS, "ISG RIS activity report 2023," 2023. `https://www.etsi.org/committee-activity/activity-report-ris`.

[25] ETSI, "Reconfigurable intelligent surfaces (RIS); use cases, deployment scenarios and requirements," Tech. Rep. GR RIS 001 V1.1.1, ETSI, 2023.

[26] ETSI, "Reconfigurable intelligent surfaces (RIS); communication models, channel models, channel estimation and evaluation methodology," Tech. Rep. GR RIS 003 V1.1.1, ETSI, 2023.

[27] ETSI, "Reconfigurable intelligent surfaces (RIS); technological challenges, architecture and impact on standardization," Tech. Rep. GR RIS 002 V1.1.1, ETSI, 2023.

[28] J. Chen, Y.-C. Liang, H. V. Cheng, and W. Yu, "Channel estimation for reconfigurable intelligent surface aided multi-user mmWave MIMO systems," *IEEE Transactions on Wireless Communications*, vol. 22, no. 10, pp. 6853–6869, 2023.

[29] Q. Wu and R. Zhang, "Intelligent reflecting surface enhanced wireless network via joint active and passive beamforming," *IEEE Transactions on Wireless Communications*, vol. 18, no. 11, pp. 5394–5409, 2019.

[30] W. Tang, M. Z. Chen, X. Chen, J. Y. Dai, Y. Han, M. Di Renzo, Y. Zeng, S. Jin, Q. Cheng, and T. J. Cui, "Wireless communications with reconfigurable intelligent surface: Path loss modeling and experimental measurement," *IEEE Transactions on Wireless Communications*, vol. 20, no. 1, pp. 421–439, 2020.

[31] K. K. Nguyen, S. R. Khosravirad, D. B. Da Costa, L. D. Nguyen, and T. Q. Duong, "Reconfigurable intelligent surface-assisted multi-UAV networks: Efficient resource allocation with deep reinforcement learning," *IEEE Journal of Selected Topics in Signal Processing*, vol. 16, no. 3, pp. 358–368, 2021.

[32] Z. Chu, W. Hao, P. Xiao, and J. Shi, "Intelligent reflecting surface aided multi-antenna secure transmission," *IEEE Wireless Communications Letters*, vol. 9, no. 1, pp. 108–112, 2019.

[33] Z. Zhang, L. Dai, X. Chen, C. Liu, F. Yang, R. Schober, and H. V. Poor, "Active RIS vs. passive RIS: Which will prevail in 6G?," *IEEE Transactions on Communications*, vol. 71, no. 3, pp. 1707–1725, 2022.

[34] R. Neuder, M. Späth, M. Schüßler, and A. Jiménez-Sáez, "Architecture for sub-100 ms liquid crystal reconfigurable intelligent surface based on defected delay lines," *Communications Engineering*, vol. 3, no. 1, p. 70, 2024.

[35] O. Melnyk, R. Jones, R. Macêdo, Y. Garbovskiy, G. Hagen, A. V. Glushchenko, K. Spendier, and R. E. Camley, "Fast switching dual-frequency nematic liquid crystal tunable filters," *ACS Photonics*, vol. 8, no. 4, pp. 1222–1231, 2021.

[36] S. Abadal, T.-J. Cui, T. Low, and J. Georgiou, "Programmable metamaterials for software-defined electromagnetic control: Circuits, systems, and architectures," *IEEE Journal on Emerging and Selected Topics in Circuits and Systems*, vol. 10, no. 1, pp. 6–19, 2020.

[37] S. Dash, C. Liaskos, I. F. Akyildiz, and A. Pitsillides, "Wideband perfect absorption polarization insensitive reconfigurable graphene metasurface for THz wireless environment," in *2019 IEEE Microwave Theory and Techniques in Wireless Communications (MTTW)*, vol. 1, pp. 93–96, IEEE, 2019.

[38] Ö. Özdogan, E. Björnson, and E. G. Larsson, "Intelligent reflecting surfaces: Physics, propagation, and pathloss modeling," *IEEE Wireless Communications Letters*, vol. 9, no. 5, pp. 581–585, 2019.

[39] F. H. Danufane, M. Di Renzo, J. De Rosny, and S. Tretyakov, "On the path-loss of reconfigurable intelligent surfaces: An approach based on Green's theorem applied to vector fields," *IEEE Transactions on Communications*, vol. 69, no. 8, pp. 5573–5592, 2021.

[40] T. Wang, G. Chen, M.-A. Badiu, and J. P. Coon, "Performance analysis of RIS-assisted large-scale wireless networks using stochastic geometry," *IEEE Transactions on Wireless Communications*, vol. 22, no. 11, pp. 7438–7451, 2023.

[41] C. Huang, A. Zappone, G. C. Alexandropoulos, M. Debbah, and C. Yuen, "Reconfigurable intelligent surfaces for energy efficiency in wireless communication," *IEEE Transactions on Wireless Communications*, vol. 18, no. 8, pp. 4157–4170, 2019.

[42] E. Björnson, H. Wymeersch, B. Matthiesen, P. Popovski, L. Sanguinetti, and E. De Carvalho, "Reconfigurable intelligent surfaces: A signal processing perspective with wireless applications," *IEEE Signal Processing Magazine*, vol. 39, no. 2, pp. 135–158, 2022.

[43] Q. Wu and R. Zhang, "Beamforming optimization for wireless network aided by intelligent reflecting surface with discrete phase shifts," *IEEE Transactions on Communications*, vol. 68, no. 3, pp. 1838–1851, 2019.

[44] H. Li, M. Nerini, S. Shen, and B. Clerckx, "A tutorial on beyond-diagonal reconfigurable intelligent surfaces: Modeling, architectures, system design and optimization, and applications," *IEEE Communications Surveys & Tutorials*, 2025.

[45] S. Shen, B. Clerckx, and R. Murch, "Modeling and architecture design of reconfigurable intelligent surfaces using scattering parameter network analysis," *IEEE Transactions on Wireless Communications*, vol. 21, no. 2, pp. 1229–1243, 2021.

[46] M. Nerini, S. Shen, and B. Clerckx, "Closed-form global optimization of beyond diagonal reconfigurable intelligent surfaces," *IEEE Transactions on Wireless Communications*, vol. 23, no. 2, pp. 1037–1051, 2023.

[47] Z.-Q. He and X. Yuan, "Cascaded channel estimation for large intelligent metasurface assisted massive MIMO," *IEEE Wireless Communications Letters*, vol. 9, no. 2, pp. 210–214, 2019.

[48] A. Abdallah, A. Celik, M. M. Mansour, and A. M. Eltawil, "RIS-aided mmwave MIMO channel estimation using deep learning and compressive sensing," *IEEE Transactions on Wireless Communications*, vol. 22, no. 5, pp. 3503–3521, 2023.

[49] L. Wei, C. Huang, G. C. Alexandropoulos, C. Yuen, Z. Zhang, and M. Debbah, "Channel estimation for RIS-empowered multi-user MISO wireless communications," *IEEE Transactions on Communications*, vol. 69, no. 6, pp. 4144–4157, 2021.

[50] J. He, H. Wymeersch, M. D. Renzo, and M. Juntti, "Learning to estimate RIS-aided mmwave channels," *IEEE Wireless Communications Letters*, vol. 11, no. 4, pp. 841–845, 2022.

[51] W.-C. Tsai, C.-W. Chen, and A.-Y. Wu, "Deep unfolding-based channel estimation for IRS-aided mmwave systems via two-stage LAMP network with row compression," *IEEE Transactions on Vehicular Technology*, vol. 73, no. 11, pp. 16832–16845, 2024.

[52] Z. Tang, Y. Chen, Y. Wang, T. Mao, Q. Wu, M. D. Renzo, and L. Hanzo, "Near-field sparse channel estimation for extremely large-scale RIS-aided wireless communications," in *2023 IEEE GLOBECOM Workshops (GC Wkshps)*, 2023.

[53] Y. Liu, X. Mu, J. Xu, R. Schober, Y. Hao, H. V. Poor, and L. Hanzo, "STAR: Simultaneous transmission and reflection for 360° coverage by intelligent surfaces," *IEEE Wireless Communications*, vol. 28, no. 6, pp. 102–109, 2022.

[54] X. Mu, Y. Liu, L. Guo, J. Lin, and R. Schober, "Simultaneously transmitting and reflecting (STAR) RIS aided wireless communications," *IEEE Transactions on Wireless Communications*, vol. 21, no. 5, pp. 3083–3098, 2021.

[55] Y. Zhu, G. Zheng, and K.-K. Wong, "Stochastic geometry analysis of large intelligent surface-assisted millimeter wave networks," *IEEE Journal on Selected Areas in Communications*, vol. 38, no. 8, pp. 1749–1762, 2020.

[56] T. Shafique, H. Tabassum, and E. Hossain, "Stochastic geometry analysis of IRS-assisted downlink cellular networks," *IEEE Transactions on Communications*, vol. 70, no. 2, pp. 1442–1456, 2022.

[57] C. Zhang, W. Yi, Y. Liu, K. Yang, and Z. Ding, "Reconfigurable intelligent surfaces aided multi-cell NOMA networks: A stochastic geometry model," *IEEE Transactions on Communications*, vol. 70, no. 2, pp. 951–966, 2021.

[58] M. A. Kishk and M.-S. Alouini, "Exploiting randomly located blockages for large-scale deployment of intelligent surfaces," *IEEE Journal on Selected Areas in Communications*, vol. 39, no. 4, pp. 1043–1056, 2020.

[59] T. Bai, R. Vaze, and R. W. Heath, "Analysis of blockage effects on urban cellular networks," *IEEE Transactions on Wireless Communications*, vol. 13, no. 9, pp. 5070–5083, 2014.

[60] T. Wang, G. Chen, M.-A. Badiu, and J. P. Coon, "Performance analysis of RIS-assisted large-scale wireless networks using stochastic geometry," *IEEE Transactions on Wireless Communications*, vol. 22, no. 11, pp. 7438–7451, 2023.

[61] Z. Li, H. Hu, J. Zhang, and J. Zhang, "RIS-assisted mmWave networks with random blockages: Fewer large RISs or more small RISs?," *IEEE Transactions on Wireless Communications*, vol. 22, no. 2, pp. 986–1000, 2022.

[62] X. Gan, C. Huang, Z. Yang, X. Chen, F. Bader, Z. Zhang, C. Yuen, Y. Liang Guan, and M. Debbah, "Modeling and coverage analysis of RIS-assisted integrated sensing and communication networks," *IEEE Transactions on Wireless Communications*, vol. 24, no. 7, pp. 6006–6019, 2025.

[63] Z. Li, H. Hu, J. Zhang, and J. Zhang, "Enhancing indoor mmWave wireless coverage: Small-cell densification or reconfigurable intelligent surfaces deployment?," *IEEE Wireless Communications Letters*, vol. 10, no. 11, pp. 2547–2551, 2021.

[64] H. Qin, Z. Liu, and C. Yang, "Indoor mm-ave coverage enhancement: Reconfigurable intelligent surface deployment strategy based on human mobility model," *IEEE Communications Letters*, vol. 26, no. 10, pp. 2475–2479, 2022.

[65] A. Azam, M. Imran, M. Ali, H. Z. Khan, A. Wakeel, and M. Naeem, "Joint user and throughput maximization in re-configurable intelligent surface assisted beyond 5g/6g networks," *Transactions on Emerging Telecommunications Technologies*, vol. 34, no. 8, p. e4807, 2023.

[66] H. Zhang, S. Zeng, B. Di, Y. Tan, M. Di Renzo, M. Debbah, Z. Han, H. V. Poor, and L. Song, "Intelligent omni-surfaces for full-dimensional wireless communications: Principles, technology, and implementation," *IEEE Communications Magazine*, vol. 60, no. 2, pp. 39–45, 2022.

[67] W. Cai, M. Li, Y. Liu, Q. Wu, and Q. Liu, "Joint beamforming design for intelligent omni surface assisted wireless communication systems," *IEEE Transactions on Wireless Communications*, vol. 22, no. 2, pp. 1281–1297, 2022.

[68] F. Yu, C. Zhang, and T. Q. Quek, "STAR-RIS-enabled simultaneous indoor-and-outdoor communication networks: A stochastic geometry approach," *IEEE Transactions on Wireless Communications*, 2024.

[69] Z. Liu, X. Chu, D. López-Pérez, and N. Tang, "Deployment strategy of intelligent omni-surface-assisted outdoor-to-indoor millimeter-wave communications," *IEEE Transactions on Wireless Communications*, vol. 23, no. 12, pp. 19172–19182, 2024.

[70] Y. Zhang, B. Di, H. Zhang, Z. Han, H. V. Poor, and L. Song, "Meta-wall: Intelligent omni-surfaces aided multi-cell MIMO communications," *IEEE Transactions on Wireless Communications*, vol. 21, no. 9, pp. 7026–7039, 2022.

[71] X. Mo, L. Gui, K. Ying, X. Sang, and X. Diao, "Reconfigurable intelligent surface deployment for wideband millimeter wave systems," *IEEE Transactions on Communications*, vol. 72, no. 5, pp. 2989–3004, 2024.

[72] X. Qian, X. Hu, C. Liu, and M. Peng, "Wideband beamforming with RIS: A unified framework via space-frequency transformation," *IEEE Transactions on Signal Processing*, vol. 73, pp. 173–187, 2024.

[73] Y. Chen, D. Chen, and T. Jiang, "Beam-squint mitigating in reconfigurable intelligent surface aided wideband mmwave communications," in *2021 IEEE Wireless Communications and Networking Conference (WCNC)*, pp. 1–6, 2021.

[74] K. D. Katsanos, N. Shlezinger, M. F. Imani, and G. C. Alexandropoulos, "Wideband multi-user MIMO communications with frequency selective RISs: Element response modeling and sum-rate maximization," in *2022 IEEE International Conference on Communications Workshops (ICC Workshops)*, pp. 151–156, IEEE, 2022.

[75] R. Li, B. Guo, M. Tao, Y.-F. Liu, and W. Yu, "Joint design of hybrid beamforming and reflection coefficients in RIS-aided mmWave MIMO systems," *IEEE Transactions on Communications*, vol. 70, no. 4, pp. 2404–2416, 2022.

[76] S. Liu, R. Liu, M. Li, Y. Liu, and Q. Liu, "Joint BS-RIS-user association and beamforming design for RIS-assisted cellular networks," *IEEE Transactions on Vehicular Technology*, vol. 72, no. 5, pp. 6113–6128, 2022.

[77] C. Huang, R. Mo, and C. Yuen, "Reconfigurable intelligent surface assisted multiuser MISO systems exploiting deep reinforcement learning," *IEEE Journal on Selected Areas in Communications*, vol. 38, no. 8, pp. 1839–1850, 2020.

[78] A. Faisal, I. Al-Nahhal, O. A. Dobre, and T. M. Ngatched, "Deep reinforcement learning for RIS-assisted FD systems: Single or distributed RIS?," *IEEE Communications Letters*, vol. 26, no. 7, pp. 1563–1567, 2022.

[79] A. Abdallah, A. Celik, M. M. Mansour, and A. M. Eltawil, "Multi-agent deep reinforcement learning for beam codebook design in RIS-aided systems," *IEEE Transactions on Wireless Communications*, vol. 23, no. 7, pp. 7983–7999, 2024.

[80] W. Tang, X. Chen, M. Z. Chen, J. Y. Dai, Y. Han, M. Di Renzo, S. Jin, Q. Cheng, and T. J. Cui, "Path loss modeling and measurements for reconfigurable intelligent surfaces in the millimeter-wave frequency band," *IEEE Transactions on Communications*, vol. 70, no. 9, pp. 6259–6276, 2022.

[81] C. X. Liu, F. Yang, X. J. Fu, J. W. Wu, L. Zhang, J. Yang, and T. J. Cui, "Programmable manipulations of terahertz beams by transmissive digital coding metasurfaces based on liquid crystals," *Advanced Optical Materials*, vol. 9, no. 22, p. 2100932, 2021.

[82] V. Jamali, H. Ajam, M. Najafi, B. Schmauss, R. Schober, and H. V. Poor, "Intelligent reflecting surface assisted free-space optical communications," *IEEE Communications Magazine*, vol. 59, no. 10, pp. 57–63, 2021.

[83] A. R. Ndjiongue, T. M. Ngatched, O. A. Dobre, and H. Haas, "Design of a power amplifying-RIS for free-space optical communication systems," *IEEE Wireless Communications*, vol. 28, no. 6, pp. 152–159, 2021.

[84] T. V. Nguyen, H. D. Le, and A. T. Pham, "On the design of RIS–UAV relay-assisted hybrid FSO/RF satellite–aerial–ground integrated network," *IEEE Transactions on Aerospace and Electronic Systems*, vol. 59, no. 2, pp. 757–771, 2022.

[85] Y. Xia and J. Ouyang, "PEDOT: PSS films with significantly enhanced conductivities induced by preferential solvation with cosolvents and their application in polymer photovoltaic cells," *Journal of Materials Chemistry*, vol. 21, no. 13, pp. 4927–4936, 2011.

[86] F. Zabihi, Y. Xie, S. Gao, and M. Eslamian, "Morphology, conductivity, and wetting characteristics of PEDOT: PSS thin films deposited by spin and spray coating," *Applied Surface Science*, vol. 338, pp. 163–177, 2015.

[87] T. D. Dorney, R. G. Baraniuk, and D. M. Mittleman, "Material parameter estimation with terahertz time-domain spectroscopy," *Journal of the Optical Society of America A*, vol. 18, no. 7, p. 1562, 2001.

[88] P. Jepsen, D. Cooke, and M. Koch, "Terahertz spectroscopy and imaging - modern techniques and applications," vol. 5, no. 1, pp. 124–166, 2011.

[89] M. Born and E. Wolf, *Principles of Optics: Electromagnetic Theory of Propagation, Interference and Diffraction of Light*. Elsevier, 2013.

[90] C. A. Balanis, *Antenna Theory: Analysis and Design*. John Wiley & Sons, 2015.

[91] X. Li, N. Tan, M. Pivnenko, J. Sibik, J. A. Zeitler, and D. Chu, "High-birefringence nematic liquid crystal for broadband THz applications," *Liquid Crystals*, vol. 43, no. 7, pp. 955–962, 2016.

[92] F. Firyaguna, J. Kibilda, C. Galiotto, and N. Marchetti, "Performance analysis of indoor mmWave networks with ceiling-mounted access points," *IEEE Transactions on Mobile Computing*, vol. 20, no. 5, pp. 1940–1950, 2020.

[93] R. P. Torres, J. R. Pérez, J. Basterrechea, M. Domingo, L. Valle, J. González, L. Rubio, V. M. Rodrigo, and J. Reig, "Empirical characterisation of the indoor multi-user MIMO channel in the 3.5 GHz band," *IET Microwaves, Antennas & Propagation*, vol. 13, no. 13, pp. 2386–2390, 2019.

[94] G. Ghatak, S. R. Khosravirad, and A. De Domenico, "Stochastic geometry framework for ultrareliable cooperative communications with random blockages," *IEEE Internet of Things Journal*, vol. 9, no. 7, pp. 5150–5161, 2021.

[95] Z. Li, H. Hu, J. Zhang, and J. Zhang, "Coverage analysis of multiple transmissive RIS-aided outdoor-to-indoor mmWave networks," *IEEE Transactions on Broadcasting*, vol. 68, no. 4, pp. 935–942, 2022.

[96] H. Radpour, M. Hofer, D. Löschenbrand, L. W. Mayer, A. Hofmann, M. Schiefer, and T. Zemen, "Reconfigurable intelligent surface for industrial automation: mmWave propagation measurement, simulation, and control algorithm requirements," in *2024 IEEE 35th International Symposium on Personal, Indoor and Mobile Radio Communications (PIMRC)*, pp. 1–7, 2024.

[97] O. Abbas, N. Kouzayha, M. Kishk, H. Sarieddeen, M.-S. Alouini, and T. Y. Al-Naffouri, "Performance analysis of indoor THz networks with intelligent reflective surfaces," in *ICC 2023 - IEEE International Conference on Communications*, pp. 2816–2821, 2023.

[98] C. Psomas, H. A. Suraweera, and I. Krikidis, "On the association with intelligent reflecting surfaces in spatially random networks," in *ICC 2021 - IEEE International Conference on Communications*, pp. 1–6, 2021.

[99] A. M. Mathai, *An Introduction to Geometrical Probability: Distributional Aspects with Applications*, vol. 1. CRC Press, 1999.

[100] H.-X. Xu, T. Cai, Y.-Q. Zhuang, Q. Peng, G.-M. Wang, and J.-G. Liang, "Dual-mode transmissive metasurface and its applications in multibeam transmitarray," *IEEE Transactions on Antennas and Propagation*, vol. 65, no. 4, pp. 1797–1806, 2017.

[101] Y. Liu, W. Li, and Z. Lin, "A dynamic subarray structure in reconfigurable intelligent surfaces for terahertz communication systems," in *2022 IEEE Conference on Standards for Communications and Networking (CSCN)*, pp. 224–229, IEEE, 2022.

[102] T. Mao, Z. Zhou, Z. Xiao, C. Han, and Z. Wang, "Index-modulation-aided terahertz communications with reconfigurable intelligent surface," *IEEE Transactions on Wireless Communications*, vol. 23, no. 7, pp. 8059–8070, 2024.

[103] E. Björnson, Ö. T. Demir, and L. Sanguinetti, "A primer on near-field beamforming for arrays and reconfigurable intelligent surfaces," in *2021 55th Asilomar Conference on Signals, Systems, and Computers*, pp. 105–112, IEEE, 2021.

[104] L. Chen, X. Yuan, and Y.-J. A. Zhang, "Coverage analysis of RIS-assisted mmWave cellular networks with 3D beamforming," *IEEE Transactions on Communications*, vol. 72, no. 6, pp. 3618–3633, 2024.

[105] K. Venugopal, M. C. Valenti, and R. W. Heath, "Device-to-device millimeter wave communications: Interference, coverage, rate, and finite topologies," *IEEE Transactions on Wireless Communications*, vol. 15, no. 9, pp. 6175–6188, 2016.

[106] K. K. Tiwari and G. Caire, "Flat-Top beamforming with efficient array-fed RIS," in *2025 IEEE 101st Vehicular Technology Conference (VTC2025-Spring)*, pp. 1–5, IEEE, 2025.

[107] C. A. Balanis, *Antenna Theory: Analysis and Design*. John Wiley & Sons, 2016.

[108] H. A. David and H. N. Nagaraja, *Order Statistics*. John Wiley & Sons, 2004.

[109] D. R. Smith, R. Liu, and T. J. Cui, *Metamaterials: Theory, Design, and Applications*. Springer, 2010.

[110] S. Yadav, R. Gour, G. C. Alexandropoulos, and D. S. Gurjar, "Performance analysis of RIS-aided two-way communications under hardware impairments and Rayleigh fading," in *2023 IEEE International Conference on Advanced Networks and Telecommunications Systems (ANTS)*, pp. 473–478, IEEE, 2023.

[111] Ö. Özdogan, E. Björnson, and E. G. Larsson, "Massive MIMO with spatially correlated rician fading channels," *IEEE Transactions on Communications*, vol. 67, no. 5, pp. 3234–3250, 2019.

[112] W. C. Jakes and D. C. Cox, *Microwave Mobile Communications*. Wiley-IEEE Press, 1994.

[113] S. L. Loyka, "Channel capacity of MIMO architecture using the exponential correlation matrix," *IEEE Communications Letters*, vol. 5, no. 9, pp. 369–371, 2001.

[114] E. Björnson, L. Sanguinetti, and M. Debbah, "Massive MIMO with imperfect channel covariance information," in *2016 50th Asilomar Conference on Signals, Systems and Computers*, pp. 974–978, IEEE, 2016.

[115] X. Ma, S. Guo, H. Zhang, Y. Fang, and D. Yuan, "Joint beamforming and reflecting design in reconfigurable intelligent surface-aided multi-user communication systems," *IEEE Transactions on Wireless Communications*, vol. 20, no. 5, pp. 3269–3283, 2021.

[116] Q. Sun, Y. Wu, X. Chen, and J. Zhang, "SLNR-based joint RIS-UE association and beamforming design for multi-RIS aided wireless communications," *IEEE Transactions on Vehicular Technology*, vol. 73, no. 6, pp. 8660–8670, 2024.

[117] Y. Zang, J. He, K. Li, H. Fu, Q. Fu, and J. Xing, "Sequential cooperative multi-agent reinforcement learning," in *Proceedings of the 2023 International Conference on Autonomous Agents and Multiagent Systems*, pp. 485–493, 2023.

[118] P.-G. de Gennes and J. Prost, *The Physics of Liquid Crystals*. Oxford: Clarendon Press, 2 ed., 1993.

[119] I.-C. Khoo, *Liquid Crystals*. John Wiley & Sons, 3 ed., 2022.

[120] S. Chandrasekhar, *Liquid Crystals*. Cambridge: Cambridge University Press, 2 ed., 1992.

[121] J. G. Andrews, A. K. Gupta, and H. S. Dhillon, "A primer on cellular network analysis using stochastic geometry," *arXiv preprint arXiv:1604.03183*, 2016.

[122] M. Haenggi, *Stochastic Geometry for Wireless Networks*. Cambridge University Press, 2013.

[123] H. Guo, Y.-C. Liang, J. Chen, and E. G. Larsson, "Weighted sum-rate maximization for reconfigurable intelligent surface aided wireless networks," *IEEE Transactions on Wireless Communications*, vol. 19, no. 5, pp. 3064–3076, 2020.

[124] R. S. Sutton, A. G. Barto, *et al.*, *Reinforcement Learning: An Introduction*, vol. 1. MIT Press, 1998.

[125] V. Mnih, K. Kavukcuoglu, D. Silver, A. Graves, I. Antonoglou, D. Wierstra, and M. Riedmiller, "Playing atari with deep reinforcement learning," *arXiv preprint arXiv:1312.5602*, 2013.

[126] V. Mnih, K. Kavukcuoglu, D. Silver, A. A. Rusu, J. Veness, M. G. Bellemare, A. Graves, M. Riedmiller, A. K. Fidjeland, G. Ostrovski, *et al.*, "Human-level control through deep reinforcement learning," *Nature*, vol. 518, no. 7540, pp. 529–533, 2015.

[127] T. P. Lillicrap, J. J. Hunt, A. Pritzel, N. Heess, T. Erez, Y. Tassa, D. Silver, and D. Wierstra, "Continuous control with deep reinforcement learning. arXiv 2015," *arXiv preprint arXiv:1509.02971*, 2015.

[128] D. Silver, G. Lever, N. Heess, T. Degris, D. Wierstra, and M. Riedmiller, "Deterministic policy gradient algorithms," in *International Conference on Machine Learning*, pp. 387–395, PMLR, 2014.

[129] S. Fujimoto, H. Hoof, and D. Meger, "Addressing function approximation error in actor-critic methods," in *International Conference on Machine Learning*, pp. 1587–1596, PMLR, 2018.

[130] V. Mnih, A. P. Badia, M. Mirza, A. Graves, T. Lillicrap, T. Harley, D. Silver, and K. Kavukcuoglu, "Asynchronous methods for deep reinforcement learning," in *International Conference on Machine Learning*, pp. 1928–1937, PMLR, 2016.

[131] J. Schulman, F. Wolski, P. Dhariwal, A. Radford, and O. Klimov, "Proximal policy optimization algorithms," *arXiv preprint arXiv:1707.06347*, 2017.